UNIVERSIDADE
DE VIGO

Metodología 3D para el análisis de sobrecalentamiento en elementos estructurales de transformadores de potencia

Tesis Doctoral

Mención de Doctor Internacional

Patricia Penabad Durán

Director
Prof. Dr. Ing. Xose M. López Fernández

Dpto. Ingeniería Eléctrica
Universidade de Vigo
Vigo, Julio 2013

UNIVERSIDADE
DE VIGO

Metodología 3D para el análisis de sobrecalentamiento en elementos estructurales de transformadores de potencia

Tesis Doctoral

Mención de Doctor Internacional

Patricia Penabad Durán

Supervisor
Prof. Dr. Eng. Xose M. López Fernández

Autora:

Patricia Penabad Durán

Visto y place del director:

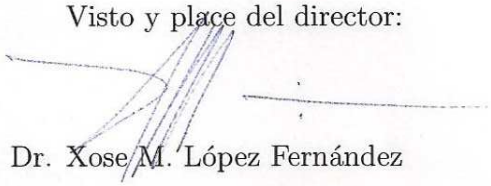

Prof. Dr. Xose M. López Fernández

Dpto. Ingeniería Eléctrica
Universidade de Vigo
Vigo, Julio 2013

3D Methodology for the Overheating Assessment on Power Transformers Structural Parts

Submitted for the degree of

Doctor of Philosophy

International Doctor mention

Patricia Penabad Durán

Supervisor
Prof. Dr. Eng. Xose M. López Fernández

Dept. Electrical Engineering
University of Vigo
Vigo, Spain
July 2013

A mi familia

Acknowledgments

This research was conducted in the University of Vigo under a four-year program "Axudas predoutorais: Programa específico para a formación predoutoral en áreas de especial dificultade para contratar doutores" within the Research Scholarships Program 2009. I highly appreciate the financial support from the University of Vigo, also for covering partly mobility expenses from my doctoral stay at the University of Pavia and from several International Conferences I attended, which gave value to this work permitting to exchange comments and hear the feedback from experts and researches from other international institutions.

I would like to express my most sincere acknowledgment to my supervisor, Prof. Xose M. López Fernández, from the Department of Electrical Engineering, University of Vigo, for his constructive supervision, encouragement, intensive discussion, critical comments and proper direction. He has always motivated and supported me to do high quality research work.

I also express my sincere gratitude to Prof. Paolo Di Barba, from the University of Pavia, Italy, from whom I did benefit from his expertise in Inverse Problems and Optimization in Electricity and Magnetism. I am indebted to him for having me in his Electromagnetic Devices CAD Laboratory in the University of Pavia for a training period of four months to conduct part of this doctoral research, for his cooperation and for his valuable suggestions on this work.

I would like to thank Prof. Janusz Turowski, retired from the Institute of Electrical Machines and Transformers, Lodz, Poland, for his constructive comments and devoted expertise.

I thank Prof. Antonio Savini from University of Pavia, Italy and Prof. Kazimierz Zakrzewski from Technical University of Lodz, Poland for supporting this dissertation and their recommendation for the International Doctor Mention.

I am thankful to Efacec Energía S. A. Power Transformers for promoting the industrial context and the experimental work providing a deeper knowledge within this research field.

I thank my colleague Casimiro Alvarez Mariño from the Department of Electrical Engineering, University of Vigo, for his support from time to time and joint work.

My sincere thanks to all those who have helped me directly of indirectly in my research program.

Patricia Penabad Durán

Abstract

On power transformer structural parts the main design criterion is the limit temperature rise caused by leakage field due to the high current leads. Previous works found in the literature focus their results on the consequences of electromagnetic leakage flux in terms of stray power losses. The calculation of stray losses is, of course, also important to guarantee the total losses. However, the drawback of such computational proposals is that the direct measurement of stray losses is not achievable in the vast majority of cases and, therefore, they are difficult to validate. For this reason, this dissertation proposes to compute the consequences of leakage flux not only in terms of losses but also in terms of temperature distribution. The objective is to offer a practical tool to compute the temperature distribution and to localize the hot spot areas on metallic structural parts heated by electromagnetic induction.

A three-dimensional methodology for the overheating hazard assessment based on electromagnetic analytical formulation linked with thermal finite element method is presented. The proposed methodology is carefully focused on those cases where the electromagnetic wave penetration depth compared to the big machine dimensions is a key issue. Thus, stray losses into the thin skin depth penetration can be readily calculated with the analytical model, based on Poynting's Vector formulation. Then, the temperature distribution is computed by means of 3D FE thermal analysis, where the penetration depth sets the volume thickness where losses are introduced.

Moreover, the material data required for computation might be inaccurate as they are taken from catalogues or the literature and boundary conditions of heat exchange are difficult to determine from theory or measurements. An attempt to identify these parameters by means of multi-objective deterministic and non-deterministic optimization algorithms is proposed ensuring thus the accuracy of obtained results.

An experimental work is presented, and numerical results are discussed and compared to measurements. Test are carried out for transformer cover plate and tank wall over a wide range of currents and varying also other design parameters, i.e. plate thickness, distance between conductors or including amagnetic material, in order to validate the computational methodology.

To stress the potentiality of the tool, some practical applications are presented, which include the overheating analysis on complex 3D structural parts, the design of amagnetic inserts on three-phase transformer cover plates and the evaluation of the overheating hazard due to zero sequence flux on tank walls taking into account the influence of the tertiary stabilizing windings.

List of Publications

X. M. Lopez-Fernandez, P. Penabad-Duran, and J. Turowski, "Three-dimensional methodology for the overheating hazard assessment on transformer covers," *Industry Applications, IEEE Transactions on*, vol. 48, pp. 1549-1555, Sept.-Oct. 2012.

X. M. Lopez-Fernandez, P. Penabad-Duran, J. Turowski, and P. M. Ribeiro, "Non linear heating hazard assessment on transformer covers and tank walls," *Przeglad Elektrotechniczny* (Electrical Review), vol. 88, no. 7b, pp. 28-31, 2012.

P. Penabad-Duran, X. M. Lopez-Fernandez, J. Turowski, and P. M. Ribeiro, "3D heating hazard assessment on transformer covers. Arrangement decisions," *COMPEL: The International Journal for Computation and Mathematics in Electrical and Electronic Engineering*, vol. 31, no. 2, pp. 703-7015, 2012.

X. M. Lopez-Fernandez, C. Alvarez-Mariño, P. Penabad-Duran and J. Turowski, "RNM2D_0 Fast Stray Losses Hazard Evaluation on Transformer Tank Wall & Cover due to Zero Sequence", *Proc. of* 3rd *Advanced Research Workshop on Transformers* (ARWtr2010), Santiago de Compostela, Spain, pp. 338-343, Oct. 2010.

P. Penabad-Duran and X. M. Lopez-Fernandez, "Part A: Introduction to FEM Analysis," in *ARWtr FEM Tutorial. Finite Element Method applied to design and analysis in power transformers* (Xose M. Lopez-Fernandez, editor & publisher), Santiago de Compostela, Spain, 2010, ISBN:978- 84-614-3527-2.

P. Penabad-Duran, X. M. Lopez-Fernandez, C. Alvarez-Mariño, "Transformer Tertiary Stabilizing Windings: Part I: Apparent Power Rating," XXth *International Conference on Electrical Machines* (ICEM2012), Marseille, France, pp. 2362-2368, Sept. 2012.

P. Penabad-Duran, C. Alvarez-Mariño, X. M. Lopez-Fernandez, "Transformer Tertiary Stabilizing Windings: Part II: Overheating hazard on tank walls," XXth *International Conference on Electrical Machines* (ICEM2012), Marseille, France, pp. 2369-2374, Sept. 2012.

P. Penabad-Duran, P. Di Barba, X. M. Lopez-Fernandez and J. Turowski, "Electromagnetic and Thermal Parameter Identification Method for Best Prediction of Temperature Distribution on Transformer Tank Covers," Accepted to be presented in: XVIth *International Symposium on Electromagnetic Fields* (ISEF2013), Ohrid, Macedonia, September 12-14, 2013.

P. Penabad-Duran, X. M. Lopez-Fernandez and J. Turowski, "3D Non-Linear Magneto-Thermal Behavior on Transformer Covers," Submitted for first review to *Electric Power Systems Research* on Apr. 2013.

Contents

List of Figures

List of Tables

Resumen - Spanish Summary

Metodología 3D para el análisis de sobrecalentamiento en elementos estructurales de transformadores de potencia

Existen un gran número de técnicas de simulación disponibles en electromagnetismo para asistir al diseño de dispositivos electromagnéticos, en particular, de transformadores de potencia. Sin embargo, se necesitan satisfacer las necesidades de los clientes cada vez más exigentes y ser cada vez más competitivos en términos de costes de fabricación, alta eficiencia, fiabilidad o peso. Además con el desarrollo de nuevas tecnologías y materiales, se hace especialmente crítico analizar cada diseño propuesto con el máximo detalle, para que se puedan conseguir soluciones óptimas. Por tanto, el desarrollo de técnicas novedosas y métodos emergentes para aplicaciones de simulación multifísica hacen que sea un área de investigación muy amplia y próspera, dentro de la cual se enmarca esta tesis doctoral.

El trabajo de investigación aquí presentado, se ha realizado en el marco de ayudas a la investigación 2009 concedidas por la Universidad de Vigo, dentro del "Programa específico para la formación predoctoral en áreas con especial dificultad para contratar doctores".

Introducción

En máquinas y equipos eléctricos de gran potencia los conductores con intensidades elevadas que pasan cerca de paredes metálicas o atraviesan las paredes de la carcasa, son elementos térmicamente peligrosos y fuente adicional de pérdidas. En el caso particular de los transformadores de potencia, la fiabilidad, los puntos calientes y el mantenimiento dependen de los efectos térmicos producidos por la distribución del flujo electromagnético.

Los métodos de diseño de las partes activas, el núcleo y los devanados, están bien establecidos. Por el contrario, el diseño de componentes inactivas como los elementos estructurales no es tan directo y se requiere un estudio minucioso. El control y la minimización del sobrecalentamiento en los pasatapas de los transformadores juegan un papel importante y decisivo en el comportamiento del transformador. Sus consecuencias más significativas son el ahorro de energía y reducir el peligro de los apagones, que causan elevados costes a las distribuidoras y clientes, debido a que los transformadores son un unos de los elementos más importantes de las redes eléctricas.

This is a PhD thesis summary, written in Spanish to meet requirements from the University of Vigo.

Por tanto, la predicción y localización de las pérdidas por dispersión y puntos calientes y sus consecuencias se vuelven una cuestión vital para los fabricantes. Normalmente, estos efectos se minimizan aumentando la distancia entre los conductores y la pared o colocando apantallamientos electromagnéticos y en el caso de los pasatapas se utiliza acero amagnético. Este es un fenómeno muy conocido, pero los fabricantes y diseñadores cada vez están más sensibilizados con este problema debido a una serie de factores: el aumento de potencia de los transformadores, elevado coste de los materiales y la reducción del tamaño del transformador, impuestos por un mercado cada vez más competitivo.

Motivación

Las referencias encontradas en la literatura centran sus resultados en las consecuencias del flujo electromagnético de dispersión en términos de pérdidas. Sin embargo, el inconveniente de esas propuestas es que no es posible la medida directa de la distribución de pérdidas en la mayoría de los casos, y por tanto son difíciles de validar. Por otro lado, es una realidad que la temperatura superficial se puede medir y monitorizar fácilmente a través de sensores disponibles en el mercado.

Aunque el cálculo de pérdidas por dispersión en transformadores de potencia es también importante para garantizar las pérdidas totales, el incremento de temperatura local debido a altos valores de densidad de flujo son más importantes. Uno de los principales factores que influye en el envejecimiento de los transformadores es la temperatura y la distribución de la densidad de pérdidas puede dar lugar a valores de temperatura peligrosos si los materiales no se seleccionan de manera adecuada. Además, el principal criterio de diseño de pasatapas y otros elementos estructurales es el incremento de temperatura causado por la exposición a campos magnéticos generados por corrientes elevadas de hasta varios kA. Las normas que se aplican establecen unos valores de temperatura límite de hasta 140 °C para todas las partes metálicas, y comprobar este requerimiento en los diseños se hace esencial.

En este escenario surge la necesidad de una herramienta práctica capaz de evaluar la temperatura de manera precisa y establecer criterios claros para identificar el peligro de sobrecalentamiento en transformadores. Esta herramienta sólo se puede considerar utilizando un análisis 3D magneto-térmico, donde el cálculo de temperatura permite verificar indirectamente el cálculo del flujo de dispersión y las pérdidas. Esto resulta de una gran importancia práctica, puesto que así se puede validar la temperatura de manera experimental y localizar los puntos calientes.

Los problemas que conllevan el uso de materiales magnéticos siempre están caracterizados por la pequeña profundidad de penetración del campo dentro del metal, pero además aparecen complicaciones adicionales debido a su característica no lineal y saturación. Existen paquetes de software comerciales basados en el Método de Elementos Finitos (MEF), muy utilizados en el mercado, pero en esos casos, incluso los cálculos 2D se hacen complicados, y requieren gran cantidad de tiempo computacional y memoria. Esto se debe a que se necesita una discretización muy fina para calcular las pérdidas dentro de la pequeña profundidad de penetración del flujo electromagnético, que es de

aproximadamente 1 mm, comparado con las dimensiones de varios metros del volumen del transformador. Además la solución de problemas 3D de corrientes inducidas con MEF requiere un conocimiento profundo de la formulación para garantizar las condiciones de contorno adecuadas, estabilidad de cálculo, minimizar el número de variables o la habilidad para tratar discontinuidades en las propiedades de los materiales.

Por tanto se puede concluir que los complejos modelos 3D no son adecuados todavía para implementar en la etapa de diseño de transformadores de potencia ya que el modelado y resolución demandan mucho tiempo y esfuerzo comparado con los tiempos de mercado, además de usuarios expertos. Además, si se requieren resultados fiables, se necesita precisión en el cálculo de las pérdidas y temperatura. Por otro lado, se pueden obtener fórmulas sencillas a través de métodos analíticos, que permiten un cálculo más rápido para determinar las pérdidas, y tienen la ventaja de que su resultado se puede incorporar en otros programas que calculan, por ejemplo, la temperatura resultante.

Objetivos y contribución

Los fabricantes y diseñadores de transformadores requieren métodos de cálculo rápidos, específicos y fáciles de utilizar para acelerar los procesos de diseño. Los métodos de cálculo analíticos, combinados con datos experimentales u otros métodos proporcionan modelos eficientes para una representación precisa de determinadas características del trasformador. En esta dirección, el trabajo de investigación que se presenta en esta tesis describe el desarrollo del herramientas de cálculo de pérdidas y temperatura aplicadas al diseño de pasatapas, tapas y paredes del tanque del transformador.

Otros trabajos que encuentran en la literatura, se refieren al sobrecalentamiento en elementos estructurales en términos de densidad de pérdidas o intensidad de campo magnético, que son difíciles de validar experimentalmente. Por el contrario, las consecuencias del flujo de dispersión en términos de distribución de temperatura son fáciles de validar y por esta razón la metodología propuesta se centra en el cálculo de la temperatura.

Por tanto, se presenta una metodología 3D que combina una formulación analítica para el cálculo electromagnético con el análisis térmico por el MEF para evaluar el peligro de sobrecalentamiento en elementos estructurales de transformadores. Así, se solventan las dificultades del cálculo de pérdidas en la profundidad de penetración, mientas que el análisis 3D MEF térmico permite comprobar experimentalmente los resultados obtenidos. Se presentan además una serie de experimentos que permiten validar la metodología de cálculo propuesta, en los que se evalúan los efectos térmicos inducidos en chapas de acero por conductores de alta intensidad.

La precisión en el cálculo de pérdidas es necesaria para estimar el incremento de temperatura y diseñar métodos para eliminar y controlar sus efectos más peligrosos. Por tanto, en este trabajo de investigación se profundiza en la implementación de una formulación analítica considerando el comportamiento no lineal de la profundidad de penetración. Este comportamiento permite un mejor entendimiento del fenómeno electromagnético y permite además establecer la profundidad del volumen en el que se localizan las pérdidas en el modelo térmico.

Por último, un aspecto importante en la metodología propuesta es garantizar la precisión del los resultados para otras condiciones de carga o distinto número de conductores. Esto se consigue incluyendo un proceso de optimización que identifica los parámetros de entrada adecuados para los cálculos electromagnético y térmico. La calibración del modelo se basa en datos experimentales, y se incluye la sensibilidad del modelo a posibles errores en la medida.

Metodología de cálculo

La metodología de cálculo propuesta en esta tesis doctoral, empieza con el modelo analítico electromagnético que permite calcular las pérdidas debidas al flujo de dispersión. Después de introducir parámetros geométricos, propiedades de los materiales y el valor de la fuente de intensidad, se obtiene la representación del campo magnético aplicando la ley de Biot-Savart. El siguiente paso es el cálculo de la distribución de pérdidas disipadas debido a la presencia de conductores con corrientes elevadas integrando la formulación analítica del teorema de Poynting.

Los aspectos físicos y matemáticos relacionados con el modelo electromagnético se explican en detalle. Se demuestra como aplicando el Vector Poynting en un modelo que consta de un conductor con intensidad elevada posicionado cerca de una superficie metálica permeable se puede calcular cómo la energía electromagnética fluye en el sistema, la transferencia de energía y la disipación de pérdidas en forma de calor.

Se comienza con la formulación de las ecuaciones de onda electromagnéticas dentro del un conductor, a partir de las ecuaciones de Maxwell. Cuando una onda electromagnética incide en un metal conductor, se propaga un pequeña distancia que es la llamada profundidad de penetración δ. Además, a partir de la relación entre los valores superficiales del campo eléctrico y magnético se define el valor de la impedancia superficial $\mathbf{Z}_s$ que tiene valores de Ohmios (Ω).

El teorema de Poynting es el teorema principal de conservación de energía para campos electromagnéticos y permite identificar todas las fuentes de energía en un determinado volumen. La formulación del Vector Poynting se obtiene a partir de las ecuaciones de Maxwell e indica la dirección y densidad de potencia en un punto determinado del sistema. Por tanto es posible representar como se propaga el flujo de energía en el espacio a través de ondas electromagnéticas dentro y fuera de los conductores, y como esta se transforma en pérdidas dentro del conductor.

Por tanto a partir de la formulación del Vector Poynting e integrando en la superficie a calcular se pueden obtener las pérdidas por dispersión, siendo conocida la distribución de campo magnético en la superficie del metal. Si se han de tener en cuenta además la característica no lineal del acero e histéresis, se deben aplicar factores de linealización que dependen del material y del tipo de superficie estudiada. En esta tesis se explica en detalle el origen de estos factores, y su interpretación física. Se destaca el comportamiento no lineal de la permeabilidad magnética en la superficie del metal y su comportamiento no lineal dentro del propio metal. También se debe considerar el factor de apantallamiento, que depende de la relación entre el espesor del metal y la longitud de onda del campo, que pueden dar lugar a fenómenos de reflexión y consecuente disminución de las pérdidas.

Por último, se describe la formulación analítica en términos de impedancia superficial y profundidad de penetración no lineal. Esta formulación permiten combinar el comportamiento en la zona lineal y saturación a través de una función de peso que tiene en cuenta el grado de saturación del material. Así es posible introducir de manera sencilla el comportamiento no lineal y la saturación de materiales ferromagnéticos en el modelo analítico.

Se incluye en la descripción de la metodología computacional también la formulación analítica del campo magnético para los dos tipos de excitación que aparecen en el transformador: tangencial y normal. La excitación tangencial aparece en la tapa y pasatapas del transformador, donde los conductores atraviesan la chapa metálica, y la excitación normal se debe a conductores que pasan paralelos a las paredes del tanque.

Por otro lado, a partir de la solución analítica, la potencia disipada se introduce dentro de la región de la impedancia superficial en el modelo térmico, como fuentes de calor. Además la profundidad de penetración no lineal obtenida a partir de la representación analítica permite establecer en el modelo térmico la profundidad exacta de regiones en las que se ubican dichas fuentes de calor. Aplicando las condiciones de contorno adecuadas se calcula la distribución de temperatura en régimen estacionario, conectando de esta manera los dos modelos.

Ensayos de laboratorio

Con el objetivo de ilustrar la capacidad de la metodología de cálculo presentada en esta tesis como una herramienta práctica para el análisis de puntos calientes en elementos estructurales del transformador se realizan una serie de ensayos experimentales. Este estudio ha sido realizado gracias a la colaboración de Efacec Energía S. A. Power Transformers. Los ensayos están diseñados para determinar las áreas que alcanzan un mayor incremento de temperatura en chapas de acero utilizadas en pasatapas, tapas y paredes del tanque, como consecuencia de la presencia de conductores con intensidades elevadas.

Se toman medidas de temperatura en régimen estacionario en varios tipos de ensayos. Por un lado se hacen ensayos tipo tapa, en los que una chapa de acero posicionada en horizontal sobre un soporte es atravesada por uno o varios conductores. Por otro lado se hacen ensayos tipo pared, en los que uno o varios conductores pasan paralelos a una chapa de acero colocada en posición vertical. Por último se hacen ensayos en pasatapas con forma redonda y cuadrada atravesados por un conductor.

Se tienen en cuenta varios parámetros de diseño a la hora de realizar los ensayos, como la magnitud y fase de la corriente (desde 200 A a 2.5 kA), distancia entre conductores, la distancia entre los conductores y la chapa de acero, el número de conductores y su disposición (en vertical u horizontal), el espesor de las chapas de acero y los materiales.

Los ensayos se realizan en aire de manera que se obtiene condiciones de refrigeración más severas que las que realmente tienen lugar con el aceite del transformador. Pero una vez que haya validado el método de cálculo las condiciones de contorno se pueden cambiar por factores correspondientes a condiciones reales.

Identificación de parámetros de cálculo

Una vez establecida la metodología de cálculo se ha encontrado la dificultad de establecer datos de propiedades de los materiales y condiciones de contorno a partir de catálogos o en la literatura que sean realmente fiables. En la metodología de cálculo propuesta estas incertidumbres se evitan introduciendo un método de identificación de parámetros, es decir se calibran los modelos de cálculo. Su objetivo es identificar y ajustar los parámetros de entrada electromagnéticos y térmicos para la simulación, de manera que los resultados se ajustan a las mediciones de temperatura tomadas como referencia. Una vez que los parámetros de entrada han sido identificados, la distribución de temperatura se puede calcular, por ejemplo, para otros valores de carga o distinto número de conductores. Este trabajo se ha realizado durante una estancia de investigación en la Universidad de Pavia, Italia, bajo la supervisión del Prof. Paolo Di Barba, beneficiándonos de su experiencia en problemas inversos y optimización en electricidad y magnetismo.

Se describe una técnica para la identificación de estos parámetros basada en algoritmos de optimización mono-objetivo y multi-objetivo. Además se detallan una serie de estudios claves como la influencia relativa de cada parámetro en la distribución de temperatura final, o la sensibilidad del modelo a posibles errores introducidos en la medida.

El proceso de solución del problema inverso comienza con la implementación de un algoritmo de optimización mono-objetivo para identificar los parámetros de entrada óptimos para la simulación. El siguiente paso es determinar la sensibilidad de dicha solución. Para ello se introduce una perturbación en los parámetros de entrada del modelo y se determina cuanto afecta a la salida. Se ha comprobado, que existen soluciones que son menos sensibles a estas perturbaciones, es decir, menos sensibles a errores introducidos en la medida. Por tanto este conjunto de soluciones (frente de Pareto) se identifican a través de algoritmos de optimización multi-objetivo. Se aplican un algoritmo determinístico y otro no determinístico, GATT y NSGA-II respectivamente. No obstante, existen en la literatura una gran variedad de algoritmos que se pueden utilizar para automatizar el proceso de calibración.

A través de la optimización multi-objectivo se obtienen una serie de soluciones que se pueden seleccionar dependiendo de los requerimientos de precisión y sensibilidad de cada modelo. Además se ha comprobado que con los dos algoritmos se consigue la identificación de soluciones bien distribuidas en el frente, pero el GATT requiere más tiempo de cálculo y correr el algoritmo varias veces variando la solución inicial y discretizando las direcciones de búsqueda para centrarse en la región de interés.

Resultados y conclusiones

Una vez identificados los parámetros de entrada óptimos, se presentan una serie de casos de estudio para analizar en detalle el comportamiento no lineal en el modelo analítico. A través del modelo de profundidad de penetración no lineal que se describe en esta tesis, se representan resultados de un amplio rango de corrientes destacando el comportamiento según se trabaje en la zona lineal o de saturación de la curva del acero.

También se presentan una serie de resultados de simulaciones térmicas tanto para

uno o dos conductores y se validan con medidas obtenidas en forma de termografías a través de los ensayos, donde realmente se demuestra el potencial de esta metodología. Se compara la distribución de temperatura entre simulaciones y ensayos a la hora de evaluar la influencia del espesor de la chapa, y también el uso de materiales amagnéticos. De esta manera, indirectamente se valida también el cálculo de las pérdidas. Además en el caso de las paredes del tanque la metodología de cálculo se extiende al uso de modelos en 2D, en los que también se validan los resultados de la distribución de temperatura con termografías.

Para destacar la potencialidad de esta herramienta de cálculo, se presentan aplicaciones prácticas que incluyen el cálculo de temperatura en elementos estructurales 3D más complejos y que combinan distintos materiales, el diseño de injertos amagnéticos en tapas planas de tanque de transformadores trifásicos y la evaluación del peligro de sobrecalentamiento en paredes del tanque debido a la presencia del flujo de secuencia cero, teniendo en cuenta si el devanado de estabilización está o no conectado.

Futuras líneas de trabajo implicarían el uso de la herramienta de cálculo en el ámbito industrial, validando casos prácticos, con valores de corriente mucho más elevados, con distinto número de conductores y distintos desfases.

Chapter 1

Introduction

In field simulation there are a large number of techniques available to assist in the design of electromagnetic devices, and in particular of power transformers. Commercial software packages offer efficient modeling and modern simulation tools and the vast literature available on the subject covers various aspects of field simulations in the context of optimum design and performance prediction of the studied device. Nevertheless, designers of modern transformers need to satisfy customers and be competitive in terms e.g. of low manufacturing and operating costs, high efficiency, reliability or minimum weight. Moreover, new types of technologies and new materials are being developed and investigated. Thus, it becomes increasingly critical to analyze any proposed design in considerable detail, so that an optimum solution might be achieved. Emerging new techniques and methods for multi-physics applications [1], also in the area of multiobjective optimization [2] make it to be a prosperous area of research.

1.1 Background

In the recent years the power industry is faced with an important challenge to keep design and development cost at a minimum and at the same time they need to design power transformers with energy efficient criteria. Methods for design of active parts, core and windings, are well established. Contrarily the design of inactive components such as the structural parts, is still not straightforward and requires careful treatment [3].

Losses produced on structural parts of large power transformers are due to both, leakage flux from windings and high current leads passing near conducting parts of the tank walls, including also low voltage bushing terminations. In addition, high current leads passing close to conducting plates and housing walls of large power equipment are thermally hazardous elements of construction [4]. Therefore, they not only reduce the efficiency of transformers, but also give rise to local high temperatures, more important in terms of safety and reliability. Hot spots, reliability and maintenance closely depend on the thermal effects produced by the distribution of electromagnetic leakage flux [5]

and they shorten transformers service life [6]. Specially, low voltage bushing terminations are areas of high risk and hot spots are more likely to develop since the cooling effect of transformer oil is negligible and eddy current densities are very high. The excessive overheating in those components could be dangerous at overloading, which is not uncommon nowadays [5].

The subject of tank wall losses near the low voltage bushings in power and distribution transformers has received little attention. The minimization and control of the consequent overheating in bushing plates and other structural parts play a decisive role in transformer performance. Their significant consequences are energy savings and reduce the risk of shutdowns. They involve high cost to utilities and customers as transformers are one of the most expensive components in electric system networks [4]. This means that the accurate prediction and localization of stray losses and their thermal consequences become a vital issue for manufacturers. Usually these losses are mitigated by moving the conductors farther away from the wall [7] or by placing a shield of high conductivity and low permeability on the tank wall near the high current conductors [8]. In the case of bushing turrets and tank cover plates, they are usually made of stainless steel [9].

This is a well know phenomenon but manufacturers and designers are nowadays more concerned about this problem due to the combination of factors: the increasing of power rating in power transformers, the high cost of materials, and the reduction of the overall size of the transformer imposed by a more and more competitive market [10]. Efforts made on efficient design of transformers, not only focus on loss reduction, but also on manufacturing costs reduction and the present study is part of such effort.

1.2 Motivation

References and previous works found in the literature [11], [12], focus their results on the consequences of electromagnetic leakage flux in terms of stray power losses [13], [14]. The drawback found by authors of such computational proposals is that the direct measurement of stray losses is not achievable in the vast majority of cases, and therefore they are difficult to validate. Meanwhile it is a fact that the surface temperature can be easily monitored nowadays by means of temperature sensors available at the market.

Although stray losses computation in large rating transformers is, of course, also important to guarantee the total losses, the local temperature rise due to high values of incident flux density is more important. One of the fundamental criteria which influences the transformer ageing and the degree of loading is the transformers temperature. The loss density distribution may attain levels leading to hazardous local temperature rise if the material and design are not selected properly. Besides, the main design criterion of the bushing adapters in large transformers is the limit of the temperature rise caused by the exposure of the adapters to the magnetic field generated by high current leads carrying several kA. The applicable standards used for the design of power transformers specify a temperature limit of 140 °C for all metallic parts of the transformer because above this temperature gas formation starts developing in the oil, with its consequent

insulation damage [15], [16]. Many papers are devoted to accurately calculate transformer oil and windings temperature [17], but only in recent years some attention has been paid the temperature calculation on structural parts starts [9], [18], [19]. To proof a design against this requirement becomes essential.

In this scenario, there arises the need for a practical tool capable of assessing the temperature distribution accurately and establish clear criteria to identify overheating hazard in transformers. Such tool can be correctly considered only by using a coupled 3D magneto-thermal analysis [20], [21] where the temperature calculation indirectly permits to verify the underlying leakage field and stray losses calculation. It is of great practical importance for transformer designers since the temperature can be validated experimentally and overheated points can be localized.

Problems involving magnetic materials are almost always characterized by small penetration depths but in addition there are further complications due to the non-linear material characteristics and saturation of ferromagnetic materials [22], [23], [24]. Any calculation of the electromagnetic field or losses due to eddy currents in ferromagnetic bodies is complicated by the fact that the permeability of the material depends on the magnetic field itself. In such cases, even two dimensional problems could place unreasonable demands on the computational time and storage.

In the recent years, some authors invested efforts to demonstrate that the 3D Finite Element Method (FEM) is capable of routinely providing a solution to a large, complex real-world problem and can hence be incorporated in the design cycle of large transformers [24], [25], [26], [27]. However, solving a 3D FEM eddy current problem is not straightforward and requires advanced knowledge on the formulations, particularly in the case of a multiply connected problems, such as the tank cover. Additionally, from industrial perspective computing transformer losses on its structural parts from a 3D model taking into account non-linear material properties and complex geometries is not the most adequate from a practical point of view due to its non-affordable computational time. Often authors advise to perform a separate study with different solvers and formulations to compute stray losses due to windings or high currents leads on certain structural parts of transformers such are the tank walls and bushing adapters [28].

Thus, it can be concluded that full 3D models are still not suitable to implement on the design stage of power transformers. Modeling and solving still demand much time and effort in the scale of a rapid response in market time, and it does require experienced users. Moreover, for the computation of the stray losses and resulting temperature from the electromagnetic induction heating, such accurate model must be taken into account if calculations are to be reliable [28], [29]. On the other hand, simple formulae can be obtained by means of analytical methods, which provided with a deep experience and understanding of the phenomenon permit quicker and easier determination of losses. Their correctness can easily be proved by measurements made on a model, and their accuracy can be improved by correction factors determined experimentally of from other empirical data [16]. Analytic methods can not only help one to quickly assess the effect on losses of e.g. repositioning the bus bars or using shields of different materials, but also make possible to incorporate such loss calculations in other computer programs which

calculate, for example, the plate temperature rise resulting from these losses [7].

1.3 Objectives

The complexity of transformer design demands reliable and rigorous solution methods. Since complicated methods are impractical for day-to-day use, solutions using simpler methods but giving sufficiently accurate answers are in constant demand by designers. Transformer developers need rapid, easy to use and specialized software tools for specific features on transformer analysis to speed up their processes [28]. Such are experimental methods, combining data provided by measurements with analytical or other methods, in order to provide efficient models for the accurate representation of certain transformer characteristics [30].

In this direction, the work presented in this thesis reports the development stray loss and temperature computation tools applied to the design of transformer tank covers, bushing adapters and tank walls of power transformers.

References found in the literature refer to overheating and hot spots only in terms of magnetic field strength or stray loss density distribution. However, in practice stray loss densities are difficult to measure and those methods might result inaccurate. For that reason, the temperature computation is the novelty addressed in this research, where the specific objectives are:

- To present a computational methodology based on an electromagnetic analytical formulation linked with a 3D FE thermal analysis. Thus, the problems to compute the stray power losses into the thin skin depth penetration are overcome analytically. Meanwhile, the 3D FE thermal analysis easily allows checking experimentally the obtained results.

- To include a non-linear penetration depth formulation for the calculation of stray loss on magnetic steel components. It provides more insight into non-linear electromagnetic and thermal behavior. Obtained results also yield an improvement on the thermal model, allowing to adequately locate the heat sources within the penetration depth thickness.

- To implement a calibration process to guarantee the accuracy of computed results. It is done based on measurements and including optimization algorithms which identify the adequate value of electromagnetic and thermal parameters involved in the computation. An exhaustive investigation on the influence of parameters and sensitivity to measurement error is also addressed.

- To validate experimentally the obtained results. A series of experiments are presented in order to validate the proposed methodology, where the influence of several design factors on thermal effects caused by high current leads on steel plates is evaluated.

- To demonstrate the practicality of the proposed computational methodology. Some practical applications are included proving the development of efficient models with low computational cost and runtime which provide accurate results and are suitable to be included in the design stage or large power transformers.

1.4 Outline of the Thesis

This dissertation revolves around the concept of stray losses and its unwanted effects in terms of temperature rise. The study presented here is based on an analytical electromagnetic analysis, which allows to evaluate the stray loss densities on various structural parts of the transformer, and a steady state FE thermal analysis for the computation of the consequent temperature distribution. The presented work is structured as follows:

Chapter 2 presents a review of the literature focusing on eddy currents, stray fields and losses computation methods. The advantages and drawbacks of each of them when applied to the analysis of power transformers are given. Moreover, an exhaustive discussion on previous works related the analysis of leakage fields and consequent stray losses caused by high current leads and windings is presented.

In Chapter 3 a computational methodology for the calculation of the overheating hazard in transformer tank and low voltage bushing terminations is described. Physical and mathematical principles in which the electromagnetic analytical formulation is based are rigorously reported. The FE thermal formulation and computational models are also described.

Chapter 4 presents an experimental setup for temperature measurements in steel cover plates, tank walls and bushing turrets of power transformers. The experimental work presented in this chapter serves on one hand to describe a parameter identification method and on the other hand to validate the computational results.

In Chapter 5 a parameter identification method is described for best prediction of temperature distribution in the transformer structural parts. It is done by means of the implementation of optimization algorithms from which the adequate input parameters for the simulation are obtained. Sensitivity to measurement error is introduced by means of multi-objective optimization, where deterministic and non-deterministic algorithms are used for the sake of comparison. The efficiency of the algorithms and the selection of the most suitable for the parameter identification problem is reported.

In Chapter 6 computational results from applying the proposed methodology are discussed. The electromagnetic and thermal non-linear behavior on transformer covers are analyzed in detail, allowing thus a better understanding and more insight into the phenomenon an required analysis. Computed temperature distribution is compared with thermal imaging from measurements where the accuracy of the computational model is enhanced.

In Chapter 7 practical applications applying the proposed computational methodology are given, stressing its potentiality on further analysis on structural parts of power

transformers. Thus, the overheating hazard is evaluated in 3D complex structures, such is the transformer tank cover with bushing turrets. In addition, a practical tool is presented for the arrangement of amagnetic inserts in order to control and reduce the overheating hazard on flat three-phase transformer covers. The methodology is also applied to evaluate the overheating hazard on transformer tank walls due to zero-sequence flux with and without tertiary stabilizing winding.

Finally in Chapter 8 overall conclusions and future lines of work are given.

Chapter 2

Literature Survey

The role of eddy currents increases when designing and manufacturing large power transformers [31]. As transformer ratings increase, the amount of leakage flux traversing the windings and the air gaps around them increases also. Consequently, wherever the leakage flux enters magnetic material the flux densities within increase and may cause significant eddy current and hysteresis losses, i.e. stray losses. Other than the core, pieces made of magnetic material in a large power transformer are structural parts such as the core clamps and the tank, which would be made mainly of mild steel.

Stray losses, hot spots, reliability, maintenance, and overloading characteristics of large power transformers closely depend on suitable distribution of eddy currents and thermal effects produced by strong leakage fields [32]. In particular losses generated due to high current leads in the tank wall and the structure surrounding the transformer bushings can be the cause of hot spots that can damage the transformer oil and could put the transformer out of service. Hot spots in transformers are one of the most important parameters that determine their lifetime [6].

The serious failures due to thermal effects of eddy currents on those structural parts caused the necessity of their careful analysis, and its investigation becomes a fundamental question for manufacturers and utilities. To ensure proper operation of the system the most vulnerable points of field concentration and hot spots have to be localized and minimized. Moreover, due to environmental considerations and rising energy costs, customers have been putting high requirements on transformer efficiency. Although the efficiency of a modern transformer lies above 99 %, the loss cost is still significant, and recent studies focus their effort to further increase efficiency [6]. Accurate estimation and subsequent reduction of stray losses by shielding techniques as well as the use of amagnetic materials will give competitive advantages in a increasingly demanding market.

A great amount of papers are devoted to the application of calculation techniques for the estimation and control of stray loss in transformers, many of them collected in the publications [13] and [14] and their references. The investigation of these problems requires the analysis of eddy currents as an essential subject in the research of electromagnetic fields for the consequent stray loss computation [33].

In this work the state of art is focused in two main parts. In one hand a review of the calculation methods for eddy current analysis and stray loss computational aspects, and on the other hand, a review of published papers devoted to loss estimation and minimization on tank walls and cover plates of power transformers.

2.1 Stray Fields and Eddy Currents Calculation Methods

Aspects about the research in transformer performance, in particular the analysis of complex design problems that involve electromagnetic fields and stray losses come out since the 1950's and still continue [13]. They are related with the electromagnetic leakage flux estimation methods which have progressed from analytical to numerical methods. Such methods can in general lead to correct estimation of leakage flux and stray losses calculation, but their differences are on attributes such as accuracy, ease and practice of use, time consume of computation, cost and flexibility. Therefore, the use of one method or other is finally decided by the user, depending on the his experience, means and needs of each particular problem [5].

Although the analytical methods and two-dimensional modeling of leakage fields and hot spot localization in transformers is still convenient and useful in some design problems, it was found insufficient for analysis and computation of three-phase transformers where the three-dimensional solution of three-phase systems becomes necessary [32]. Various numerical techniques are available for tackling the electromagnetic field and the stray loss calculation problem. Numerical techniques can be principally categorized into methods based on differential formulations (e.g. Finite Difference Method, FDM), integral formulations (e.g. Boundary Element Method, BEM) and variational formulations (e.g. Finite Element Method, FEM) as in [33].

There are also hybrid methods, which are combinations of the above mentioned. Using advanced numerical techniques and coupled formulations, researchers are now able to analyze complex phenomena in transformers. Ease of modeling complex geometries, including non-linear behavior of materials, and its solid mathematical basis have lead to a domination of FEM to be used in engineering applications. The number of papers and the range of commercial software available are proof of the research carried out in academic institutions as well as industry [13], [14] and [34]. However, in the case of power transformers 3D FEM becomes especially difficult to apply. It is because a very fine mesh is required to compute the stray losses into thin skin depth of flux penetration of about one millimeter against dimensions of a few meters of the volume of the device [35], [36], [37]. Additionally, the problems when solving 3D FEM eddy currents are connected with a proper and adequate mathematical formulation [38].

In spite of the existence of numerous methods only a few of them are commonly used on eddy current and leakage flux analysis applied to power transformers. An overview of 2D and 3D eddy current calculation methods is presented in next subsections.

Practicality of application and dealing with field penetration depth, non-linear behavior of magnetic material and complex geometries, including multiply-connected regions (i.e. conductors having a hole) is discussed.

2.1.1 Analytical Methods

Authors are aware of the present situation on which numerical methods are dominant but suppose that the analytical methods have still some advantages. Many field problems can be solved by means of the two-dimensional theory, on which the field components vary only on two directions [15].

Eddy currents and stray losses might be appreciable different depending whether the material is excited by tangential or normal field. Therefore the analytical equations and methods derived for the field calculation also differ from each other.

Radial or normal field excitation is the case when the flux enters perpendicular to a metal surface, e.g. case of current carrying conductors placed parallel to a metal surface. Some methods are presented based analytical approaches for calculating the electromagnetic fields in metal sheets in the presence of bus bars carrying heavy alternating current.
Since any current distribution in space can be looked upon as made up of an infinite number of sinusoidal distributions with the help of the Fourier integral, the field due to any current distribution can be calculated. The expression for field intensity is developed based on the solution of Maxwell's field equations and superimposition is justified due to the linear relation between current density and electric field [39]. Assuming sinusoidal field distribution, the general solution of the field components, either electric or magnetic field, can be found from field diffusion equations in different media. Applying suitable boundary conditions of the model, the resultant field can be calculated then at the metal surface.

The field distribution at the metal surface can be also found by means of the mirror images method, where in case of ac currents, convenient coefficients have to be applied [15]. The method of mirror images and the direct application of the Biot-Savart law is also very convenient for calculation of leakage field due to high current leads placed parallel to a metal surface. Using this method we can easily substitute the double medium space by a single one by means of the appropriate coefficients. For instance, a metal medium can be eliminated from the model and obtain a homogeneous dielectric environment.

Tangential excitation occurs when a current lead passes through a metal plate, as in the case of cover plates or bushing turrets on power transformers. In the case of tangential excitation, the field at the surface can be calculated by the help of Biot-Savart law [4], which integrating and summing for every current gives the full analytical solution of the magnetic field.

Thus, the expression for average losses can be developed per unit area of the tank surface either for radial or tangential excitation. To calculate the loss of the system,

it is sufficient if one knows the field expression which combined with a concept of surface impedance leads to the calculation of losses taking place due nearby current carrying conductors [40]. The concept of surface impedance comes from the formulation of Poynting's Vector [15]. Despite being an analytical model, for the calculation of stray losses on transformers, some relevant parameters can be taken into account with satisfactory accuracy such as real shape of the tank walls, three-phase excitation, hysteresis and non-linearity by means of approximation and linearization coefficients [39].

The role of analytical methods and approximated formulae obtained by them is to put a tool in hands of the designer to facilitate the assessment of loss arising in a given component. Thus, it is possible to evaluate whether their values are to be considered hazardous or harmless, and decide in case, which factors have to modify to reduce the hazard [16]. They might help to quickly assess the effect on losses e.g. of repositioning the bus bars or using shields of different materials. Moreover, loss calculations from analytical methods might be incorporated in other computer programs which calculate, for example, the plate temperature rise resulting from these losses [7].

2.1.2 RNM- Reluctance Network Method

The Reluctance Network Method (RNM) model is based on the network of reluctances in its electromagnetic part and on the modified nodal analysis in the electric network calculations. The input data for the calculation are constructional geometry and electrical parameters of a transformer, from which the values of the network elements (reluctances) are calculated. There are two principal kinds of elements in the reluctance network, i.e. magnetic resistances for non conductive areas, and magnetic impedances for conductive areas. The first ones are calculated from pure geometry of each spatial element described by its coordinates, and the latter ones take into account analytically the skin effect, eddy current reactions with phase shift, non-linear permeability inside solid metals, depth of field penetration, and screening effects [32], [41].

The proper values of these elements are placed into the network scheme, either 2D or 3D, along with voltage sources which model an elementary magnetomotive force in a winding. All network elements are calculated on the basis of analytical formulas prior to the network solution.

The RNM appears to be one of the most appropriate methods for three-dimensional modeling of leakage fields in three-phase power transformers, when taking into account its possibility to fulfill the principal practical attributes, i.e. ease of implementation on moderately sized computers, yielding useful design data, low computational cost and the possibility to consider multiply-connected problems [42], three-dimensionality and three-phase systems [32] or non-linear permeability [43].

A novel formulation combining a Reluctance and a Resistance Network (RRN) has been recently applied to inducted currents analysis in multiply connected conductors [44]. As the classical **A**-**T** formulation in terms of magnetic and electric vector potentials of the RRN is not capable of treating multiply connected regions with

solid conductors, authors complement the formulation by introducing supplementary equations $\mathbf{T_0}$ representing the induced current distribution in the region around the holes.

2.1.3 IEM - Integral Equation Method

The Integral Equation Method (IEM) has been used to solve eddy current problems from the 70's [45]. The conducting material is represented by a network of current carrying line elements. Consequently, Maxwell's field equations can be replaced by Kirchhoff's circuit rules. The loop equations for voltages, supplemented by the node equations for the currents, comprise a set of linear equations that can be solved repeatedly to give the time development of the eddy currents. A network of mesh lines is used to represent the conductor. For each node, Kirchhoff's node rule holds, ie. the algebraic sum of the currents into each node is zero. Also for each loop, Kirchhoff's loop rule holds, ie. the sum of the IR voltage drops around each loop equals the EMF of that loop. In this case the emf is due to the change in applied flux through the loop plus the change in the flux due to all line currents. The flux through the loop due to currents can be calculated based on the approximation that the flux through loop equals the area times the field at the centroid of loop [45]. The equation of the EMF entering the loop involve time derivatives of the current, approximated as the ratio of the current difference to the time step. For multiply-connected conductors, each loop equation must be written for each hole. If the holes are large, a better approximation for the flux through the holes might be required.

This method treats the eddy current directly as an unknown value. Current values, magnetic fields, and power can be also calculated at each time step. The integral equation approach, which has been first applied successfully magnetostatic problems, seems especially applicable to eddy current problems. Two-dimensional IEM using scalar and vector potentials have been reported in [46]. The IEM overcomes the difficulties arising from modeling such as to treat disjoint bodies without having to include the space between and around them in the calculation or complicated boundary conditions [45].

In the 3D domain, to calculate eddy current on multiply connected magnetic materials, the frequency domain volumetric integral method has been reported in [47]. The frequency domain method is adopted to avoid the instabilities which occur in time integration. The saturation effect of the permeability has been also included successfully into the volume integral equation method in order to analyze non-linear eddy current problems [48].

2.1.4 BEM- Boundary Element Method

The Boundary Element Method (BEM) has been suggested at the beginning of 80's to be used in stationary eddy current calculations. It appeared that due to the nature of BEM it is just well-suited to solve eddy current problems. In the BEM only the boundary

is considered, so the eddy current distribution within the domain of interest does not influence at all the boundary mesh. Hence the depth of penetration can be arbitrarily small. The features of the BEM are specially seen when dealing with transient problems. It is due to the fact that time is analytically included in the fundamental solution. Also due to its partially analytical nature the BEM gives the possibility of calculating the eddy currents directly while other methods require the differentiation of the magnetic vector potential [33].

The BEM, formulated in terms of magnetic vector potential and electric scalar potential, can be successfully applied to three dimensional, multiply connected and open boundary problems [49]. It is assumed that exciting currents vary sinusoidally with time. Boundary integral equations are expressed by means of the vector Green's theorem for magnetic vector potential $\mathbf{A}$ and the Green's theorem for electric scalar potential V in conducting and non conducting regions.

The BEM is specially advantageous in the open boundary problems, which are solved by means of just one method without adopting any artificial boundary conditions as to the external regions. Nevertheless, this leads to a high computational cost due the full non-symmetric matrix to be inverted and the elementary functions to be computed many times.

2.1.5 FEM- Finite Element Method

One of the effective and widely used methods of numerically computing eddy current fields in two and three dimensions is the Finite Element Method (FEM). Considering first 2D problems, since the early 70's the FEM successfully replace the FDM, which had been employed in the past. Initially they were static fields which had been solved by means of FEM. Later the method was employed to the linear harmonic eddy current problem, and after years became possible to analyze transient non-linear problems [50]. But the great hope researches put in the FEM has not fulfilled in the eddy current problems. It is nature of eddy currents that makes the calculation somehow cumbersome. The main problem occurs in the mesh generation starting from the fact that one must know *a priori* where the skin effect occurs to provide an appropriate mesh, with several elements within the skin depth [33].

Moreover, the problems when solving 3D FEM eddy currents are connected with a proper and adequate mathematical formulation. There exist various formulations in which these problems are stated but the main question is how to ensure all the interface conditions and dealing with multiply-connected regions, the uniqueness of the solution and the minimization of the number of variables.

One of the crucial points is the appropriate selection of the potentials in terms of which the field quantities are formulated. In 3D eddy current problems, both the electric and the magnetic field must be described in conductors while in eddy current-free regions it suffices to take into account the magnetic field only. These fields can be derived from potentials in various ways leading to various FEM formulations. The requirements for a satisfactory formulation include, among others, numerical stability insensitive

to frequency as well as the ability to treat discontinuities in material properties. An excellent survey on the formulations dealing with those aspects is given by [38], focusing on multiply-connected 3D eddy current problems. The requirement of numerical stability demands formulations involving unique potentials. The uniqueness of a vector potential describing a uniquely defined field can be ensured by fixing its divergence and its normal or tangential component on the boundary, a procedure called gauging, with the Coulomb gauge emerging as the most appropriate one [51]. For the calculation of transient eddy currents in non linear media, fast and simple iterative techniques are used to solve the non-linear algebraic equations arising [52].

Several finite element formulations in terms of various potentials are reviewed and summarized in the following paragraphs. However, solving a 3D FEM eddy current problem is not straightforward and requires advanced knowledge on the formulations, particularly in the case of multiply-connected problems.

$\mathbf{A_r}, V - \mathbf{A_r}$ *Formulation*

The simpler formulation capable of treating eddy current problems with multiply connected conductors uses a magnetic vector potential $\mathbf{A}$ overall supplemented by an electric scalar potential V in the conductor. To avoid the modeling of the coil structure, a reduced magnetic vector potential $\mathbf{A_r}$ can be used, where the vector potential due to the current sources is computed using Biot-Savart Law [38]. At the far boundaries Dirichlet boundary conditions are given for the tangential components of $\mathbf{A}$, which are set to zero, but no Dirichlet boundary conditions can be given for V. Moreover, on the interfaces between ferromagnetic and non ferromagnetic regions, the normal component of the $\mathbf{A_r}$ should be allowed to be discontinuous in order to improve the accuracy of computation [52]. It has the advantage that no cutting is necessary for the multiply-connected region problem but the great disadvantage of the present formulation is the use of a vector potential involving three degrees of freedom to describe the static magnetic fields outside the conductor.

$\mathbf{A}, V - \mathbf{A} - \Phi$ *Formulation*

Scalar potential functions involve only one degree of freedom per node in their formulation but are not completely adequate for three-dimensional representation of current regions. Thus, by combining the previous formulation with the magnetic scalar potential Φ outside the conductor, it is possible to reduce the computational effort. However, in case of multiply connected conductors, Φ cannot be used everywhere in regions free of eddy currents. Indeed, this would enforce zero net current around the hole in the plate which is clearly wrong [38]. To overcome this difficulty, a magnetic vector potential $\mathbf{A}$ can be used in the hole, leaving the surround domain with Φ. Therefore a boundary condition is set by the prescription of the normal component of $\mathbf{A}$ to vanish on the interface between the $\mathbf{A}$ or $\mathbf{A}, V$ and the Φ regions, but if this surface coincides with an iron-air interface, poor accuracy might result [52]. The second necessary Dirichlet boundary condition is the setting of Φ to zero at the far boundaries, provided these boundaries are

far enough. Similarly to the $\mathbf{A}, V - \mathbf{A}$ version, no Dirichlet boundary conditions specify the electric scalar potential V [38] and the fact that on the present problem, the only boundary conditions on V are of Neumann type constitutes a difficulty for the above two formulations involving the electric scalar potential, i.e. ill conditioned systems might result.

$\mathbf{T}, \Phi - \Phi$ *Formulation*

The use of the electric scalar potential can be avoided by employing an electric vector potential $\mathbf{T}$. The formulation in terms of the electric current vector potential $\mathbf{T}$ and the magnetic scalar potential Φ in the conductor is one of the most efficient formulation for the solution of eddy-current problems [53]. The major advantage of the formulation is the use of the magnetic scalar potential in non-conducting region, which enables considerable savings of the number of unknowns. However, in the case of conductors containing holes, it is well known that the non-conducting region is multiply-connected and the scalar potential is multivalued. To preserve Ampere's theorem, cuts through the conductor to the holes that make the non-conducting region simply-connected have to be introduced and jump of scalar potential through the cuts has to be allowed [54]. To avoid the troublesome generation of cuts, the most commonly used method consists of filling the holes by fake conductors of very low conductivity, but often ill-conditioned systems result if the conductivity value is not chosen adequately. However, identification of holes in the conducting region is not an easy task for complicate geometries. Automatic algorithm for cuts has been presented recently in [55].

$\mathbf{T}, \Phi - A - \Phi$ *Formulation*

A further possibility to use the electric vector potential in multiply connected conductors is to introduce a magnetic vector potential $\mathbf{A}$ in the hole with $\mathbf{T}, \Phi$ in the conductor and Φ elsewhere [38], avoiding thus the generation of magnetic cuts through the conductor. Similarly to the $\mathbf{T}, \Phi - \Phi$ formulation Dirichlet boundary conditions are prescribed for each of the potentials. Φ is set to zero at the far boundaries, the tangential components of $\mathbf{T}$ are zero on the interface between the $\mathbf{T}, \Phi$ and the Φ region, the normal component of $\mathbf{T}$ is zero on the interface between the $\mathbf{T}, \Phi$ and the $\mathbf{A}$ region, and the normal component of $\mathbf{A}$ vanishes on the interface between $\mathbf{A}$ and Φ regions. This formulation seems difficult to apply when solving a 3D eddy current problem as requires advanced knowledge on the formulations [38], however has been demonstrated to be the optimal for the solution of the present problem, as shown compared to experiment results from TEAM problem no. 7, asymmetrical conductor with a hole [56].

$\mathbf{A_r}, \mathbf{T} - \mathbf{A_r}$ *Formulation*

A formulation to compute eddy currents with the aid of a magnetic vector potential $\mathbf{A}$ to describe the magnetic field everywhere and an electric current vector potential $\mathbf{T}$ to represent the eddy currents in conducting regions is reported in [57], taking care of

multiply-connected regions. To obtain the uniqueness of the vector potentials in case of the mostly used nodal elements and to gain a better convergence behavior of the system matrix, the Coulomb Gauge is employed leading to a lack of accuracy in the solution. Therefore and because continuous nodal elements lead to numerical problems on interfaces between regions with different permeabilities, edge elements are often employed for the vector potentials to obtain a better accuracy of the field solution than nodal elements without free normal components [58]. Moreover, the Coulomb Gauge on the vector potentials is enforced in the equations itself leading to a system with very good convergence behavior.

The 3D FEM, which started gaining importance in the 80's is being constantly upgraded to improve its modeling capabilities and accuracy for eddy current analysis, however the efforts required for 3D modeling may be justified only for large power transformers where improvement in accuracy will be appreciable.

2.2 Stray Loss Calculation into Thin Penetration Depth. Surface Impedance

Although improved numerical techniques have been developed for the computation of the stay field in transformers, some authors come up concerning with the difficulty of computing stray losses in metal structural parts due to the thin skin depth penetration.

The increases in rating of large power transformers have demanded more accurate and efficient methods of predicting leakage fields, and the consequent eddy current losses [35]. Thus there has been a great deal done with FEM analysis of three-dimensional eddy current field as seen above. In most of these investigations only model problems were taken to verify the methods presented. But a more complicated and troublesome problem is using the method for practical power devices [36]. In this sense, some authors develop hybrid formulations in order to calculate leakage fields in large power transformers and associated losses.

Firstly, Djurovic *et al.* in 1975 [35] proposed a three-dimensional method for calculating currents induced in leg plates and other conducting parts in which edge effects are important by coupling the FEM with a finite difference network.
In 1985 Fawzi *et al.* [23] analyze the use of an Impedance Boundary Condition (IBC) for the reduction of the field problem encountered in the computation of eddy currents in conductors with small penetration depths. The formulation of an approximate IBC problem in terms of boundary integral equations is developed for two-dimensional and three-dimensional linear problems. The use of the IBC for such problems offers an approximate but efficient formulation, however the real importance of IBCs is in their potential adaptation for numerical methods such as finite differences, finite elements and boundary methods.

The concept of Surface Impedance (SI), which comes up based on the Poynting's Vector formulation, was firstly introduced into field theory by Schelkunoff in 1938. At the surface

of good conductors the tangential component of the electric field **E** is approximately proportional to the tangential component of magnetic field **H** and thus

$$\mathbf{Z} = \frac{\mathbf{E}}{\mathbf{H}} = (1+j)\frac{1}{\sigma\delta}, \tag{2.1}$$

being **Z** the complex surface impedance and δ the skin depth in a conductor defined as

$$\delta = \sqrt{\frac{2}{\omega\mu\sigma}}. \tag{2.2}$$

Where ω is the angular frequency, σ is the electrical conductivity and μ is the magnetic permeability of the material.

In 1987 Dexin *et al.* [36] presented a 3D FEM analysis using the complex magnetic vector potential for the eddy current problem to a three phase power transformer. He combined the 3D FEM with an analytical formulation in the tank wall and other thin structural parts where an adequate discretization becomes a problem because of thin skin depth. Numerical results using the proposed method have been validated with experimental values giving good agreement.

Holland *et al.* in 1992 [37] proposed a method for calculating eddy losses in thick conducting materials. The concept of SI is used in a finite element software package and applied to the design of large power transformers. The solver permits to calculate stray fields from windings using a 3D FEM formulation and the consequent stray losses in the tank wall by means of the SI, removing the need for complex layers of elements to account for skin effects which reduces the complexity and size of models. A three-phase transformer in a mild steel tank with magnetic shunts is modeled. Non-linearity in the tank wall is accounted for by the application of Agarwal's approximation which considers the real BH characteristic lies between a linear and a step function, detailed in [59]. Many commercial FEM softwares have now the feature of this SI element modeling and thus permit designers to calculate tank losses efficiently and accurately.

In 2000 Higuchi *et al.* [60] developed a technique to estimate the stray loss distribution in transformers based on the IEM with SI model. This method overcomes the difficulties of mesh generation in FEM but the integral methods can require much memory.

From the physical point of view it can be stated from the above proposals that stray losses are a 3D phenomena and its numerical formulation strongly depends on the problem to solve, which often involves an additional difficulty to tackle. Even in the era of three-dimensional calculations, two-dimensional methods can be useful for stray loss calculations in some cases, or to study individual components, but not to consider the complex systems. Many commercial FEM softwares have now the feature of this SI element modeling combined with the FE, which permits designers the calculation of stray losses in large power transformers.

2.3 Stray Losses in Transformer Structural Parts

Stray losses include eddy and circulating current loss in windings, losses in flitch plate, core edge loss, loss due to high current fields, and frame and tank losses. Although stray losses in large rating transformers might not form a significant part of the total losses of a transformer, a small reduction in losses produce significant energy savings since the number of transformers in the power systems is high [13], which would benefit utilities and customers. In addition, the loss density due to high values of incident flux density may attain levels that may lead to hazardous local temperature rise if the material and design are not selected properly.

In general, high values of incident flux density in transformer components arise due to high current leads carrying several kA located nearby those metal components. Within the most hazardous components withstanding local overheating and hot spots due to high current fields are the transformer structural parts. The following review of papers is focused on aspects and findings related to the transformer stray loss problem from the point of view of calculation, reduction and measurement on the transformer tank walls and cover plates.

2.3.1 Stray Losses due to Normal Excitation Field from High Current Leads

Earlier studies and methods are concerned with calculation of losses due to normal excitation fields which are caused by current carrying conductors passing parallel to metal plates. A report of highly referenced papers in the subject of stray loss estimation in transformer tank walls is given below, reporting mainly experimental and analytical formulae, and providing means reduction and control.

There are several studies related to a single-current carrying conductor in the presence of conducting permeable surfaces. The problem of determining the behavior of magnetic flux within solid material of high permeability is a difficult one unless some simplifying assumptions are made.

In 1923 Rosenberg [61] developed a method where he determines the depth of penetration of the flux into the iron and the losses in iron caused by the circulating eddy currents. Rosenberg made the assumption that the flux density is uniform from the surface to a certain depth decreasing then rapidly to zero, and the magnetizing forces used are of sufficient magnitude to saturate the magnetic material at the surface.

In 1954, Vogel and Adolphson [62] proposed an analytical expression to determine stray losses and heating of tanks for a core-type transformer caused by radial field when the penetration depth is known. Eddy current losses in solid magnetic materials were found to vary directly with the square root of the resistivity for thick plates and to vary inversely with the resistivity for thin plates. It is found in this work that losses are not a function of the thickness of the tank wall for the usual magnetizing forces involved. An oval-shaped tank is considered in this article, and the losses in the tank wall versus

the distance for the top of the high-voltage coils are determined. The method for loss estimation is indirectly validated from temperature hottest spot measurements in a transformer tank.

In 1954 Poritsky and Jerrard [63] discussed the eddy-current losses in a semi-infinite solid slab subject to an alternating current solving Maxwell's by applying Fourier integral superposition in air and solid conductor. Real cases involve plates of finite thickness, however, in the case of tank walls the thickness is greater than the penetration depth at power frequencies acting thus as a semi-infinite plate.

Experimental methods were used by Deuring [64] in 1957, on which he experimentally dealt with a single current carrying conductor placed near conducting permeable surface of typical steel of transformer tank plate material. The author presented empirical equations to calculate losses establishing the correlation between current and conductor to place distances and determined curves of watts per foot for shielded and unshielded plates.

In 1959, Agarwal [59] developed formulas for the calculation of eddy currents in solid and laminated iron. He very clearly explained what occurs when the depth of penetration is less than or greater than the half-thickness of the plate. The author used Maxwell's equations and assumed an ideal (rectangular) magnetization curve in order to obtain the losses per unit of area in saturating material. Agarwal compared experimental and computed values of eddy current losses for different lamination thickness.

In 1970 Jain *et al.* [40] evaluated field pattern and eddy current losses in aluminum sheet due to current carrying strip bus bars. Current distribution is expressed as made of an infinite number of sinusoidal distributions with the help of Fourier integral, and then the field due to any current distribution is obtained by superimposition of fields due to sinusoidal components. He developed formulae to calculate the loss of the system with known peak value of the field strength of the source. Both strip and conductor are assumed to be of infinite length to avoid the consideration of end effects for which the mathematical formulation is involved. Various curves for loss are given, which are of practical use.

In 1972, Kozlowski and Turowski [65] presented an analytical formula to determine the power losses for the adequate selection of the type and thickness of tanks. They assessed the maximum power above which shielding is indispensable. When non magnetic shields are applied, unshielded tank losses should be multiplied by an analytical coefficient, which depends on the copper or aluminum conductivity, the steel parameters, and the shield thickness. The authors determined optimum copper and aluminum shield thickness so that minimum losses appear in the tank. When magnetic shunts are applied, unshielded tank losses should be multiplied by an empirical coefficient, which depends on the number of sheets that compose the thickness of the shunt.

Krakowski *et al.* [66] have presented a method for analyzing the electromagnetic field in a system that comprises of parallel current carrying bars placed above a steel wall. The current density within the cross-section of bars is computed using the integral equation technique. The components of the magnetic and electric field strength at the surface of the wall are evaluated.

Turowski in his relevant book [15] presented a method for calculation of eddy current losses in transformer structural parts based on Poynting's theorem. Turowski's equation for eddy losses power dissipated in metal wall applies linearization coefficients to take into account non-linear magnetic permeability from known distribution of the magnetic field at the metal surface. His formula was widely applied in several works in the literature e.g. [67], where the magnetic field distribution can be calculated by several methods either analytical or numerical.

Koppikar *et al.* in 1997 [68] in their work give the formula for complex power loss computation in a steel plate by integrating the Poynting's Vector over the metal surface. They provide the analytical solution of the field for a single line current which can be also superimposed for three-phase system. They calculated eddy current loss for several current values on a system consisting of a current conductor placed parallel to mild steel plate, and verified the theoretical results by means of a laboratory experiment as well as by FEM computation.

In 2003 Del Vecchio [7] presented an analytical method for the calculation of eddy-current losses in a conducting plate due to a collection of bus bars carrying currents of different magnitudes and phases. Although these losses in the wall or shield can be calculated by modern finite element codes, an analytical method would obtain these losses quickly during the design phase. He developed a formula for the calculation stray losses in transformer tank walls to several configurations of rectangular bus bars.

2.3.2 Tank Losses due to Windings Leakage Flux

It can be seen that most of the earlier papers published have concentrated on analytical methods, which due to some assumptions and approximations, are useful to only simplified 2D geometries and cannot be applied to complex 3D structures. With improvements numerical methods and in 3D software capabilities, now such complicated structures can be easily simulated and analyzed and accounting of certain 3D phenomena can be closely approximated. Therefore, numerical methods applied to the calculation of stay losses in structural parts of power transformers do not concern anymore to the leakage field caused by a single conductor, or collection high current leads, but to the leakage field caused by the transformer windings. A high number of papers concerning the stray losses the transformer tank due to windings is found in the literature, given in this section.

A good physical understanding of the eddy loss generation in massive iron pieces allows the definition of simplifying assumptions for their calculation. Thus Sironi in 1978 [69] proposed a quasi three-dimensional computation of eddy current losses in transformer tank wall from two-dimensional flux calculations in several main planes solved by the method of images. Important aspects such as the non-linear BH characteristic, and skin depth penetration are recalled in this paper.

In 1980, Valkovic [39] presented an analytical method for the calculation of stray losses in three-phase three-legged core type transformer tanks. The author assumed in this calculation that the thickness of the tank wall is several times greater than the

penetration depth, and non-linearity and hysteresis were taken into account. Tank losses were calculated by means of Poynting's theorem, taking into account the curvature of the winding and real shape of the tank. A computational model based on the RNM is proposed by [32] for the assessment of a three-dimensional leakage field distribution and hot-spot localization in three-phase power transformers. The Reluctance Network Method has also been applied for analysis of transformers using a hybrid analytical-numerical approach.

In 1993, Pavlik *et al.* [70] calculated stray losses in the tank walls of core type transformers using a two-dimensional finite element model and some projection planes to approximate 3D fields. With the FE programs solutions of much more complicated geometries can be obtained, an accounting of certain 3D phenomena can be closely approximated. The stray and eddy losses in transformers can be analyzed thus as a complete system and not on an individual components. The authors presented a series of stray loss reduction studies, leading to changes of structural elements that affect the stray and eddy current losses.

Also in 1993, Guerin *et al.* [71] dealt with the 3D electromagnetic modeling of eddy current losses in transformer tanks. In this work, a single-phase, 390 kVA transformer was modeled. Mesh problems are found when the skin depth is small in relation to the dimensions of the solid conducting regions. This occurs when the permeability, the conductivity, or the frequency are high. The authors made several parametric analyses, changing the relative permeability of the tank, the tank thickness, and the relative permeability of the magnetic core. In every case, they determined the eddy-current losses.

In 1994, Yongbin *et al.* [72] applied the $\mathbf{T} - \Phi$ method to the computation of the three-dimensional eddy current field in a 360 MVA/500 kV large power transformer, the structure of which is complicated. The magnetic flux density and eddy current losses in the cases of tank wall with magnetic shunt, aluminium screen and without any shield are analyzed and the optimal size, material and structure of tank shield are suggested. Due to the variety of medium and the complexity of the structure, it needs a lot of storage capacity and CPU time to compute the eddy current field.

In 1996 Renyuan *et al.* [73] calculated the eddy current field in large power transformers due to windings and including heavy current leads which had ignored in previous models. High current leads play an important role in this problem and their resultant magnetic field must be taken into account. Based on the numerical solution of eddy current fields, the local overheating problem in metallic structural parts are studied.

A large list of papers given in [13] report 2D and 3D methods to determine the eddy-current density and the tank flux distribution in power transformers and describe the main techniques to reduce stray losses and local overheating in the tank wall caused by windings and heavy current leads. Many of them evaluate the influence of shields material and represented the maximum density as a function of the thickness, position, and distance from the windings.

2.3.3 Stray Losses due to Tangential Excitation Field from High Current Leads

Tank cover plates and bushing turrets represent a particular case of the transformer tank in the calculation of stray losses, due to the incident field is in this case tangential to the steel surface. High current lead pass through a steel tank cover plate and bushing box of power transformers creating a three-dimensional leakage field which cannot be simplified to a two-dimensional problem. Means of preventing the local overheating on the structure surrounding the distribution transformer bushings are very scarce and very few solutions of this particular problem are proposed so far.

In 1981, Saito *et al.* [74] experimentally analyze eddy currents in the structure that surrounds the large current bushings of transformers. The three-phase bushing model is made of stainless steel with conducting currents of about 20 kA. Eddy currents and temperature are measured on a series of experiments from each of the components separately and considering also the bushing system as a whole (bushing pocket, base plate, bus cover and isolated phase bus enclosure). Means to prevent overheating are applied as the use of stainless steel on the base plate, or inner copper shield on the bushing pocket. Therefore there is no possibility that leakage flux causes local overheating: the magnetic density in the tank cover and is less than 0.001 T, and the maximum temperature rise is 16 °C. A 2D formulation based on some approximations and experimental data was used to estimate the eddy current patterns for various configurations of terminations.

In 1990, Renyuan *et al.* [75] presented an IEM to determine stray losses produced by a heavy current in transformer leads. In the case of the tank cover, which is usually made of amagnetic steel, the region to be solved is open and boundary conditions difficult to determine. The main advantage of the IEM is that boundary conditions are taken into account inherently by the mathematical model. The method is applied to calculate the sinusoidal eddy current field in three dimensions and evaluates the influence of tank materials, distribution of leads, source current and shields.

The BEM was applied in 1992 by the same authors in [49] to localize the maximum values of the magnetic flux density occurring in the low voltage bushing from a three-phase transformer. In this case the transformer consists of three single-phase transformers and lot of low-voltage leads connecting them are arranged in the lead box with three holes in the front wall. The magnetic flux density and eddy current losses in the cases of tank wall with magnetic shunt, aluminium screen and without any shield, are analyzed. Finally, a range of optimal size parameters such as the distance between holes, material and structure of tank shield are suggested as corrective measures to reduce the eddy current losses. In 1994 [76] they use an improved BEM increasing numerical accuracy for calculating eddy currents distribution and stray loss density on the surface of a transformer tank cover and bushings. From the results authors give permissible lead current and limiting distance between high current leads and metallic parts.

Analysis of eddy current pattern, in a three dimensional model of a 40 MVA furnace transformer Low Voltage (LV) lead termination, is reported by Koppikar *et al.* in 1997

[68]. The current carried by the LV conductors was 56 kA, and the lead termination bushing made of non magnetic stainless steel. The results clearly point out the hot spot locations that are observed in tests. Total eddy losses estimated are found to be in close agreement with that observed during load test, and an improved construction geometry was proposed for the LV termination bushing in order to reduce the transformer load losses.

In 1997, Turowski and Pelikant in [12] and later in 1998 [4] applied a computer analysis based on Maxwell's equations and Biot-Savart law for field computation of heavy current leads passing through steel cover plates. The stray losses are then calculated from the numerical integration of the Poynting's Vector. They developed a formula for the maximum permissible bushing current in a flat cover. The results given in these papers provide practical information and various constructional means for the optimization of the cover structure for loss and hot spot reduction taking into account materials, geometry excitation currents, iron saturation, skin effect and local overheating.

In 1999, Kim *et al.* [77] presented an improved design of cover plates to reduce the stray loss distribution due to heavy currents passing through the steel cover plates of a transformer. Authors applied an indirect boundary integral equation method to the problem of heavy currents in transformer leads and compared calculated and experimental results. An improved design of cover plates to reduce eddy-current losses was presented consisting of two slits between the holes of the current leads.

From the most recent works, in 2004 Kulkarni *et al.* [11] calculated the eddy current losses in bushing mounting plates using both an analytical formulation and a 3D FEM from a small laboratory model. Authors proved there is a close agreement between those methods and the losses indirectly calculated from the experimental measurement of the temperature rise. Authors also analyzed tank plates of small pad-mounted distribution transformers verified with experiments. The analysis has resulted in a detailed understanding of the loss pattern and the temperature rise phenomenon in those structures and found out in [78] by means of 3D FEM that T-shaped non magnetic stainless steel inserts as the most cost-effective solution for the tank plates in order to reduce the load loss. In [79] authors proved that a 2D FEM model could be useful to estimate the percent of loss reduction by comparing models with and without non-magnetic inserts, stressing however that the 2D FEM underestimates by several orders the computed loss values.

Also in 2004 Turowski [5] presented an analytical but more accurate analysis since newer constructions present complex high current bushing turret made of solid iron and also screened iron. He considered in the whole structure the bushing box, steel walls, cover of tank and copper screens. The analysis of each of the individual components has its specific dimensions, materials, theory and physical parameters, dependence on thermal and magnetic non-linearity, eddy current reaction, approximations and simplifications. However, all of them are interdependent from each other. The average temperature rise of walls and cover, as well as the highest temperature rise are estimated from very simplified calculations.

In 2011 Olivares *et al.* [80] presented a techno-economic evaluation of reduction

of low-voltage bushings diameter in single-phase distribution transformers. Mexican bushing manufacturers reduced the diameter of low-voltage bushings used in distribution transformers to reduce manufacturing costs but not evaluating the impact of this change in load losses. The main contribution of this work is the evaluation of such losses by means FE simulations of LV bushings of transformers, where the SI boundary condition was used in the simulations.

Although the eddy current losses due to high current leads are negligible as compared to other losses of transformers, the loss density and consequent local temperature rise, are considerable affecting the reliability of transformers.

Within the most extended flux estimation methods used by manufactures and designers is the FEM and studies found in the literature based on the FEM focus on flux estimation caused by windings. However high current leads play an important role in the local overheating problem, and some of the mentioned theoretical or practical researches present a separate study to take their effect into account.

The subject of tank-wall losses and particularly near the cover or low voltage bushing mounting plates in power transformers has received little attention, and authors observed that work needs to be done for improvement of geometry of tank wall surrounding the high current bushings [78]. Very recent studies reported in the literature for analyzing losses in high current terminations are predominantly for distribution transformers [78], [11]. In the design large power transformers, very high current values flow through the LV leads and due to the lack of awareness in the matter of stray loss calculation the whole structure surrounding the bushings is made of non magnetic stainless steel. Non magnetic steel is by several times more costly than mild steel increasing thus the manufacturing cost of the transformer.

The contribution of this dissertation is to provide more insight into the phenomena of stray losses in structural parts of transformers, focusing on the 3D cover plate problem. Thus, from a better understanding of the non-linear electromagnetic and thermal behavior provide means for an improved, optimum and cost-effective design of those structural parts. The work presented here covers also the lack found in the literature of studies regarding thermal analysis, which in fact represent the real hazard created by the high current leads.

Chapter 3

Computational Methodology

The 3D methodology proposed in this dissertation is aimed to assess the overheating hazard on transformer structural parts. The novelty lies in that its computational procedure is based on a link between an analytical formulation with the finite element method. In this way, stray losses into the thin field penetration depth can be readily calculated with the analytical model and then the temperature distribution is computed by means of a 3D FE thermal analysis.

The computational flowchart can be followed in Fig. 3.1. The methodology starts with the electromagnetic analytical model that allows the computation of the stray power losses dissipated within the studied device. After introducing geometric dimensions, initial material properties data and the source current value, an analytical representation of electromagnetic field is obtained applying the Biot-Savart law. Next, stray losses distribution generated by alternating high currents through cover plates are calculated from the numerical integration of the analytical formulation of Poynting's theorem [81]. From that electromagnetic solution the power dissipated within the SI is introduced in the FE thermal model as heat sources. They are used together with boundary conditions and the initial nodal temperatures as input for the thermal problem. The numerical solution gives the steady state temperature distribution linking in this way the two models. According to (2.2), the field frequency and material properties set the penetration depth of the electromagnetic field into the metal, and consequently the thickness of the volume regions where heat sources are located in the thermal model.

To choose the adequate data of electromagnetic and thermal parameters is essential for the accuracy of temperature results. Some parameters needed in the computation models related with boundary conditions and material properties might be inaccurate as they are usually taken from catalogs and the literature. Therefore, in the proposed methodology, models are adjusted by means of a calibration process which identifies the appropriate input data for the simulation to match the measured temperature taken as reference (T_s). Once the simulation input parameters are determined and their interdependence stated, the temperature distribution can be predicted on transformer covers for any load condition and different number of conductors, i.e. single-phase or three-phase bushings.

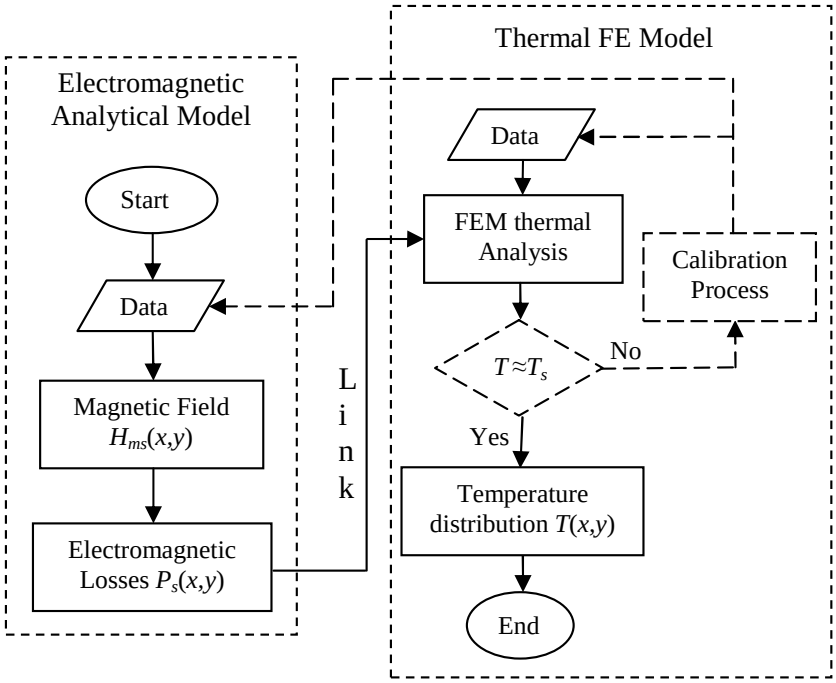

Figure 3.1: Flowchart corresponding to the 3D proposed methodology for the electromagnetic and thermal linked models.

The computational methodology is detailed in the next sections, while an attempt to solve the parameter identification problem is given in Chapter 5.

3.1 Electromagnetic Analytical Approach

In the next sections the physical-mathematical aspects regarding the electromagnetic analytical approach of the proposed methodology are explained in detail. It is shown how the use of the Poynting's Vector for a model involving high current carrying conductor and a nearby permeable surface can help qualitatively explain how the electromagnetic energy flows in the system, the transfer of energy and stray loss dissipation.

3.1.1 Electromagnetic plane waves propagation

When electromagnetic waves are incident on a good, but not perfect conductor, they penetrate a small distance into the material. The equations of electromagnetic fields inside a conductor can be formulated from the solution of Maxwell's equations. For general time-varying fields, Maxwell's equations [82] may be written in differential form as

$$\nabla \cdot \mathbf{B} = 0 \tag{3.1}$$

$$\nabla \times \mathbf{E} = -\frac{\partial \mathbf{B}}{\partial t} \tag{3.2}$$

$$\nabla \cdot \mathbf{D} = \rho \tag{3.3}$$

$$\nabla \times \mathbf{H} = \frac{\partial \mathbf{D}}{\partial t} + \mathbf{J} \tag{3.4}$$

where $\mathbf{B}$ is the magnetic flux density in $\mathrm{Wb/m^2}$ or T, $\mathbf{E}$ is the electric flux intensity in V/m, $\mathbf{D}$ is the electric flux density in $\mathrm{C/m^2}$, $\mathbf{H}$ is the magnetic field density in A/m, $\mathbf{J}$ is the electric current density in $\mathrm{A/m^2}$ and ρ is the electric charge density in $\mathrm{C/m^3}$.

The current density $\mathbf{J}$ and the charge density ρ are the sources of the field and they are related through the equation of continuity, specifying the conservation of charge, which can be written as

$$\nabla \cdot \mathbf{J} = -\frac{\partial \rho}{\partial t} \tag{3.5}$$

The above equations are supplemented by the constitutive equations describing the macroscopic properties of the medium

$$\mathbf{D} = \varepsilon \mathbf{E} \tag{3.6}$$

$$\mathbf{B} = \mu \mathbf{H} \tag{3.7}$$

$$\mathbf{J} = \sigma \mathbf{E} \tag{3.8}$$

where the constitutive parameters ε, μ and σ denote respectively, the dielectric permittivity F/m, magnetic permeability H/m, and electrical conductivity S/m of the medium. For isotropic materials these parameters are scalars, but for anisotropic materials they become tensors.

Thus Maxwell's equations (3.2) and (3.4) can be written in terms of only $\mathbf{E}$ and $\mathbf{H}$ as

$$\nabla \times \mathbf{E} = -\mu \frac{\partial \mathbf{H}}{\partial t} \tag{3.9}$$

$$\nabla \times \mathbf{H} = \varepsilon \frac{\partial \mathbf{E}}{\partial t} + \sigma \mathbf{E} \tag{3.10}$$

Maxwell's equations (3.9) and (3.10) couple the electric and the magnetic fields. If $\mathbf{B}$ is time dependent, $\nabla \times \mathbf{E}$ is non-zero. This implies that $\mathbf{E}$ is a function of position. Furthermore, if $\partial \mathbf{B}/\partial t$ itself changes with time, so does $\nabla \times \mathbf{E}$. In such a case $\mathbf{E}$ also

varies with time since the ∇ operator cannot cause time variation. Thus, in general, a time varying magnetic field gives rise to an electric field which varies both in space and time. It will be seen that these coupled fields propagate in space.

Firstly, it is analyzed how the equations lead to transverse waves. Taking the curl of (3.9) and substituting on the left hand side (3.10) yields

$$\begin{aligned} \nabla \times (\nabla \times \mathbf{E}) &= -\mu \frac{\partial}{\partial t} (\nabla \times \mathbf{H}) \\ &= -\mu \frac{\partial}{\partial t} \left(\varepsilon \frac{\partial \mathbf{E}}{\partial t} + \sigma \mathbf{E} \right) = -\mu\sigma \frac{\partial \mathbf{E}}{\partial t} - \mu\varepsilon \frac{\partial^2 \mathbf{E}}{\partial t^2} \end{aligned} \tag{3.11}$$

In the same way, taking the curl of (3.10) and substituting on the left hand side (3.9) yields

$$\begin{aligned} \nabla \times (\nabla \times \mathbf{H}) &= \varepsilon \frac{\partial}{\partial t} (\nabla \times \mathbf{E}) + \sigma (\nabla \times \mathbf{E}) \\ &= \varepsilon \frac{\partial}{\partial t} \left(-\mu \frac{\partial \mathbf{H}}{\partial t} \right) + \sigma \left(-\mu \frac{\partial \mathbf{H}}{\partial t} \right) = -\mu\sigma \frac{\partial \mathbf{H}}{\partial t} - \mu\varepsilon \frac{\partial^2 \mathbf{H}}{\partial t^2} \end{aligned} \tag{3.12}$$

Moreover, having the vector identity (3.13)

$$\nabla \times (\nabla \times \mathbf{F}) = \nabla (\nabla \cdot \mathbf{F}) - \nabla^2 \mathbf{F} \tag{3.13}$$

which described for any vector $\mathbf{F}$ and applied to (3.11) and (3.12), yields

$$\nabla \times (\nabla \times \mathbf{E}) = \nabla (\nabla \cdot \mathbf{E}) - \nabla^2 \mathbf{E} = -\mu\sigma \frac{\partial \mathbf{E}}{\partial t} - \mu\varepsilon \frac{\partial^2 \mathbf{E}}{\partial t^2} \tag{3.14}$$

$$\nabla \times (\nabla \times \mathbf{H}) = \nabla (\nabla \cdot \mathbf{H}) - \nabla^2 \mathbf{H} = -\mu\sigma \frac{\partial \mathbf{H}}{\partial t} - \mu\varepsilon \frac{\partial^2 \mathbf{H}}{\partial t^2} \tag{3.15}$$

Having also from (3.1) that

$$\nabla \cdot \mathbf{H} = 0 \tag{3.16}$$

and from (3.3), in absence of any source of charge $\rho = 0$

$$\nabla \cdot \mathbf{E} = 0 \tag{3.17}$$

Thus, Helmholtz'equations are obtained describing the propagation of electromagnetic fields waves.

$$\nabla^2\mathbf{E} = -\mu\sigma\frac{\partial\mathbf{E}}{\partial t} - \mu\varepsilon\frac{\partial^2\mathbf{E}}{\partial t^2} \tag{3.18}$$

$$\nabla^2\mathbf{H} = -\mu\sigma\frac{\partial\mathbf{H}}{\partial t} - \mu\varepsilon\frac{\partial^2\mathbf{H}}{\partial t^2} \tag{3.19}$$

Equations (3.18) and (3.19) can be written in frequency domain as

$$\nabla^2\mathbf{E} = \mu\sigma\,(j\omega)\,\mathbf{E} + \mu\varepsilon\left(j\omega\right)^2\mathbf{E} = j\omega\mu(\sigma + j\omega\varepsilon)\,\mathbf{E} \tag{3.20}$$

$$\nabla^2\mathbf{H} = \mu\sigma\,(j\omega)\,\mathbf{H} + \mu\varepsilon\left(j\omega\right)^2\mathbf{H} = j\omega\mu(\sigma + j\omega\varepsilon)\,\mathbf{H} \tag{3.21}$$

Which can be reduced to

$$\nabla^2\mathbf{E} - \Gamma^2\mathbf{E} = 0 \tag{3.22}$$

$$\nabla^2\mathbf{H} - \Gamma^2\mathbf{H} = 0 \tag{3.23}$$

where the complex constant Γ is defined as the propagation constant in 1/m.

$$\Gamma = \sqrt{j\omega\mu\,(\sigma + j\omega\varepsilon)} = \alpha + j\beta \tag{3.24}$$

The real part of the propagation constant α is defined as the attenuation constant in Np/m and the imaginary part β is defined as the phase constant rad/m. The attenuation constant defines the rate at which the fields of the wave are attenuated as the wave propagates, and the phase constant defines the rate at which the phase changes as the wave propagates.

The electromagnetic waves **E** and **H** are defined as plane waves, i.e. they lie in a plane xy perpendicular to the direction of propagation z and the are perpendicular to each other as seen in Fig. 3.2. Moreover, **E** and **H** vary only in the direction of propagation, thus (3.22) and (3.23) can be written in the form

$$\frac{\partial^2 E_x}{\partial z^2} - \Gamma^2 E_x = 0 \tag{3.25}$$

$$\frac{\partial^2 H_y}{\partial z^2} - \Gamma^2 H_y = 0 \tag{3.26}$$

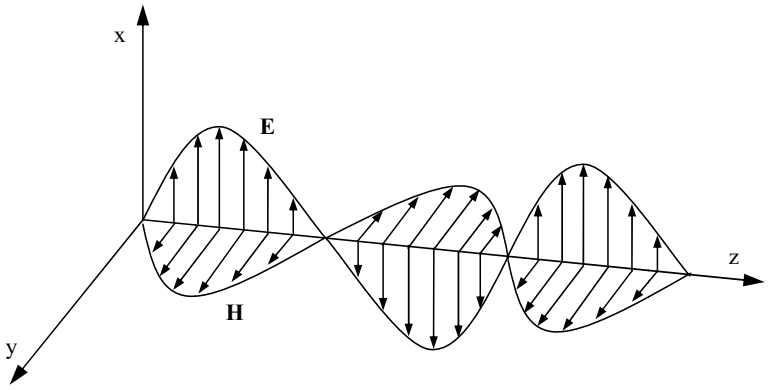

Figure 3.2: Propagation of electromagnetic plane waves.

The general solution to the above equations (3.25) and (3.26) is given in the form

$$E_x(z) = A_{1x}e^{-\Gamma z} + A_{2x}e^{\Gamma z} \tag{3.27}$$

$$H_y(z) = A_{1y}e^{-\Gamma z} + A_{2y}e^{\Gamma z} \tag{3.28}$$

where A_{1x}, A_{2x}, A_{1y} and A_{2y} are integration constants, which must fulfill the boundary conditions.

Lets evaluate the case when of an electromagnetic wave incident on a surface of change from a mean 1 to a different mean 2. Part of the wave is reflected and part penetrates the mean 2. Under such conditions if we consider the boundary conditions for the electric field **E** as defined below

$$\begin{aligned} &\text{if } z = 0 \quad && E_x(z=0) = A_{1x} + A_{2x} = E_{ms} \\ &\text{if } z \to \infty \quad && E_x(z=\infty) = A_{2x} = 0 \end{aligned} \tag{3.29}$$

and analog boundary conditions are applied for the magnetic field **H**

$$\begin{aligned} &\text{if } \ z = 0 \quad && H_y(z=0) = A_{1y} + A_{2y} = H_{ms} \\ &\text{if } \ z \to \infty \quad && H_y(z=\infty) = A_{2y} = 0 \end{aligned} \tag{3.30}$$

the solution of their Helmholtz's equation can be written as

$$E_x(z) = E_{ms}e^{-\Gamma z} \tag{3.31}$$

$$H_y(z) = H_{ms}e^{-\Gamma z} \tag{3.32}$$

where E_{ms} and H_{ms} are the surface values of the electric and magnetic field respectively. Moreover, at the boundary surface $z = 0$

$$\frac{\partial E_x}{\partial z} = -\Gamma E_{ms} e^z = -\Gamma E_{ms} \tag{3.33}$$

and considering also that

$$-\mu \frac{\partial \mathbf{H}}{\partial t} = -\mu j\omega H_{ms} \tag{3.34}$$

yield from (3.9) to

$$\Gamma E_{ms} = \mu j\omega H_{ms} \tag{3.35}$$

From the relationship between the surface values of the electric and magnetic fields, having units of Ohms (Ω), is thus defined the complex surface impedance in (3.36).

$$\mathbf{Z}_s = \frac{E_{ms}}{H_{ms}} = \frac{\mu j\omega}{\Gamma} \tag{3.36}$$

Also combining (3.8) and (3.36) yield to

$$J_x = j\frac{\sigma\mu\omega}{\Gamma} H_y \tag{3.37}$$

which represents the induced currents due the field H_y are 90° shifted.

3.1.2 Conservation of energy and Poynting's Vector

Poynting's theorem is the fundamental energy-conservation theorem for electromagnetic fields [83]. Using Poynting's theorem, all sources of energy related to electromagnetic fields in a given volume can be identified. The corresponding Poynting's Vector defines the vector power density (direction and density of power flow at a point). To derive Poynting's theorem, we start with the time-dependent Maxwell equations (3.2) and (3.4) above. The energy is propagated trough the space from one point to another in a continuous way, by means of electromagnetic waves. The electromagnetic waves transport electromagnetic power and the product of $\mathbf{E}$ and $\mathbf{H}$ gives units of $\mathrm{W/m^2}$, i.e. volume power density. As shown for the uniform plane wave in Fig. 3.2, the direction of $\mathbf{E} \times \mathbf{H}$ gives the direction of wave propagation z, i.e. the direction of power flow. Thus, a relationship defining the cross product of $\mathbf{E}$ and $\mathbf{H}$ is sought.

Using the vector identity (3.38) bellow,

$$\nabla \cdot (\mathbf{E} \times \mathbf{H}) = \mathbf{H} \cdot (\nabla \times \mathbf{E}) - \mathbf{E} \cdot (\nabla \times \mathbf{H}) \tag{3.38}$$

and combining with equations (3.2) and (3.4), leads to

$$\nabla \cdot (\mathbf{E} \times \mathbf{H}) = -\mathbf{H} \cdot \frac{\partial \mathbf{B}}{\partial t} - \mathbf{E} \cdot \frac{\partial \mathbf{D}}{\partial t} - \mathbf{E} \cdot \mathbf{J} \tag{3.39}$$

The three terms on the right hand side of (3.39) may be rewritten as

$$\mathbf{H} \cdot \frac{\partial \mathbf{B}}{\partial t} = \mu \left(\mathbf{H} \cdot \frac{\partial \mathbf{H}}{\partial t} \right) = \mu \frac{1}{2} \frac{\partial}{\partial t} (\mathbf{H} \cdot \mathbf{H}) = \frac{\partial}{\partial t} \left(\frac{1}{2} \mu H^2 \right) \tag{3.40}$$

$$\mathbf{D} \cdot \frac{\partial \mathbf{D}}{\partial t} = \varepsilon \left(\mathbf{E} \cdot \frac{\partial \mathbf{E}}{\partial t} \right) = \varepsilon \frac{1}{2} \frac{\partial}{\partial t} (\mathbf{E} \cdot \mathbf{E}) = \frac{\partial}{\partial t} \left(\frac{1}{2} \varepsilon E^2 \right) \tag{3.41}$$

$$\mathbf{E} \cdot \mathbf{J} = \sigma (\mathbf{E} \cdot \mathbf{E}) = \sigma E^2 \tag{3.42}$$

which gives

$$\nabla \cdot (\mathbf{E} \times \mathbf{H}) = -\frac{\partial}{\partial t} \left(\frac{1}{2} \mu H^2 + \frac{1}{2} \varepsilon E^2 \right) - \sigma E^2 \tag{3.43}$$

Integrating (3.43) over a given volume V, enclosed by a surface S and applying the divergence theorem yields

$$\begin{aligned} \int_V \nabla \cdot (\mathbf{E} \times \mathbf{H}) \mathrm{d}v &= \int_S (\mathbf{E} \times \mathbf{H}) \cdot \mathrm{d}s \\ &= -\frac{\partial}{\partial t} \int_V \left(\frac{1}{2} \mu H^2 + \frac{1}{2} \varepsilon E^2 \right) \mathrm{d}v - \int_V \sigma E^2 \, \mathrm{d}v \\ &= -\frac{\partial}{\partial t} \int_V (w_m + w_e) \, \mathrm{d}v - \int_V p_\sigma \, \mathrm{d}v \end{aligned} \tag{3.44}$$

In (3.44) the left hand side term is the net power flow out of the volume V. On the right hand side, the terms represent from left to right the rate of loss of the stored magnetic w_m and electric w_e energy within V and the Joule losses p_σ within V, i.e. the energy transformed by the conductor into heat. Thus

$$\mathbf{S} = \mathbf{E} \times \mathbf{H} \tag{3.45}$$

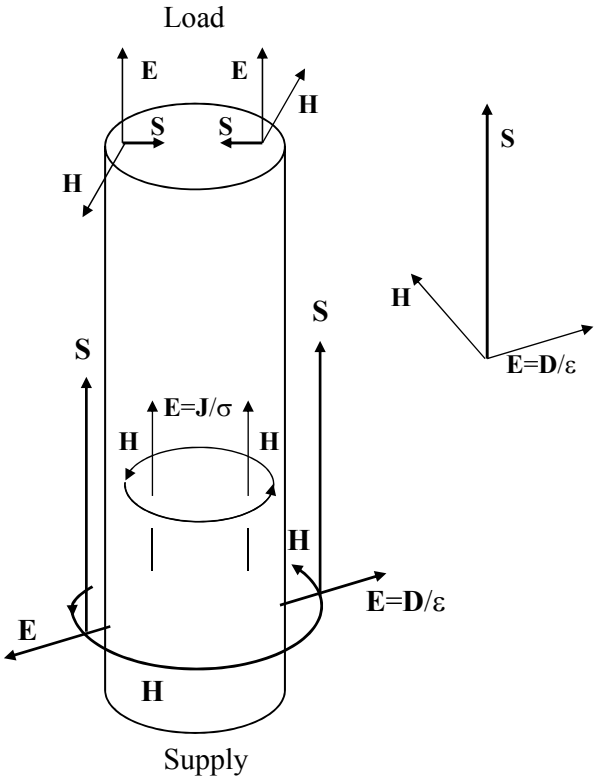

Figure 3.3: Poynting's Vector representation within a conductor wire.

is identified as the instantaneous Poynting's Vector **S**, representing direction and density of power flow at a point. Thus, it has been proven that there is a general law for the transfer of energy, according to which it moves in perpendicular direction to the plane containing electric and magnetic field strengths. In Fig. 3.3 the representation on the Poynting's Vector in and around a conductor wire is given.

Outside the conductor, the lines of magnetic field are circles around the axis of the conductor and the lines of electric field point in this particular case inwards the conductor centre. Poynting's Vector is then parallel to the conductor surface, which means that electromagnetic energy is transmitted by the dielectric mean surrounding the conductor.

Inside the conductor, lines of magnetic field are again circles around the axis, but lines of electric field are along the wire. Thus, any tangent plane to the conductor surface contains the directions of both, the electric and magnetic intensities. Therefore, the energy flow represented by Poynting's Vector is perpendicular to that surface, i.e. radial direction, and pointing to the conductor axis. Across the ends, there is no energy flowing, so the the energy entering through the external surface is accounted for the energy transformed by the conductor into heat, as from Joule losses.

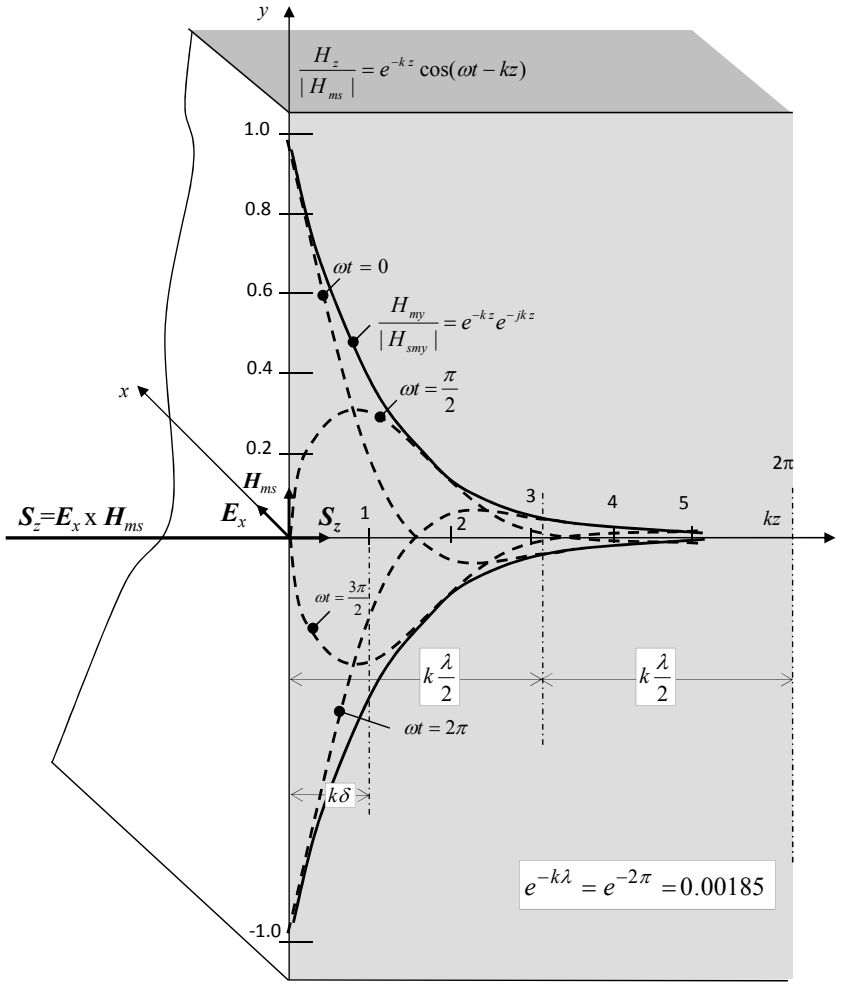

Figure 3.4: Electromagnetic wave penetration inside solid metal.

3.1.3 Stray Losses applying Poynting's Vector

If a conductor mean is considered $\sigma \neq 0$ and $\varepsilon \approx 0$, thus, from Maxwell's equations (3.1) to (3.4) and the solution of their Helmholtz's equation (3.19), the envelope of maximum magnetic field H_m changes with penetration depth in direction of the propagation z of electromagnetic fields H_m and E_m from surface as seen in Fig. 3.4 following the laws [15] describing processes inside solid metal

$$H_m = H_{ms}e^{-\Gamma z} \tag{3.46}$$

and from (3.36) and (3.48)

$$E_m = \frac{\Gamma}{\sigma}H_m \tag{3.47}$$

where H_{ms} is the maximum value of the magnetic field intensity at the surface.

The propagation coefficient of the electromagnetic field in solid metal Γ is defined in (3.48)

$$\Gamma = (1 + j)k \tag{3.48}$$

where $\alpha = \beta = k = 1/\delta$ is the attenuation constant, and δ defined in (3.49), is the skin depth penetration of electromagnetic wave in solid metal, i.e. the distance in z over which a plane wave is attenuated by a factor of e^{-1} in a good conductor.

$$\delta = \sqrt{\frac{2}{\omega\mu\sigma}} \tag{3.49}$$

The length of electromagnetic wave in solid metal from (3.46) is given by

$$\lambda = 2\pi\delta \tag{3.50}$$

Thus, given a plane wave incident on a conducting surface, the electric field, and thus the current density, are found to be concentrated at the surface of the conductor. The effect is frequency-dependent, and the phenomenon is known as the skin effect.

Having a 3D Cartesian coordinate system (x, y, z), the propagation in z-axis of power of electromagnetic fields at any point (x, y) in VA/m^2 can be formulated by Poynting's Vector, being its instantaneous value at time t calculated as

$$\mathbf{S}(z, t) = \mathbf{E}(z, t) \times \mathbf{H}(z, t) = \frac{1}{2}\Re e[\mathbf{E}(z) \times \mathbf{H}^*(z)] \tag{3.51}$$

where $\Re e$ is the complex real operator and $\mathbf{H}^*$ the complex conjugate of magnetic field vector.

For a time-harmonic field, the time average Poynting's Vector is found by calculating the mean value over one period of time T, resulting

$$\mathbf{S}_{av}(z) = \frac{1}{T}\int_0^T \mathbf{S}(z, t)\mathrm{d}t \tag{3.52}$$

Considering (3.48) and (3.48), the complex power losses over a metallic surface s in VA/m^2 result

$$\mathbf{S}_{av}(z = 0) = p_s + jq_s = \frac{1}{2}\frac{(1 + j)}{\sigma\delta}H_{ms}^2 \tag{3.53}$$

The active part from (3.53) are the eddy current losses per unit surface area in $\mathrm{W/m^2}$, in the absence of hysteresis and non-linearity of magnetic characteristic is

$$P_s = \frac{1}{2\sigma\delta} H_{ms}^2 \tag{3.54}$$

where the magnetic field H_{ms} is incident at the metal surface.

All representations of the Poynting's Vector represent energy densities. Thus, to determine the total power passing through a surface, the Poynting's Vector must be integrated over the considered surface. Equation (3.54 might be written in terms of surface impedance $\mathbf{Z}_s$ (3.36) as

$$P_s = \Re e(\mathbf{Z}_s) \frac{H_{ms}^2}{2} \tag{3.55}$$

By using an analogy with Ampère's law, considering $H_{ms} = I_m$ the peak current per unit width, the stray loss equation (3.54) can be written in the form

$$P_\sigma = \left(\frac{I_m}{\sqrt{2}}\right)^2 \frac{1}{\sigma\delta} = I_{rms}^2 R' \tag{3.56}$$

where $R' = (\sigma\delta)^{-1}$ is the resistance of unit length of a layer of thickness δ (3.49) and unit width [82]. The correct value of loss is therefore obtained if the current is assumed to flow with uniform density in a layer of depth δ, for this reason δ is known as the eddy current skin depth.

The representation on the Poynting's Vector and the flow of energy within a conductor traversing a steel cover plate system, and within a single-phase cover plate system are given in Fig. 3.5 and Fig. 3.6 respectively. It is seen that electromagnetic waves hit the steel plate surface, as in Fig. 3.4, propagating inside metal wall. This phenomenon causes the power dissipation within the steel plate and consequent dissipation of heat.

3.1.4 Magnetic field analytical formulation

In the literature review, in Chapter 2, a large list of papers and methods devoted to estimation electromagnetic leakage flux are given. Here, analytical methods are chosen since the still have some advantages compared with more sophisticated ones, such as quickly asses and evaluate the influence of several parameters and they make possible to incorporate their results in other computer programs which calculate, for example, the resulting losses and temperature rise. However, any available method might be used in order to compute leakage magnetic field in transformer structural parts, to be introduced then in the stray loss calculation by means of Poynting's Vector (3.54).

In transformers, there are predominantly two kinds of surface excitation [84] as shown

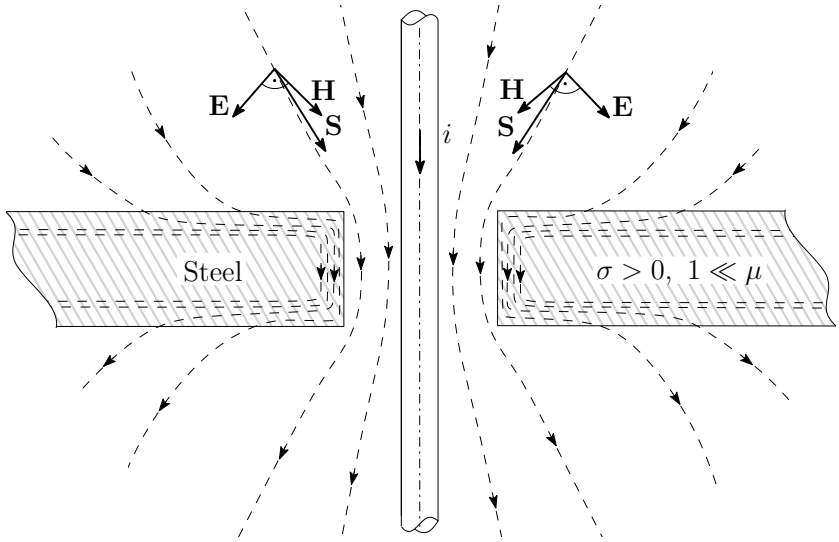

Figure 3.5: Energy flow of Poynting's Vector within a conductor traversing a steel cover plate.

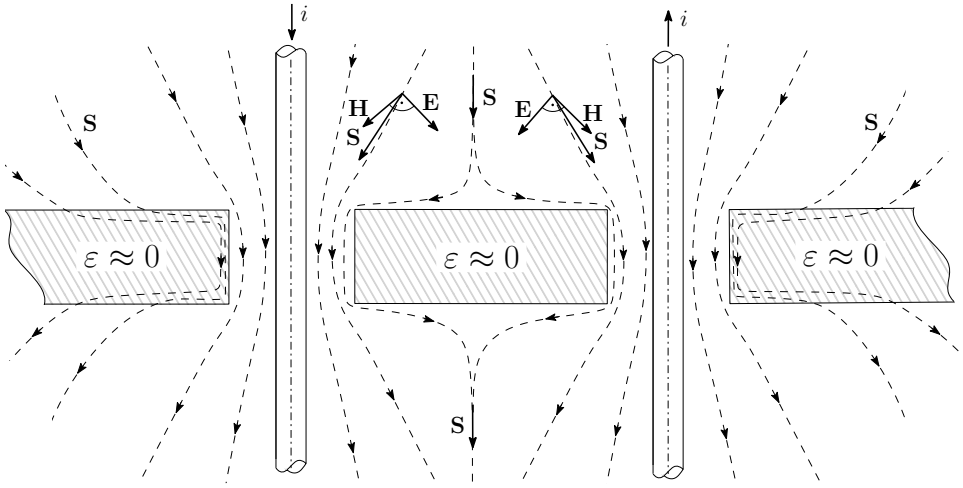

Figure 3.6: Energy flow of Poynting's Vector within a single-phase cover plate system.

in Fig. 3.7. Eddy currents and stray losses might be appreciable different depending whether the material is excited by tangential or normal field, therefore the analytical equations and methods derived for the field calculation also differ from each other. The field computation differs for the case of transformer covers or bushing mounting plates, where the field is tangential to the plate surface, as seen in Fig. 3.7(a), and the tank wall where the field is normal to the iron surface as seen in Fig. 3.7(b). In case the incident field is tangential, the field is directly proportional to the source current since

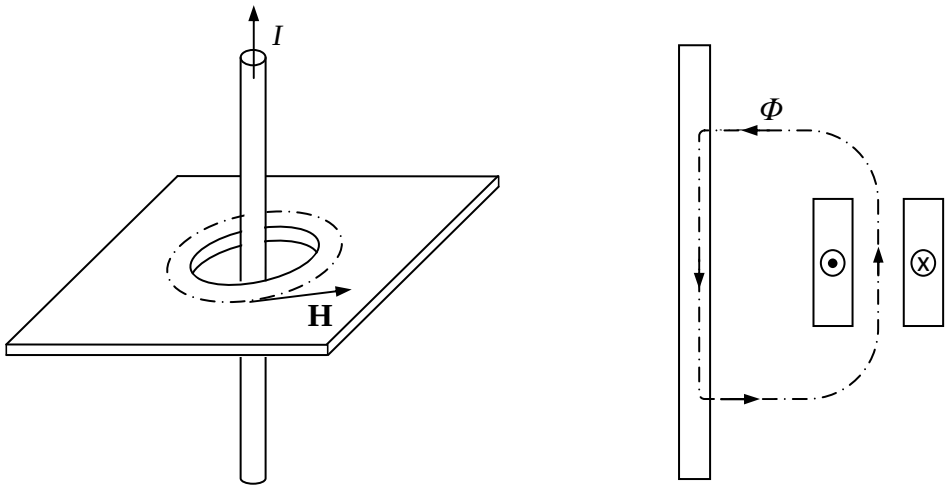

(a) Tangential field. (b) Normal field.

Figure 3.7: Types of excitation field.

the magnetic field intensity **H** on the plate surface can be determined by the principle of superposition. In case Fig. 3.7(b), for estimation of stray losses in the tank due to a leakage field incident on it, only the normal or radial component of the incident field Φ can be considered as proportional to the source current. The tangential field component evaluation is more complicated and in many analytical formulations, the loss is calculated based on the tangential components, which need to be evaluated from the normal component of the incident field with the help of Maxwell's equations.

The estimated values of these two tangential field components can be used to find the resultant tangential component and thereafter the tank loss as per equation (3.54).

3.1.4.1 Transformer cover. Tangential field formulation

In the analytical formulation, the field intensity peak value at any point on the plate surface is responsible for the loss distribution according to (3.87). In calculating the magnetic fields due to electric currents, it is sometimes easier to use Biot-Savart's law, which allows to calculate the magnetic field near a long straight current-carrying wire located along the z-axis with current moving in the positive z-direction, as seen from Fig. 3.8.

$$\mathrm{d}\mathbf{H} = \frac{1}{4\pi}\frac{I\,\mathrm{d}\mathbf{l}\times\mathbf{u}_r}{D^2}\sin\varphi \tag{3.57}$$

where dl is an element of length along the path taken by the ac current i, r is the position vector of the point at which **H** is to be calculated. Equation (3.57) can be solved for the magnetic field at any space-point due to a current of any shape. In principle one needs

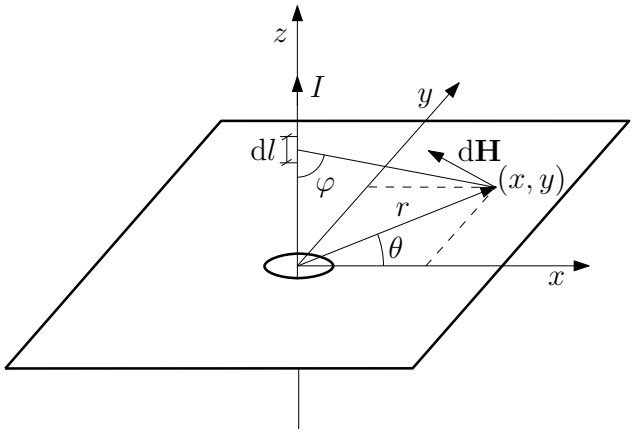

Figure 3.8: Biot-Savart law applied to calculate the magnetic field near a long straight current-carrying wire.

only integrate along the path followed by the charges in the current. If a conductor of infinite length is considered, the field distribution in the transformer cover is then assumed purely tangential. As seen in Appendix A.1, in the case of an infinite conductor (3.57) yields

$$h(t) = \frac{i(t)}{2\pi r} \tag{3.58}$$

Thus, the maximum magnetic field on cover surfaces is calculated from the Biot-Savart law as a vector sum of the field intensity due to all source currents flowing through the conductors [15] applying

$$H_m^2 = \frac{2}{T}\int_0^T h^2(t)\mathrm{d}t \tag{3.59}$$

Expressing h as

$$h^2(t) = h_\theta^2(t) + h_r^2(t) \tag{3.60}$$

where h_r and h_θ are the radial and tangential components of the magnetic field respectively.

The particular formulation for one conductor, single phase and three phase bushings are collected in the following paragraphs.

Cover plate with one conductor

The magnetic field calculation for one conductor passing through a steel plate is

$$h^2(t) = h_\theta^2(t) = \frac{i_1^2(t)}{4\pi^2 r_1^2} = \frac{I_m^2 \sin^2 \omega t}{4\pi^2 r_1^2} \tag{3.61}$$

where $i_1(t)$ is the alternating current (ac) flowing through the conductor, I_m is the peak value of current, and r_1 is the distance form a given point to the conductor. Then, the resulting maximum magnetic field H_m, calculated from (3.59) in cylindrical coordinates (r, θ) results

$$H_m(r, \theta) = \frac{I}{\sqrt{2}\,\pi r} \tag{3.62}$$

and in Cartesian coordinates (x, y), is expressed as

$$H_m(x, y) = \frac{I}{\sqrt{2}\,\pi \sqrt{x^2 + y^2}} \tag{3.63}$$

being I the root mean square (rms) value of the current $i_1(t)$.

Single-Phase Bushing

For a single-phase bushing, the magnetic field is calculated as

$$h^2(t) = \frac{1}{4\pi^2} \left\{ \left(\frac{i_1(t)\cos\beta'}{r_1} + \frac{i_2(t)\cos\beta}{r_2} \right)^2 + \left(\frac{i_1(t)\sin\beta'}{r_1} + \frac{i_2(t)\sin\beta}{r_2} \right)^2 \right\} \tag{3.64}$$

where $i_1(t)$ and $i_2(t)$ are the single-phase ac currents and r_1 and r_2 are the distances from a given point to each conductor, as shown in Fig. 3.9(a). The maximum magnetic field from (3.59) in cylindrical coordinates (r, θ) results

$$H_m(r, \theta) = \frac{I\,a}{\sqrt{2}\,\pi} \frac{1}{\sqrt{r^4 - \dfrac{a^2}{2} r^2 \cos(2\theta) + \dfrac{a^4}{16}}} \tag{3.65}$$

and in Cartesian coordinates (x, y) is expressed as

$$H_m(x, y) = \frac{I\,a}{\sqrt{2}\,\pi} \frac{1}{\sqrt{x^4 + y^4 + 2x^2y^2 - \dfrac{a^2(x^2 - y^2)}{2} + \dfrac{a^4}{16}}} \tag{3.66}$$

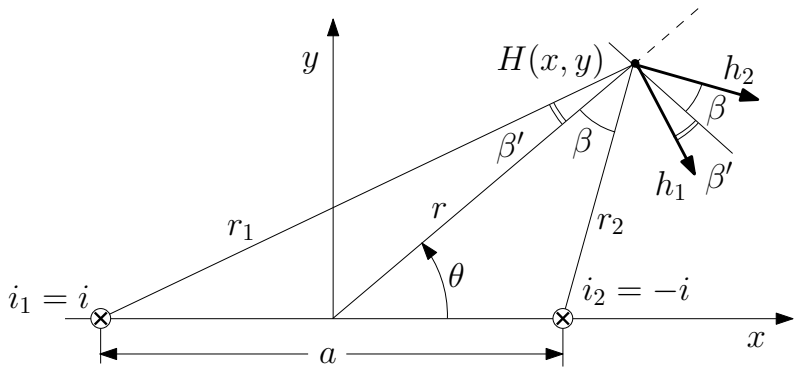

(a) Single-phase bushing.

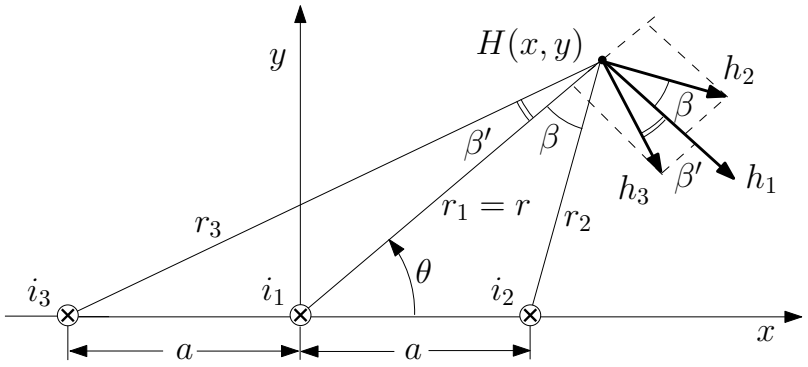

(b) Three-phase bushing.

Figure 3.9: Magnetic field distribution calculation over transformer cover plates.

where I is the rms value of the ac currents and a is the distance between conductors as seen in Fig. 3.9(a).

Three-Phase Bushing

For a three-phase bushing, the magnetic field is calculated as

$$h^2(t) = \frac{1}{4\pi^2}\left\{\left(\frac{i_1(t)}{r_1} + \frac{i_2(t)\cos\beta}{r_2} + \frac{i_3(t)\cos\beta'}{r_3}\right)^2 + \left(\frac{i_2(t)\sin\beta}{r_2} + \frac{i_3(t)\sin\beta'}{r_3}\right)^2\right\} \tag{3.67}$$

where $i_1(t)$, $i_2(t)$ and $i_3(t)$ are three-phase ac currents and r_1, r_2, and r_3 are the distances

from a given point to each conductor as can be seen in Fig.3.9(b). The maximum magnetic field in cylindrical coordinates (r, θ) from (3.59) results

$$H_m(r,\theta) = \frac{I\,a}{\sqrt{2}\,\pi r}\sqrt{\frac{3r^2+a^2}{r^4-2a^2r^2\cos(2\theta)+a^4}} \tag{3.68}$$

and in Cartesian coordinates (x, y) is expressed as

$$H_m(x,y) = \frac{I\,a}{\sqrt{2}\,\pi}\sqrt{\frac{3x^2+3y^2+a^2}{(x^2+y^2)(x^4+y^4+2x^2y^2-2a^2x^2+2a^2y^2+a^4)}} \tag{3.69}$$

where I is the rms value of the ac currents and a is the distance between conductors as seen in Fig.3.9(b).

3.1.4.2 Transformer tank walls. Normal field formulation.

The proposed methodology in [81] can be extended to the case of tank walls. A steel plate located on the xy plane is considered. A current conductor passing parallel to the steel plate on the x direction, and at a distance a on the z direction, departs radial stray flux which intrudes normal into the iron surface. However, inside metal, the flux turns mostly tangential, being thus the tangential component of the magnetic field inside metal the responsible for the losses.

To calculate the normal component of the magnetic field penetrating into the metal surface, the method of images (or method of mirror images) may be used [15]. Using this method a double medium space can be replaced by a single one by means of appropriate coefficients. The method of images is a mathematical tool for solving differential equations in which the domain of the investigated function is extended by the addition of its mirror image, with respect to a symmetry plane, and thus reproducing the boundary conditions. It has been typically applied to calculate the electrostatic potential due to a electric charge, and might extended to the electromagnetic problem as both fields satisfy the same form of Laplace's equation [85]. Thus, the magnetic potential due to the presence of a highly permeable metal surface, is the same as if the metal medium is replaced by a parallel image current, located symmetrically to the metal surface. Thus, the distribution of the magnetic field can be calculated at the vicinity of the conducting surfaces for any current distribution.

When calculating losses in tank walls where the field varies only in the xy plane, the problem is reduced to a 2D model [15]. Then, the maximum field can be calculated from applying Biot-Savart law (3.58) to the currents system resulting from the method of images, as seen in Fig. 3.10. Thus, the value of the maximum magnetic field in air H_{mz0} at $z = 0$, i.e. the metal surface, can be calculated from (3.59), and the field inside metal becomes

$$H_{mz}(y,z) \approx \frac{\mu_0}{\mu} H_{mz0}(y,0) e^{-\Gamma z} \tag{3.70}$$

From Maxwell equations, and the behavior of electromagnetic fields in solid metal (3.46) and (3.47), the component of electric field inside metal is

$$E_{mx}(y,z) = -j\omega\mu_0 F_y e^{-\Gamma z} \tag{3.71}$$

where

$$F_y = -\int H_{mz0}(y,0) e^{-\Gamma z} + C_0 \tag{3.72}$$

being C_0 the integration constant to be determined from boundary conditions. The tangential component of the magnetic field on the surface of the tank wall in y direction H_{my} can be calculated thus from (3.36)

$$H_{my} = \frac{\Gamma}{\mu j\omega} E_{mx} \tag{3.73}$$

which combined with 3.71 yields

$$H_{my}(y,z) = (1+j)\mu_0 \sqrt{\frac{\omega\sigma}{2}} \frac{1}{\sqrt{\mu}} F_y e^{-\Gamma z} \tag{3.74}$$

where C_0 is calculated assuming that $H_{my} = 0$ at both ends of the steel plate.

Thus, the tangential field component at the metal surface can be determined for any conductor distribution. The particular formulation for one, two, three conductors passing parallel to a metal surface are presented in the next subsections.

Current carrying conductor passing parallel to a steel plate

In the case of one current carrying conductor passing parallel to a tank wall, the normal component of the magnetic field reaching the metal surface, is calculated from Biot-Savart law (3.58) as seen in Fig. 3.10(a), at the metal surface ($z = 0$) resulting

$$H_{mz0}(y,0) = n_Q \frac{I\sqrt{2}}{\pi} \frac{y}{y^2 + a^2} \tag{3.75}$$

where I is the rms value of the ac current i flowing through the conductor, a is the distance from the conductor to the steel plate and n_Q comes from applying the image coefficient in steel $M = 0.6$ to the imaged current Mi, as seen in Fig. 3.10.

$$n_Q = \frac{1+M}{2} \tag{3.76}$$

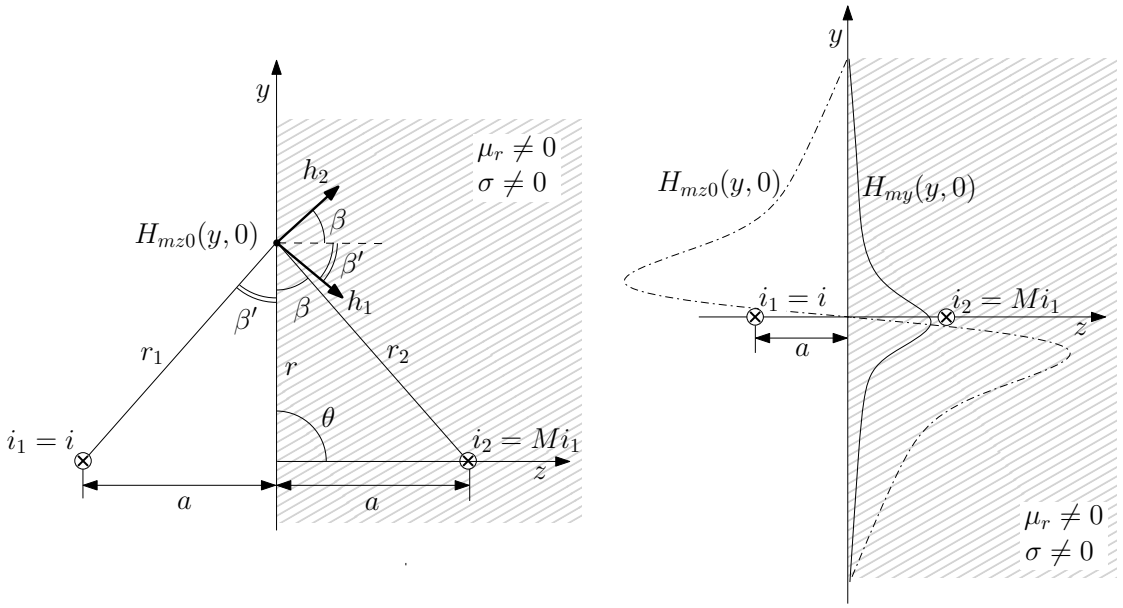

(a) Field calculation. (b) Field distribution.

Figure 3.10: Method of images applied to a current carrying conductor to calculate the magnetic field distribution at the vicinity of a conducting surface.

The tangential component of the magnetic field, responsible for the losses, as seen in Fig. 3.10(b), is then calculated from (3.74) as

$$H_{my}(y,z) = (1+j)\mu_0\sqrt{\frac{\omega\sigma}{2}}\frac{1}{\sqrt{\mu}}F_y e^{-\Gamma z} \tag{3.77}$$

being F_y from calculated from (3.72)

$$F_y = -n_Q\frac{I}{\sqrt{2}\pi}\ln(y^2+a^2) + C_0 \tag{3.78}$$

where C_0 is determined by considering $H_{my} = 0$ at the tank wall boundary.

Single phase conductor system passing parallel to a steel plate

In the case of considering two conductors carrying single phase currents passing parallel to a tank wall, two different lead arrangements are considered in the analytical formulation, i.e. vertical and horizontal layout, as seen in Fig. 3.11.

The normal component of the magnetic field reaching the metal surface, is calculated from Biot-Savart law (3.58) at the metal surface ($z = 0$) resulting in the case of vertical layout

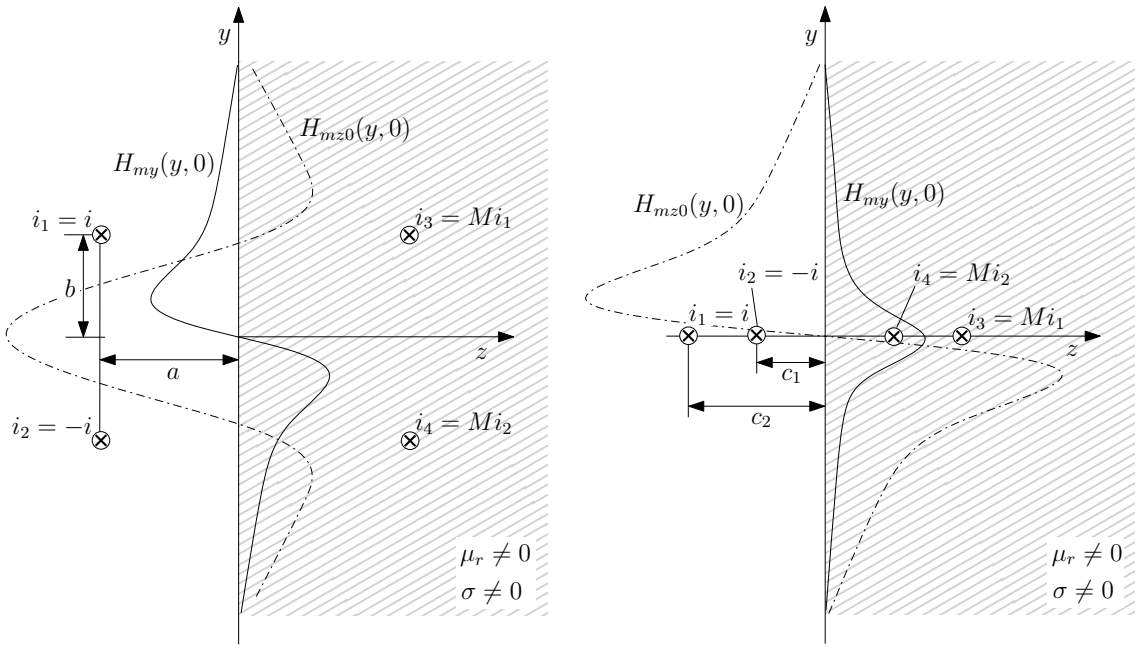

(a) Vertical layout. (b) Horizontal layout.

Figure 3.11: Method of images applied to a single-phase conductor system to calculate the magnetic field distribution at the vicinity of a conducting surface.

$$H_{mz0}(y,0) = n_Q \frac{I\sqrt{2}}{\pi}\left(\frac{y-b}{(y-b)^2+a^2} - \frac{y+b}{(y+b)^2+a^2}\right) \tag{3.79}$$

where I is the rms value of the ac current, a is the distance from the conductor to the steel plate, b is half of the distance between the conductors, and n_Q the image coefficient described in (3.76). The tangential component of the magnetic field, seen in Fig. 3.11(a), responsible for the losses is calculated as from (3.77), where

$$F_y = -n_Q \frac{I}{\sqrt{2}\pi}\left(\ln((y-b)^2+a^2) - \ln((y+b)^2+a^2)\right) + C_0 \tag{3.80}$$

When considering horizontal layout the magnetic field distribution reaching the metal surface results

$$H_{mz0}(y,0) = n_Q \frac{I\sqrt{2}}{\pi}\left(\frac{y}{y^2+c_2^2} - \frac{y}{y^2+c_1^2}\right) \tag{3.81}$$

and the tangential component of the magnetic field, seen in Fig. 3.11(b), is calculated as from (3.77), where

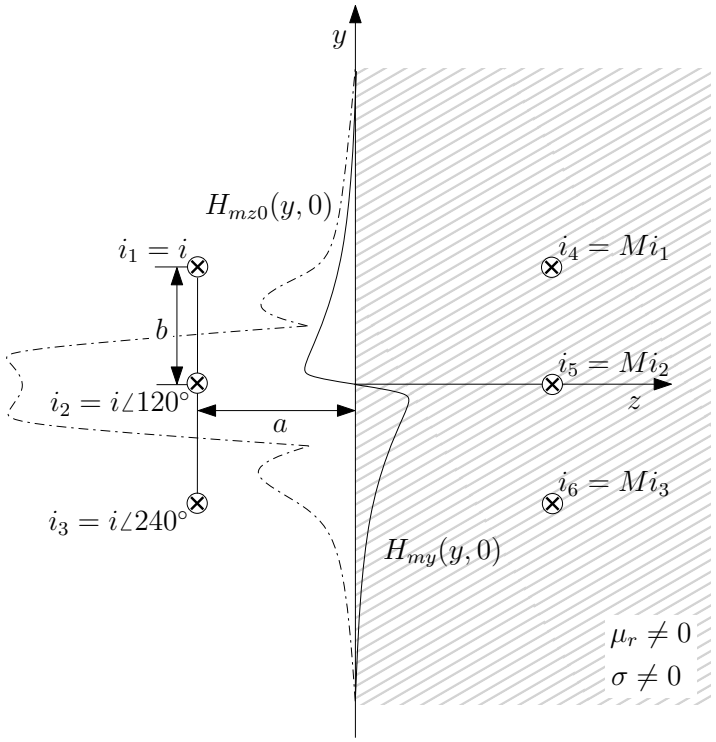

Figure 3.12: Method of images applied to a three-phase conductor system to calculate the magnetic field distribution at the vicinity of a conducting surface.

$$F_y = -n_Q \frac{I}{\sqrt{2}\pi} \left(\ln((y)^2 + c_2^2) - \ln((y+b)^2 + c_1^2) \right) + C_0 \tag{3.82}$$

being c_1 and c_2 the distance from either of the conductors to the steel surface, and C_0 determined by considering $H_{my} = 0$ at the tank wall boundary.

Three phase conductor system passing parallel to a steel plate

In the case of considering three conductors carrying three phase currents, passing parallel to a tank wall, the normal component of the magnetic field reaching the metal surface, is calculated from Biot-Savart law (3.58) at the metal surface ($z = 0$) resulting in the case of vertical layout

$$H_{mz0}(y,0) = n_Q \frac{I}{\pi} \sqrt{(M-N)^2 + (N-L)^2 + (L-M)^2} \tag{3.83}$$

Where

$$M = \frac{(y-b)}{(y-b)^2 + a^2}$$

$$N = \frac{y}{y^2 + a^2} \tag{3.84}$$

$$L = \frac{(y+b)}{(y+b)^2 + a^2}$$

being I the rms value of the three phase currents, a the distance from the conductors to the steel plate, b is the distance between the conductors and n_Q the image coefficient described in (3.76). The tangential component of the magnetic field, seen in Fig. 3.12, responsible for the losses is calculated as from (3.77), where the function F_y involves the integral of (3.83). Unfortunately it not been found the definite integral from the function (3.83), thus the solution has been found approximating (3.83) by means of Taylor polynomials and the use of symbolic integration to find the integrals.

Moreover, a factor k_s is used in the case of normal field excitation to compensate the value of losses in a plate of finite dimensions [16].

$$P_{wall} = k_s \cdot P_s \tag{3.85}$$

Where P_s has been defined in (3.54). Considering a steel plate of height h in the x direction and length L in the y direction, k_s is defined as

$$k_s = \frac{h}{\left(\frac{L}{h}\right)^2 + 1} \tag{3.86}$$

Thus, the actual power losses in the tank wall P_{wall} are calculated from (3.85) and introduced in the thermal FEM model as heat sources.

It is here to mention that in the case of a two-dimensional problem, the solution by means of e.g. FEM, RNM or other methods described in Chapter 2 does not present the drawbacks discussed throughout this dissertation applied to the 3D problem and allow to model complex geometries. However, the modelling by means of e.g. FEM still requires a deep knowledge of the problem if calculations are to be reliable. The two-dimensional problem is applied in Section 7.3, where the magnetic field distribution at the metal surface is calculated from both RNM and FEM, and results are compared. If the magnetic field distribution at the metal surface is calculated by any means, Poynting's Vector (3.55) can be used for the stray loss calculation.

3.1.5 Stray losses applying Turowski's equation

For calculating stray losses in conducting steel plates, on the surface of which the field is incident having a maximum value of H_{ms}, Poynting's Vector equation has been defined in (3.55). However hysteresis and non-linearity of magnetic characteristic have not yet been considered in the formulation. When dealing with structural steel of real power transformers, Turowski's equation, defined in (3.87) is applied [15]. This equation is based on Poynting's Vector (3.55), applying some correction factors for non-linearities.

$$P_s = a_p \iint_s \sqrt{\frac{\omega\mu}{2\sigma}} \frac{|\ H_{ms}(x,y)\ |^{2x_p}}{2}\, \mathrm{d}x\, \mathrm{d}y \tag{3.87}$$

where x and y are the Cartesian coordinates of each point on the plate surface -Fig. 3.8- and μ is the magnetic permeability of the metal plate. By means of (3.87) the stray losses into the skin depth penetration, calculated by using the resultant value of the field intensity H_{ms} due to source currents, are integrated on the entire plate area s.

A semi-empirical correction factor x_p is used depending upon the structure of the investigated element, the nature of the field and the type of the steel [12]. Thus, $x_p = 1$ for non-magnetic metals, and $x_p = 1.05$ to 1.14 for magnetic steel.

The factor a_p is a linearization coefficient which takes into account the variation of the relative permeability inside the material (z-direction) and hysteresis losses. It varies from $a_p = 1$ in the linear case, to $a_p = 1.7$ in the pure saturation case [59]. Moreover, analytical expressions are incorporated to the equation for the non-linear permeability μ on the metal surface (xy-plane). These latter concepts are clarified in the following subsections.

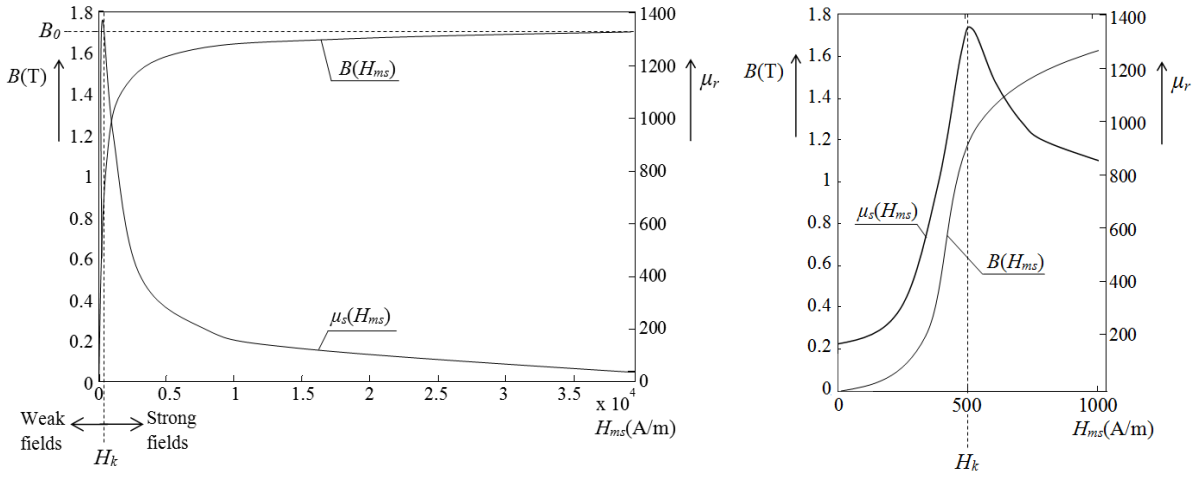

Figure 3.13: Non-linear magnetic BH curve and surface magnetic permeability behavior.

3.1.6 Non-linear permeability on the metal surface

The non-linear behavior of the magnetic permeability μ is well known. In a non-linear medium the permeability varies with the strength of the magnetic field $\mu(H_{ms})$, and it is calculated from the BH curve of the material, as seen in Fig. 3.13. Its well known effect is the saturation of the magnetic material, i.e. as the magnetic field H_{ms} increases, the value of the flux density B approaches a maximum level or saturation level B_0 and then is kept constant. Such non-linear characteristic must be considered in the case of transformer cover plates, where some parts are strongly saturated and others not. Considering the incident magnetic field distribution $H_{ms}(x, y)$ on the metal surface ($z = 0$) can be calculated from Biot-Savart law [15], the non-linear magnetic permeability on the metal surface $\mu_s(H_{ms}, x, y)$ defined in (3.88) can be easily considered from the real BH curve of the material as seen in Fig. 3.13.

$$\mu_s(H_{ms}, x, y) = \frac{B_{ms}}{H_{ms}(x, y)} \tag{3.88}$$

being $B_{ms} = B(H_{ms})$ the value of the flux density corresponding to H_{ms}. The surface permeability increases with H_{ms} as it approaches the saturation level, after reaching a maximum at saturation, corresponding to a value of H_k, it inverts the behavior and decreases towards the value of the permeability of air μ_0. The non linear behavior of μ_s can be incorporated into any model by introducing the BH curve of the material and interpolating at each iteration to approach the permeability value at each magnetization level.

However, when using the above proposed method, i.e. stray losses calculated from Poynting's vector and the magnetic field from Biot-Savart law, Turowski in [15] has calculated analytical expressions to take into account the non linear iron permeability at the metal surface, approaching the behavior of the BH curve.
In the case of the transformer cover or bushing box, for calculating stray losses in conducting steel plates, on the surface of which the field is incident having a tangential peak value of H_{ms}, Turowski's equation (3.87) is applied, and analytical approximation (3.89) for the non-linear magnetic characteristic might be used.

$$\sqrt{\mu_r}\,\mathbf{H}^2 = c_1\mathbf{H} + c_2\mathbf{H}^2 \tag{3.89}$$

where for structural steel the coefficients are $c_1 = 310 \cdot 10^2$ A/m and $c_2 = 7.9$.

In the case of normal excitation, when calculating losses in tank wall where the field varies only in the xy plane, having a peak value of H_{mz0} at the surface ($z = 0$), the problem is reduced to a 2D model [15]. From Maxwell equations, the field along the tank wall in y direction is defined in (3.74). In [15] the following analytical approximation for the non linear permeability is used

$$\frac{1}{\sqrt{\mu}} = A_1 + A_2\sqrt{\mu}\,\mathbf{H} \tag{3.90}$$

where the coefficients for structural steel A_1 and A_2 are defined as

$$A_1 = 14 \sqrt{\frac{\mathrm{Am}}{\mathrm{Vs}}} \tag{3.91}$$

$$A_2 = 0.13 \frac{\mathrm{m}^2}{\mathrm{Vs}} \tag{3.92}$$

By using the above described analytical approximations to account for the non linear behavior of the surface permeability, the non linear calculations, and integrals from (3.87) are greatly simplified.

3.1.7 Non-linear permeability inside metal

In Turowski's equation (3.87) for stray losses calculation, the factor a_p is a linearization coefficient which takes into account the variation of the relative permeability inside the material. Its physical meaning is explained in detail in this section, as well as the several approaches found in the literature to explain the above mentioned linearization coefficient are presented below.

As it has been previously explained in Section 3.1.3, it can be seen in Fig. 3.4 that the envelope of the maximum magnetic field H_m changes with field penetration in the direction of propagation z from the surface until a certain depth λ (3.50) as from the law (3.46). Moreover, from the permeability changes with the magnetic field as seen from the BH curve in Fig. 3.13. It comes then from the above statements that the permeability, would change inside solid metal in the z-direction $\mu(H_m, z)$ as the field is attenuating, as seen in Fig. 3.14.

The magnetic permeability behavior inside solid metal influences the electromagnetic fields, but also the active and reactive power losses distribution inside the ferromagnetic material [15], therefore it must be considered when calculating losses. If the magnetizing force reaching the surface H_{ms} is strong enough, the value of the saturation flux density B_0 might be considered constant within the penetration depth and a step function becomes a satisfactory approximation of the BH curve as it is shown in Fig. 3.16. Such simplification allows the analytical derivation of equations for the surface impedance (3.36) in the case of a rectangular (step) BH characteristic [59].

Rosenberg's semi-empirical approximation

Rosenberg in 1923 [61], assuming that the field inside solid metal H_m attenuates exponentially from the surface as from the function (3.46). Considering also that the decrease of the magnetic field for strong or saturated fields, i.e. $H_{ms} > H_k$, yields an increase of the magnetic permeability, Rosenberg stated that the flux density inside metal

$B_m(z)$ would approximate a step function $B'_m(z)$ within the penetration depth defined at saturation δ_{Sat}, as seen in Fig. 3.14.

The active power equation deduced from Rosenberg's theory, combined with empirical data, for saturated iron per unit surface is

$$P_{Rosenberg} = 1.34\sqrt{\frac{\omega\mu_0}{2\sigma}} \iint_s \sqrt{\mu_r}\, \frac{H_{ms}^2}{2} \tag{3.93}$$

The above Rosenberg's equation, compared with Turowski's equation (3.87), and with the linear theory (3.55) yields a value of the linearization coefficient $a_p = 1.34$.

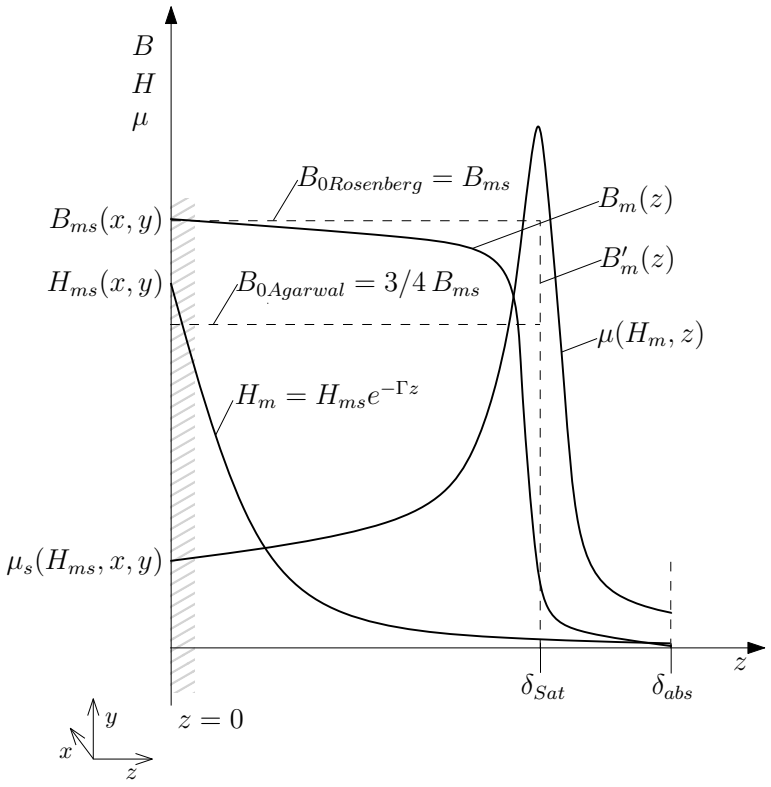

Figure 3.14: Non-linear magnetic fields behavior inside metal.

Method of square waves

In 1954 MacLean [86] proposed to calculate the solution of non linear waves inside metal as approximated by square waves. Thus, from a sinusoidal time varying field $H_s = H_{ms}\sin\omega t$, the maximum penetration depth at each point would be

$$\delta_{Sat} = \sqrt{\frac{2}{\omega\sigma B_0/H_{ms}}} \tag{3.94}$$

Thus, the field penetrates up to this depth when the thickness d of the metal is greater than δ_{Sat}. From the solution of Maxwell's equations and applying Fourier, the active component of the Poynting's Vector would be

$$P_{MacLean} = \frac{8}{3\pi}\frac{H_{ms}^2}{\delta_{Sat}} = \frac{8}{3\pi}\sqrt{\frac{\omega B_{ms}/H_{ms}}{2\sigma}}H_{ms}^2 = 1.67\sqrt{\frac{\omega B_{ms}/H_{ms}}{2\sigma}}\frac{H_{ms}^2}{2} \tag{3.95}$$

Where the value of the saturation flux density $B_0 = B_{ms}$ is taken from the magnetization curve of the material, corresponding to the peak of the magnetic field intensity H_{ms} at the metal surface and assumed constant within the penetration depth as proposed by Rosenberg [61] and seen in Fig. 3.14.

However, the aforementioned Rosenberg's proposal was found to be not correct, even for strong magnetization [59]. Therefore, a value of B_0 lower than the peak value at the surface B_{ms} would be more appropriate and Agarwal in 1959 [59] stated that an exact solution of the eddy current phenomena is not possible, and empirical calibration factors have to be determined. The best value of B_0 is found in [59] to be equal to $^3/_4 B_{ms}$, yielding

$$P_{Agarwal} = \frac{8}{3\pi}\sqrt{\frac{3}{4}}\sqrt{\frac{\omega B_{ms}/H_{ms}}{2\sigma}}H_{ms}^2 = 1.47\sqrt{\frac{\omega B_{ms}/H_{ms}}{2\sigma}}\frac{H_{ms}^2}{2} \tag{3.96}$$

The above MacLean and Agarwal's theories, compared with Turowski's equation (3.87) and with the linear theory (3.55), yield values of the linearization coefficient $a_p = 1.67$ as for the pure saturation case proposed by Rosenberg, and $a_p = 1.47$ corrected by Agarwal.

Neiman's method

The concept of complex magnetic permeability μ is considered from the ratio between the instant values of magnetic flux density $B(t)$ and magnetic field intensity $H(t)$, where

$$\mu = \frac{B_m}{H_m} = \mu e^{j\psi} \tag{3.97}$$

and

$$\sin\psi = \frac{\mu P_v}{\pi B_m^2 f} \tag{3.98}$$

where P_v are the hysteresis power losses per volume unit in $\mathrm{W/m^3}$, and f is the frequency. The function $\mu = \mu(z)$ can be predicted and formulated from the plane waves formulation, considering the amplitudes ratio of H_m and B_m from an analytical approximation [15] as

$$\mu(z) = \frac{\mu_s e^{j\psi}}{\left(1 - \frac{z}{z_k}\right)^2} \tag{3.99}$$

where the surface magnetic permeability of the material μ_s is determined from its BH curve, as seen in Fig. 3.13, for the maximum magnetic field value at the material surface H_{ms} [15], z is the distance from the metal surface,, z_k is the substitution depth at which the field almost disappears, and ψ is the mean value of the complex magnetic permeability argument, corresponding with the hysteresis loses through the whole depth of the mean.

After the investigation of many magnetic materials, with different properties, Neiman concluded that the magnetic permeability variation inside solid metal and hysteresis losses can be considered with satisfactory accuracy assuming constant coefficients $a_p = 1.3$ to 1.5, and $a_q = 0.7$ to 0.8 for the active and reactive power losses in $\mathrm{W/m^2}$ and $\mathrm{VAr/m^2}$ respectively, also reported and extended by Turowski in [15].

Moreover, the surface impedance in the conductor might be written as

$$\mathbf{Z}_{Sat} = (a_p + a_q)\frac{1}{\sigma\delta} \tag{3.100}$$

and the equivalent penetration depth

$$\delta_{Sat} = \frac{\delta}{a_p} \tag{3.101}$$

In the above equations, the non linearities and hysteresis loses are thus taken into account by means of constant coefficients, proved to be accurate in many 3D electromagnetic structures in the case of strong fields ($H_{ms} > H_k$) [12]. In the case of weak fields ($H_{ms} < H_k$), or constant values of magnetic permeability the coefficients $a_p = 1$ and $a_q = 0.6$ are the recommended values to apply in the above equations.

Substitution permeability

When evaluating the above equations (3.93), (3.95) and (3.96), it can be seen that power losses P_s in steel at saturation, as well as surface impedance $\mathbf{Z}_{Sat}$ (3.100) and penetration depth δ_{Sat} (3.101), can be calculated with the classical formulae (3.55), introducing a multiplier coefficient a_p.

The same can be applied to the magnetic permeability, introducing the concept of constant substitution permeability μ_{subs}, defined as

$$\mu_{subs} = a_p^2\,\mu_s \tag{3.102}$$

In general, the linearization coefficient a_p can be understood as a factor which multiplies

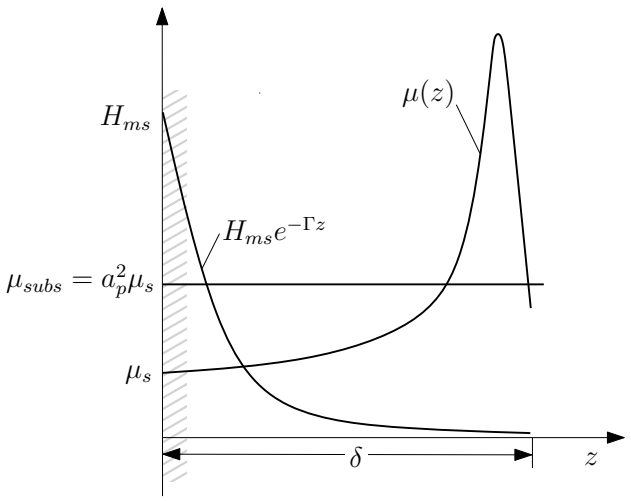

Figure 3.15: Non-linear magnetic permeability behavior inside solid metal.

the surface permeability value μ_s, to average out the permeability inside the penetration depth as seen in Fig. 3.15. The concept of substitution permeability μ_{subs} was introduced by Turowski [15], and corresponds to a mean value of the magnetic permeability $\mu(z)$ inside metal. In the case of strong fields, this value is greater than the magnetic permeability value at the metal surface, as seen in Fig. 3.15.

3.1.8 Influence of metal thickness

It is also necessary to investigate the influence of thickness d of metal plates used in the structural parts of the transformer [5]. Sometimes it has no influence but in case internal wave reflection occurs, it plays decisive role at stray power loss reduction or increase.

From (3.50), at the depth $z = \lambda$, $e^{-2\pi} = 0.0019$, and even at $z = \lambda/2$, $e^{-\pi} = 0.0432$, which means that at such depths the electromagnetic wave practically disappears in solid metal, as seen in Fig. 3.4. Therefore when the thickness d of the metal plate is $d > \lambda/2$ the metal plate can be considered as half space with no internal wave reflections.

In the case mild steel, with electrical conductivity $\sigma = 6.8 \cdot 10^6\,\mathrm{S/m}$ and relative magnetic permeability $\mu_r = 500$, at frequency $f = 50\,\mathrm{Hz}$, the length of electromagnetic wave (3.50) is $\lambda/2 = 3.8\,\mathrm{mm}$ and steel plate of thickness $d = 10\,\mathrm{mm}$, i.e. usually the minimum used for a transformer tank, it can be considered as half space without internal wave reflections.

In case of amagnetic steel, with electrical conductivity $\sigma = 1.13 \cdot 10^6\,\mathrm{S/m}$, and relative magnetic permeability $\mu_r = 1.02$, at frequency $f = 50\,\mathrm{Hz}$, the length of electromagnetic wave (3.50) is $\lambda/2 = 208.3\,\mathrm{mm}$. Therefore when $d > \lambda/2$ the metal plate can be considered as half space with no internal wave reflections. Otherwise, when $d < \lambda/2$, there exists an internal wave reflection which reduces the losses significantly. In such case, a loss

reduction coefficient ζ is introduced to calculate the active power in metal plates excited symmetrically from both sides, i.e. transformer cover. According to [15], the coefficient ζ is defined as

$$\zeta = \frac{\sinh(k\mathrm{d}) - \sin(k\mathrm{d})}{\cosh(k\mathrm{d}) + \cos(k\mathrm{d})} \tag{3.103}$$

The power dissipated in the case there exists internal wave reflection are calculated as

$$P_s = \zeta\, a_p \iint_s \sqrt{\frac{\omega\mu_s}{2\sigma}} \frac{\mid H_{ms}(x,y) \mid^{2x_p}}{2} \mathrm{d}x\mathrm{d}y \tag{3.104}$$

3.1.9 Non-linear Surface Impedance

When linear materials are modeled, the calculation of the surface impedances is straightforward, but the description of conductive construction parts with the magnetically linear surface impedance is only approximate. Since we are dealing with conductive parts that have mostly non linear behavior, the magnetic BH characteristic must be taken into account when calculating the losses [81]. The importance of introducing the non linear SI relies on the fact that it is possible to represent the distribution of non linear magnetic quantities on the electromagnetic analytical model. It provides more precise information for stray loss computation taking into account saturation of ferromagnetic materials as detailed below.

The concept of SI, which comes up based on the Poynting's Vector formulation, was first introduced into field theory by Schelkunoff in 1938 for time harmonic fields [23]. At the surface of good electrical conductors into which the penetration of the field is limited, the tangential component of the electric field $\boldsymbol{E}$ can be considered under sinusoidal performance proportional to the tangential component of magnetic field $\boldsymbol{H}$ and thus

$$\mathbf{Z_s} = \frac{\mathbf{E}}{\mathbf{H}} = (1+j)\frac{1}{\sigma\delta}, \tag{3.105}$$

being δ the skin depth in a conductor defined in (3.49), σ is the linear electrical conductivity. If the magnetic permeability μ is considered constant in all directions, then (3.49) is referred as the linear penetration depth δ_L and (3.105) as the linear Surface impedance $\mathbf{Z}_L$.

Unfortunately, a real material presents a non-linear BH characteristic and therefore a non linear magnetic permeability both at the metal surface (xy-plane) -Section 3.1.6- and inside metal(z-direction) -Section 3.1.7- must be taking into account, which have a significant practical importance on the accuracy of the model.

In the case of transformer cover plates, where the incident magnetic field H_{ms} at any point (x, y) of the metal surface ($z = 0$) can be calculated from Biot-Savart law [81], the

surface value of the non linear magnetic permeability $\mu_s(x, y)$ can be easily considered function of the real BH curve of the material. In this case, it is important to note that the value of the skin depth (3.49), considering $\mu = \mu_s(H_{ms}, x, y)$ represents now the maximum -or absolute- depth δ_{abs} defined in (3.106), the ac magnetic field wave front penetrates into the conductor [87], as seen in Fig. 3.14.

$$\delta_{abs} = \sqrt{\frac{2}{\omega\sigma\mu_s(x,y)}} = \sqrt{\frac{2}{\omega\sigma}\frac{H_{ms}(x,y)}{B(H_{ms})}} \tag{3.106}$$

On the other hand, inside the solid metal, assuming saturation it was stated that a multiplier coefficient a_p should be applied to the linear theory (3.107). The sinusoidal magnetic field formula is valid when the magnetic field reaches the surface in a mostly tangential direction, as it does occur in the case of transformer tank covers [87]. Therefore by analogy with (3.105) the surface impedance $\mathbf{Z_{Sat}}$ for a rectangular BH curve (saturation) and sinusoidal magnetic field results as defined in (3.107).

$$\mathbf{Z_{Sat}} = a_p \frac{1}{\sigma\delta_{abs}}(1+j) \tag{3.107}$$

When linear materials are modeled, the calculation of the surface impedances is straightforward, but the description of conductive construction parts with the magnetically linear surface impedance is only approximate. Since we are dealing with conductive parts that have mostly non linear behavior, the magnetic BH characteristic must be taken into account when calculating the losses [81].

In real 3D structures, some areas are strongly saturated and others are not. Since the real magnetization curve of iron lies between the linear case and saturation, as shown in Fig. 3.16, then the rigorous solution for the linear and saturation case can establish the limits within which the actual iron performs. The non-linear SI concept is introduced assuming that the BH curve is presented by the two extreme forms and it seems reasonable then that the most adequate multiplier coefficient a_p for each magnetization level would shift from unit to 1.47 with increasing saturation.

An interesting proposal was established by Deeley in [88], where the formula of the SI in the linear case (3.105) and the formula (3.107) obtained with the rectangular BH characteristic have been combined in (3.108) in a final non linear surface impedance Z_{snl}, taking into account the degree of saturation by means of a weighted function $f(H_{ms})$ to give accurate results from weak to strong magnetization.

$$Z_{snl} = f(H_{ms})Z_L + (1 - f(H_{ms}))Z_{Sat} \tag{3.108}$$

Guerin in [87] after tests found the best weighting function to be the one proposed by Deeley [88].

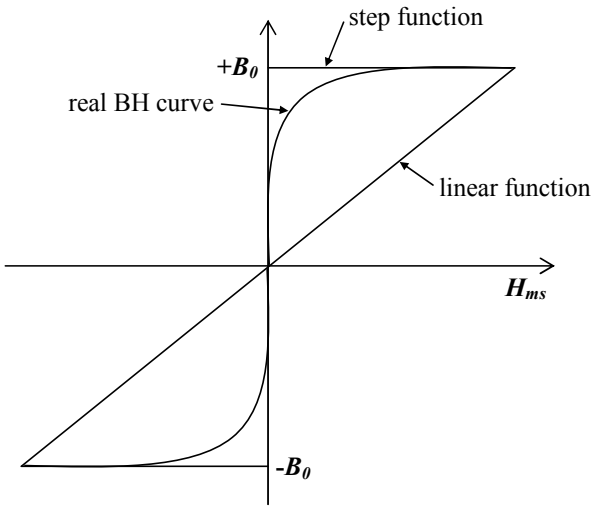

Figure 3.16: Non-linear BH curve approximation with a linear and step function.

$$f(H_{ms}) = \frac{1}{1 + k\dfrac{H_{ms}}{H_k}} \tag{3.109}$$

Where H_k corresponds to the value of the magnetic field at the knee of the BH curve and k is a constant coefficient to be chosen depending on the nature of the field. According to [87], the best value of k has been found to be $k = 5$ in the case of sinusoidal magnetic field.

Thus, the stray losses for non linear materials P_{snl} are then calculated in (3.110) in a similar way as it is done for linear case (3.55) but in this case, the linear surface impedance $\mathbf{Z_L}$ is substituted by the non linear surface impedance $\mathbf{Z_{snl}}$ (3.108).

$$P_{snl} = \iint_s \Re e(\mathbf{Z_{snl}}) \frac{|\, H_{ms}(x,y)\,|^2}{2} \mathrm{d}x\, \mathrm{d}y \tag{3.110}$$

3.1.10 Non-linear penetration depth

The penetration depth δ_{abs} defined in (3.106) represents the absolute penetration of magnetic field into conductor as it has been previously mentioned [87]. However, an equivalent penetration depth (3.111) assuming saturation δ_{Sat} can be defined from the concept of the SI $\mathbf{Z_{Sat}}$ (3.107), i.e. dividing by the coefficient a_p as shown in Fig. 3.14 [15].

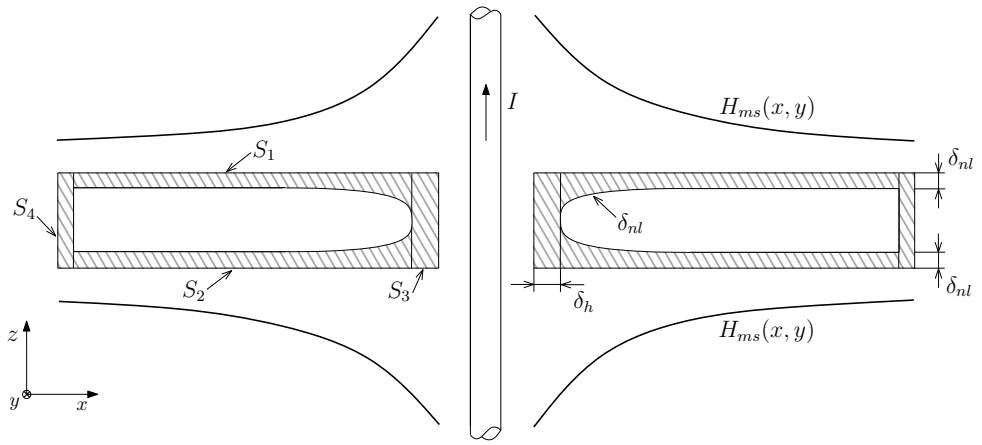

Figure 3.17: Analyical model for power losses computation on a steel plate with hole.

$$\delta_{Sat} = \frac{\delta_{abs}}{a_p} \tag{3.111}$$

Equation (3.111) means that at saturation, the penetration depth δ_{Sat} is smaller than the maximum penetration depth defined for non-linear materials δ_{abs}.

Therefore, in the same way as for the non linear SI Z_{snl} (3.108), the penetration depth can be combined for the linear region and saturation by means of the weighted function (3.109) in a final penetration depth δ_{nl} (3.112) of the electromagnetic field into the metal.

$$\delta_{nl} = \frac{1}{f(H_{ms})\dfrac{1}{\delta_{abs}} + (1 - f(H_{ms})\dfrac{1}{\delta_{Sat}}} \tag{3.112}$$

When dealing with conductive parts that have mostly non-linear behavior, it must be taken into account at calculating losses [29]. Thus, the stray losses for non-linear materials P_{snl} are calculated in (3.113) in a similar way as it is done for linear case (3.55)-(3.105) but in this case using the concept of non-linear penetration depth δ_{nl} defined in (3.112).

$$P_{snl} = \iint_s \frac{1}{\sigma\delta_{nl}} \frac{\mid H_{ms}(x,y) \mid^2}{2} \mathrm{d}x\,\mathrm{d}y \tag{3.113}$$

Consequently, non-linear penetration depth δ_{nl}, as seen in Fig. 3.17, allows to introduce the saturation of ferromagnetic materials in the electromagnetic analytical model, and on the other hand to set the thickness of the volume regions where heat sources (3.113) are localized in the thermal FE model as detailed in next section.

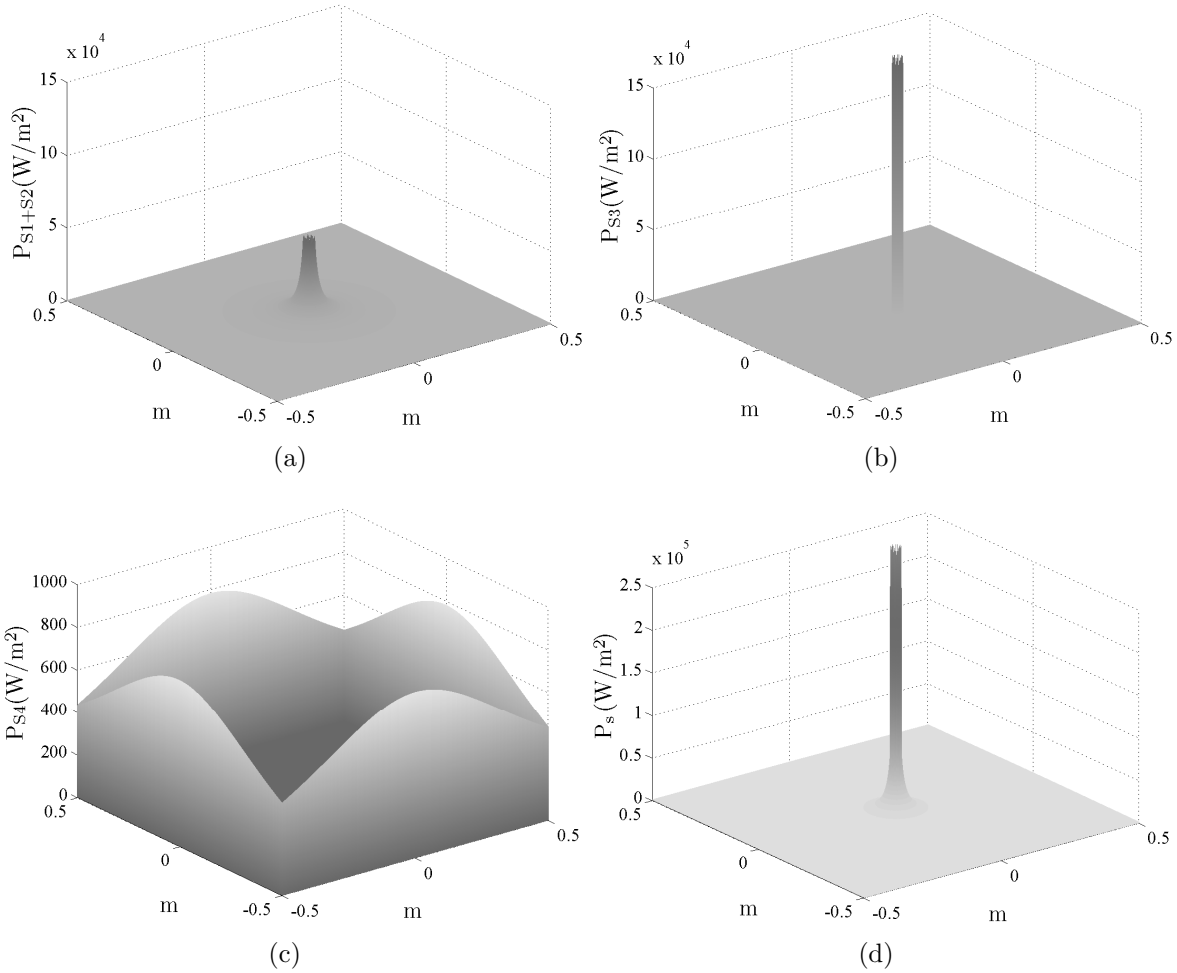

Figure 3.18: Power loss distribution for a 2500 A test over a) S_1 and S_2 −upper and lower surface respectively−, b) hole region S_3, c) lateral surface S_4 and d) total power loss distribution $S_1 + S_2 + S_3 + S_4$.

3.1.11 Computational electromagnetic model

Physical aspects concerning the computation of stray losses in metal plates have been described all along previous sections, however there are several practical issues related with the computational model which must be taken into account here detailed.

The electromagnetic analytical model for power losses computation is shown in Fig. 3.17. Power losses are calculated from (3.113) integrating over the steel plate surface S_1 and S_2 from the magnetic field distribution $H_{ms}(x, y)$ at each point. However, border effects from the hole region S_4 and lateral region S_4 must be also taken into account.

In Fig. 3.18 the individual contributions from each surface are shown. Stray losses in the hole region S_3 are decisive to properly calculate the hottest spot temperature. Density values in the hole region S_3 −as seen in Fig. 3.18(b)− are several times greater compared to those at upper and lower surface (S_1 and S_2) from Fig. 3.18(a), and they

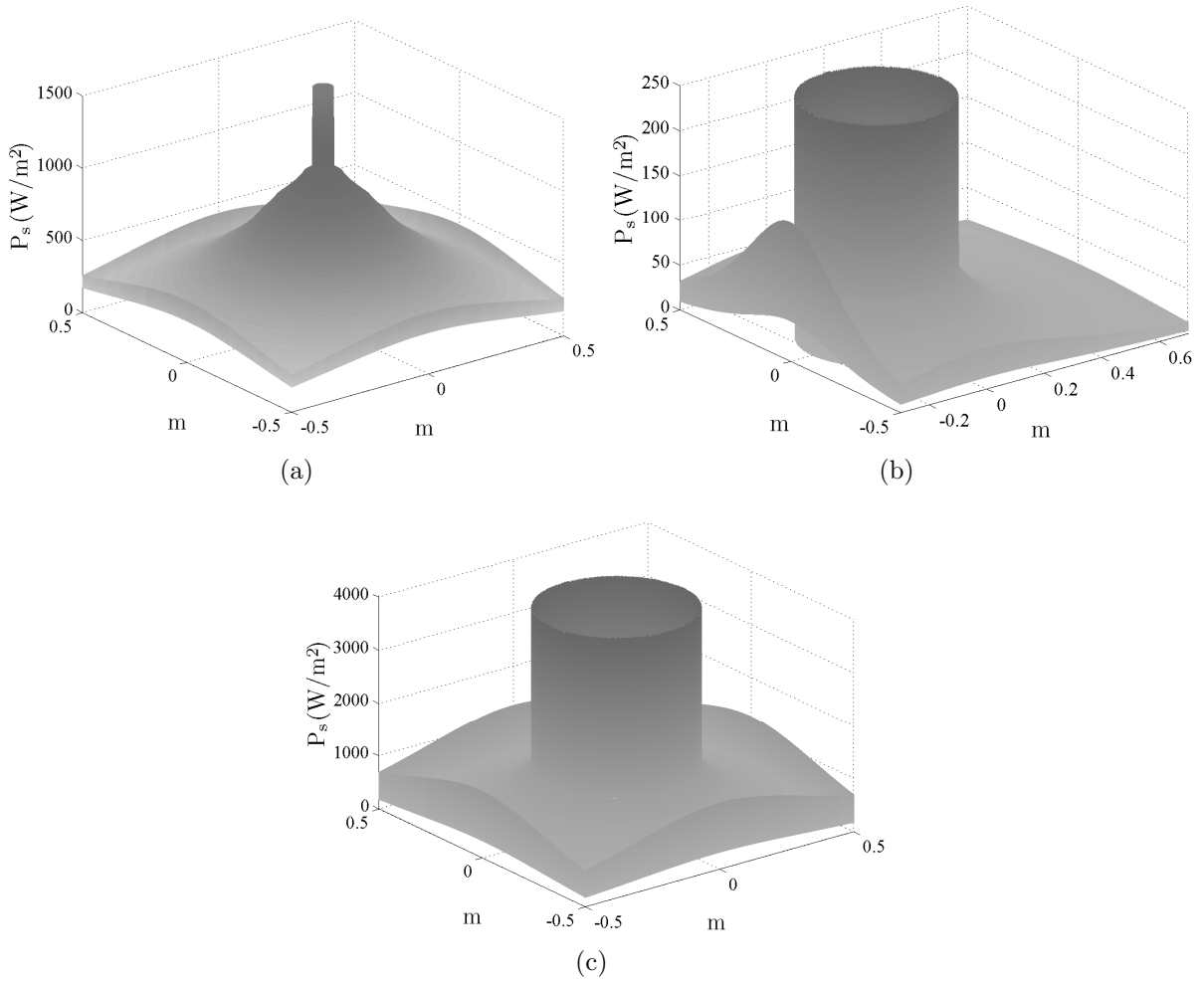

Figure 3.19: Border effect in case of a) 2500 A test on steel plate of thickness 1 mm, b) case of 500 A test on a steel plate of thickness 6 mm with a asymmetry and conductor hole of diameter 450 mm, c) case of steel plate with amagnetic insert of radius 250 mm.

increase proportionally to the plate thickness.

In the case of the lateral region S_4 sometimes it has small influence as shown in Fig. 3.18(c). Note that the scale (W/m^2) has been changed here and values are of the order of 150 times lower. However border effects might be relevant in case of e.g. small plate thickness, large conductor hole, asymmetry distribution of conductors or if considering amagnetic inserts. Situations where these called border effects might be most influential can seen in Fig. 3.19.

Therefore the final stray loss computational model is built by the sum of the stray loss distribution individually calculated at each region, as shown in Fig. 3.18.

3.2 Thermal FEM Analysis

Regarding the thermal FEM model, the basic relations of conduction heat transfer are the Fourier's law and the equation of heat conduction [81] where the volume density of power of the heat sources is calculated from (3.110).

3.2.1 Thermal field FEM formulation

Related with the thermal FEM model [89] the used basic relations of conduction heat transfer are the Fourier's law

$$\mathbf{q_k} = -k_t \cdot \nabla T \tag{3.114}$$

and the equation of heat conduction

$$\nabla \mathbf{q_k} + \rho\, C_p \frac{\partial T}{\partial t} = p_v \tag{3.115}$$

Where $\mathbf{q_k}$ is the heat flux density, k_t is the thermal conductivity, ρ is the density, C_p is heat capacity, T is the temperature and p_v is the volume density of power of the heat sources.

In the case of heating hazard transformer covers, authors are interested to assess the thermal steady state by means of the Poisson diffusion equation as following

$$\frac{\partial}{\partial x}\left(k_t \frac{\partial T}{\partial x}\right) + \frac{\partial}{\partial y}\left(k_t \frac{\partial T}{\partial y}\right) + \frac{\partial}{\partial z}\left(k_t \frac{\partial T}{\partial z}\right) = -p_v \tag{3.116}$$

The boundary conditions at surrounding environment are given by convection and radiation as

$$\mathbf{q_{cr}} = -h_c(T - T_a) - \epsilon_r \sigma_r (T^4 - T_a^4) \tag{3.117}$$

Where h_c is the convection heat exchange coefficient, ϵ is the radiation heat exchange coefficient or emissivity, σ_r is the Stephan-Boltzmann constant and T_a is the ambient temperature.

Having a 3D domain Ω, with a boundary surface s, it is discretized in a mesh of volume finite elements Ω_e with surface s_e. Considering the Galerkin's Method, the previous Poisson equation (3.116) is expressed in the following integral by means of N_i shape functions

$$\int_{\Omega_e} N_i \nabla(-k_t \nabla T)\, \mathrm{d}x\, \mathrm{d}y\, \mathrm{d}z - \int_{\Omega_e} N_i\, p_v\, \mathrm{d}x\, \mathrm{d}y\, \mathrm{d}z = 0 \tag{3.118}$$

Integrating by parts the first element from (3.118) and applying the Ostrogradsky's theorem leads to

$$\int_{\Omega_e} k_t \nabla N_i \nabla T \, \mathrm{d}x \, \mathrm{d}y \, \mathrm{d}z - \int_{s_e} N_i \, k_t \frac{\partial T}{\partial n} \, \mathrm{d}s - \int_{\Omega_e} N_i \, p_v \, \mathrm{d}x \, \mathrm{d}y \, \mathrm{d}z = 0 \tag{3.119}$$

Thus, boundary conditions can be easily applied in the surface integral s_e from the previous equation.

In each finite element of the mesh resulting from discretizing the 3D domain, the temperature is expressed by the approximation polynomial

$$T = \sum_{j=1}^{n} T_j N_j(x, y, z) \tag{3.120}$$

Equation (3.119) can be written for each element Ω_e of the mesh of transformer cover in matrix form as

$$[S^e] \, [T^e] = [F^e] \tag{3.121}$$

Where $[S^e]$ is the stiffness or coefficient matrix, $[T^e]$ are the nodal temperatures and $[F^e]$ is the heat source vector or forcing vector. The coefficient matrix is calculated from

$$S_{ij}^e = \int_{\Omega_e} k_t \left(\frac{\partial N_i}{\partial x} \frac{\partial N_j}{\partial x} + \frac{\partial N_i}{\partial y} \frac{\partial N_j}{\partial y} + \frac{\partial N_i}{\partial z} \frac{\partial N_j}{\partial z} \right) \mathrm{d}x \, \mathrm{d}y \, \mathrm{d}z \tag{3.122}$$

The power volume density of the heat source due to electromagnetic losses for each element is defined as

$$F_i^e = \int_{\Omega_e} p_{vi} \, \mathrm{d}x \, \mathrm{d}y \, \mathrm{d}z + \int_{s_e} N_i \, k_t \, \frac{\partial T}{\partial n} \, \mathrm{d}s \tag{3.123}$$

3.2.2 Thermal FE model

The non-linear penetration depth δ_{nl} (3.112) has been found to influence electromagnetic analytical model results i.e. computation of power loss. However, it must be also considered when setting the volume thickness where heat sources are located in the thermal FE model.

In the thermal model the volume over the skin depth penetration δ_{nl} is divided into n sub-volume regions V_n, with surface s_n, characterized by its radius from the conductor centre R_i as seen in Fig. 3.17. Once the power losses are computed with the analytical model for each surface region s_n, they are exported to the thermal 3D FE model and

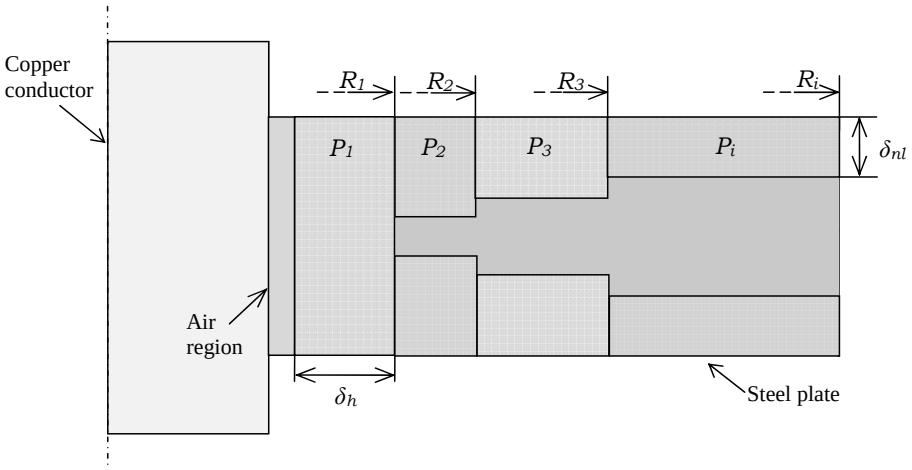

Figure 3.20: Discretization of FE thermal model volume regions.

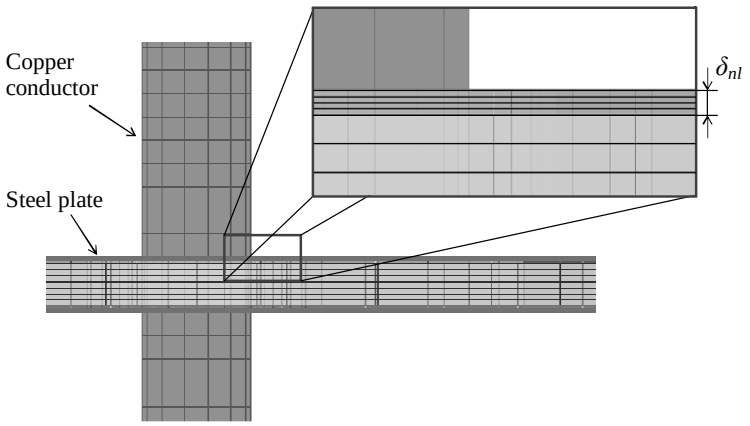

Figure 3.21: Structured FE mesh, with thinner discretization into the penetration depth.

introduced as heat sources p_v according to (3.123).

Particularly, the penetration depth in hole region δ_h −seen in Fig. 3.17− strongly influences the hottest spot temperature results. Thus, the heat sources in the thermal FE model must be set in the corresponding volume regions of thickness δ_{nl}, as seen in Fig. 3.20.

Regarding the mesh, it must be mentioned that, in case of an electromagnetic analysis, the finite element grid should be extended to the surrounding insulating media, whereas the thermal problem is confined just to the eddy current carrying parts, i.e. the steel plate. Moreover, an structured is found to be the most adequate for the studied problems as seen in Fig. 3.21, but the requirement of several elements within the penetration depth δ_{nl} is not mandatory for thermal analysis.

Chapter 4

Experimental Work

In order to illustrate the capability of the computational methodology presented in Chapter 3 as a practical tool to assess the overheating on tank covers an other structural parts of power transformers, an experimental work is carried out. The design of tests and their execution are supported by Efacec Energía S. A. Power Transformers, Porto, Portugal, transformer manufacturers.

A series of experiments are designed to determine the hottest spot areas over structural steel plates used in tank walls and cover of power transformers, as consequence of the induced magnetic field due to the presence of high current conductors (kA). Temperature is monitored from the several experiments listed bellow.

- Cover plate. Case in which the steel plate has one or several holes, to each be passed through by current carrying conductors, being the plate on horizontal position.
- Tank wall. Case in which one or several conductors pass parallel to the metal plate at a certain distance, being the plate on vertical position.
- Bushing box. Experiments with round and square bushings box have been also carried out, where one high current carrying conductor passes through.

The influence of various design factors is taken into account in the experiments, as e.g.:

- Current magnitude and phase. Current values from 200 A until 2.5 kA, in phase and single-phase currents.
- Distance from the conductors to each other.
- Distance from the conductor to the steel plate, in case of tank wall tests.
- Number of conductors, either 1 or 2 conductors.
- Conductors layout. Vertical or horizontal layout in case of tank wall tests.
- Steel plate thickness. Plates of 1 mm, 6 mm and 12 mm are considered.

– Materials. Mild steel and stainless steel are considered.

Important aspects which have been taken into account during the experimental work are detailed in the next sections, as well as brief descriptions on the equipment used and measurement conditions. Technical data is included in Appendix B.1.

Experiments were carried in air in order to obtain cooling conditions more severe than those that could be obtained with transformer oil. However, once the model is calibrated, and the computation methodology well established, cooling conditions might be changed to those factors corresponding to real conditions on power transformers e.g. oil or forced air.

4.1 Current Supply

One of the most important issues to carry out the heating tests in metal plates due to nearby high current leads is the current supply itself. This is the source to the induction heating problem. High constant values of current must be supplied, which create the magnetic field intruding either tangential or normal into the metal plate.

Current Source

A variable current source from Majo System Integrator is used, where intensity values up to 5 kA might be achieved. However, in the case of steady state heating tests, values of no more than 2.5 kA are recommended. Technical data is provided in Appendix B.1.

Conductors

Solid copper conductors are used to be placed through or parallel to the steel plates. Their section must be chosen greater than 1500 mm^2 in order to avoid they are overheated. Conductors of 48 mm diameter ($\approx$ 1810 mm^2) and length 1200 mm are used for test. Moreover, two insulated stranded conductors connect the solid copper conductors to the current source as seen in Fig. 4.1. The latter are flexible conductors which permit to bring them further from the steel plate, so that the incident field on the steel plate is purely that created from the solid conductors and unaffected by the turn wire. Some wood supports are designed in order put the stranded conductors further from the steel plates.

Current Measurement and Control

A three-phase power and energy analyzer Fluke 435 is used in order to measure and set the appropriate current for each test. Technical data is provided in Appendix B.1. Typically conductors resistance vary with temperature, and because of it the current must be controlled and readjusted from time to time while tests are running.

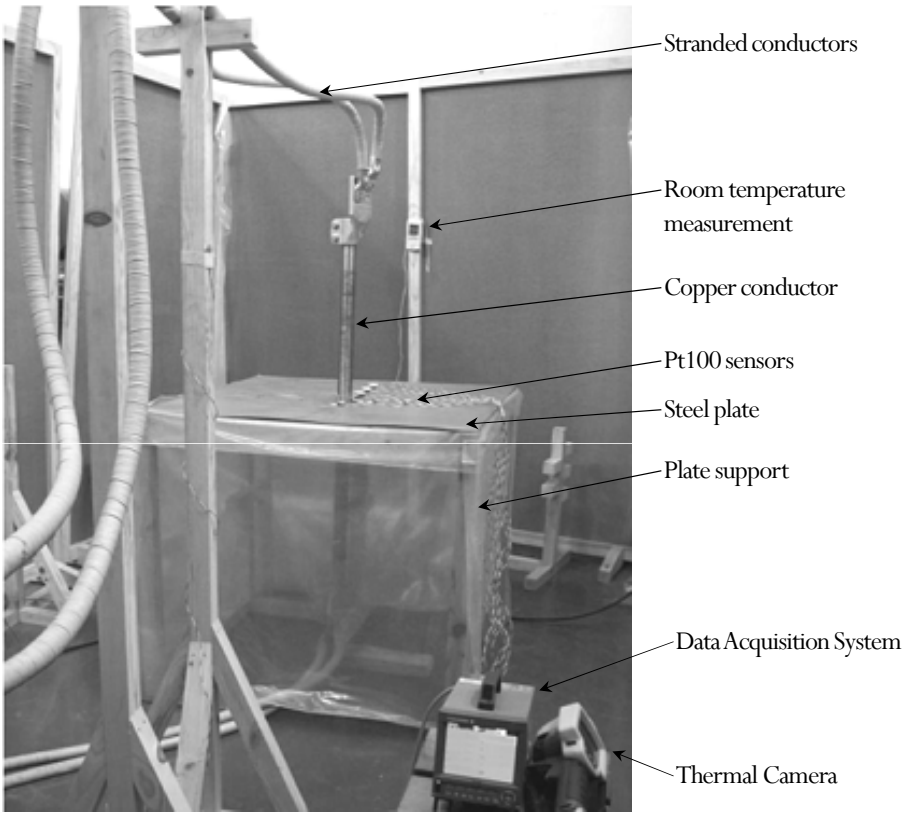

Figure 4.1: Laboratory setup for temperature measurement over a steel cover plate.

4.2 Temperature Measurement

Temperature measurement must be consistent. There are so many factors influencing the plate temperature that must be taken into account and be recorded in order to later validate properly each test. The power laboratory area where the experiments are carried out is carefully closed with wood panel walls as seen in Fig. 4.1, so that it is a thermally stable area, in general. The room temperature is measured and monitored at several points on the test laboratory. Meanwhile, temperature on the steel plate is measured by means of distributed sensors, and also by means of a thermal infrared camera, as detailed bellow.

Temperature Sensors Pt100

For the temperature measurement several temperature sensors Pt100 are distributed over the steel plate as seen in Fig. 4.2. Pt100 temperature sensors use Resistance Temperature Detector (RTD) made from platinum with resistance $R_0 = 100\,\Omega$ at $0\,^{\circ}\mathrm{C}$ [90]. For the

precise measurement of temperature, the platinum resistance thermometer offers better advantages than other sensors (e.g. thermocouples) in repeatability and stability over a long period. In addition high accuracy over a wide range of temperatures (from $-200\,^{\circ}\mathrm{C}$ to $+850\,^{\circ}\mathrm{C}$) allows replacement of a sensor without any need of readjusting of the connected measuring devices [91]. Another advantage compared to other temperature sensors, is that it is not necessary to use special cables to connect to the sensor.

Since the temperature measurement is based on the element resistance, any other resistance (e.g. lead wire resistance or connections) added to the circuit will result in measurement error. However, some wiring arrangements allow the monitoring or control equipment to factor out the unwanted lead wire resistance and other resistances that occur in the circuit. Here, sensors using the 3-wire construction, the most common in industrial process and monitoring applications, are used for temperature measurement. The lead wire resistance is factored out as long as all of the lead wires have the same resistance as explained in Appendix B.1; otherwise, errors might result.

Finally, surface measurements can be one of the most difficult to make accurately. Measurements can be highly sensitive depending on how the sensor is attached to the surface. Several ways of gluing the sensors were investigated. In order to set the sensors on the metal plate, some wood clamps are glued to the steel surface holding the sensor in a fixed position. In addition, a thermal compound [92] and paper tape are used to enhance the contact between the sensor and the plate.

Data Acquisition System

In order to measure temperature, the RTD elements must be connected to some sort of monitoring or control equipment. A digital data acquisition system YOKOGAWA DQStation DX1000 with 12 input channels is used to monitoring the measured temperature from each of the Pt100 sensors, allowing their storage *vs.* time until the test reaches steady state [93]. Information on DQStation wiring for temperature measurement can be seen in Appendix B.1. Steady state temperature is considered when the maximum temperature increase is $\approx 1\,^{\circ}\mathrm{C}$ per hour.

Thermal Infrared Camera

Moreover, a thermal infrared camera Fluke Ti32 is available for temperature measurement and thus thermal images are taken for each test once steady state is reached. Thermal images are taken from each of the experiments in order to validate and compare with Pt100 measurements.

An infrared camera measures the emitted infrared radiation from an object. The fact that radiation is a function of the object temperature makes possible to calculate and display this temperature. However, radiation sources from the surroundings also reflect on the object surface and it must be compensated when taking thermal images so that temperatures are measured accurately. This is done automatically by the camera but there are some important parameters which must be calibrated, e.g. emissivity of the object, distance between the object and the camera, relative humidity or room

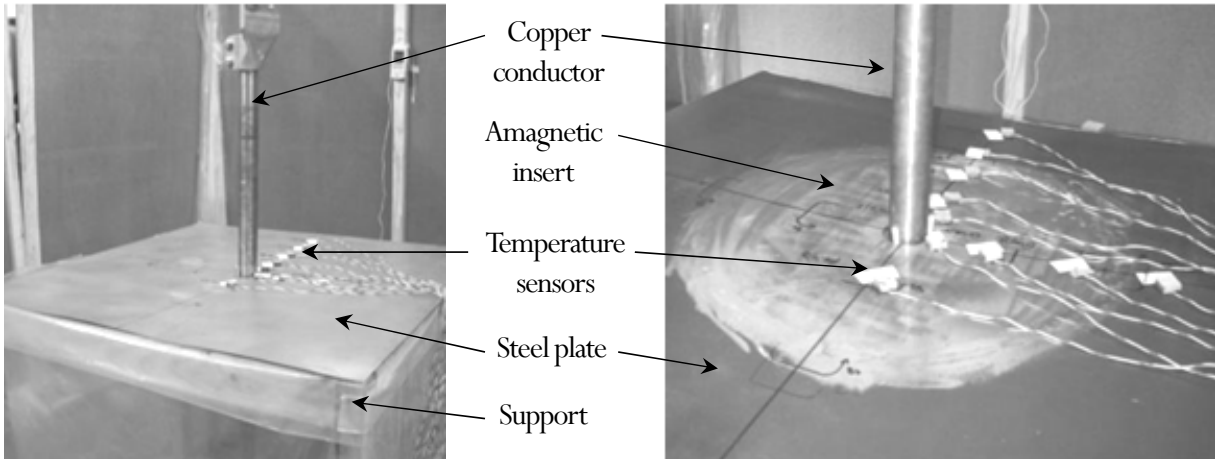

Figure 4.2: Laboratory setup for temperature measurement over mild steel cover plate (left) and cover plate with amagnetic insert (right).

temperature. The most important factor to set correctly is the material emissivity, chosen for the steel plate, rough and plane surface $\epsilon = 0.95 - 0.98$ [94]. The room temperature must be set according to each test.

4.3 Cover Plate Tests

A square mild steel plate of 1 m side is used for experimental setup as shown in Fig. 4.1. In the plate, holes of 60 mm diameter are done to be passed through by solid copper conductors. Through the conductors flows a 50 Hz current, which creates a magnetic field intruding tangential to the steel plate. The steel plate is held by a closed-support which states the boundary conditions. The temperature is measured by means of several temperature sensors Pt100 distributed on the steel surface. Several paths are drawn for the sensors depending on the tests. In general perpendicular paths departing either from the plate center or from the conductor centre as seen in Fig. 4.2. Tests are running until the plate temperature reaches steady state. The ambient temperature is also measured during tests as well as the temperature inside the cover plate support. This setup is used for the calibration process of electromagnetic and thermal parameters as described in Chapter 5, as well as for validation of the results.

Tests are carried out for one current carrying conductor passing through the steel plate, and for two conductors carrying in-phase and single-phase currents. For each setup, several design factors are taken into account as described in the next sections.

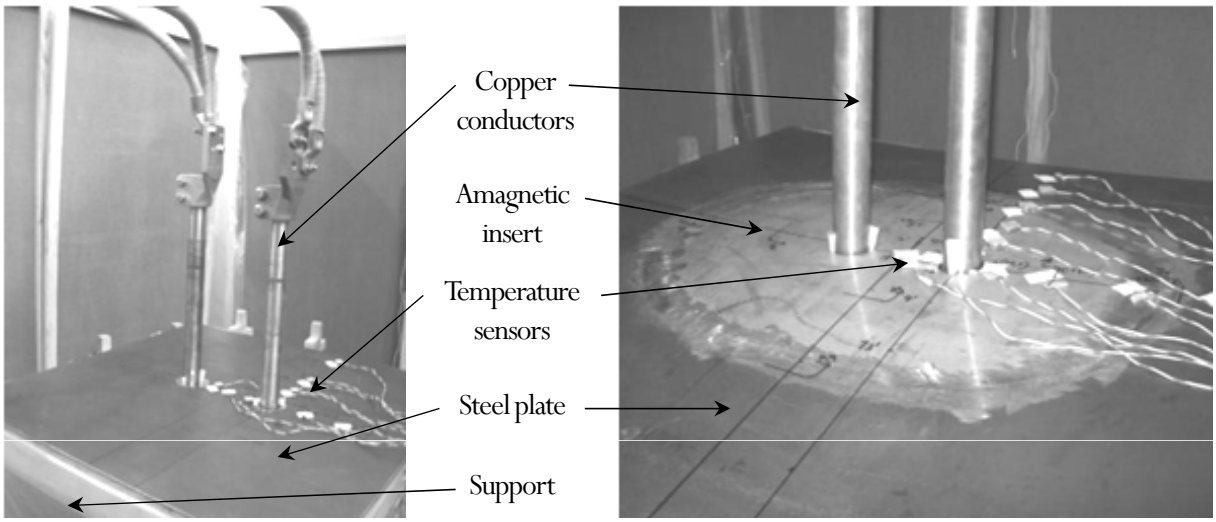

Figure 4.3: Laboratory setup for temperature measurement over a mild steel single-phase cover plate, $a = 250\,\text{mm}$ (left) and considering amagnetic insert, $a = 150\,\text{mm}$ (right).

One current carrying conductor

Mild steel plates of thickness 1 mm, 6 mm and 12 mm are used for tests, with one hole in the plate center to be passed through by a conductor, as seen in Fig. 4.2. Current values from 200 A to 2500 A are considered. Temperature measurements are also taken on a steel plate with the same dimensions, 6 mm thickness and welding an amagnetic insert of 250 mm radius, as seen in Fig. 4.2 (right).

Two current carrying conductors

Two steel plates of thickness 6 mm are considered, with two holes separated a distance a of 150 mm and 250 mm from each other, respectively, as seen in Fig. 4.3. In-phase and single-phase currents from 250 A to 1250 A flow through each of the conductors. Temperature measurements are also taken on a steel plate with the same dimensions, $a = 150\,\text{mm}$ and welding an amagnetic insert surrounding both conductors of 250 mm radius, as seen in Fig. 4.3 (right).

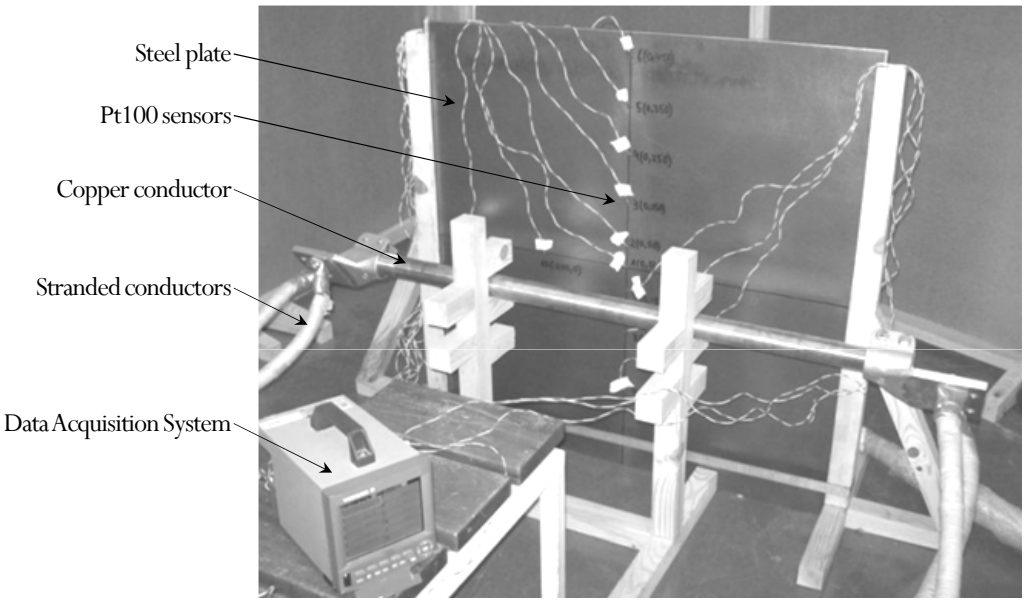

Figure 4.4: Measurement setup for tank wall tests.

4.4 Tank Wall Tests

In the case of tank wall tests, current carrying copper conductors are placed parallel to a mild steel plate. A mild steel square plate 6 m side is placed in vertical position. The tank wall plate and the conductors are held by wood supports as seen in Fig. 4.4. Through the conductors flows a 50 Hz current, which creates a magnetic field intruding normal to the steel plate and causing induction heating.

Temperature is measured by means of several temperature sensors Pt100 distributed on the steel surface. Several paths are drawn for the sensors depending on the number of conductors and the distance between each other. In general two perpendicular paths are drawn departing from the plate centre as seen in Fig. 4.4. Tests are running until the plate temperature reaches steady state. The ambient temperature is also measured during tests to state boundary conditions. The setup here described is used for the calibration of the computational model, as well as for validation of the results.

Test are carried out for one current carrying conductor, and for two parallel conductors carrying in-phase and single-phase currents. For each setup, several factors are taking into account described in the next sections.

One parallel conductor

A mild steel plate of thickness 6 mm is considered in the case of one current carrying conductor placed parallel to the steel plate. Test are carried out for current values from 500 A to 2500 A, and varying the distance to the steel plate from 50 mm to 200 mm. The setup for temperature measurement can be seen in Fig. 4.4.

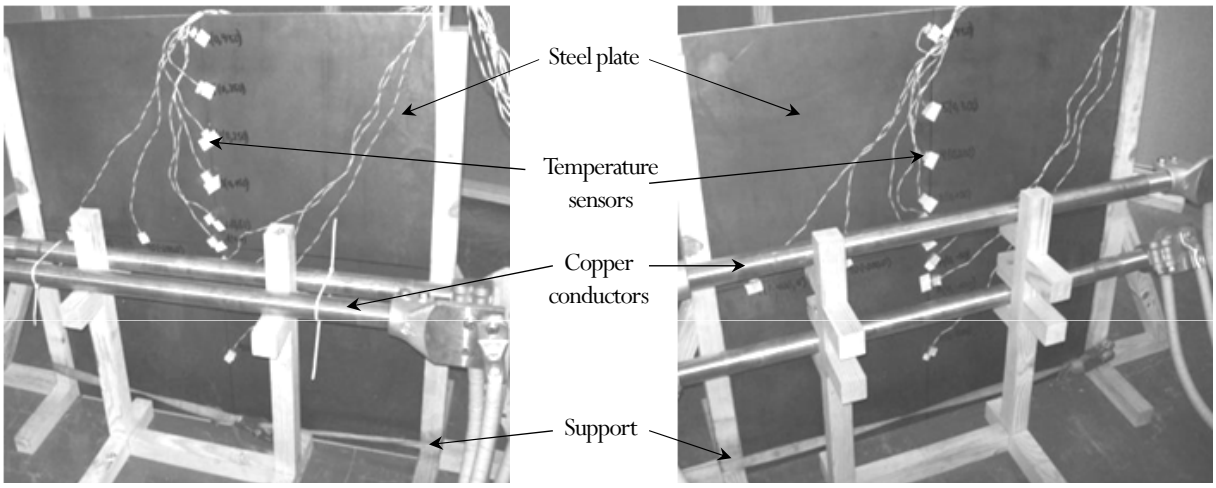

Figure 4.5: Laboratory setup for temperature measurement on a mild steel tank wall plate with two conductors, horizontal (left) and vertical (right) layout.

Two parallel conductors

A steel plate of thickness 6 mm is considered, with two conductors placed parallel to it. Conductors are arranged, as seen in Fig. 4.5, either in horizontal (left) or vertical (right) layout. In-phase and single-phase currents from 500 A to 1250 A flow through each of the conductors. Test are carried out considering a separation distance between conductors of 100 mm or 200 mm, and distance to the steel wall varying from 100 mm to 200 mm.

4.5 Bushing Turret

Tests are also carried out to assess the heating hazard on transformer bushing turrets, as seen in Fig. 4.6. Square and round turrets made from both mild steel and amagnetic steel are considered, where a solid copper conductor is placed passing through. The ac current source supplies 2500 A. Temperature is measured by means of several temperature sensors Pt100 distributed on the bushing turrets, either top and lateral surface. Tests are running until the turret temperature reaches steady state. The room temperature is also measured during tests to state boundary conditions.

Either tangential (top surface) and normal fields (lateral surface) take part on the induction heating of the bushing box. Hence, the setup here described is used for the validation of the computational model, for both the cover and tank wall, as well as a practical application of the methodology proposed in this dissertation.

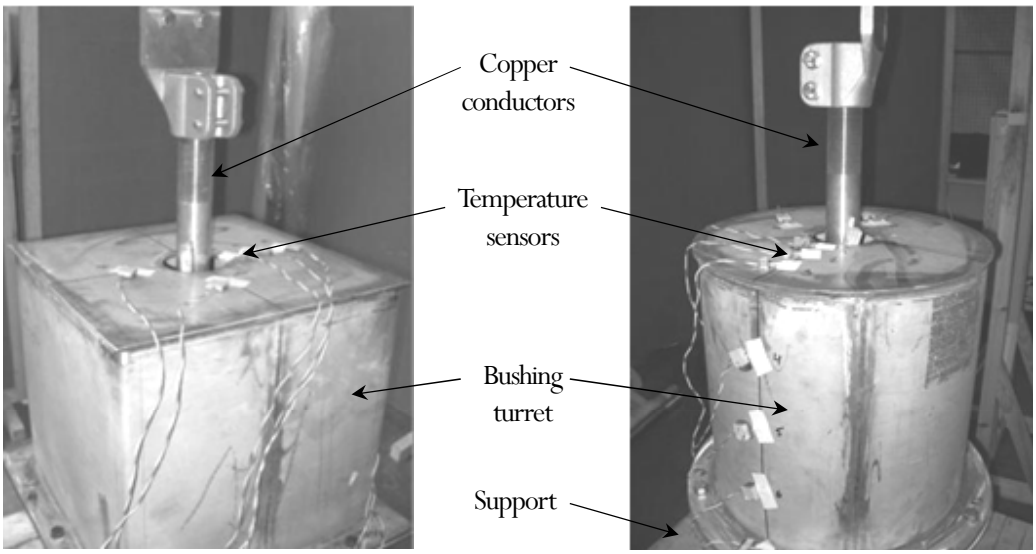

Figure 4.6: Setup for heating hazard assessment on a transformer square bushing turret (left) and round bushing turret (right).

Chapter 5

Parameter identification problem

A methodology for the solution of 3D induction heating problems on transformer covers based on electromagnetic analytical formulation linked with finite element method for 3D thermal analysis has been published in [81] and in this dissertation in Chapter 3. The proposed methodology allows computing the temperature on metallic device elements heated by electromagnetic induction and it is specially recommended for the heating hazard assessment in those cases where depth of electromagnetic wave penetration compared with machine dimensions is a key issue and power losses must be calculated using Poynting's Vector (3.87). An experimental work is presented in Chapter 4 and measurements are intended to compare with simulations results from FE thermal analysis. However, the difficulty to trust material properties and boundary condition data from catalogues or available in the literature is experienced. These uncertainties are avoided in the proposed methodology by introducing a parameter identification method (i.e. calibration of the computational model) as seen in Fig. 3.1. Its objective is to identify and adjust the electromagnetic and thermal input parameters, so that the computed results match the measured temperature values taken as reference. Once the simulation input parameters are identified, the temperature distribution can be accurately predicted on transformer cover plates for other load conditions and different number of conductors [81].

An attempt to identify these parameters is described based on single-objective and multi-objective deterministic and non-deterministic optimization algorithms. Nevertheless, in the literature there exist a wide variety of methods which might be used to automate the calibration process, as for example population-based algorithms [95], [96], [97]. Therefore, the algorithm to be implemented in the calibration process is left to the free election of designers, according to their own criteria to identify and adjust involved parameters. The only consideration designer must be aware is the suitability of the computational approach to couple with optimization algorithms, in terms of computational effort. In addition, key aspects on the parameter identification process are developed in this chapter, such as considering e.g. the relative influence of each input parameter on model output and sensitivity to measurement error.

Moreover, in many fields of engineering the lack of reliable information on the model

inputs might hinder the computational effort and the pursued accuracy by the use of sophisticated methods. Thus, the idea behind the parameter identification presented here might be used as philosophy of verification and validation the computational models used in the manufacturing industry.

Results from simulations with optimum/identified parameters are given in the next Chapter 6 and compared to measurements. In Chapter 7 some practical applications are shown to stress the potentiality of the whole methodology presented in this dissertation including the parameter identification technique.

5.1 Background

Optimization strategies and optimal design of electromagnetic devices have constantly grown in research [96], [98], [99], [100], [101]. In most recent years sophisticated design optimization softwares are being integrated in the manufacturing industry in general, and in particular to the design of power transformers [102]. The main target might be the cost minimization of specific components or specific transformer characteristics, e.g. load or no-load losses, so solving a direct optimization problem [30], [103]. If the objective is to meet technical requirements then a synthesis or shaped design problem is solved [2], [8], [104], [105], where the objective function is expressed in terms of basic set of design variables. Deterministic [106] and non-deterministic [2] algorithms have been applied to global transformer design optimization.

On the other hand, within the complexity of transformer design, experimental methods combining data provided by measurements with analytical or numerical methods, become of interest in order to provide efficient models for the accurate representation of certain transformer components [30]. Generally, physical parameter values are roughly known and have to be modified to obtain a simulation which corresponds to the experience. But when a lot of influential parameters take part, to adjust each of them becomes a difficult task, and needs many calculations. To this effect, optimization algorithms might used to determine material data or linearization coefficients from measurements, so solving the inverse or parameter identification problem [98], to which the present chapter is devoted.

The aforementioned need for computational parameters identification to come up with accurate coupled electromagnetic-thermal models has been referenced in the literature e.g. for linear actuators [107], medium voltage switchgear cells [108] or power transformers [19]. In particular, the material data required for computation, i.e. electrical and thermal conductivity and permeability (or BH curve), often show significant deviation owing to e.g. the varying chemical composition, mechanical or thermal treatment. Moreover some parameters present in the FE thermal model as convective heat exchange coefficients are difficult to determine from theory or measurements. It is also found a significant dependence between the numerical results and the type of mathematical solver used [81]. Thus, all necessary input parameters for eddy currents and thermal analysis need to be identified in order to calibrate numerical models.

The parameter identification problem applied to metal partition walls located

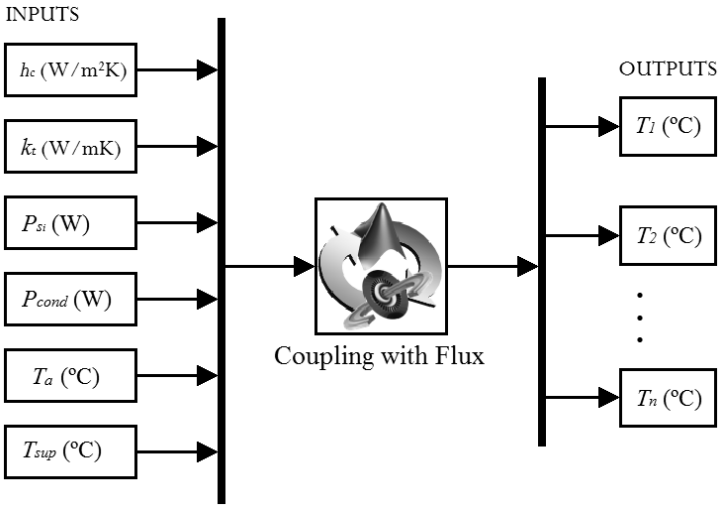

Figure 5.1: Simulink model for the Matlab-to-Flux3D coupled simulations.

between two medium voltage switchgear cells, where conductors go through, has been described in the recent literature. Both, linear and non-linear electromagnetic parameters (permeability and conductivity) are considered, but in case of non-linearity only the identification of thermal parameters is possible. Of course, in such case the BH characteristic and the conductivity of the material must be known beforehand. Particle Swarm Optimization [108], [109], and Differential Evolution [110] algorithms have been used to solve the parameter identification problem. However, in the above related studies the relative weight of unknown parameters on the objective function is not referred, leading to a high number of parameters to be identified, and various objective functions. Thus the problem complexity and time consumption might become impractical. In addition, no reference to possible measurement errors are made, which might hinder a reliable parameter identification (intended to be used for further analysis or other calculations in different device parts).

As final remark from the literature review, it is proven that there is a widespread interest towards the topic of parameter identification problem in order to achieve accurate and reliable computational models, which are often the base of the design process adopted by manufacturers of electromagnetic devices.

5.2 Simulation Tools

When implementing an optimization process it is important to consider the software capabilities to be coupled with each other, in order to automate the simulation procedure [100]. Additionally, there exist a large amount of numerical packages available for the solution of coupled electromagnetic and thermal problems which are able to solve both

2D and 3D problems. However, their main drawbacks are the high computational effort and time [111], [112].

In this dissertation, the analytical problem described in Section 3.1 for the electromagnetic computation is implemented in MATLAB® [113]. The Finite Element model for thermal analysis described in Section 3.2 is built in Flux 3D [114]. To couple the electromagnetic analytical simulation and the FE thermal analysis there is available a Simulink® block [115], enabling the MATLAB to Flux communication in both directions. Therefore, the thermal model input parameters might be introduced in Flux3D through Simulink and simulation results from the FE thermal analysis might be exported back to MATLAB for further analysis. Thus, the Matlab-Flux co-simulation is successfully implemented to build an automated coupled model. The analytical-numerical approach provides in addition a suitable computational tool for the solution of 3D electromagnetic-thermal problem with low computational times. It must be also stressed the advantageous fact that, unlike shape design problems, the parameter identification problems are mostly linear and do not need to modify the geometry or FE mesh discretizing the field region at each iteration [116].

Moreover, MATLAB provides and adequate environment to develop and incorporate optimization algorithms into the coupled simulation, as well as having available a Global Optimization Toolbox [117] with implemented tools for defining and solving optimization problems and monitoring solution progress.

It can be seen in Fig. 5.1 the block diagram build for the coupled simulations, where the inputs to the FE model are the power losses: $P_{si}-$ thermal heat sources on the steel plate calculated from (3.87) and $P_{cond}-$ copper conductor losses; and thermal parameters: h_c- convective heat exchange coefficient, k_t- thermal conductivity, T_a- room temperature, $T_{sup}-$ temperature inside plate support (in case of transformer cover tests). The output is the computed temperature corresponding to each sensor position (T_1 to T_{n_s}), where n_s is the number of sensors.

5.3 Problem Description

The problem to be solved is the tank cover plate, with one conductor carrying 2500 A passing through it, as described in Section 4.3. The physical aspects and general computation methodology are described in detail in Chapter 3, even though the main equations are here recalled. For calculating stray losses responsible for the induction heating on the steel plate, Turowski's equation is used −already defined in (3.87):

$$P_s = a_p \iint_s \sqrt{\frac{\omega\mu}{2\sigma}} \frac{|\ H_{ms}(x,y)\ |^{2x_p}}{2}\, \mathrm{d}x\, \mathrm{d}y \tag{5.1}$$

being x and y are the Cartesian coordinates of each point, μ the magnetic permeability, σ the electric conductivity, ω the angular frequency and where H_{ms} may be calculated according to (3.63). The factor a_p is a linearization coefficient which takes into account

the variation of the relative permeability inside solid steel and x_p depends on the structure of the investigated element, the nature of the field and the type of the steel [15].

Related with the FE thermal model, the interest here is to assess the thermal steady state by means of the Poisson diffusion equation from (3.116):

$$\frac{\partial}{\partial x}\left(k_t\frac{\partial T}{\partial x}\right)+\frac{\partial}{\partial y}\left(k_t\frac{\partial T}{\partial y}\right)+\frac{\partial}{\partial z}\left(k_t\frac{\partial T}{\partial z}\right)=-p_v \tag{5.2}$$

where k_t is the thermal conductivity, and p_v is the volume density of power of the heat sources. In addition, the boundary conditions are given by convection and radiation at surrounding environment from

$$\mathbf{q_{cr}}=-h_c(T-T_a)-\epsilon_r\sigma_r(T^4-T_a^4) \tag{5.3}$$

where h_c is the convection heat exchange coefficient, ϵ is the radiation heat exchange coefficient or emissivity -0.95 to 0.97 is used for steel$-$, σ_r is the Stephan-Boltzmann constant $5.6703\cdot10^{-8}\,\mathrm{W/m^2K^4}$ and T_a is the room temperature. Note that the term from (3.117) corresponding to radiation would be neglected at the temperature values concerned in this work [118].

The strategy for implementing the parameter identification process relies on the fact that only a few parameters are chosen to be adjusted and their values can be handled individually. The process consists of three main stages. The first step is to define the most appropriate objective function and to set the parameters to be identified, based on the relative weight or influence of each parameter on the temperature results. Next, the identification problem is solved for the chosen parameters, where the main goal is the accuracy $-$single-objective optimization$-$. Finally, sensitivity to measurement error is included as an additional objective function, so making the identification problem a multi-objective one. These three main stages are detailed in the next sections.

5.3.1 Objective function

The goal of the parameter identification problem is to attain the minimum temperature discrepancy between measured temperature values and numerically calculated ones, i.e. the accuracy of computed values is the objective function to be minimized. The accuracy f_1 has been defined as the quadratic mean of the temperature discrepancy between calculated and measured values (in °C).

$$f_1=\sqrt{\frac{1}{n_s}\sum_{n=1}^{n_s}(T_n-T_{sn})^2} \tag{5.4}$$

where $n=1$ to n_s is the sensor number and T_n and T_{sn} are respectively the computed

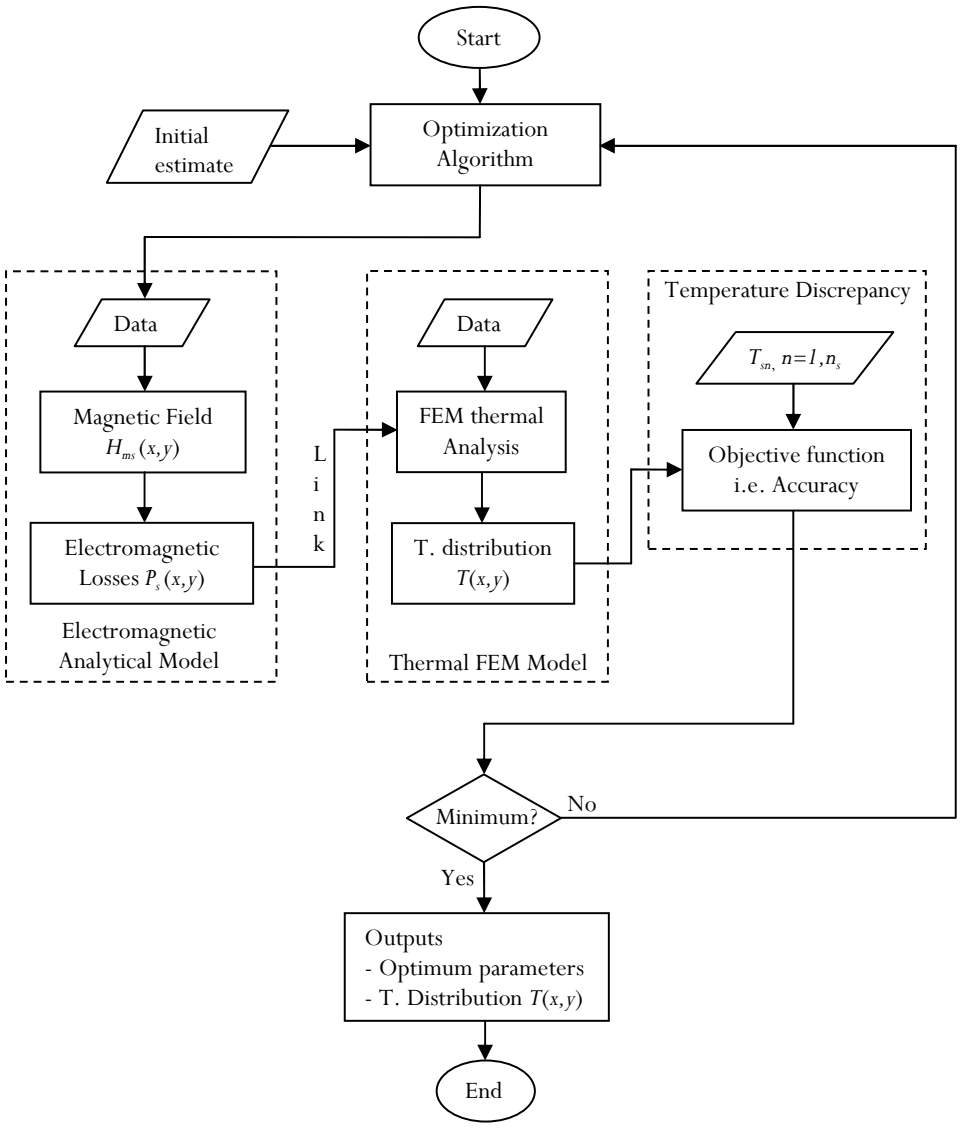

Figure 5.2: General flowchart of the computational methodology with calibration of the numerical model by means of optimization algorithm.

and measured temperature at each sensor. The choice of the error function is very important so that measured and simulated data must be related in a direct way and ill-posed problems are avoided. Defining the objective function as from (5.4) is due to more accurate results are obtained with less iterations number compared e.g. to the discrepancy of the two-norm of T_n and T_{sn} or the infinity-norm (or maximum deviation). In addition to this, the measured data taken into account is carefully analyzed and a low (but representative) number of measurement points is considered. The temperature sensors chosen are all in the same path or direction at various distances from the steel plate center x (mm), in order to avoid e.g. asymmetry on the temperature distribution

Parameter	Lower bound	Upper bound	References
a_p	1.3	1.5	[15]
μ_r	100	1400	[15], [87], [119]
σ	$5.37 \cdot 10^6$ S/m	$7.2 \cdot 10^6$ S/m	[15], [120], [121]
x_p	1	1.14	[15]
k_t	40 W/mK	80 W/mK	[121], [110]
h_c	1 W/m^{2}K	15 W/m^{2}K	[110], [118]

Table 5.1: Parameter bounds for mild steel cover tests.

due to the turn wire effect. The general flowchart for the implementation of the parameter identification problem is shown in Fig.5.2.

5.3.2 Parameters

From the above equations (5.1), (5.2) and (5.3), the unknown or uncertain parameters considered for the electromagnetic and thermal problem are:

- a_p linearization coefficient for magnetic permeability inside metal
- μ linear steel magnetic permeability in H/m or in case μ_r steel relative permeability
- σ linear steel electrical conductivity in S/m
- x_p semi-empirical correction factor depending upon the investigated structure, the nature of the field and the type of the steel
- k_t steel thermal conductivity in W/mK
- h_c convective heat exchange coefficient −natural convection in air− in W/m^{2}K

It must be stressed that the main unknowns of the identification problem are mixed unknowns in the sense that some depend on the environment e.g. h_c, while others depend on the material e.g. k_t and σ. This fact must be taken into account if the computation is to be extended to other structural elements. Parameter bounds are collected in Table 5.1 and have been defined according to values found in the literature and manufacturer catalogues.

The relative weight of parameters on the temperature distribution is discussed in the next paragraphs in order to identify the most relevant parameters to be considered in the modeling. Results can be seen in Fig. 5.3, where the analysis is done by varying the parameter to be investigated within its bounds and all other parameters are kept constant.

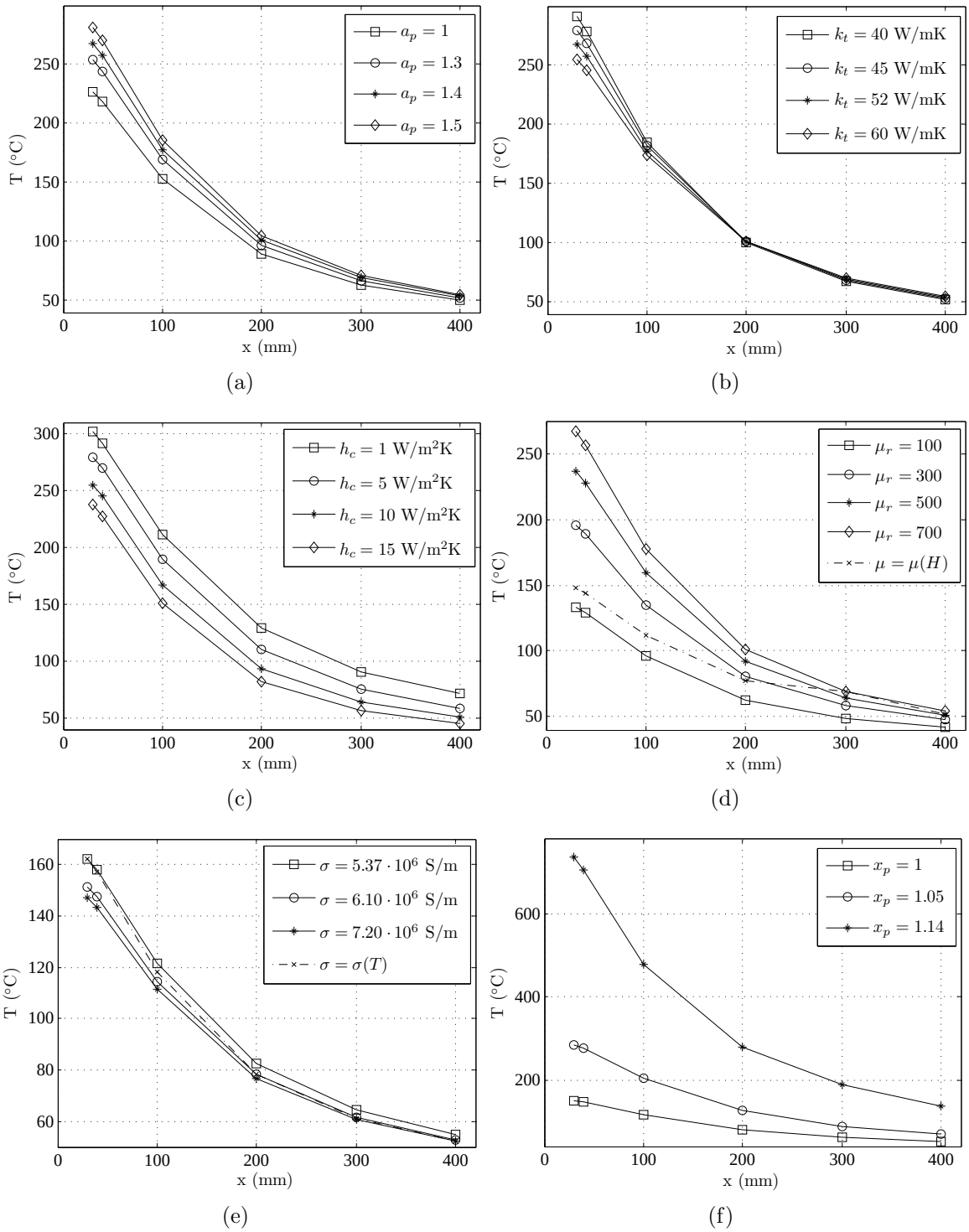

Figure 5.3: Sensitivity of electromagnetic and thermal parameters on a FE temperature computation for the steel cover plate with one conductor passing thought it carrying 2500 A: a) a_p- linearization coefficient, b) k_t- thermal conductivity, c) h_c- convective coefficient, d) μ_r- relative permeability, e) $\sigma-$ electrical conductivity and f) empirical coefficient x_p.

Linearization coefficient a_p

Starting from Fig. 5.3(a) the influence of the linearization coefficient a_p for the magnetic permeability inside metal is shown. The temperature distribution is computed for three values within the limits shown in Table 5.1, but also with $a_p = 1$ −value taken at weak fields or linear behavior− for the sake of comparison. Its value does influence significantly the temperature results, and it does depend on the material and the structure to be investigated. Its value it uncertain and might be determined from measurements.

Thermal conductivity

In Fig. 5.3(b), the influence of the thermal conductivity k_t on the temperature distribution is analyzed. Its value is relevant on the temperature results and due to its uncertainty it must be considered in the calibration of the numerical model.

Convective heat exchange coefficient

In Fig. 5.3(c), the influence of the heat exchange convective coefficient h_c is meaningful on the temperature distribution. Due to its uncertainty it must be considered in the calibration of the numerical model. However, it does influence the results by rising or dropping the temperature profile and it is not related with the material properties, therefore, after the calibration of the computational model −and material properties− its value can be replaced for any other conditions i.e. forced-air cooling, forced-oil cooling or water-cooling, if coefficients are familiar.

Magnetic permeability

In Fig. 5.3(d), simulations results are shown for several values of constant magnetic relative permeability μ_r. It can be seen from the results how its value does strongly influence the temperature results. Moreover, the non-linear behavior of the magnetic permeability $\mu(H)$ −Fig. 3.13− is well known, and detailed in Section 3.1.6. Either the BH material curve or the analytical approximation for the non-linear magnetic permeability at the metal surface (3.89) might be used, where the coefficients structural steel are determined in [15]. Temperature results for $\mu = \mu(H)$ are also shown in Fig. 5.3(d), stressing its importance in the coupled electromagnetic-thermal computation. If the non-linear behavior is to be considered, the process of numerical model calibration of the non-linear model is not possible, and the non-linear characteristic $\mu = \mu(H)$ must be known in advance for the considered materials. In references from J. Turowski 1993 [15], C. Guerin *et al.* 1996 [87], L. Susnjic *et al.* 2008 [119] and O. Biro *et al.* 2009 [24], BH characteristic data for structural steel used in transformer tanks can be found. Saturation values vary from 1.65 T to 2 T as seen in Fig. 5.4(a). In Fig. 5.4(b) the comparison of temperature results from computation with the various aforementioned BH characteristics is seen. Despite the significant differences on the magnetic characteristics, the final temperature results are slightly affected from the use of one or another. From

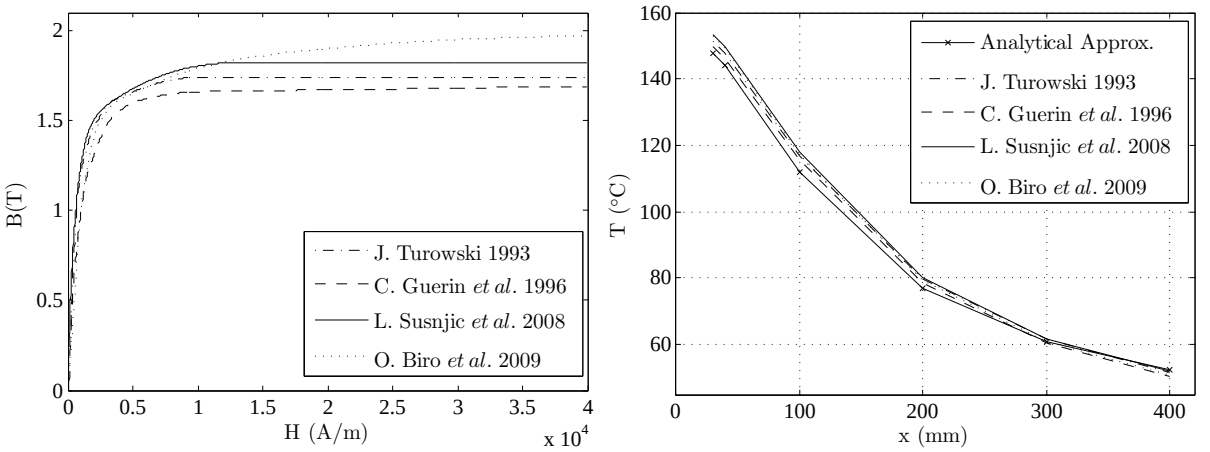

(a) (b)

Figure 5.4: Comparison of a) BH characteristics found in the literature for structural steel and b) temperature computation for cover plate with one conductor passing through carrying 2500 A from different BH characteristics.

this analysis it is concluded that the non-linear behavior must be considered in the computation and the BH curve might be assumed as known, taken from the literature.

Electrical conductivity

In Fig. 5.3(e) the influence of steel electrical conductivity σ at steady state temperature distribution is analyzed, considering from here $\mu = \mu(H)$ in order to attain a more reliable evaluation. The non-linear behavior of electrical conductivity $\sigma = \sigma(T)$ is well known [122]. The same as for the magnetic permeability, if non-linear property is to be taken into account, its value must be known beforehand. However if the linear problem is solved, its value can be identified within the calibration procedure. As from Fig. 5.3(e), by considering different values of constant electrical conductivity σ, it is seen how it does influence the temperature results but the influence is more relevant on the region of higher temperatures, close to the conductor and plate hole. In addition, results from considering non-linear electrical conductivity from (5.5) are also shown in Fig. 5.3(e).

$$\sigma(T) = \sigma(T_{ref}) \frac{1}{1 + \alpha(T - T_{ref})} \tag{5.5}$$

where α is the temperature coefficient of resistivity of the material, T_{ref} is the reference temperature at which α is specified, $\sigma(T_{ref})$ is the electrical conductivity at T_{ref}. Here $\alpha = 0.003$ [122], a value of $\sigma = 5.37 \cdot 10^6\,\mathrm{S/m}$ corresponding to the highest temperature 160 °C, and $\sigma = 7.1 \cdot 10^6\,\mathrm{S/m}$ at the lowest temperature 55 °C have been used. By comparing results from constant $\sigma = 5.37 \cdot 10^6\,\mathrm{S/m}$ and $\sigma = \sigma(T)$ and owing to the wide dispersion found on the steel temperature coefficient varying from $\alpha = 0.003$ to 0.006 [122], [123] and electrical conductivity −Table 5.1−, it is found more consistent to let

σ to be identified in the calibration of numerical model. It can be concluded from the sensitivity of results in 5.3(e) that the identified value will correspond mainly to the highest temperature region. Once the σ constant value is identified, its effect on the detriment of accuracy might be assessed. Moreover to introduce non-linear electrical conductivity in the computational methodology does present a disadvantage in the sense that the required computational effort is increased.

Coefficient x_p

Finally, in Fig. 5.3(f), the influence of the parameter x_p is evaluated. It does depend on the the structure of the investigated element, the nature of the field and the type of the steel [15], nevertheless in the studied case here, values different from unity are found to greatly alter the numerical results. Hence, $x_p = 1$ will be considered in the computation.

5.4 Single-objective Optimization

In order to solve the parameter identification problem described in the previous sections, the constrained minimization Single-Objective (SO) optimization problem must be solved. The MATLAB Global Optimization Toolbox [117] function *fmincon* might be used to find the solution that is a local minimum. It does attempt to find a constrained minimum of a non-linear scalar function of several variables starting at an initial estimate. If x is the vector of design variables and belong to a feasible region $\Omega \subseteq \Re^{n_v}$, where n_v is the number of design variables, then the solution to the inverse problem is given by the minimization of a suitable objective function $f_1(x)-$quadratic mean of temperature deviation defined in (5.4)$-$ as:
given $x_0 \in \Omega \subseteq \Re^{n_v}$

$$\min_x f_1(x), \text{ such that } x_l \leq x \leq x_u \tag{5.6}$$

being x_0 the initial estimate, x_l and x_u the lower and upper bounds of the design variables in x respectively. This is generally referred to as constrained nonlinear optimization or nonlinear programming and the active-set algorithm is used [117]. The active-set algorithm is a gradient-based algorithm but does not require gradient is to be defined by the user, neither does accept a user-supplied Hessian (it computes a quasi-Newton approximation). It is a local search algorithm and deterministic algorithm which starts from a candidate solution and then iteratively moves to a neighbor solution. As stopping criteria, both tolerance on the function value and tolerance on parameters are set to 10^{-4} and the maximum number of solver iterations is limited to 100.

Parameter	Recommended values
a_p	1.4
σ	$7.2 \cdot 10^6$ S/m
k_t	52 W/mK
h_c	7.5 W/m^{2}K

Table 5.2: Recommended input parameter values from the literature.

	T_{s2}	T_{s3}	T_{s4}	T_{s5}	T_{s6}
Measurement	164.7 °C	133.4 °C	90.1 °C	66.9 °C	56.7 °C
Initial estimate	147.81 °C	115.9 °C	79.25 °C	60.79 °C	51.23 °C
Optimum parameters	165.8 °C	131.2 °C	89.9 °C	68.3 °C	56.9 °C

Table 5.3: Temperature results from recommended −initial estimate− and optimum parameter values compared with measurements.

5.4.1 Results from single-objective optimization

The electromagnetic and thermal parameter identification is applied to a transformer cover steel plate with one conductor carrying 2500 A passing through it, as described in Section 4.3. The number of variables to be identified is $n_v = 4$ (i.e. a_p, σ, h_c, k_t), where the lower and upper bounds are defined in Table 5.1. Non-linear magnetic permeability is considered from BH characteristic [15], and the coefficient $x_p = 1$ is considered. Non linear penetration depth in the hole region calculated from (3.112). As boundary conditions $T_a = 26.4\,°\text{C}$ is measured from tests, as well as temperature inside support $T_{sup} = 40.4\,°\text{C}$.

Convergence of the SO optimization algorithm is shown in Fig. 5.5, where only the best individual from each iteration is represented. It is found to quickly converge to the same solution. The initial estimate, i.e. set of recommended parameters from the literature, are shown in Table 5.2. Temperature results from FE thermal analysis from the initial estimate and identified parameters after SO optimization applying *fmincon* are compared with measured values from sensors T_{s2} to T_{s6} in Table 5.3. Results are evaluated in terms of Mean Deviation (MD) and Highest Deviation (HD) temperature, calculated from (5.7) and (5.8) respectively.

$$\text{MD}(\%) = \frac{\sum_n \|(T_n - T_{sn})\|}{n_s} \frac{1}{T_{s2}} \cdot 100\% \tag{5.7}$$

$$\text{HD}(\%) = \frac{\max_n \|(T_n - T_{sn})\|}{T_{s2}} \cdot 100\% \tag{5.8}$$

Results are given in Table 5.4, where it can be noticed the fine-tuning of computation with optimum parameters, compared to the initial estimation. Thus, if the set of

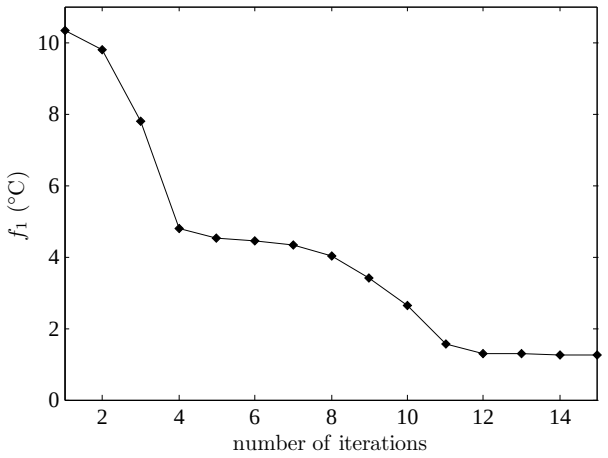

Figure 5.5: Convergence of the optimization algorithm from solving single-objective optimization problem with *fmincon*.

	Mean Deviation		Highest Deviation	
	(°C)	(%)	(°C)	(%)
Initial estimation	11.3 °C	6.9 %	17.4 °C	10.6 %
SO Optimization	1.01 °C	0.61 %	2.13 °C	1.29 %

Table 5.4: SO optimization results compared to initial estimation.

identified parameters are used for thermal analysis on different parts, and other load conditions, more accurate results would be obtained.

5.5 Sensitivity Analysis

A sensitivity analysis is carried out for the study of how the uncertainty in the output of a model (numerical or otherwise) can be apportioned to different sources of uncertainty in the model input.

In the particular problem assessed here, the uncertainty affecting the output (i.e. temperature discrepancy) is mainly the measurement error, however the accuracy of the numerical model might also to be taken into account.

To simulate the error affecting measured data, some parameter perturbation is introduced in the computational model (h_{ci}, k_{ti}). Thus, sensitivity to measurement error can be calculated as follows

$$f_2 = \frac{\max(\|f_{1i} - f_1\|)}{f_1} \cdot 100\,\% = \frac{\Delta f_{1max}}{f_1} \cdot 100\,\% \tag{5.9}$$

Element	Symbol	ε_r (%)
Temperature sensor Pt100	$\varepsilon_{\text{Pt100}}$	0.67 %
Acquisition data equipment	$\varepsilon_{\text{AcqData}}$	0.32 %
Acquisition data display	$\varepsilon_{\text{Display}}$	0.06 %
Measurement ripple	$\varepsilon_{\text{Ripple}}$	0.8 %
Sensor position	$\varepsilon_{\text{Position}}$	0.75 %
Current source value	$\varepsilon_{\text{Current}}$	0.58 %
Numerical model	$\varepsilon_{\text{Model}}$	0.58 %

Table 5.5: Relative error from elements affecting the accuracy of the model.

where f_{1i} is the objective function (5.4) from the i-th perturbed values (h_{ci}, k_{ti}), and Δf_{1i} is the deviation from (5.4) at perturbed values f_{1i} with respect to the non-perturbed ones f_1.

To carry out the sensitivity analysis, a random grid of unknown parameters h_c and k_t values is generated, as seen in Fig. 5.7(a). Each combination, i.e. set of parameters (h_c, k_t), is randomly perturbed, with i combinations and sensitivity is calculated from (5.9). The measurement error and equivalent percentage of perturbation on the input parameters is to be studied in order to perform a more reliable sensitivity analysis. Thus, firstly the accuracy of the temperature measurement is investigated. The second step is to identify the percentage of variation on parameters (h_c, k_t) which do reproduce the measurement error.

Propagation of errors

The error introduced in the identification problem is due to uncertainties in the measurement, i.e. the instrument precision (e.g. from data acquisition equipment, Pt100), the error introduced from parameters influencing temperature distribution (e.g. source current) or the measurement itself (e.g measurement ripple and sensors position). Some error is also introduced from the numerical model (e.g. model mesh). All those factors are taken into account and the relative error estimations ε_r (%) are calculated in Appendix B.2. Thus, the probable ε_P might be calculated from the propagation of errors theory. Instead of taking the sum of the errors −maximum error−, the square root of the sum of the individual relative errors ε_{ri} squared is considered as from

$$\varepsilon_P = \sqrt{\sum_i \varepsilon_{ri}^2} = 1.56\,\% \tag{5.10}$$

where ε_{ri} are collected in Table 5.5. The probable error ε_P is always less than the maximum error calculated to be 3.76 %. In temperature values, the probable deviation from measurement to calculated values, referred e.g. to sensor T_{s2} is ±2.55 °C, and the maximum ±6.2 °C.

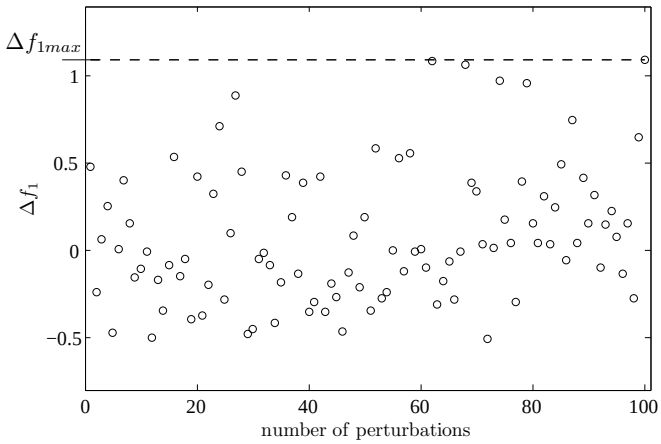

Figure 5.6: Deviation from objective function Δf_1 for a set of parameters randomly perturbed (with number of perturbations $i = 100$).

Parameters perturbation

In order to carry out the sensitivity analysis, the measurement error which has been estimated in the previous subsection is to be reproduced in the computational model by means of some perturbation on the input parameters. Thermal heat transfer coefficients h_c and k_t are chosen as the parameters to be perturbed. The influence of the percentage of input parameters perturbation on the output temperature must be calculated, and should be close to the measurement error ε_P. Thus, a more reliable sensitivity analysis can be implement.

A perturbation of 4 % on each of the parameters h_c and k_t, i.e. $h_c \pm 4\%$, $k_t \pm 4\%$, gives results which vary from a minimum of 1.28 % to a maximum of 2.23 %, corresponding to a deviation on sensor T_{s2} of 2.1 °C and 3.65 °C respectively. Note that these minimum and maximum variation depend on the set of input parameters (h_c, k_t), which are unknown and vary within the bounds shown in Table 5.1. The output optimum/identified parameters would be somewhere in between those values and thus, a 4 % variation on the parameters is reasonable, taking into account that the measurement error ε_P from (5.10) is in between those values.

Number of perturbations

An additional difficulty is to implement an inexpensive sensitivity analysis in terms of computational time within the optimization process. A high number of random perturbations, (e.g. $i = 100$) is chosen for the sensitivity analysis, where the deviation from objective function Δf_1 is shown in Fig. 5.6. For the sensitivity calculation (5.9), the maximum value is chosen $\Delta f_{1max} = 1.10$.

In order to successfully introduce the sensitivity analysis within the optimization process with low computation times, instead of generating a high number of random

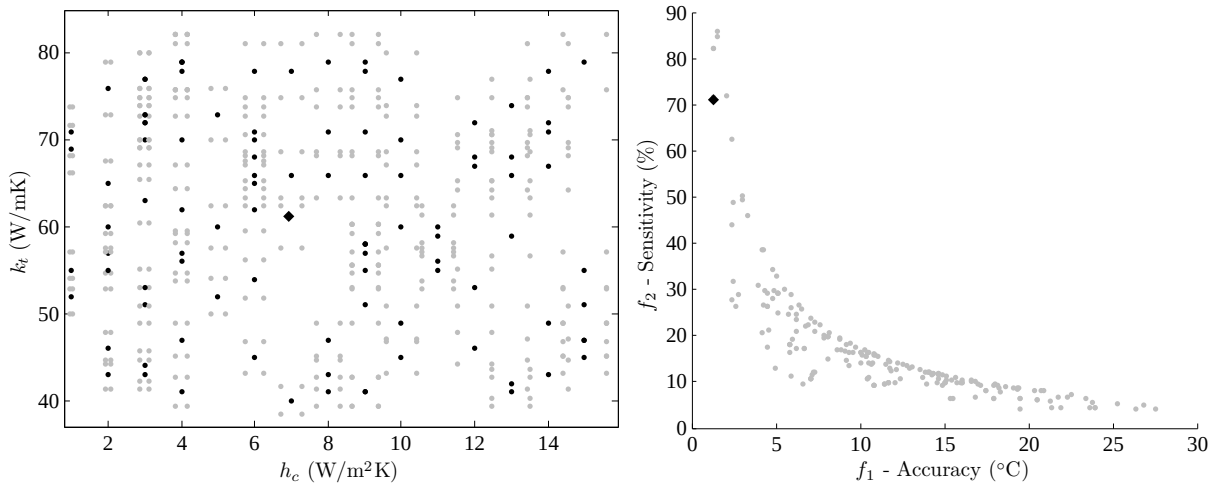

(a) (b)

Figure 5.7: Sensitivity analysis a) •− random grid of values and •− their perturbation with ♦− optimum set of parameters from SO optimization and b) Accuracy *vs.* sensitivity objective space with ♦− sensitivity from SO optimum solution.

perturbations, just the four combinations of maximum perturbations are taken (i.e. $h_c \pm 4\%$, $k_t \pm 4\%$). Thus, Δf_{1max} is calculated to be 1.15 which if compared to the previous analysis with random perturbations it seems a feasible approximation to be included in the problem of identification of the set of non dominated solutions, otherwise computational times would become excessive.

5.5.1 Results from sensitivity analysis

The random grid of values shown in Fig. 5.7(a) is used to carry out the sensitivity analysis. Sensitivity is also calculated for the set of parameters identified from SO optimization. The results from sensitivity analysis are shown in Fig. 5.7(b).

High sensitivity (70 %) results for the optimum solution and thus, from the sensitivity analysis, it comes out that there might be optimum solutions less sensitive to random perturbations (i.e. measurement error) than the best one, from SO optimization, at the expenses of a degradation in accuracy.

Thus, sensitivity to measurement error defined in (5.9), is included as an additional objective function, so making the identification problem a multi-objective one. The solution of the multi-objective (MO) optimization problem is presented in the next section, applying deterministic and non-deterministic algorithms for the sake of comparison.

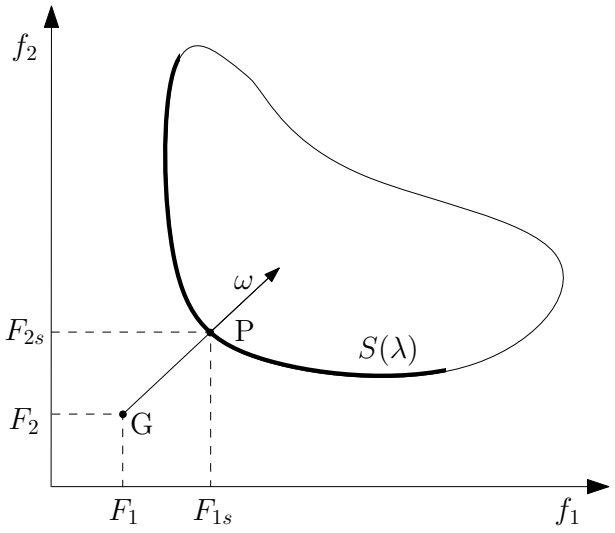

Figure 5.8: Goal attainment method for a problem with two objective functions.

5.6 Multi-objective Optimization

As previously mentioned, considering the sensitivity analysis from Fig. 5.7, it seems reasonable to consider solutions less sensitive to measurement error in the solution of the parameter identification problem. Thus, the presence of multi-objectives in a problem gives rise to a set of optimal solutions (i.e. non-dominated solutions or Pareto-optimal solutions), instead of a single optimal solution. Classical optimization methods suggest converting the multi-objective (MO) optimization problem to a single-objective one by determining one particular Pareto-optimal solution at a time [117]. On the other hand there are available in the literature a number of MO evolutionary algorithms which are able to find multiple Pareto-optimal solutions at one single simulation [124], [96]. A deterministic and a non-deterministic algorithm, i.e. the Goal Attainment Method (GATT) [125] and the Non-dominated Sorting Genetic Algorithm-II (NSGA-II) [124] respectively, are applied to the identification problem in the next sections.

5.6.1 Goal-Attainment Method

The Goal-Attainment Method (GATT) is a deterministic optimization algorithm, first formulated in [125]. It minimizes the scalar quantity $\lambda \in \Re$ with respect to the design vector $x \in \Omega \subseteq \Re^{n_v}$ subject to

$$f_i(x) - \omega_i \cdot \lambda \leq F_i \tag{5.11}$$

where $i = 1, n_f$ is the number of objective functions to be considered, $\mathbf{F} \in \Re^{n_f}$ is the

vector of ideal objective functions, which represent the goal point G and $x \in [x_l, x_u]$ is the vector of design variables being x_l and x_u the lower and upper bounds of x defined in Table 5.1. The scalar quantity to be minimized λ represents the relative gap to the initial objective $\mathbf{F}$, and it is referred as the attain factor, or degree of over (positive) or under (negative) attainment [126]. There is a useful generalization of the problem (5.11), which might be alternatively formulated as

$$\Psi(x) = \max_i \frac{f_i(x) - F_i}{\omega_i}, \; \omega_i \neq 0, \; i = 1, n_f \tag{5.12}$$

where $\Psi(x)$ is the function to be minimized by means of e.g. an algorithm of sequential quadratic programming [117], [96]. This method is single-objective in essence and needs to be applied several times to find an approximation of the Pareto front (i.e. set of non-dominated solutions) of the given problem [96]. Thus, it becomes necessary to estimate the search direction in form of weighting vector ω_i, $i \in \{1, \cdots, n_f\}$. The weighting vector defines the direction of a straight line, departing from the goal G, which intersection with the Pareto front gives the feasible point to reach P, i.e. the solution point $\mathbf{F_s}$, as seen in Fig. 5.8.

In the particular case of the parameter identification problem including measurement uncertainties, the problem described with two objective functions (i.e. f_1- accuracy and f_2- sensitivity described in (5.4) and (5.9) respectively). An initial vector of ideal objective functions (goal point) is chosen (e.g. $F_1 = 0.25\,^{\circ}\mathrm{C}$ and $F_2 = 3\,\%$). Note that the goal point might be unfeasible. To obtain the tradeoff surface several search directions are imposed such that $\omega_1 + \omega_2 = 1$ and $\omega_1, \, \omega_2 \geq 0$. The goal attainment method does also require one or several initial vectors of objective functions, given from *a priori* knowledge of the problem, and needs to be applied several times to obtain the set of desired solutions.

Optimization results are collected in Table 5.6, where different variables correspond to:

- ω_1, ω_2 are the weight coefficients.
- h_{c0}, k_{t0} are the initial estimation x_0 values for each of the parameters considered: h_c in $\mathrm{W/m^2K}$ and k_t in W/mK.
- h_c, k_t are the identified parameter values which belong to the Pareto front in $\mathrm{W/m^2K}$ and W/mK respectively.
- f_1, f_2 are the values of objective functions accuracy ($^{\circ}C$) and sensitivity (%) with respect to parameters (h_c, k_t).
- λ is the attain factor at solution (h_c, k_t).
- *iter* is the number of iterations taken to reach the solution.
- *func* is the number function evaluations.

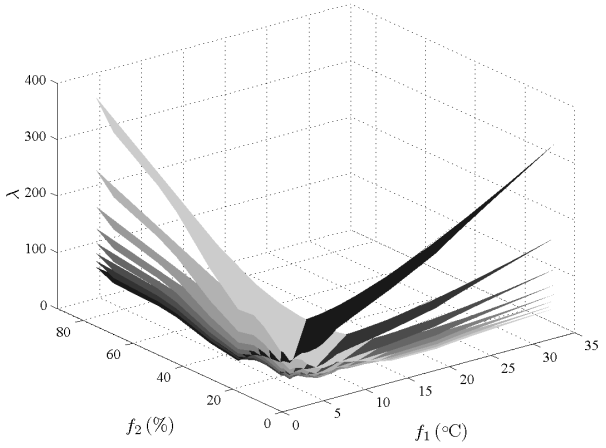

Figure 5.9: 3D representation of feasible region *vs.* attain factor λ for different search directions varying from ■– ($\omega_1 = 0.1$, $\omega_2 = 0.9$) to ■– ($\omega_1 = 0.8$, $\omega_2 = 0.2$).

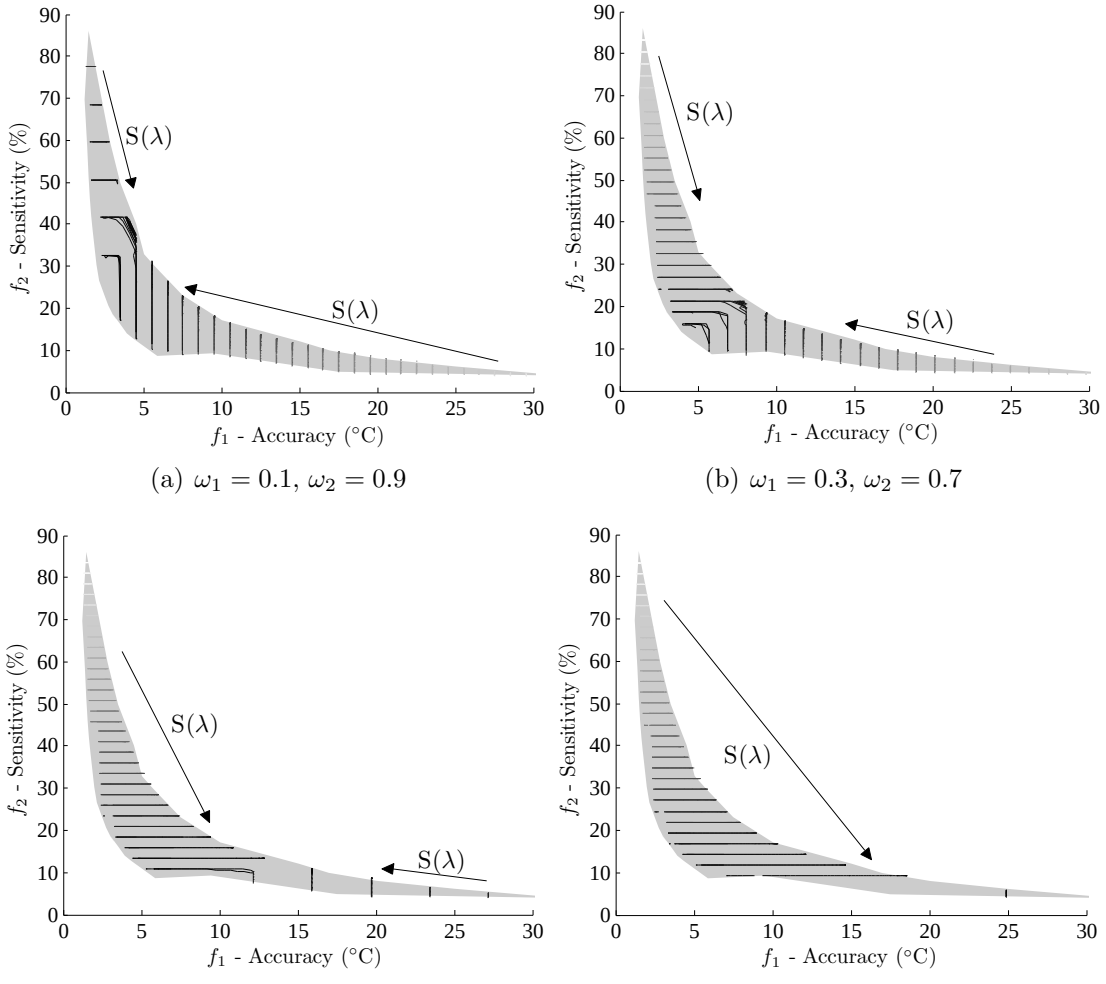

(a) $\omega_1 = 0.1$, $\omega_2 = 0.9$

(b) $\omega_1 = 0.3$, $\omega_2 = 0.7$

(c) $\omega_1 = 0.6$, $\omega_2 = 0.4$

(d) $\omega_1 = 0.8$, $\omega_2 = 0.2$

Figure 5.10: Feasible region *vs.* attain factor λ for given search directions (ω_1, ω_2).

ω_1	ω_2	h_{c0}	k_{t0}	h_c	k_t	f_1 (°C)	f_2 (%)	λ	*iter*	*func*
0.015	0.985	6.09	61.52	6.92	61.30	1.26	69.79	67.81	13	59
0.020	0.980	6.09	61.52	6.67	63.22	1.38	58.49	56.62	18	115
0.025	0.975	6.09	61.52	6.57	64.03	1.49	51.37	49.61	25	139
0.030	0.970	6.09	61.52	6.50	64.61	1.58	46.15	44.49	32	229
0.035	0.965	6.09	61.52	6.44	65.08	1.66	42.12	40.54	24	145
0.040	0.960	6.09	61.52	6.39	64.49	1.74	38.89	37.38	24	303
0.060	0.940	6.09	61.52	6.24	66.71	1.99	30.40	29.15	34	278
0.075	0.925	6.09	61.52	6.15	67.41	2.15	26.47	25.38	23	147
0.100	0.900	6.09	61.52	5.97	68.61	2.47	23.06	22.29	27	228
0.125	0.875	6.09	61.52	5.81	69.63	2.77	20.68	20.21	32	234
0.150	0.850	6.09	61.52	5.68	70.52	3.04	18.84	18.63	37	302
0.175	0.825	6.09	61.52	5.56	71.33	3.29	17.34	17.39	25	171
0.200	0.800	6.09	61.52	5.45	72.08	3.52	16.10	16.38	23	180
0.250	0.750	6.09	61.52	5.25	73.47	3.96	14.14	14.85	34	216
0.300	0.700	6.09	61.52	5.07	74.78	4.37	12.62	13.74	27	188
0.400	0.600	6.09	61.52	4.73	77.26	5.15	10.35	12.26	32	213
0.500	0.500	7.75	45.00	4.42	79.74	5.92	8.67	11.35	30	215
0.600	0.400	7.75	45.00	3.26	80.00	9.46	9.14	15.35	14	58
0.700	0.300	7.75	45.00	2.71	80.00	11.57	7.85	16.17	11	45
0.800	0.200	7.75	45.00	2.12	80.00	14.07	6.45	17.27	12	49
0.900	0.100	7.75	45.00	1.40	80.00	17.47	4.91	19.14	11	44

Table 5.6: Results of applying goal attainment to the parameter identification problem.

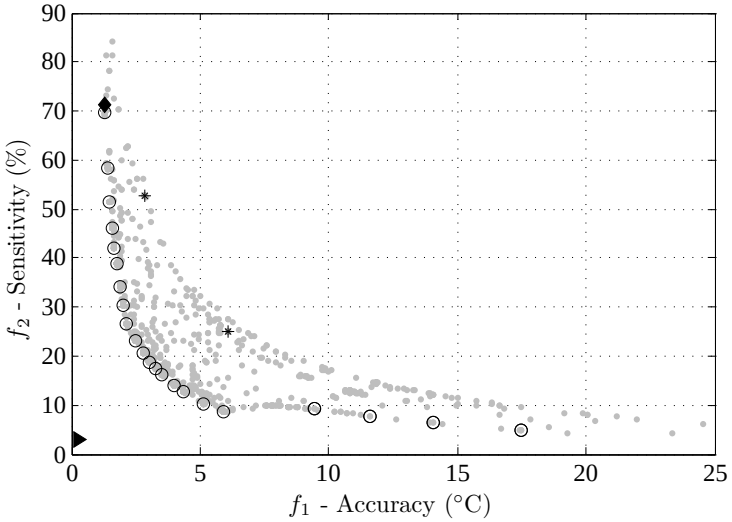

Figure 5.11: Optimization results from GATT: ○– Identified set of Pareto-optimal solutions, ·– objective space, ▶ – goal point, ∗– initial estimation and ♦– SO solution.

For a better understanding of the application of GATT within the actual case of study, Fig. 5.9 shows the representation of the parameter λ −to be minimized− for a set of search directions (ω_1, ω_2) given in Table 5.6. Besides, at certain search directions (ω_1, ω_2), the variation of λ in the feasible region (f_1, f_2) is given in Fig. 5.10.

The representation of the solution allows to plot the tradeoff surface of the identification problem as seen in Fig. 5.11. Note that the choice of weights uniformly distributed between 0 and 1 does not guarantee to obtain an uniform distribution of the solutions in the Pareto front [126]. Thus a first approach is run with coarse step on the weight functions to locate the area of interest. Then, in a second optimization phase fine discretization on the weight functions is used on the area of interest to obtain a better representation of the front.

5.6.2 Non-dominated Sorting Genetic Algorithm-II

When a multi-objective problem is addressed using Pareto optimal theory, special attention has to be paid in order to obtain a full representation of the front [127]. Among the various methods for evolutionary MO computing, Non-dominated Sorting Genetic Algorithm-II (NSGA-II) is gaining a wide popularity in computational electromagnetism. It is a improved version of NSGA which has been criticized for its computational complexity, lack of elitism and the need of specifying an optimal parameter value for sharing parameter. NSGA-II alleviates all the above three difficulties, where a selection method is used to emphasize current non-dominated solutions, and a crowding distance method is used to maintain the diversity of the population. The general procedure is synthesized in the following paragraphs.

Population initialization

The population *pop* is initialized as usual with $n_p > 1$ individuals, each having $n_f > 1$ objectives. The initial population is generated based on the problem range and constraints.

Fast non-dominated sorting approach

Once the population is initialized it is sorted based on non-domination into each front. An individual is said to dominate another if the objective functions of it are no worse than the other and at least one is better. Thus, each solution in *pop* must be compared with other solutions in the population to find if it is dominated. A first front F_1 being completely non-dominant sets in the current population, the second front F_2 is dominated only by individuals in the first front, and the front F_k goes so on. Individuals in each front are assigned rank values based on the front they belong to, e.g. individuals in first front F_1 are given a rank value of 1 and individuals in second F_2 are assigned a rank value of 2 and so on for each $k-$th front as seen in Fig. 5.12.

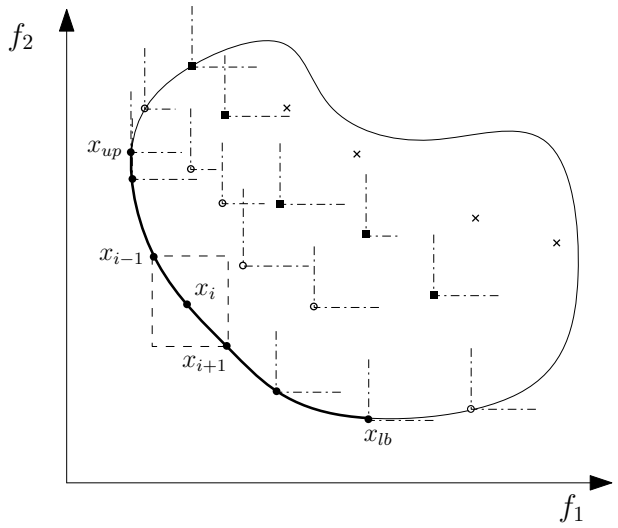

Figure 5.12: Ranking of different fronts based on non-domination criterion and crowding distance from NSGA-II algorithm, where solutions belong to •− first, ∘− second, ■− third and ×− $k-$th fronts, with their respective rank value.

Crowding distance

In addition to fitness value a new parameter called crowding distance is calculated for each individual. The crowding distance is a measure of how close an individual is to its neighbours. Large average crowding distance will result in better diversity in the population. The basic idea behind the crowding distance is finding the Euclidean distance between each individual in a front based on their n_f objectives. Given a set of solutions n_k in the $k-$th non-dominated front, for each solution x_i, $i = 1, n_k$, the crowding distance d_i with neighbour solutions $x_{i\pm1}$ is

$$\mathrm{d}_i = \sqrt{\sum_{p=1}^{n_v} \left[\frac{x_{(i-1)p} - x_{(i+1)p}}{x_{up} - x_{lp}} \right]^2}, \; i = 1, n_k \tag{5.13}$$

where n_v is the number of variables, and x_{up} and x_{lp} are the upper and lower variables in $\mathbf{x}$ respectively as shown in Fig. 5.12.

Diversity preservation

A solution with smaller value of distance d_{ij} is said to be more crowded than other solutions. A crowded comparison operator ($\prec_n$) is proposed to guide the selection process at the various stages of the algorithm towards an uniformly spread-out Pareto-optimal front. The comparison is carried out assuming that every considered solution has two attributes, i.e. the non-domination rank −depending on the front F_k they belong to−

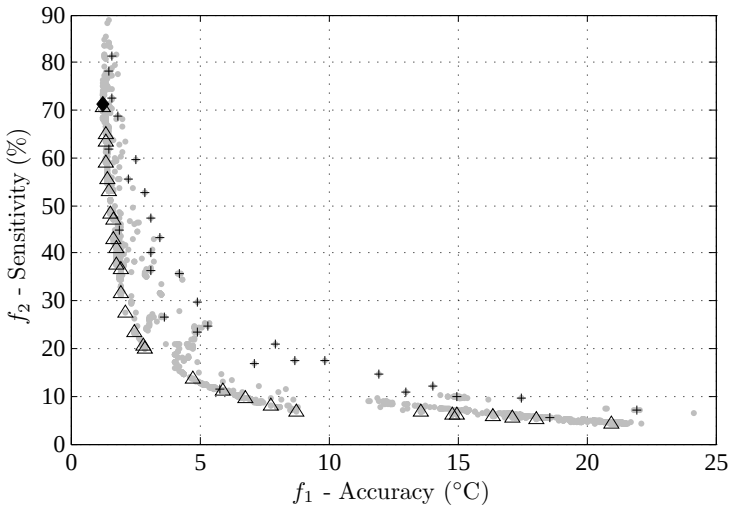

Figure 5.13: Optimization results from NSGA-II: △ − Identified set of Pareto-optimal solutions, •− objective space, +− initial population chromosome *pop* and ♦− SO optimal solution.

and the crowding distance d_{ij}. Thus, when two individuals are compared with differing non-domination rank, the solution with lower rank is preferred. Otherwise, if solutions belong to the same front (same rank), the solution to be chosen is the located in a lesser crowded region (crowding distance is greater).

Recombination and Selection

The selected population generates offsprings from crossover and mutation operators. The offspring population is combined with the current generation population and selection is performed to set the individuals of the next generation. Since all the best individuals from parent and child population are added in the population, elitism is ensured. Population is now sorted based on non-domination. The new generation is filled by each front subsequently until the population size exceeds the current population size. If by adding all the individuals in a front F_k the population exceeds is the population size n_p then individuals in front F_k are selected based on their crowding distance in the descending order until the population size is n_p. And hence the process repeats to generate the subsequent generations.

$h_c\,(\mathrm{W/m^2K})$	$k_t\,(\mathrm{W/mK})$	$f_1\,(°\mathrm{C})$	$f_2\,(\%)$
6.92	61.29	1.26	70.74
6.72	62.75	1.34	64.94
6.71	63.17	1.37	63.38
6.68	63.15	1.37	59.15
6.61	63.69	1.44	55.56
6.59	63.87	1.46	53.00
6.53	64.36	1.54	48.36
6.43	64.85	1.65	46.92
6.43	65.08	1.67	42.89
6.37	65.45	1.76	44.13
6.37	65.65	1.77	37.74
6.26	66.19	1.93	36.72
6.26	66.54	1.96	31.62
6.16	67.30	2.13	27.25
5.99	68.53	2.44	23.39
5.79	70.12	2.84	20.54
5.75	70.03	2.89	19.88
5.11	79.03	4.71	13.62
10.01	44.63	5.92	11.16
10.16	40.74	6.75	9.50
10.63	37.85	7.77	8.08
10.99	35.16	8.75	6.90
2.24	80.00	13.57	6.71
1.98	79.52	14.79	6.16
1.73	77.13	16.35	5.75
1.61	76.34	17.11	5.50
1.42	76.20	18.08	5.10
1.00	72.94	20.94	4.34

Table 5.7: Results of applying NSGA-II to the parameter identification problem.

The main arguments to get the function running are a random initial population chromosome *pop*, which should cover the entire objective space as seen in Fig. 5.13, and the population size ($n_p = 30$). As stopping criteria the total number of generations must be provided ($gen = 30$), after which the algorithm will automatically stop. Also the number of number of objective functions $n_f = 2$ and number of decision variables $n_v = 2$ and their bounds (Table 5.1) must be entered according to the objective function. The whole procedure results in a quick convergence towards the non-dominated region of the objective space and the sharing procedure helps to distribute individuals over the front. Optimization results are collected in Table 5.7 and the representation of the final generation chromosome allows to plot the tradeoff surface of the identification problem as seen in Fig. 5.13.

GATT				NSGA-II			
$h_c\,(\mathrm{W/m^2K})$	$k_t\,(\mathrm{W/mK})$	$f_1\,(^\circ\mathrm{C})$	$f_2\,(\%)$	$h_c\,(\mathrm{W/m^2K})$	$k_t\,(\mathrm{W/mK})$	$f_1\,(^\circ\mathrm{C})$	$f_2\,(\%)$
6.92	61.29	1.26	70.74	6.92	61.30	1.26	69.79
6.68	63.15	1.37	59.15	6.67	63.22	1.38	58.49
6.43	64.85	1.65	46.92	6.50	64.61	1.58	46.15
6.37	65.65	1.77	37.74	6.39	64.49	1.74	38.89
6.26	66.54	1.96	31.62	6.24	66.71	1.99	30.40
5.79	70.12	2.84	20.54	5.81	69.63	2.77	20.68

Table 5.8: Comparison of a set of Pareto-optimal solutions from GATT and NSGA-II in the region of interest of accuracy $\leq 3\,^\circ\mathrm{C}$.

5.6.3 Comparison of methods and optimization results

The application of the GATT method does require high-level of information to find an approximation of the Pareto front of the given problem. The main drawback is that it needs to be applied several times to find an approximation of the Pareto optimal solutions, even varying the initial estimation points several times and leading to high computational time. In contrast the main advantage found is that is possible to control the spread of the Pareto-optimal solutions along front by setting a finer step discretization on the weighting vector at the desired regions.

When applying NSGA-II a well-spread representation of the front is achieved with less computational time. A proof of that is the number of function evaluations needed by each of the algorithms to obtain a representation of the front. Applying the GATT method the sum of *func* from Table 5.6 for all 22 search directions is 3861; compared to the total function evaluations from NSGA-II ($gen = 30$, $n_p = 30$) which is counted to be 848 ($\approx 80\%$ less of function evaluations).

GATT and NSGA-II have been successfully applied to solve the parameter identification problem and optimization results are compared in Fig. 5.14 showing good agreement along the tradeoff surface. Also the solution from SO optimization is plotted in Fig. 5.14, stressing the consistency of results, as SO optimization represents a particular solution from the front. In Table 5.8 a set of solutions from each of the methods applied are collected for their comparison, and thus easily obtain the set of parameters chosen for computation according to desired criteria on accuracy and sensitivity to measurement error.

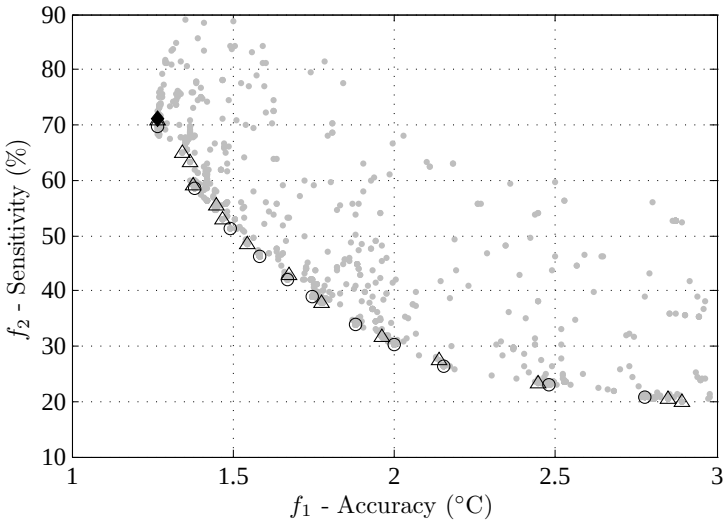

Figure 5.14: Accuracy *vs.* Sensitivity objective space with: ♦− SO optimal solution and set of Pareto-optimal solutions from ○− GATT compared to △ − NSGA-II for the region of interest ($f_1 < 3\,°\mathrm{C}$).

The above comparison yields significant conclusions on the efficiency of the algorithms and the selection of the most suitable for the parameter identification problem.

The most adequate solution of compromise between high accuracy f_1 and low sensitivity f_2 from Table 5.8 might be chosen around the point $f_1 = 2\,°\mathrm{C}$ and $f_2 = 30\,\%$. Thus, mean deviation (5.7) and highest deviation (5.8) values are compared in Table 5.9 for the initial estimation set of parameters, recommended values from the literature as seen in Table 5.2−; the set of identified parameters from SO optimization; and the set of identified parameters from MO optimization. The parameter identification taking into account sensitivity to measurement error yields an improvement on the accuracy of results when tested for other current values. The fine-tuning of computation with the set of identified parameters from MO optimization can be seen from the comparison in Fig. 5.15 with measurements and the recommended values from the literature (initial estimation). Thus, if the set of identified parameters is used for thermal analysis on different parts of transformers, and other load conditions, more accurate results would be obtained, as seen in the next Chapter 6.

	Initial estimation		SO Optimization		MO Optimization	
Test current	MD	HD	MD	HD	MD	HD
500 A	4.7 %	6.8 %	1.9 %	2.8 %	1.6 %	2.6 %
1000 A	8.1 %	12.7 %	2.9 %	5.4 %	2.4 %	5.2 %
1750 A	8.6 %	13.4 %	2.0 %	4.5 %	1.5 %	4.2 %
2500 A	6.9 %	10.6 %	0.6 %	1.5 %	1.0 %	1.9 %

Table 5.9: Relative error from initial estimation set of parameters, SO optimization solution and MO solution taking into account sensitivity to measurement error.

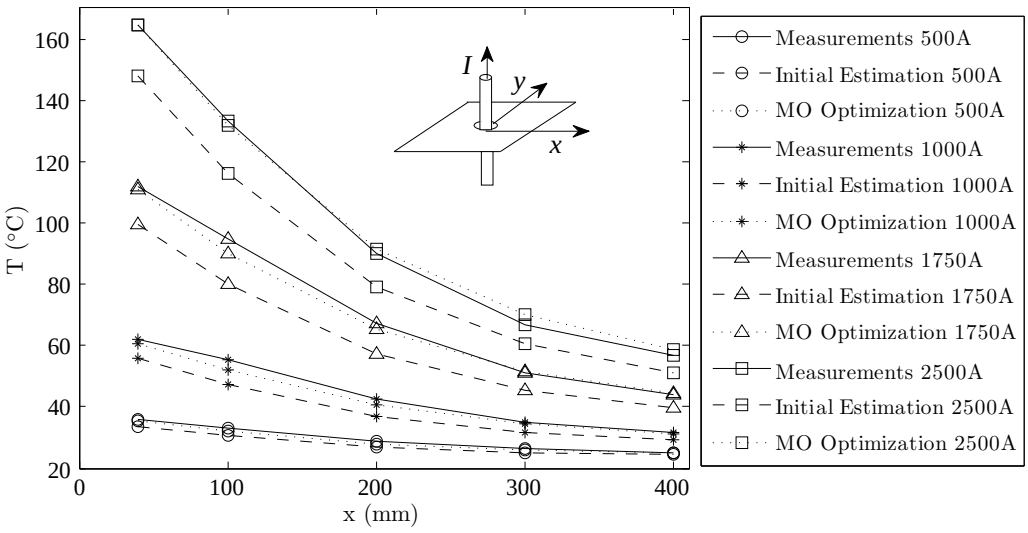

Figure 5.15: Comparison of measured and numerical-calculated temperatures by using Initial Estimation set of parameters and identified parameters from MO Optimization for the calibration current 2500 A and tested for several current values.

Chapter 6

Computation and Results

In this chapter results from the computational methodology proposed in Chapter 3 are presented. Several study cases are given to evaluate e.g. non-linear behavior or influence of metal thickness in the electromagnetic analytical model. Finally, temperature results from tests with either 1 or 2 current carrying conductors are also given in order to validated with measurements from tests described in Chapter 4.

6.1 Results from Electromagnetic Analytical Model

By means of the non-linear penetration depth analytical model described above and in Section 3.1.10, results from a wide range of currents can be presented stressing the behavior of magnetic quantities whether the iron performs at the linear or saturation region of the material BH curve.

One current carrying conductor

In the next Fig. 6.1 to Fig. 6.6 results from the electromagnetic analytical model from weak and strong field simulations (i.e. 500 A and 2500 A) are shown. It can be compared for both cases how the magnetic flux density, magnetic permeability or the magnetic field penetration depth vary over a square steel transformer cover plate, allowing a better understanding of the specific problem features.

In the analytical formulation, the surface value of the magnetic field intensity H_{ms} at any point on the steel plate is responsible for the loss distribution according to (3.110). The representation of the maximum magnetic field obtained from Biot-Savart law [81] is shown in Fig. 6.1, where from Fig. 3.13 it can be noticed how their values correspond either to the linear region in the BH curve in Fig. 6.1(a), and to the saturation region in Fig. 6.1(b).

The magnetic flux density B_{ms} is represented in Fig. 6.2. Here it can be appreciated the high saturation of iron for strong fields in Fig. 6.2(b) in contrast to the linear behavior for weak fields in Fig. 6.2(a).

In Fig. 6.3 and Fig. 6.4 the variation of the magnetic permeability over the steel plate and the non-linear penetration depth δ_{nl} as calculated from (3.112) are shown for weak and strong fields. Results from the magnetic field penetration depth are particularly important as it represents the volume thickness where the stray losses are introduced in the thermal model as heat sources. In case of saturation -Fig. 6.4(b)-, the penetration depth in the conductor hole region is more than three times higher than its value over the steel surface. This fact highlights the importance considering the non-linear penetration depth (3.112) in the thermal model to set the volumes of the heat sources mainly in the hole region.

The representation of power losses distribution can be seen in Fig. 6.6, which are then introduced in the thermal FE model as heat sources for the temperature computation.

Single-phase transformer cover

The non-linear electromagnetic model has been applied to a single phase transformer cover plate, with a distance between conductors of $a = 250\,\text{mm}$. Results from the non-linear electromagnetic analytical model from weak and strong field simulations (i.e. 250 A and 1250 A) are shown in the next Fig. 6.7 to Fig. 6.12, where the same relevant effects discussed in the previous paragraph take place.

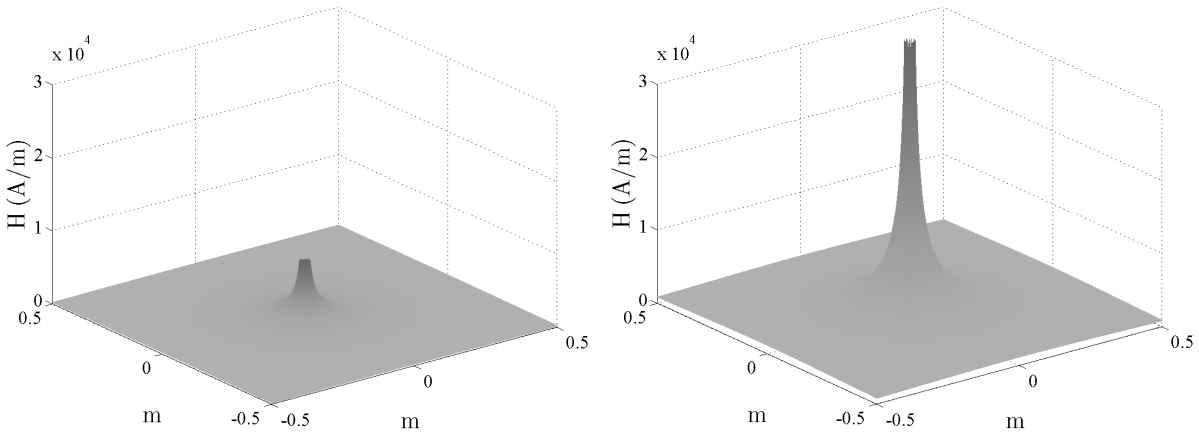

Figure 6.1: Magnetic field distribution for a) 500 A and b) 2500 A.

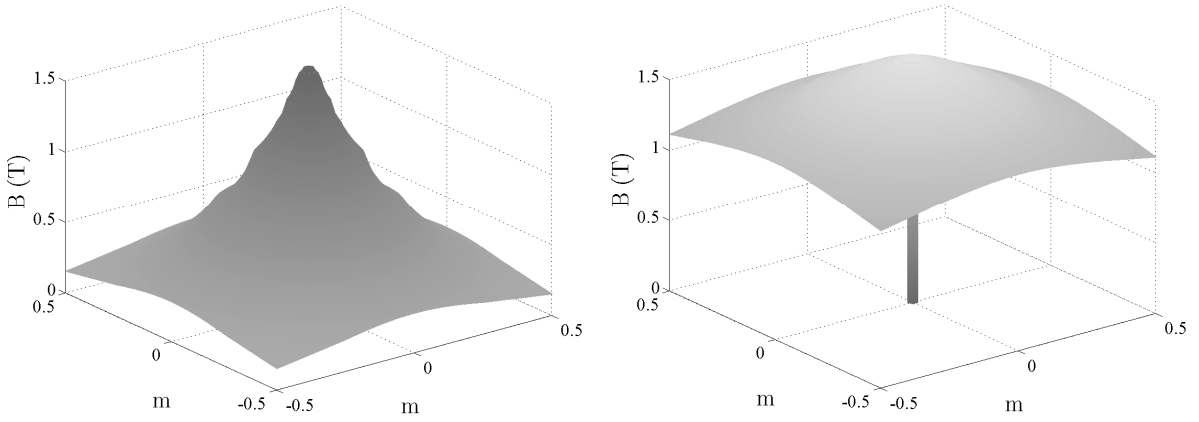

Figure 6.2: Magnetic flux density over a steel plate for a) 500 A and b) 2500 A.

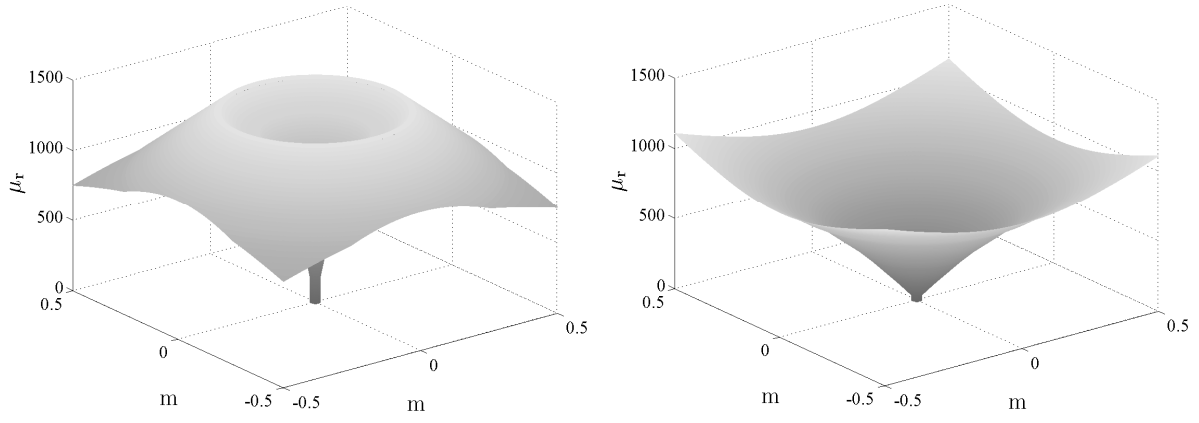

Figure 6.3: Relative magnetic permeability over a steel plate for a) 500 A and b) 2500 A.

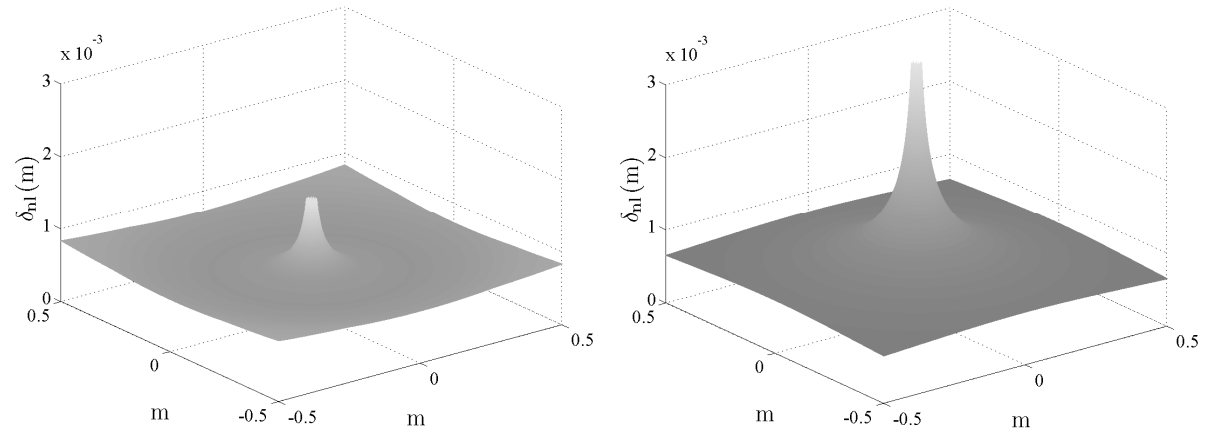

Figure 6.4: Magnetic field penetration depth over a steel plate for a) 500 A and b) 2500 A.

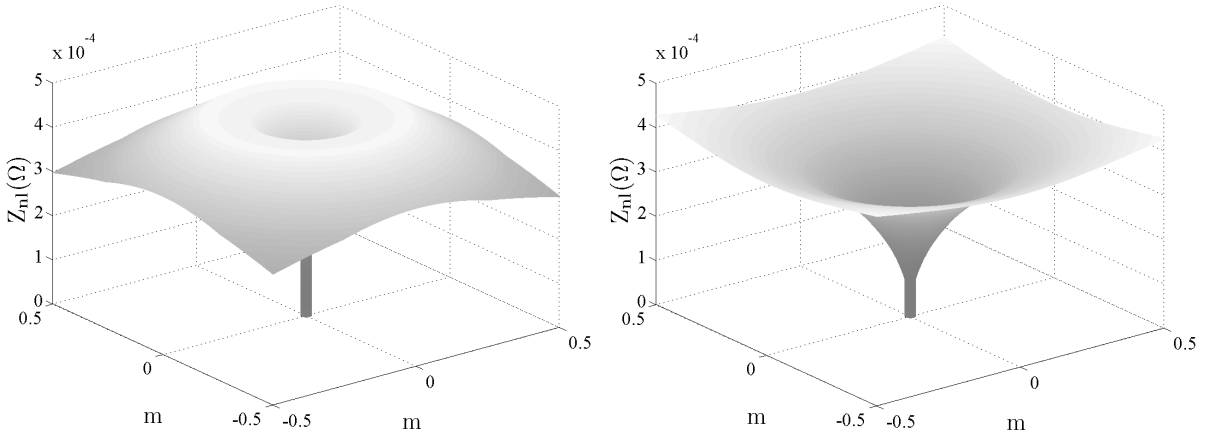

Figure 6.5: Non-linear surface impedance over a steel plate for a) 500 A and b) 2500 A.

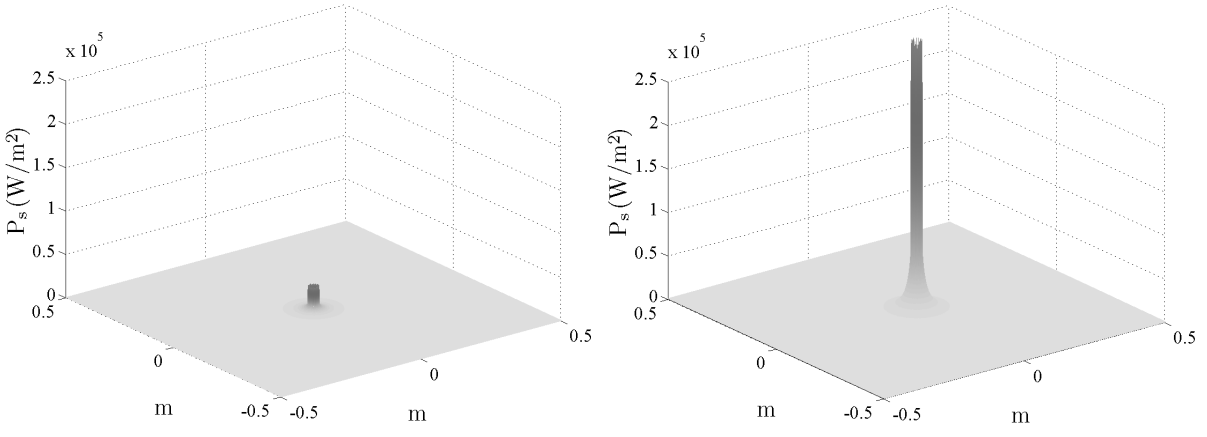

Figure 6.6: Power loss distribution over a steel plate for a) 500 A and b) 2500 A.

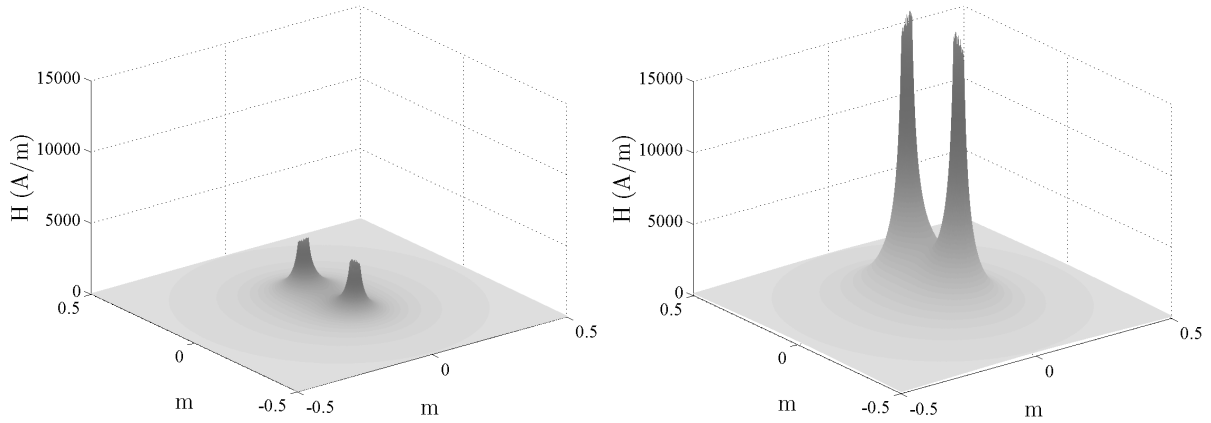

Figure 6.7: Magnetic field distribution for single-phase bushings a) 250 A and b) 1250 A.

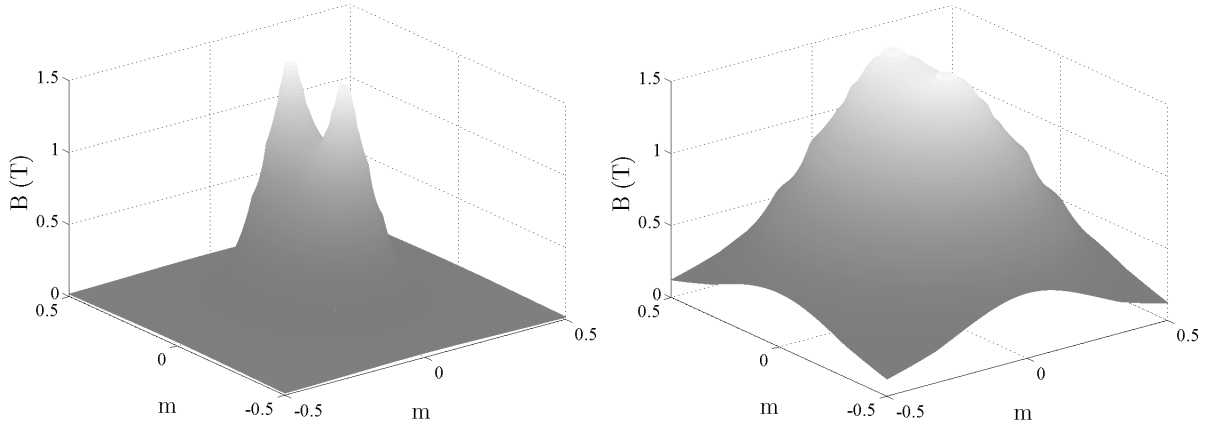

Figure 6.8: Magnetic flux density for single-phase bushings a) 250 A and b) 1250 A.

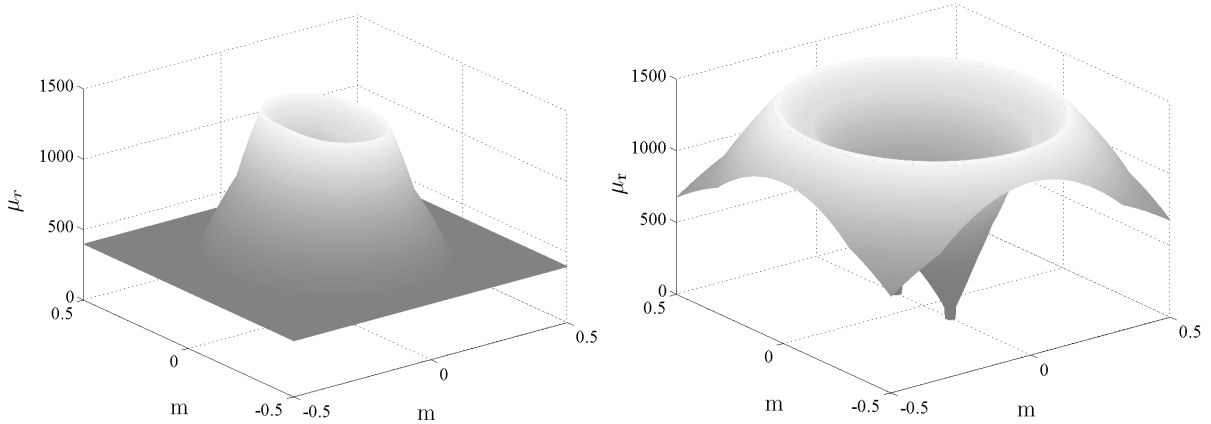

Figure 6.9: Relative magnetic permeability for single-phase bushings a) 250 A and b) 1250 A.

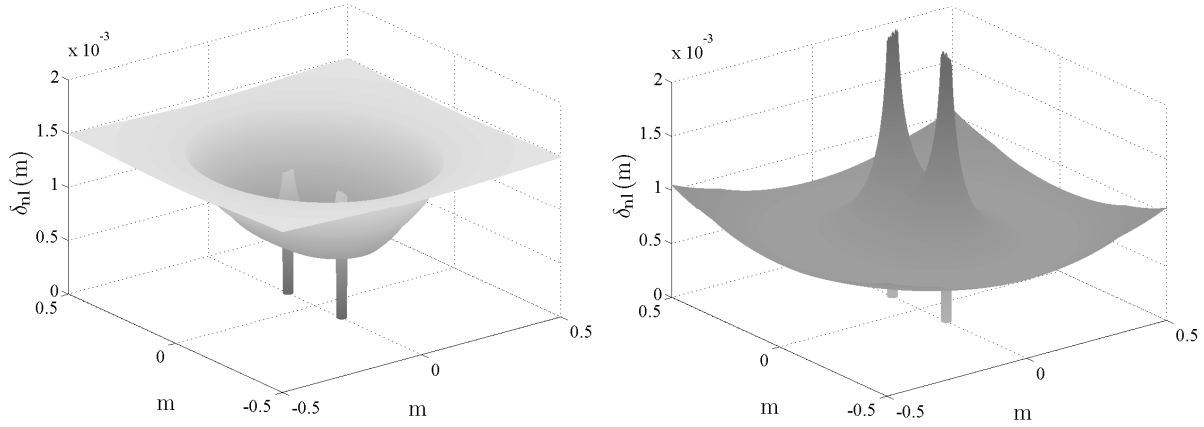

Figure 6.10: Penetration depth for single-phase bushings a) 250 A and b) 1250 A.

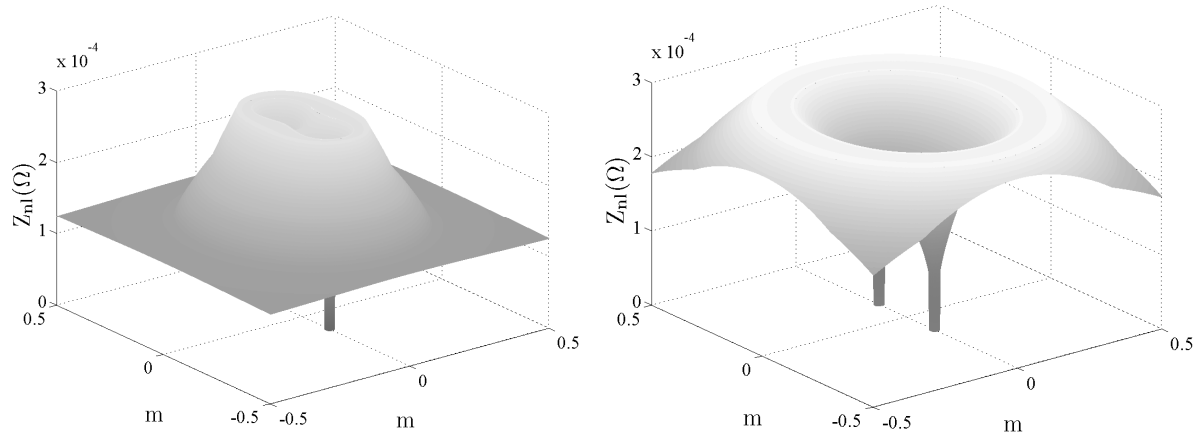

Figure 6.11: Surface impedance for single-phase bushings a) 250 A and b) 1250 A.

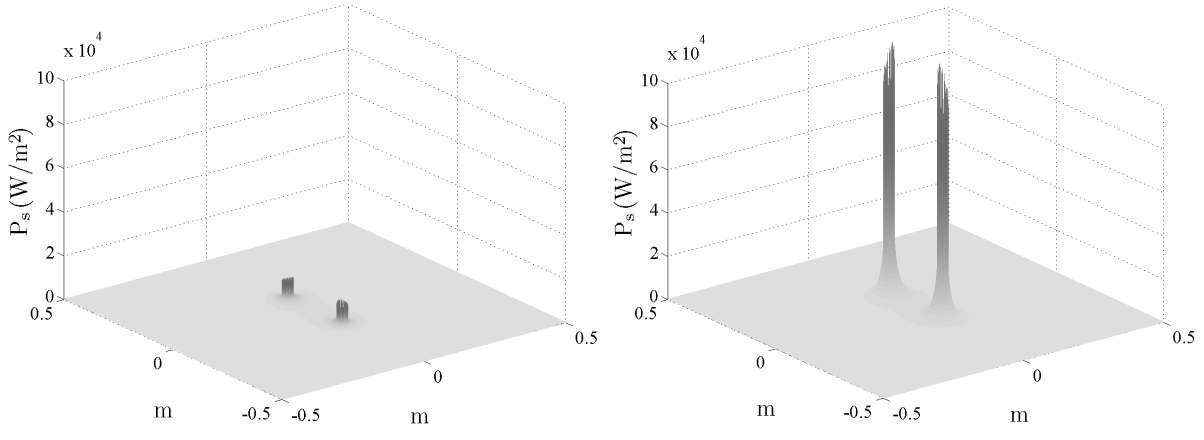

Figure 6.12: Power losses distribution for single-phase bushings a) 250 A and b) 1250 A.

	Measured	Linear Model		Non-linear PD Model	
Current	T(°C)	T(°C)	Deviation	T(°C)	Deviation
200 A	25.5 °C	24.9 °C	2.3 %	25.1 °C	1.6 %
500 A	35.1 °C	33.2 °C	5.4 %	35.5 °C	1.0 %
1000 A	61.0 °C	63.5 °C	4.0 %	61.5 °C	0.9 %
1750 A	112.7 °C	139.0 °C	23.4 %	111.9 °C	0.7 %
2500 A	171.8 °C	237.1 °C	38.0 %	167.5 °C	2.5 %

Table 6.1: Hottest spot comparison from linear and non-linear Penetration Depth (PD) models over a steel plate of thickness d = 6 mm.

6.2 Validation of FE Thermal Results with Temperature Measurements

For validation of the non-linear penetration depth computational methodology the temperature is measured over a square mild steel plate of 1 m side and 6 mm of thickness, through which a solid copper conductor is placed as seen in Fig. 4.2 (left). Through the conductor flows an ac current heating by electromagnetic induction the metal plate. Experimental tests are presented in detail in Chapter 4. The temperature is measured by means of several temperature sensors Pt100 distributed on the surface, and also by means of a Thermal Infrared (IR) camera to capture the temperature distribution at steady state. Thermal FE analysis is then carried out, where the computed losses are introduced as heat sources, and the measured temperature at each sensor can be thus compared with numerical results.

In the FE thermal model the volume over the non-linear penetration depth is divided into n sub-volume regions V_n, with surface s_n [81]. Thus, the value of δ_{nl} (3.112) varies along the steel plate as seen in previous Sections 3.1.11 and 6.1. At thermal steady state the variation of only tenths of millimeter does not vary the computed temperature, however the real value of the δ_{nl} on the conductor hole border definitely influences the results and the hottest spot temperature value. The material data required for computation, is determined from measurements as presented in Chapter 5.

To fulfill a wide range from weak to strong fields the temperature is measured for several current values from 500 A to 2500 A. Measurements are compared with the computed temperature distribution from non-linear model in Fig. 6.13 for the calibration current 2500 A and tested for several current values, showing good agreement with each other. Temperature results computed from the linear model (3.55), are also shown in Fig. 6.13 stressing the importance of the non-linear penetration depth model (3.110). Hottest spot temperatures are shown in Table 6.1, as well as the deviation of either the linear and non-linear models from measurements. Thermal IR image from Fig. 6.14(c) is compared with numerical temperature results Fig. 6.14(d) from FE computation for the non-linear penetration depth model, where the accuracy of obtained results is really shown.

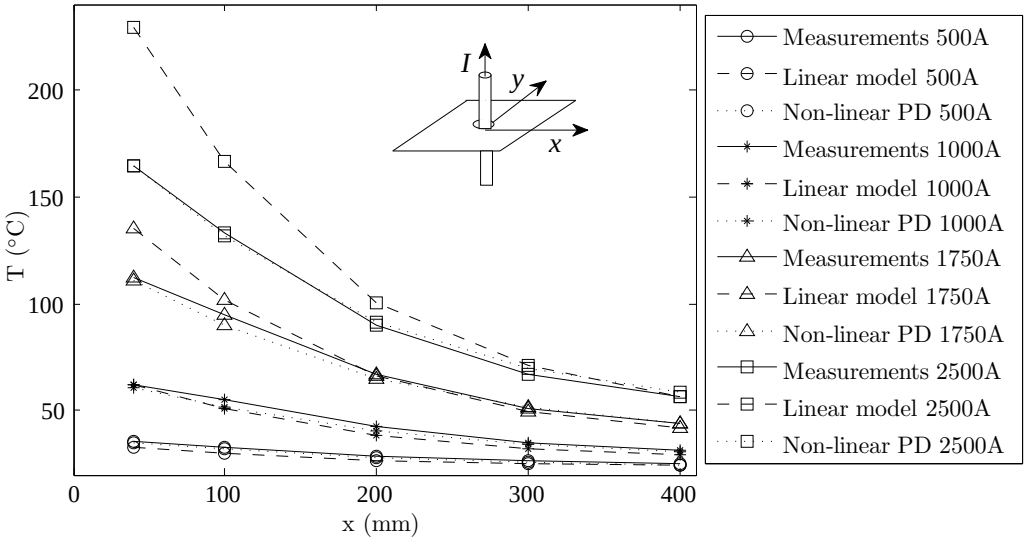

Figure 6.13: Temperature results for the linear and non-linear Penetration Depth (PD) models compared with measurements along the steel surface.

6.2.1 Influence of plate thickness

To evaluate the influence of the steel plate thickness on the temperature distribution, the computational methodology is applied to plates of d = 1 mm and d = 12 mm. The hottest spot temperature computed for several current values is compared with measured temperature in Table 6.2.

The good agreement from measured and computed temperature values is one more validation of the computational methodology for the overheating hazard assessment and also validate the accuracy of identified parameters in Chapter 5.

Slightly higher deviations are computed for the 1 mm model. It is here to mention that $d < \lambda/2$, i.e. there exists an internal wave reflection which reduces the losses significantly. In this case the screening coefficient $\zeta(x, y)$ (3.103) must be considered. The screening coefficient varies over the steel plate surface when the non-linear penetration depth model $\delta_{nl}(x, y)$ is considered.

In Fig. 6.14 thermal IR images from a 2500 A test are compared to results obtained from FE thermal computation with non-linear penetration depth, showing good agreement with each other and validating thus the computational model.

A latter study is presented in Fig. 6.15, showing the behavior of total power losses and hottest spot temperature over a wide range of plate thickness used on structural parts of power transformers. In Fig. 6.15(a) it must be mentioned firstly that values below 3 mm are strongly influenced by the screening coefficient ζ. And secondly, after 6 mm it is seen a slow rate of increase of power losses due just to the increase in the conductor hole −as from Fig. 3.17−, being stay losses computed over the metal surface constant.

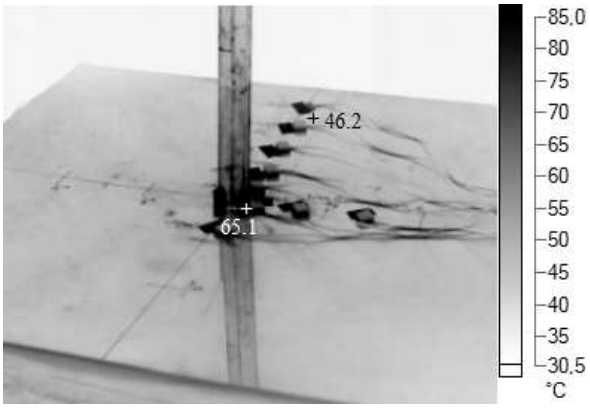

(a) Thermal IR image, 1mm thickness

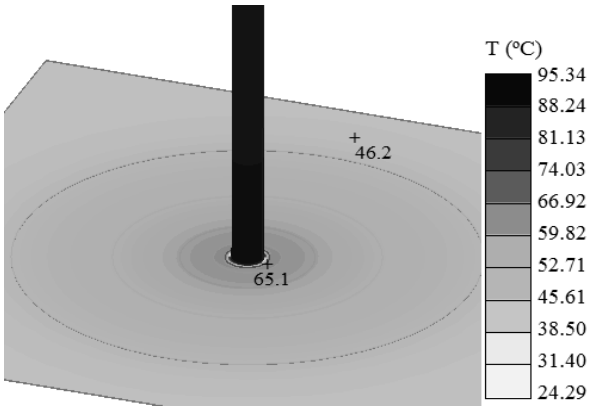

(b) FE thermal computation, 1mm thickness

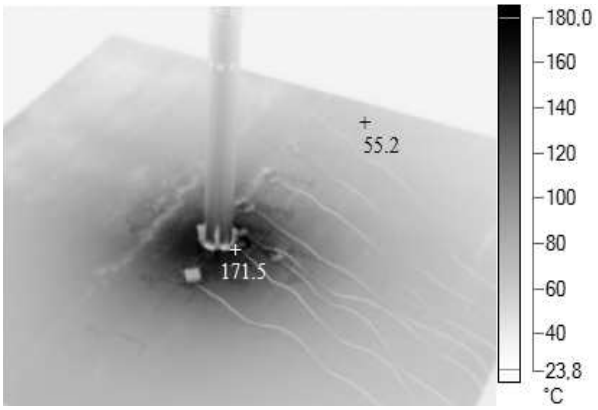

(c) Thermal IR image, 6mm thickness

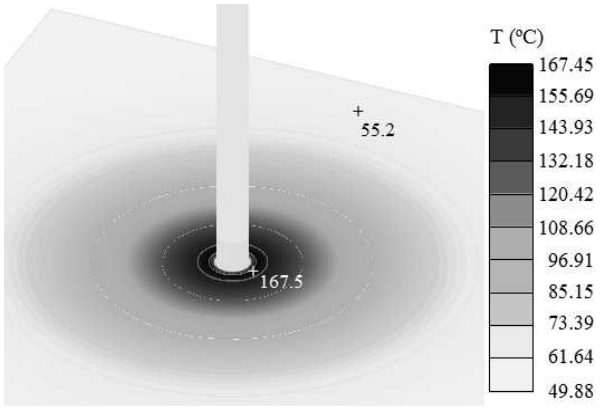

(d) FE thermal computation, 6mm thickness

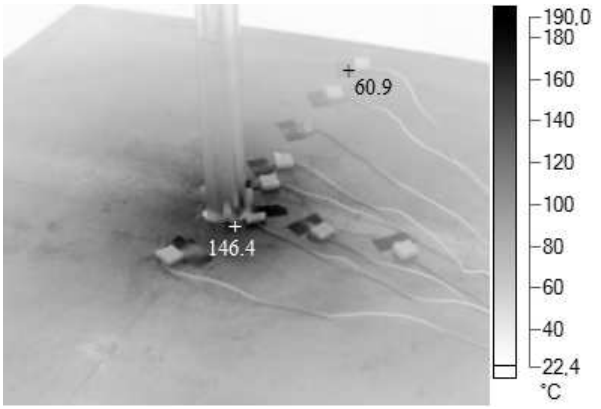

(e) Thermal IR image, 12mm thickness

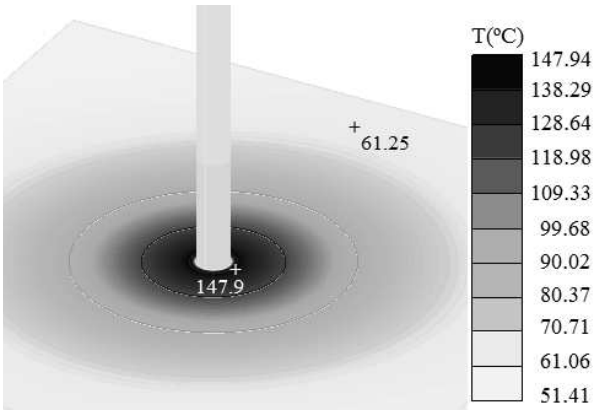

(f) FE thermal computation, 12mm thickness

Figure 6.14: Temperature distribution over a steel cover plate of different thickness for a 2500 A test.

	d = 1 mm			d = 12 mm		
	Measured	Non-linear PD Model		Measured	Non-linear PD Model	
Current	T(°C)	T(°C)	Deviation	T(°C)	T(°C)	Deviation
200 A	28.4 °C	26.9 °C	5.3 %	22.3 °C	22.7 °C	1.5 %
500 A	38.5 °C	36.8 °C	4.4 %	30.6 °C	31.7 °C	3.7 %
1000 A	45.2 °C	47.2 °C	4.3 %	54.7 °C	53.6 °C	1.9 %
1750 A	55.3 °C	57.2 °C	3.5 %	98.3 °C	97.8 °C	0.5 %
2500 A	65.1 °C	63.27 °C	2.8 %	146.4 °C	147.9 °C	1.0 %

Table 6.2: Hottest Spot Temperature from one current conductor passing through steel plates of thickness d = 1 mm and d = 12 mm.

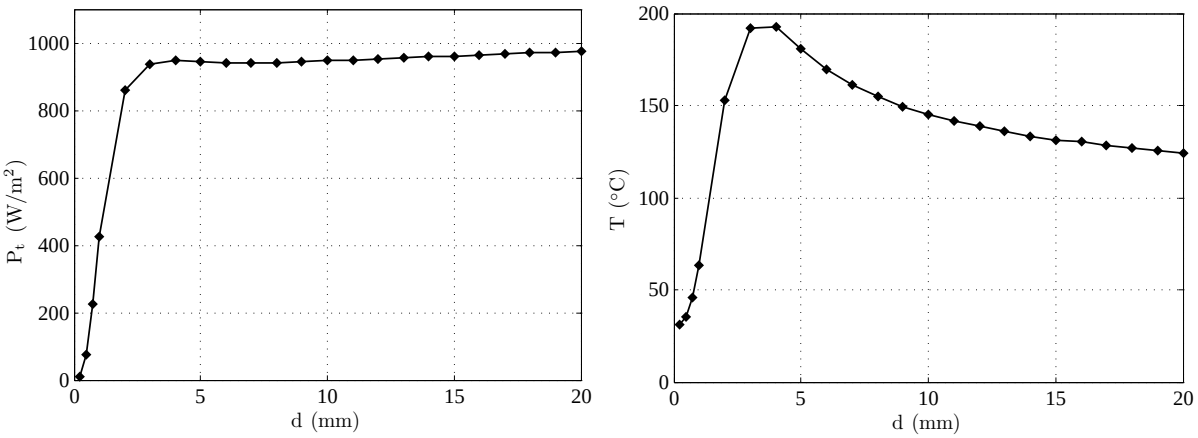

(a) Total power losses

(b) Hottest spot temperature

Figure 6.15: Influence of steel plate thickness on power losses and hottest spot.

6.2.2 Single-phase bushings through cover plate

Moreover, to stress the usefulness of the presented non-linear penetration depth model, temperature is measured over plates with two holes to each be passed through by a conductor carrying single-phase currents, as from a single-phase transformer cover plate, seen in Fig. 4.3.

Single-phase currents from 250 A to 1250 A are applied to tests, where the measured hottest spot temperature and computed values can be seen in Table 6.3, being the conductors are separated a distance of $a = 150$ mm and $a = 250$ mm respectively. In Fig. 6.16 thermal IR images from 1250 A tests are compared to results obtained from FE thermal analysis with non-linear penetration depth, showing good agreement.

It is important to note that in the thermal images seen in Fig. 6.14 and Fig. 6.16 some brighter regions correspond to paper tape to fix the sensors, which has different emissivity, but do not correspond to real higher temperatures of the steel plate.

	$a = 150\,\text{mm}$			$a = 250\,\text{mm}$		
	Measured	Non-linear PD Model		Measured	Non-linear PD Model	
Current	T(°C)	T(°C)	Deviation	T(°C)	T(°C)	Deviation
250 A	30.7 °C	30.4 °C	0.9 %	28.9 °C	28.3 °C	2.1 %
500 A	43.6 °C	44.9 °C	3.1 %	42.4 °C	42.9 °C	1.4 %
875 A	77.3 °C	79.3 °C	2.6 %	74.7 °C	75.3 °C	0.8 %
1250 A	114.5 °C	115.7 °C	1.0 %	106.3 °C	107.0 °C	0.6 %

Table 6.3: Hottest spot temperature over single-phase transformer cover plate separated a distance $a = 150\,\text{mm}$ and $a = 250\,\text{mm}$.

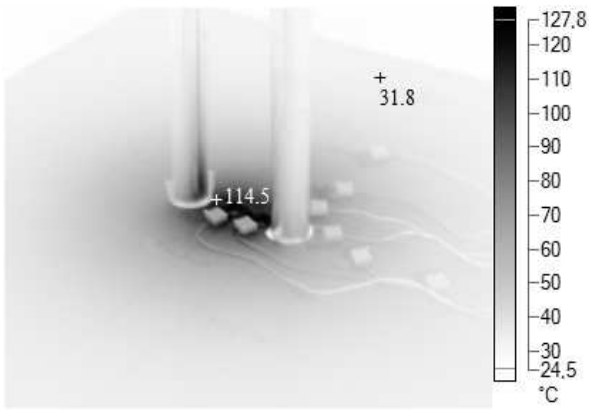

(a) Thermal IR image, $a = 150\text{mm}$

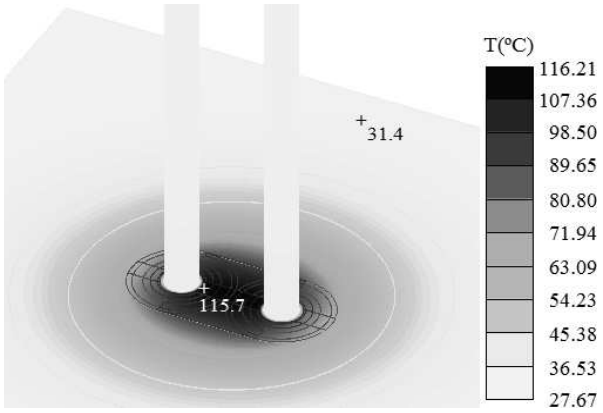

(b) FE thermal computation,$a = 150\text{mm}$

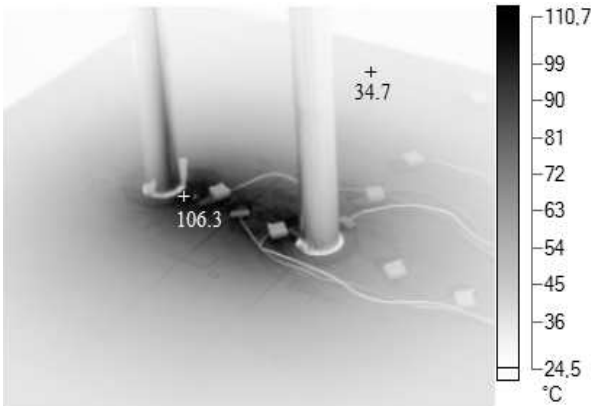

(c) Thermal IR image, $a = 250\text{mm}$

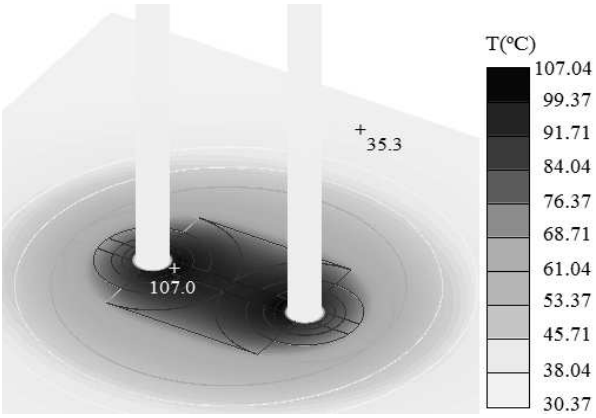

(d) FE thermal computation, $a = 250\text{mm}$

Figure 6.16: Temperature distribution over a steel cover plate with single phase conductors for a 1250 A test.

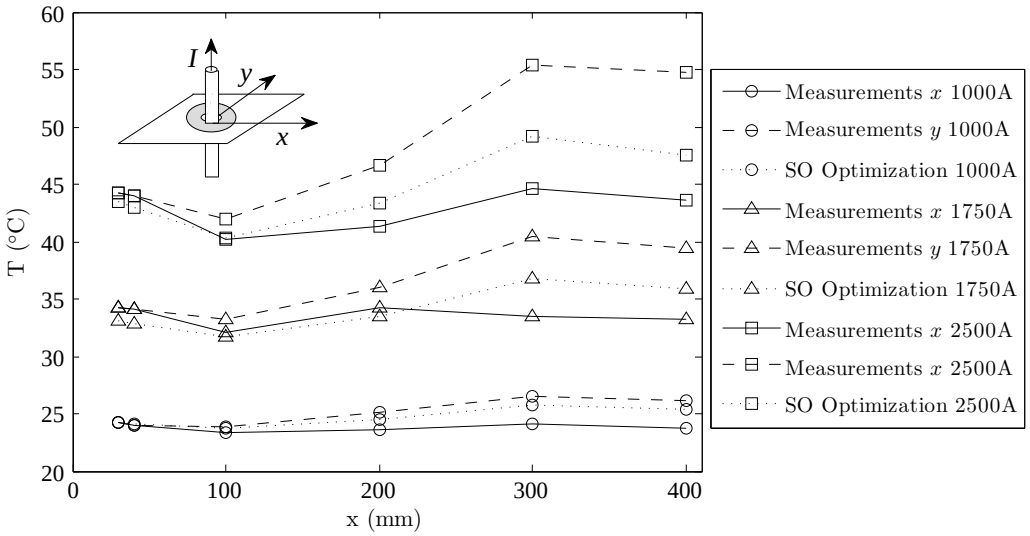

Figure 6.17: Temperature results for a mild steel plate with amagnetic insert compared to measurements along the steel surface.

Parameter	Lower bound	Upper bound	References
μ_r	1.005	15	[15], [128]
σ	$0.91 \cdot 10^6\,\mathrm{S/m}$	$1.6 \cdot 10^6\,\mathrm{S/m}$	[129]
k_t	$15\,\mathrm{W/mK}$	$35\,\mathrm{W/mK}$	[129]

Table 6.4: Parameter bounds and SO optimization solution for stainless steel tests.

6.2.3 Cover plate with amagnetic insert

The computational methodology has been validated and compared to measurements yielding good accuracy when mild steel cover plates are tested, either with 1 conductor and single-phase bushings. Further experiments are carried out on steel cover plates with amagnetic inserts as described in Chapter 4, Fig. 4.2 and Fig. 4.3.

Material properties for mild steel and boundary conditions on cover plate tests have been found from MO optimization, seen in Chapter 5. However, stainless steel material properties are still uncertain and must be determined from the solution of the parameter identification problem. The unknown parameters and their bounds are shown in Table 6.4. Parameters are identified by means of SO optimization as described in Chapter 5. Particularly, stainless steel has been found be slightly magnetic, with values of relative magnetic permeability μ_r up to 15.

Temperature results over cover plate surface are plotted in Fig. 6.17, for the calibration current 2500 A and tested for several current values. It is seen how the computed temperature matches the measured values within the amagnetic insert (i.e. $x < 250\,\mathrm{mm}$) and higher deviations are seen in the mild steel region. However, it has been found strong

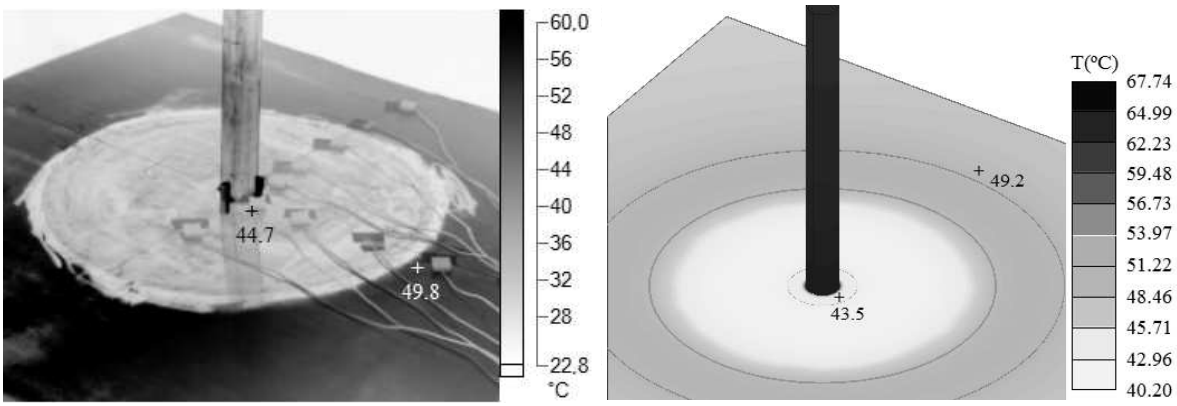

(a) Thermal IR image (b) FE thermal computation

Figure 6.18: Temperature distribution over a steel cover plate with amagnetic insert for a 2500 A test.

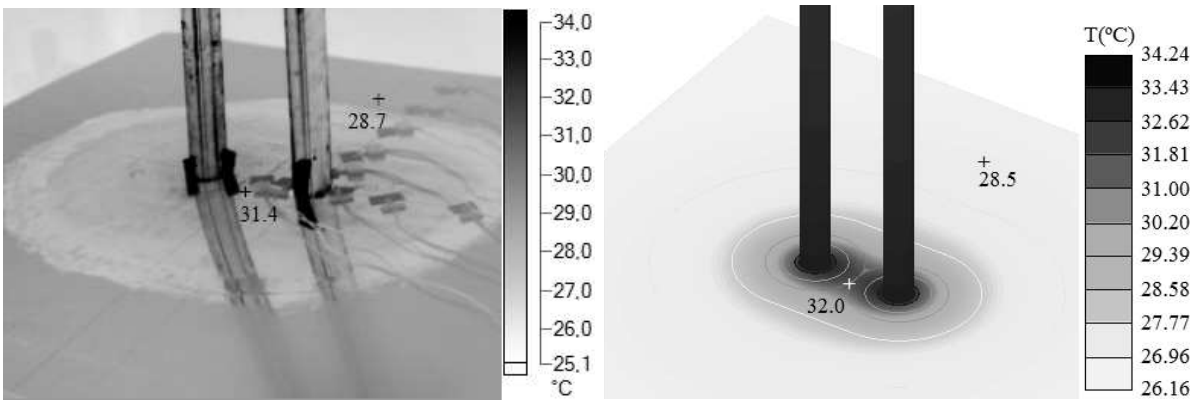

(a) Thermal IR image (b) FE thermal computation

Figure 6.19: Temperature distribution over a single-phase transformer cover plate with amagnetic insert for a 1250 A test.

discrepancy in the measurements depending on the measurement path, either x and y directions as it is clearly seen in Fig. 6.18(a) −possibly due to turn wire effect−, where computed temperature lies in between both values. Thermal IR image is compared with computed temperature distribution in Fig. 6.18 for a 2500 A test showing good agreement. Note that thermal IR image has to be calibrated as the emissivity coefficients differ from both regions within the plate [94].

Temperature results have been also tested in case of single-phase bushings separated $a = 150$ mm passing through transformer cover plate with amagnetic insert, as seen in Fig. 6.19. Temperature results show good agreement with measured temperature values, both in the magnetic and amagnetic regions, proving thus the validity of the computational methodology and the accuracy of identified parameters.

	$a = 50\,\text{mm}$			$a = 100\,\text{mm}$		
	Measured	Computed		Measured	Computed	
Current	T(°C)	T(°C)	Deviation	T(°C)	T(°C)	Deviation
500 A	25.7 °C	25.1 °C	2.3 %	23.1 °C	23.3 °C	1.1 %
1000 A	26.7 °C	25.8 °C	3.5 %	28.9 °C	28.8 °C	0.1 %
1750 A	34.7 °C	32.9 °C	5.2 %	29.6 °C	29.7 °C	0.4 %
2500 A	46.7 °C	45.24 °C	3.1 %	37.2 °C	37.1 °C	0.3 %

Table 6.5: Hottest spot temperature from one current conductor passing parallel to a steel plate at a distance $a = 50\,\text{mm}$ and $a = 100\,\text{mm}$.

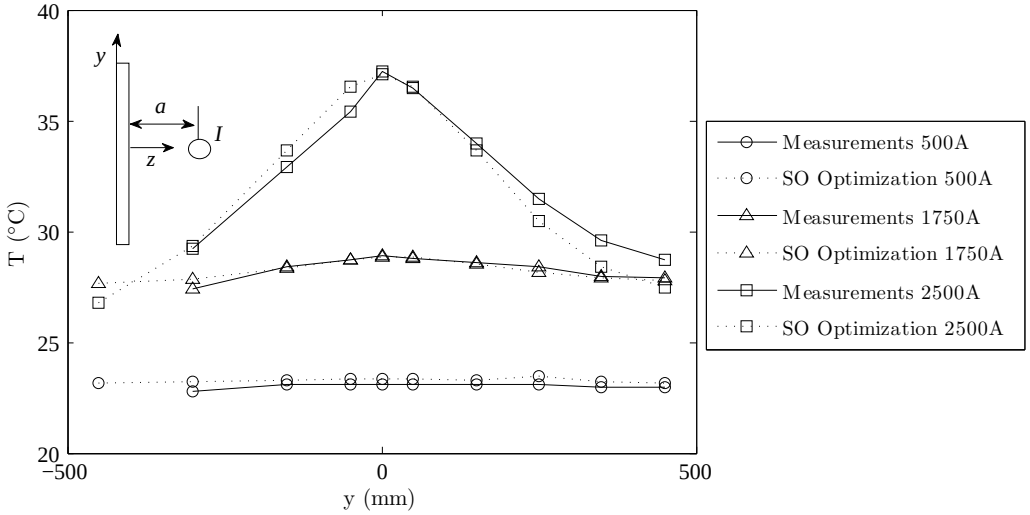

Figure 6.20: Temperature along a tank wall plate due to a parallel conductor passing at a distance $a = 100\,\text{mm}$.

6.2.4 Tank wall

The computational methodology might be extended to the case of tank walls. High current conductors passing parallel to the steel plate on the x direction, and at a distance a on the z direction depart radial stray flux which intrudes normal into the iron surface. When calculating losses in tank wall where the field varies only in the xy plane, having a peak value of H_{mz0} on the metal surface ($z = 0$), the problem is reduced to a 2D model, as shown in Section 3.1.4.2.

Thus, having the magnetic field distribution on the metal surface, power losses can be also calculated from Turowski's equation (3.113). Following the same computational methodology as for the 3D case, the temperature distribution and hottest spots are computed from 2D FE thermal analysis.

Experiments are carried out on steel tank wall plates as shown in Chapter 4, Fig. 4.4

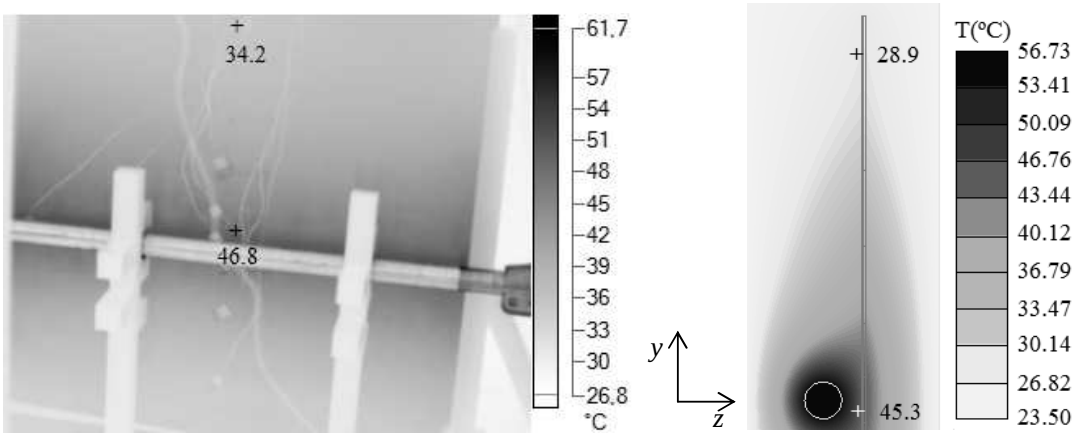

(a) Thermal IR image (b) FE thermal computation

Figure 6.21: Temperature distribution along a tank wall due to a parallel current conductor passing at a distance $a = 50\,\text{mm}$.

and Fig. 4.5. Thus, uncertain parameters for the simulation might be also determined from solving the inverse problem. Material properties for mild steel plate have been determined from MO optimization in the case of cover tests, as shown in Chapter 5. However the linerization coefficient a_p, which depends on the structure to be investigated needs to be recalculated for the tank wall plate. In addition, convective heat exchange coefficient might differ from horizontal to vertical layout. It also varies from the lower part of the plate h_{cl} (touching the floor), and the upper part of the plate h_{cu}. Parameter bounds are those shown in Table 5.1. Thus, unknown parameters are identified for the tank wall plate with one conductor passing parallel at a distance $a = 100\,\text{mm}$ carrying 2500 A. The parameter identification problem is solved by means of SO optimization parameters as described in Chaper 5.

Temperature results along the tank wall plate surface are plotted in Fig. 6.20, for the calibration current 2500 A and tested for several current values, showing good accuracy. Hottest spot temperature values are compared from measurements and tests in Table 6.5. In addition, hottest spot might be also compared with tests where the conductor is placed at a distance $a = 50\,\text{mm}$ from the tank wall. Thermal IR image is compared with computed temperature distribution in Fig. 6.21 for a 2500 A test showing good agreement.

Temperature results have been also tested in case of single-phase bushings, either in horizontal and vertical layout carrying each 1250 A, as shown in Fig. 6.22. Conductors at horizontal layout are at a distance distance $c_1 = 100\,\text{mm}$ and $c_2 = 300\,\text{mm}$ respectively from the tank wall. In the case of horizontal layout conductors are separated $2b = 200\,\text{mm}$ passing parallel to the steel plate at a distance $a = 100\,\text{mm}$. Nevertheless, temperature results show that overheating is not relevant as in the case of a single current carrying conductor, and serve also to prove the validity of the method and identified coefficients.

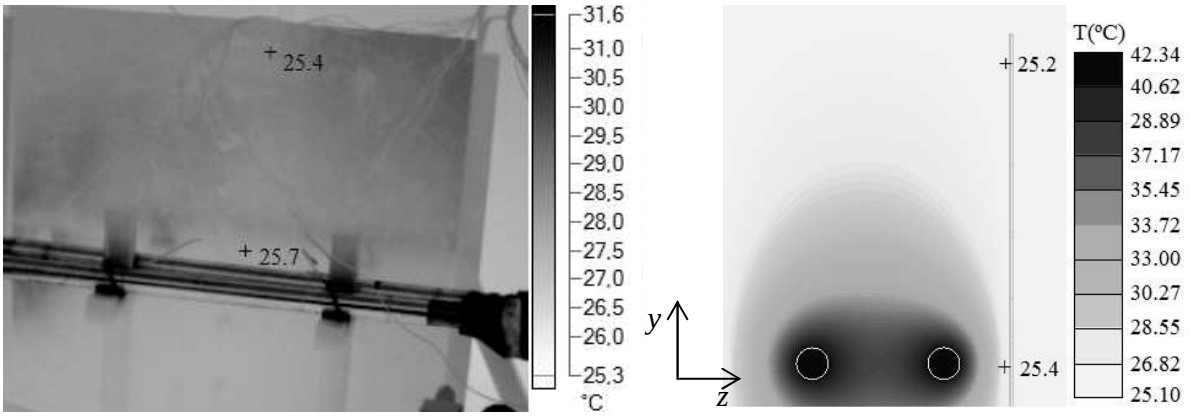

(a) Thermal IR image, horizontal layout

(b) FE thermal computation, horizontal layout

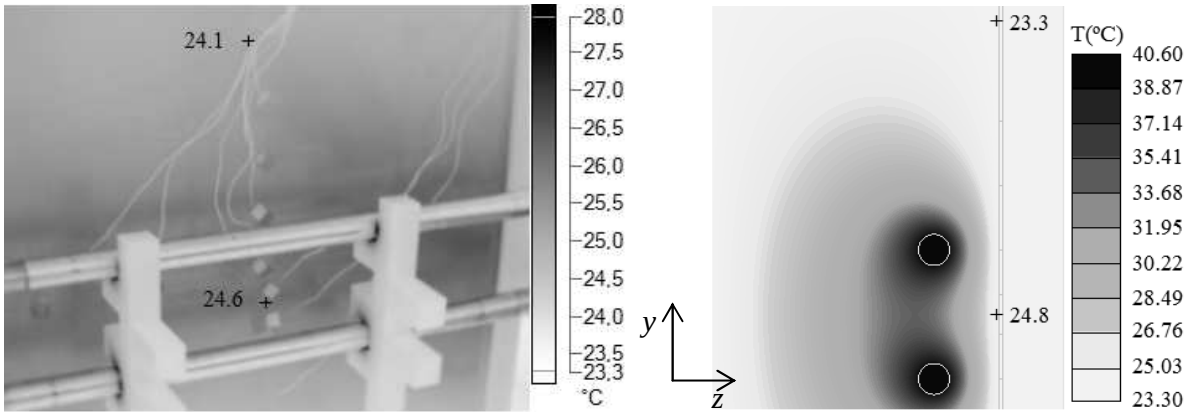

(c) Thermal IR image, vertical layout

(d) FE thermal computation, vertical layout

Figure 6.22: Temperature distribution along a tank wall due to parallel single-phase bushings carrying each 1250 A.

Chapter 7

Practical Applications

One of the main components of power transformers besides the core and the winding is the tank, and therefore its effective and reliable design is crucial. As first design approach the investigation and deep understanding of the electromagnetic and thermal phenomena occurring in the structure is essential, obtained from parametric investigation and validated with tests has has been shown through previous chapters. However, an interesting step forward is to implement the proposed the computational methodology to study real transformer models and asses the capability of the tool for being integrated it in the design process of large power transformers.

In this sense, several practical applications are presented in this chapter, which include the overheating evaluation in bushing turrets, the design of amagnetic inserts in flat transformer tank covers, and influence of tertiary stabilizing windings on the tank wall overheating due to zero-sequence flux.

7.1 Overheating Evaluation on 3D Complex Structures. Bushing Turrets

Due to the increase of rating and size of large power transformers and due to transport restrictions, new and more complex constructions of structural parts, in particular around high current bushings, are being developed. They consider the combination of different materials and screening procedures in order to minimize total losses and avoid overheating, thus requiring more accurate analysis [5].

Among 3D complex electromagnetic structures, the temperature rise due to electromagnetic induction of iron turrets surrounding low voltage bushings are reported here. The structure is undergoing both, normal and tangential field excitation, on lateral and upper surfaces respectively. However their influence can be evaluated separately and the computational methodology reported in this dissertation might be applied. Thus, stray losses are computed by applying Turowski's equation (3.87), with non-linearity correction factors and screening coefficients if needed. The magnetic field calculation,

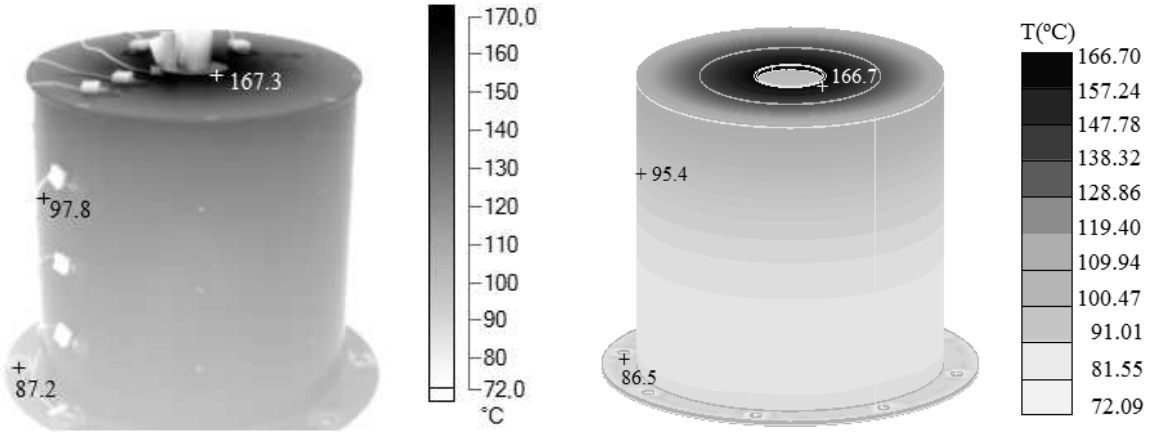

(a) Thermal IR image (b) FE thermal computation

Figure 7.1: Temperature distribution over a mild steel round bushing turret for a 2500 A test.

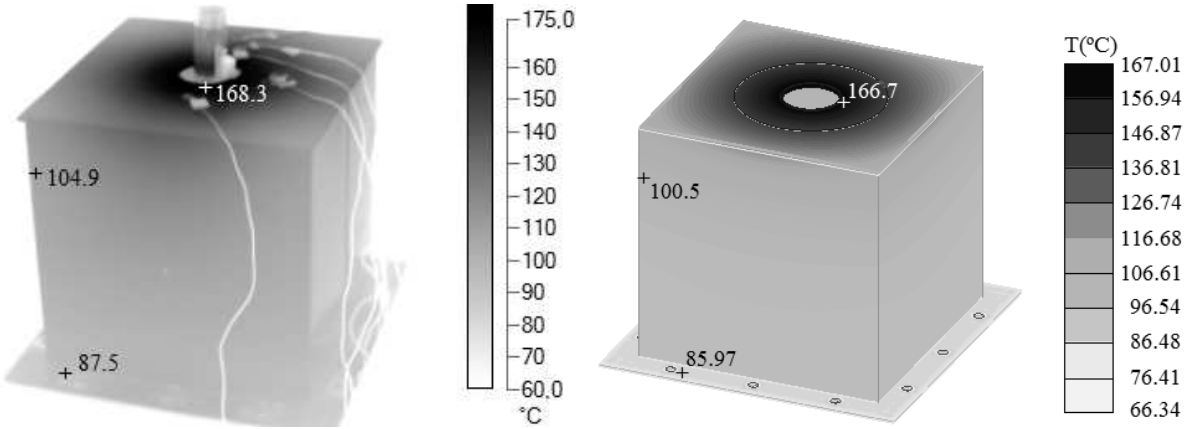

(a) Thermal IR image (b) FE thermal computation

Figure 7.2: Temperature distribution over a mild steel square bushing turret for a 2500 A test.

responsible of the losses is reported in case of tangential and normal field in Section 3.1.4.1 and Section 3.1.4.2 respectively.

Experimental tests are described in detail in Chapter 4, where round- and square-shaped bushing turrets are considered as seen in Fig. 4.6. Bushing turrets made from mild steel and stainless steel are tested and the temperature is measured over the surface at current values of 2500 A flowing through the conductor. Thermal FE analysis is then carried out applying the computational methodology and aspects described through this research, highlighting the non-linear penetration depth (3.112) aspects regarding both, the electromagnetic and thermal models. Then, measured temperature at each sensor can be compared with numerical results.

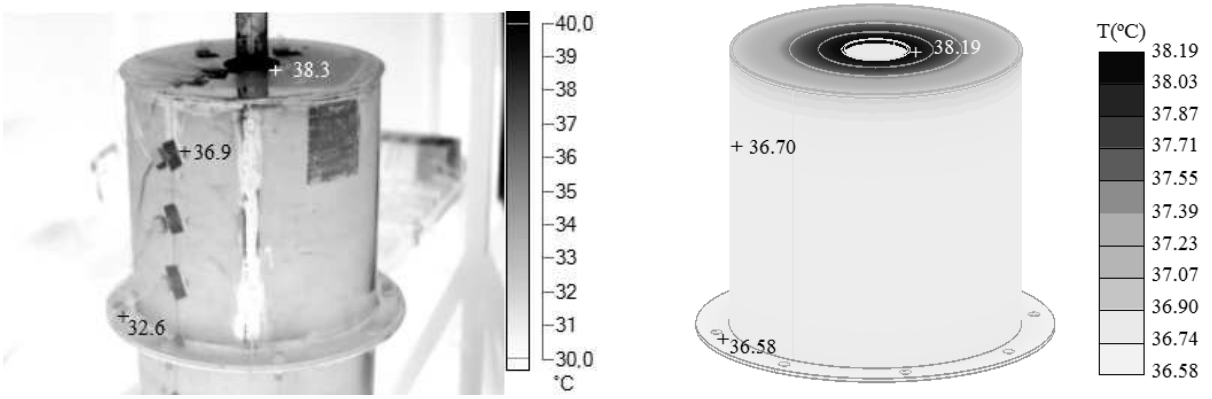

(a) Thermal IR image (b) FE thermal computation

Figure 7.3: Temperature distribution over a stainless steel round bushing turret for a 2500 A test.

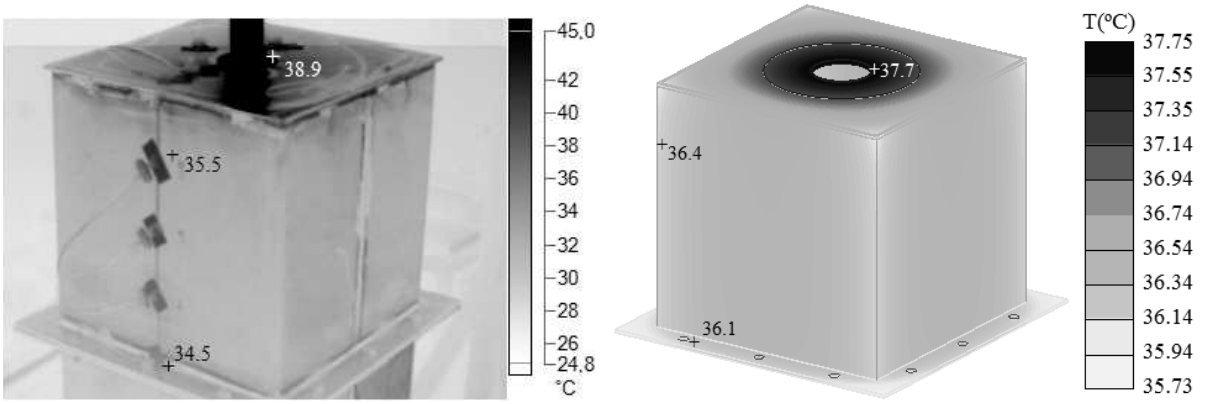

(a) Thermal IR image (b) FE thermal computation

Figure 7.4: Temperature distribution over a stainless steel square bushing turret for a 2500 A test.

The material data required for computation and boundary conditions are determined from measurements as presented in Chapter 5 for the bushing cover (upper surface), with recalculated heat exchange convective coefficients for the lateral surface in Section 6.2.4. The amagnetic material properties are also determined from tests in Section 6.2.3.

7.1.1 Results

In Fig. 7.1 and Fig. 7.2 thermal IR images from a 2500 A test on steel round and square shaped bushing turrets are compared to results obtained from FE thermal

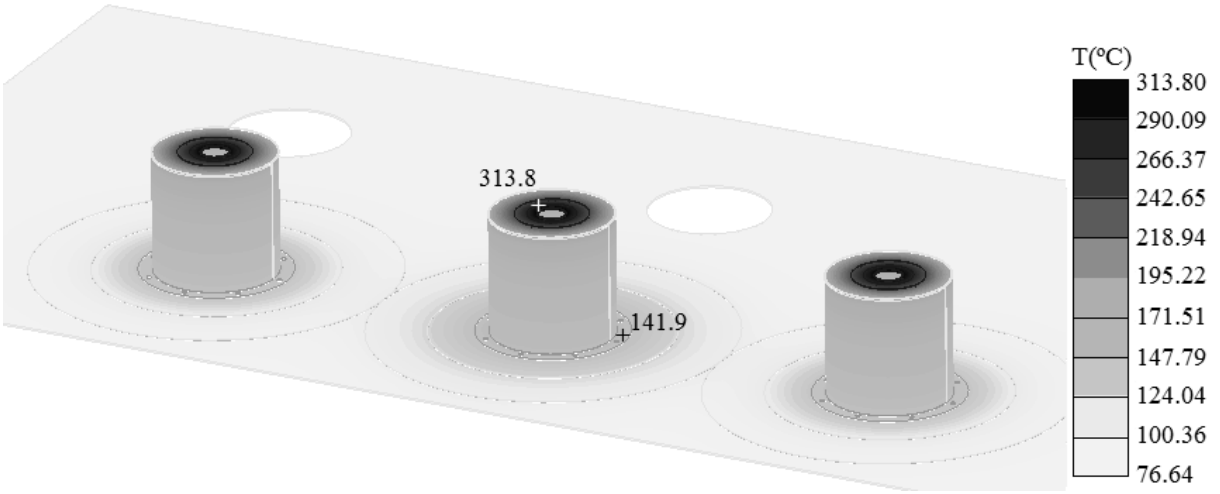

(a) Mild steel flat base and bushing turrets structure.

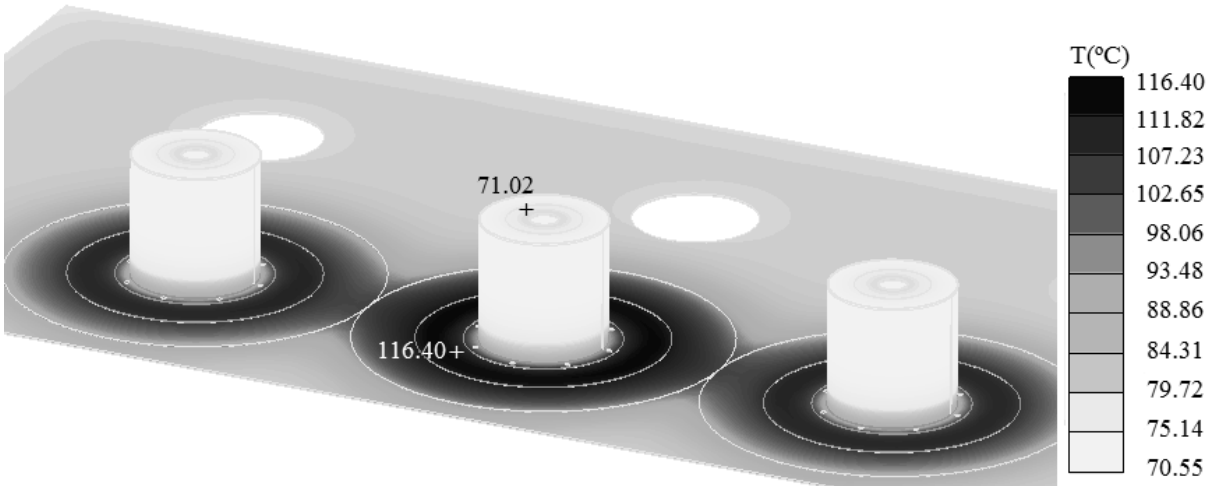

(b) Mild steel flat base combined with stainless steel bushing turrets.

Figure 7.5: Temperature distribution from 3D FE computation over a three-phase transformer cover with bushing turrets for a 5000 A test.

computation with non-linear penetration depth, showing good agreement with each other and validating thus the computational model. In Fig. 7.3 and Fig. 7.4 temperature results are compared from stainless steel bushing turrets, showing good concordance between measurements and computed values. It can be also seen that there is almost no differences between both shapes concerning the overheating.

A computation on a three-phase system with bushing turrets and flat base is also included. The transformer cover is 5 m long and 2.5 m, including bushing turrets for the LV side of 5 m and 400 mm height and separated a distance of 1.2 m between them. Holes for HV bushings are also modeled being 200 m radius, and separated a distance of 1.5 m.

The thickness of flat cover base is 6.2 mm and of bushing walls 3.8 mm. The applied current value is 5000 A. In Fig. 7.5(a) the whole structure is made from mild steel, where excessive overheating is clearly seen. Figure 7.5(b) shows the temperature distribution if the flat cover base is made from mild steel and the bushing turrets are instead made from amagnetic material. It can be seen how due to the proper combination of materials, the temperature is reduced to permitted values.

7.1.2 Contribution and conclusions

The analysis presented in Fig. 7.5 shows a drastic reduction of computation time, less than 1 minute for a coupled electromagnetic-thermal simulation, due to the introduction of the electromagnetic analytical model. The low computational effort is also due to that fact that in the FE thermal model required for the proposed methodology only the heated region needs to be modeled, providing the adequate heat exchange coefficients at boundaries. It is discretized into approximately 27000 nodes, which is a relatively small number compared to that required for a full 3D magneto-harmonic coupled with thermal FE analysis. The computational results shown represent the capability of the models for being implemented in the design stage of large power transformers.

7.2 Amagnetic Inserts on a Flat Three-phase Transformer Cover. Arrangement Decisions

In order to restraint the temperature on transformer covers, manufactures usually consider different materials such as introducing amagnetic steel on thermally hazardous areas. The main design criterion of the bushing adapters is the limit temperature rise caused by leakage field due to the high current leads, where a reference value of temperature limit of 110 °C is considered for all the transformer metallic parts [15]. However, due to the high complexity of computation and lack of reliable information manufacturers usually opt for building the transformer hazardous structural parts from stainless steel instead of mild steel. From the point of view of stray losses and reliability it is and evident best choice, but on the contrary is the higher manufacturing cost. Stainless steel is up to 4 to 5 times more expensive than mild steel and because of that, within the more a more competitive market, manufacturers are more concerned about its performance.

In this section, a practical tool to design the arrangement of amagnetic steel inserts surrounding high current leads in transformer cover plates is presented. The work presented here has been published in [130]. Future lines of work would include to implement an automated optimization process to design the leads arrangement and amagnetic insert in order to minimize material cost on one hand and power losses on the other as well as guaranteeing temperature levels withing their limits; i.e. achieving the optimum balance between the transformer cost and performance [2].

7.2.1 Computational methodology. Important issues

The 3D methodology focused on assessing heating hazard on transformer covers [81] is described in Chapter 3. The link between an analytical formulation for electromagnetic field with the finite element method for thermal field is shown in Fig. 3.1. Thus the resulting stray losses computed by means of the electromagnetic analytical formulation are introduced in the FEM thermal model as heat sources for the computation of steady state temperature distribution. The maximum value of the magnetic field intensity at the surface H_{ms} is responsible for the loss density and therefore sources for the local heating as from (3.87). Excessive hot spots appear when H_{ms} exceeds a certain limit value of $H_{ms,perm}$, permitted from the point of view of permitted temperature T_{perm}. From [15] the permissible value of the temperature in covers with convection at both sides is 140 °C corresponding with a $H_{ms,perm}$ value of 40 A/cm. Therefore, this value of $H_{ms,perm}$ will be the limit value chosen to design the amagnetic insert dimensions in the three-phase transformer tank cover for the studied case. This design criterion based on maximum permitted values of magnetic field is included into the computation methodology as seen in Fig. 7.6.

Concerning other computational aspects, it is necessary to investigate the influence of thickness d of metal plates as from (3.46). Sometimes it has no influence but in the case of stainless steel it plays a decisive role at reducing or increasing power losses as it has been discussed in Section 3.1.8. Therefore the screening coefficient ζ from (3.103) must

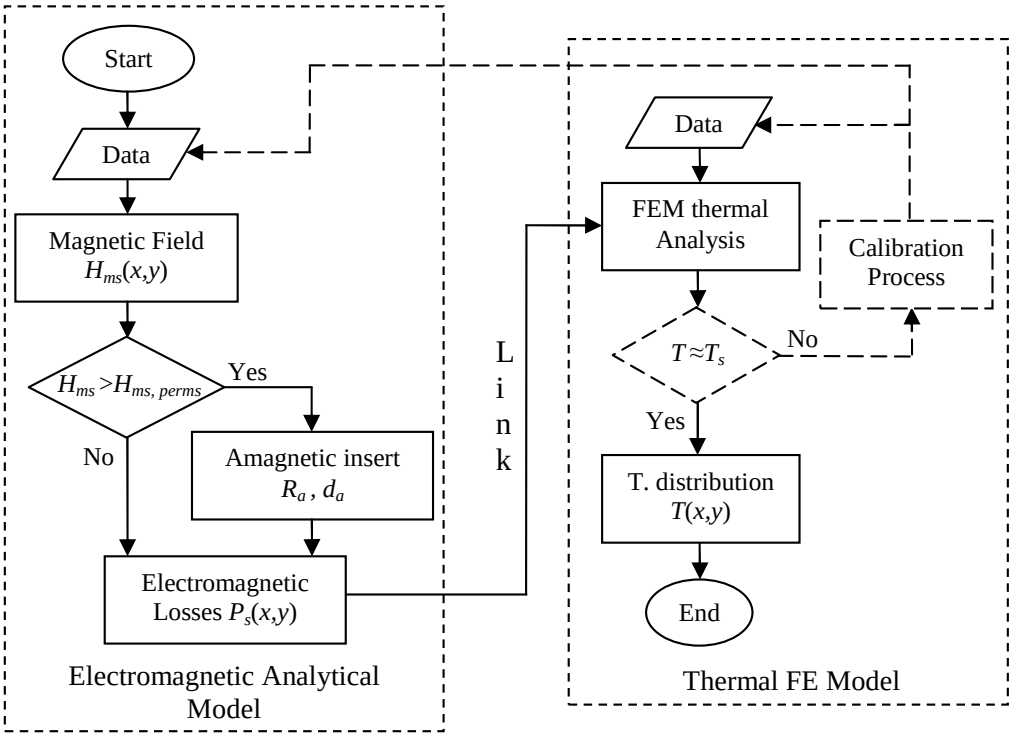

Figure 7.6: Flowchart corresponding to the 3D methodology for the electromagnetic and thermal linked models with amagnetic inserts design.

be applied to Turowski's equation as in (3.104).

The computational model is calibrated from tests with amagnetic insert as from Fig. 4.2 (right). Input parameters for test with amagnetic steel are identified and validated from Chapter 5 and Chapter 6. The input simulation parameters have been already tested for 1 conductor and single phase cover with amagnetic insert as seen from Fig. 6.18 and Fig. 6.19 respectively. Thus, once the computational methodology is validated, results from a practical application with a three-phase bushing are shown in the following sections.

7.2.2 Magnetic field and power losses results

Once the model is calibrated, the tool is used on a practical application consisting on a three-phase bushing plate to highlight its capability. The three-phase steel plate considered to model is 1.35 m width and 0.65 m length. The distance between conductors a is 0.28 m and the plate thickness d is 5 mm. In order to fulfill a wide range of high-power commercial transformers from 40 to 100 MVA a rated current value of 2 kA is chosen for the simulation in the low voltage side. The obtained computation results of electromagnetic field in A/m can be seen in Fig. 7.7, as well as the stray loss distribution in W/m^2 is

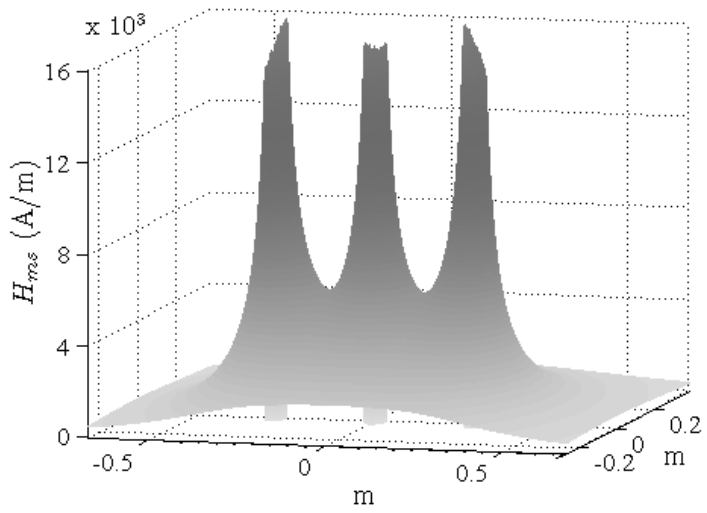

Figure 7.7: Magnetic field intensity (A/m) over a three-phase transformer cover for 2 kA current.

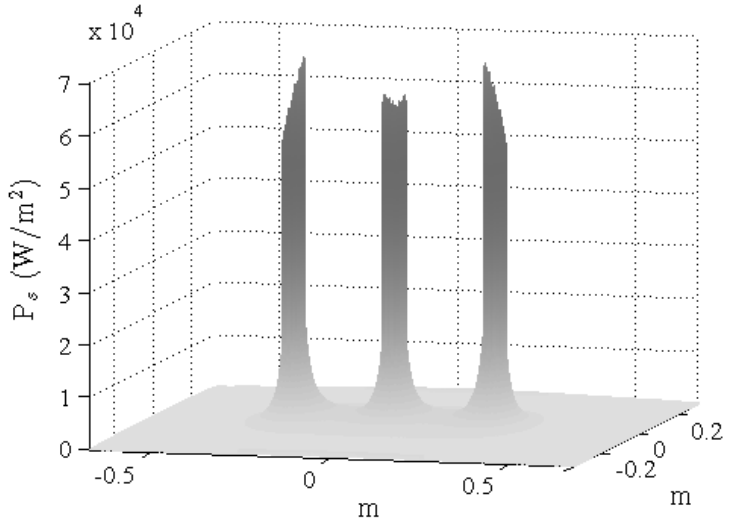

Figure 7.8: Power loss distribution (W/m^2) over a three-phase transformer cover for 2 kA current.

shown in Fig. 7.8.

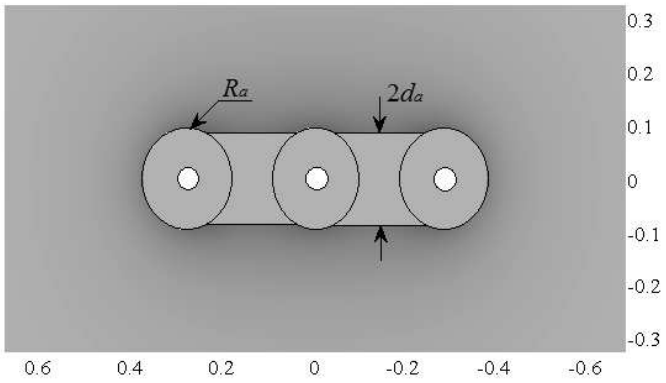

(a)

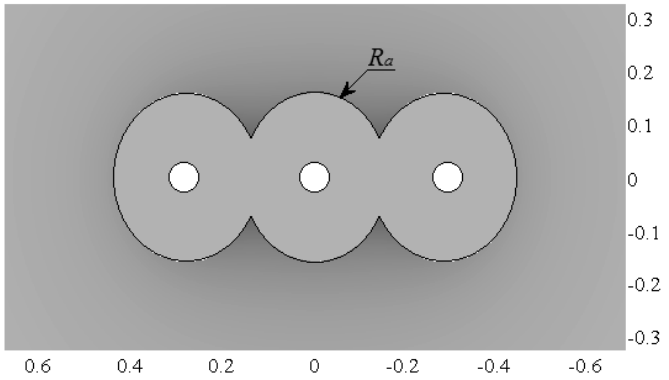

(b)

Figure 7.9: Possible choices of amagnetic inserts arrangement seen from top view of power losses distribution.

7.2.3 Amagnetic steel insert arrangement

From Fig. 7.7 it is seen how the magnetic field on the metal surface H_{ms} clearly exceeds the maximum permitted value $H_{ms,perm}$ of 4000 A/m, permitted form the point of view of maximum temperature. To eliminate possible hot spots and reduce stray losses designers use non-magnetic steel in tank covers surrounding the high current bushings [4]. Since the amagnetic steel is more expensive than magnetic mild steel, the area of the amagnetic inserts needs to be minimized. Moreover, the power industry is facing a continuous challenge to keep design and fabrication costs at a minimum, and introducing amagnetic inserts means an additional cost to the fabrication process. Therefore, the arrangement of the amagnetic inserts is the second design criteria, where complex shapes must be avoided.

For the studied case, two possibilities of amagnetic inserts are possible as seen in Fig. 7.9 from the point of view of $H_{ms,perm}$. The arrangement of amagnetic inserts is determined by the lowest area and less complicated design, being the shown in Fig. 7.9(a) the best option with dimensions $R_a = 108\,\text{mm}$ and $\text{d}_a = 105\,\text{mm}$.

From the electrical conductivity of the amagnetic steel and the relative permeability,

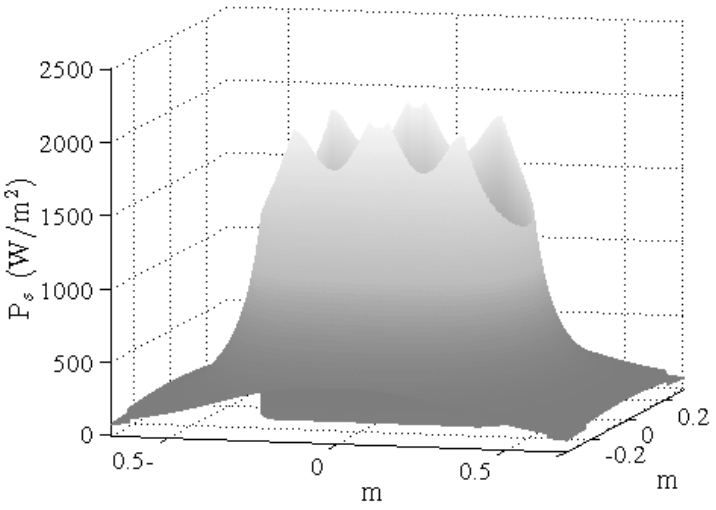

Figure 7.10: Power loss distribution (W/m^2) over a three-phase cover plate with best choice of amagnetic insert from Fig. 7.9(a) due to a 2 kA current.

the length of the electromagnetic wave λ can be calculated from (3.50) being its value 91 mm. Note that for an amagnetic steel plate of thickness d = 5 mm $< \lambda/2$, there exists an internal wave reflection which reduces power losses significantly as mentioned before. Figure 7.10 shows the stray losses distribution with best choice of amagnetic insert arrangement from Fig. 7.9(a).

7.2.4 Thermal FEM application

The implemented 3D FE models are built according to the identified parameters to carry out thermal field computation and contrast the space temperature distribution from both, the model made of mild steel, and the model with the amagnetic metal insert from Fig. 7.9(a). Numerical results from the 3D thermal computations are shown in Fig. 7.11. It can be seen from the space temperature distribution in Fig. 7.11(a) how the temperature clearly exceeds the maximum value taken as permitted T_{perm} of 140 °C [15]. It is in the model made of mild steel where the local maximum temperature reaches up to 156.3 °C. Numerical results from Fig. 7.11(b), for the model with amagnetic insert, show a significant reduction of the temperature over the entire metallic plate. Here, the local maximum temperature over the transformer cover plate reaches 42.2 °C.

7.2.5 Contribution and conclusions

The engineering too described in this section is presented as an useful to quickly design amagnetic insert arrangements. The novelty in this tool is that losses are evaluated in terms of space temperature distribution, which is easy to measure directly in any

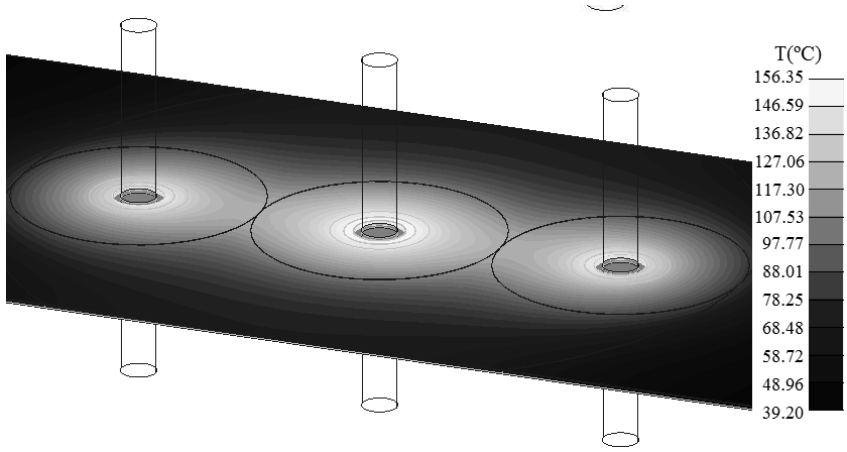

(a)

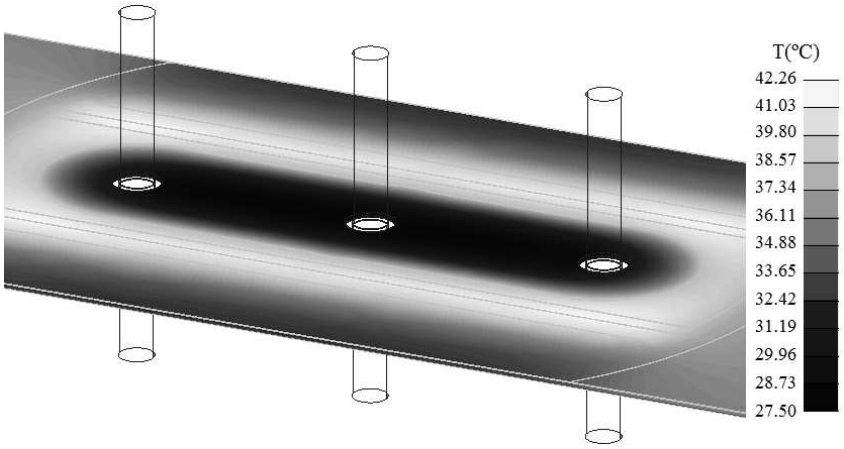

(b)

Figure 7.11: Space temperature distribution over a three-phase transformer cover for a) mild steel plate and b) plate with amagnetic insert.

structural part of a transformer by the manufacturer. 3D thermal models have been built to carry out simulations and test the capability of the tool. Thus, the temperature over a three-phase steel cover plate is computed as practical application. Overheating hazard clearly appears at commercial rated currents and amagnetic inserts are considered to reduce the stray losses and control the overheating hazard. Since amagnetic steel is rather expensive, its arrangement over the transformer cover has to be designed by minimizing its process cost. Simulation results in terms of space temperature distribution clearly prove a significant reduction of the temperature over the metallic plate when considering non-magnetic metal inserts.

7.3 Transformer Tertiary Stabilizing Winding. Overheating Hazard on Tank Walls

In the present section, the evaluation of the overheating hazard due to zero sequence flux on tank walls of power transformers is discussed taking into account the influence of the Tertiary Stabilizing Winding (TSW). Three-phase three-limb core form transformers are considered in this work, where the component of the zero sequence flux closes its path over the tank wall and cover leading to excessive temperatures. However, if a delta-connected TSW is considered, it can effectively cancel or diminish the zero sequence flux as it provides an internally closed circuit for zero sequence currents. This work has been presented in [131] and complements a previous companion paper [132] where the modeling of transformer for current calculation is discussed in cases of full single-phase load and single phase-to-ground faults with and without delta-connected TSW. Those previously calculated zero sequence currents are here the input sources for computing the zero sequence flux. The methodology presented in Chapter 3 is applied here reduced to a 2D problem, where the magnetic field distribution is computed from the Reluctance Network Method (RNM). Stay losses are then computed by applying Turowski's equation (3.87). In addition, the problem is solved by using the Finite Element Method (FEM). Both computational methodologies are described in the next paragraphs and results are compared.

7.3.1 Background

Zero sequence flux appears in a transformer without neutral conductor when in the core emerge harmonics of third order, or at asymmetric load in which zero point is loaded. Extreme cases of such asymmetric load are full single-phase load or single phase-to-ground fault. At the same time certain unbalanced states may remain undetected by the transformer protection, subjecting thus the transformer to prolonged operation with significant zero sequence flux. In the vast majority of three-phase transformers core form construction is used. A small or medium rated transformer is usually of three-limb core type. The primary and secondary windings of each phase are symmetrically arranged around core legs. Under balanced conditions, the currents in three phases are equal in magnitude, with shift angles of 120 ° where the resultant zero sequence flux is negligible. However, if some unbalance occurs in the terminal voltage the three-phase fluxes will not be cancelled and it has to return through a path out of the transformer magnetic core [133]. In the case of a three-phase transformer of three-limb core type it means that the only way of making a closed circuit for the zero sequence flux to return is via free-space or through the tank wall, which for power transformers is usually made of mild steel [134]. The classical solution adopted to avoid the presence of zero sequence flux is to include a delta-connected Tertiary Stabilizing Winding (TSW) on the transformer [135]. The delta-connected winding acts as a magnetic screen which does not transmit almost any equiphase flux inside such closed winding. It means that

with this winding almost none of equiphase fluxes are coupled. One of the dangerous consequences of the presence of zero sequence flux is the overheating hazard on structural parts of the transformer. Tank walls and cover may be heated to an unacceptable temperature due to additional stray losses. Although the performance of transformers under unbalanced conditions is well know, and the classical adopted solution to consider a delta winding or add a tertiary delta winding is assumed, the real impact of the zero sequence flux is scarcely discussed and relevant information is difficult to find [133].

The modeling of three-winding transformers under asymmetric conditions for determining the TSW apparent power is presented in [132]. The study presented here shows methods of estimating the zero sequence flux arising under these unbalanced conditions as well as assessing the overheating on structural parts of transformers with or without delta-connected TSW. For such purpose both, the RNM2D_0 software based on the Reluctance Network Method (RNM) [136] and the two-dimensional Finite Element Method (2D FEM) are applied [114]. Their results are then introduced in a FE thermal model in order to compute the temperature rise on the transformer tank. Thus, the influence of having a delta-connected TSW can be evaluated. A practical application is presented in the next sections, and results from both computational methods are compared for their validation.

7.3.2 Zero-sequence flux and stray losses with RNM

Authors presented in [136] a rapid and easy-to-use tool RNM2D_0, based on the RNM to calculate magnetic field and evaluate the stray losses hazard effects due zero sequence flux in transformers. The equivalent RNM is one of the simplest and fastest methods of modelling and computation [137]. The three-dimensional RNM (RNM-3D) was proposed to compute the leakage magnetic field in three phase transformers by Professor J. Turowski in 1969 [32], [138]. Such modelling method is extremely competitive in market time compared with the widely used FEM [120]. Theory and method of modelling and calculation of losses due to the electromagnetic field are based on Maxwell's equations and Poynting's vector theory. Full solution of Maxwell's equations with non-linear magnetic permeability $\mu(H)$ and non-sinusoidal excitation is too complicated to be used in regular engineering computation. However, the RNM permits to model and solve magnetic circuits, since it offers an easier implementation based on Ohm's Law for magnetic circuits (7.1), magnetic Kirchhoff's Laws for nodes (7.2) and for branches (7.3) [139].

$$\mathcal{F}_i = \Re_i \Phi_i \tag{7.1}$$

$$\sum_{i=1}^{n} \Phi_i = 0 \tag{7.2}$$

$$\sum_{k=1}^{m} \mathcal{F}_k = 0 \tag{7.3}$$

where i are the branches and k the nodes of the equivalent network, $\mathcal{F}$ is the magnetomotive force and Φ the magnetic flux through the magnetic element. The basic reluctances $\Re_i$, for dielectric regions, are calculated using (7.4), where s_i and l_i are the cross section and length of the mesh element respectively.

$$\Re_i = \frac{l_i}{\mu_o s_i} \tag{7.4}$$

$$\Re_i = (\Re_{re} + j\Re_{im}) \cdot \frac{l_i}{\mathrm{d}} \tag{7.5}$$

where $\Re_{re} = a_1\sqrt{\omega\sigma/\mu_s}$ and $\Re_{im} = a_2\sqrt{\omega\sigma/\mu_s}$. Meanwhile, solid metal structural elements (tank wall, cover, beams, etc.) need to be modeled by complex reluctances due to reaction eddy currents, non linear permeability and skin effect. These reluctances are calculated by means of (7.5), where d is the depth of the model, μ_s is the surface magnetic permeability, ω is the angular frequency, σ the electric conductivity and a_1 and a_2 are linearization coefficients for solid steel available in [15].

The magnetomotive forces $\mathcal{F}$ of the windings are calculated applying equation (7.6), assuming the entire ampere-turns at High Voltage (HV) and Low Voltage (LV) windings are concentrated in the air-gap space.

$$\mathcal{F} = \sqrt{2}I_{HV}N_{HV} = \sqrt{2}I_{LV}N_{LV} \tag{7.6}$$

where $I_{HV}N_{HV}$ and $I_{LV}N_{LV}$ are the ampere-turns at HV and LV windings respectively.

For the purpose of this paper, stray losses due to the zero sequence flux in conducting steel plates are calculated applying the Turowski's equation (3.87) and applying the computational methodology as described in Chapter 3 with reliable information on material properties, linerization coefficients and boundary conditions from Chapter 5.

7.3.3 Zero-sequence flux and stray losses with FEM

Even though the transformer is strictly speaking a 3D geometry, the 2D solution can be considered as a good first approach in many cases. Therefore, considering the current density vector $\mathbf{J}$ is in the $z-$direction, the 2D diffusion problem can be formulated in terms of the magnetic vector potential $\mathbf{A}$ by the system of equations [140]

$$\frac{1}{\mu}\frac{\partial^2\mathbf{A}}{\partial x^2} + \frac{1}{\mu}\frac{\partial^2\mathbf{A}}{\partial y^2} = -\mathbf{J_0} + j\omega\sigma\mathbf{A} \tag{7.7}$$

$$\mathbf{J} = -\mathbf{J_0} + j\omega\sigma\mathbf{A} \tag{7.8}$$

Model	Winding	I_U(A)	I_V(A)	I_W(A)	I_0(A)
With TSW	HV	84.74	−29.99	−30.69	8.02
	LV	−1033.87	0	0	−344.62
	TSW	239.28	239.28	239.28	239.28
Without TSW	HV	103.51	−10.82	−11.51	27.06
	LV	−1029.69	0	0	−343.23

Table 7.1: Winding currents from single-phase load condition on the LV side.

where $\mathbf{J_0}$ is the source current. The quasi-poisson equation (7.7) defines the electromagnetic field problem for the linear or the non linear field problem, since reluctivity can either be constant or function of A_z.

Eddy currents are calculated in each element from the magnetic vector potential $\mathbf{A}$ in A/m^2 as

$$\mathbf{J_{eddy}} = -j\omega\sigma\mathbf{A} \tag{7.9}$$

Stray losses are then calculated from the eddy currents as Joule effect

$$P_\sigma = \iint_s \frac{1}{\sigma} J_{eddy}^2 \,\mathrm{d}x\,\mathrm{d}y \tag{7.10}$$

where s is the area of the evaluated region. In order to study the zero sequence flux in tank walls of three-limb core form transformers, which are usually made of mild steel the skin depth penetration δ (3.49), more specifically its non-linear form given in δ_{nl} (3.112), must be taken into account. For mild steel at 50 Hz, the skin depth is approximately equal to 1 mm. Being so relatively thin, it must be taken into account as nearly all the leakage flux produced by the windings, flows through this very small skin depth in the tank wall [141].

7.3.4 Transformer model

For the computation a 45 MVA YNyn0 (d1) transformer of 224.25 kV / 24.9 kV / 13.8 kV is considered. The High Voltage (HV) and Low Voltage (LV) windings, are both Wye connected with neutral point accessible. The HV winding is connected to the local grid, while the LV is connected to the consumer load. It has a delta-connected Tertiary Stabilizing Winding (TSW), not connected to any load, with the purpose to allow the flow of the zero sequence current during fault conditions. Shunts were also considered in the simulation.

The selected transformer is modeled in order to compute the zero sequence flux and its consequences in terms of the overheating hazard in tank walls. The modeling of

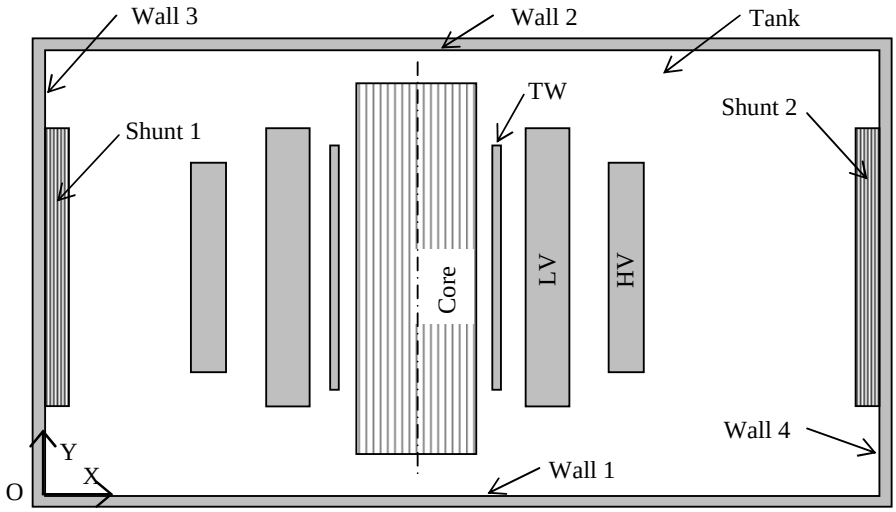

Figure 7.12: Modeled transformer geometry for the zero-sequence flux and tank walls overheating computation.

three-winding transformers and winding current calculation in the case of asymmetrical loads are described in [132]. Thus, a single-phase load is connected at the secondary side, and the zero sequence currents are calculated [142], being those currents the input field sources. The calculated unbalanced currents for each phase (U, V and W) and zero sequence currents I_0 are shown in Table 7.1. Then, the zero sequence flux is calculated for the considered unbalanced conditions. It is done with the two proposed computational methods RNM and FEM described in the previous sections, which permits to validate the results. On the other hand, the computation of temperature due to zero sequence flux is performed using the FEM as described in Section 3.2. Note that having the zero-sequence currents as input to the magnetic and thermal studies a one-phase model is assumed to be representative for the zero sequence flux computation. Figure 7.12 shows the transformer geometry to be modeled. Since the purpose of the practical application is to find reasons to justify the inclusion of the TSW on Yy-connected three-limb transformers, the analysis is performed with and without delta-connected TSW.

7.3.5 Magnetic field and power losses

In this section the magnetic field and power losses arising in the transformer tank walls under unbalanced load are calculated from the two computational methodologies proposed (RNM and FEM). Tank Wall 4 is the closest wall to the windings as shown in Fig. 7.12 and therefore the wall withstanding the higher overheating hazard. In Fig. 7.13(a) the magnetic field strength H_{ms} in A/m along the inner surface of tank Wall 4 computed from RNM is compared with the results obtained from FEM computation. Also there, the magnetic fields computed with and without TSW are compared. It can be seen how the magnetic field significantly reduces its maximum value with the

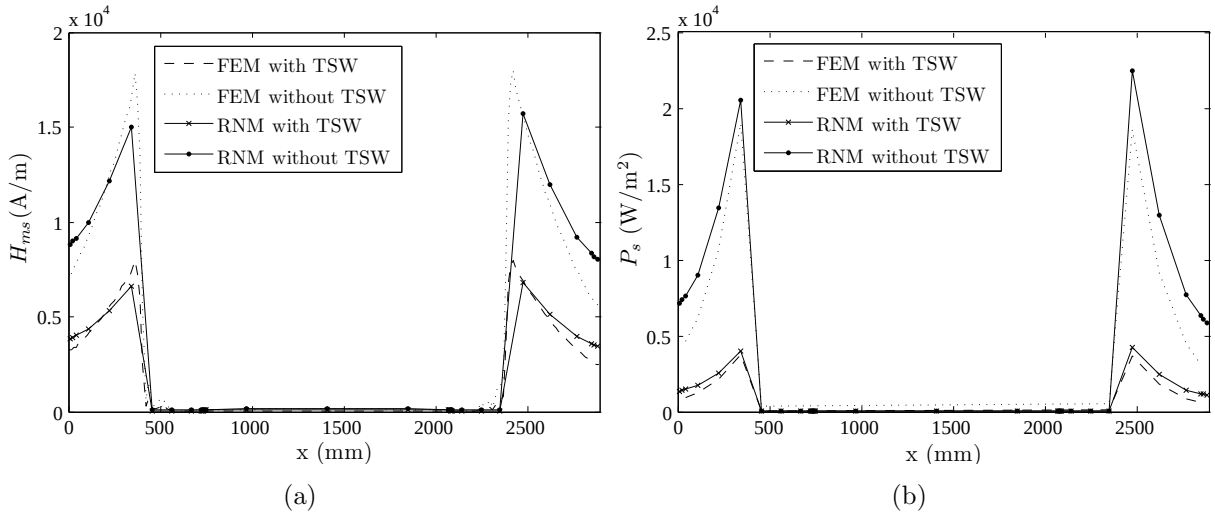

Figure 7.13: Electromagnetic analysis due to zero-sequence flux with and without TSW on a vertical tank Wall 4 from FEM and RNM a) Magnetic field distribution on the metal surface and b) Power loss density.

	Model with TSW	Model without TSW
RNM	1231 Watts	6507 Watts
FEM	1082 Watts	5503 Watts

Table 7.2: Total power losses on tank Wall 4 due to zero-sequence flux.

actuation of the TSW. A detail of the magnetic field strength penetration on tank wall without delta-connected TSW is shown in Fig. 7.14, obtained using the FEM commercial software package Flux2D [114]. It can be seen how the magnetic field concentrates on the penetration depth region according to δ (3.49). To account for this phenomenon, the size of the finite elements in the mesh is a key question to accurately compute the field and the stray losses. The small thickness of the tank wall compared with its other dimensions leads to a great number of elements, and therefore numerical memory problems arise. In Fig. 7.13(b) stray losses distribution in the tank wall due to the zero sequence flux computed from RNM are plotted along Wall 4. It is compared with the results computed with FEM. Also in Fig. 7.13(b), the stray losses distribution with and without actuation of TSW are compared. Total stray losses on tank Wall 4 are collected in Table 7.2 for the two computational methods, computed on a model of 566 mm depth, which is the core diameter. Note that the presence of TSW greatly influences the magnetic field and stray losses in the transformer tank walls, as it provides an internally closed circuit for zero sequence currents. Therefore, above results prove the effectiveness of TSWs to cancel or diminish the zero sequence flux.

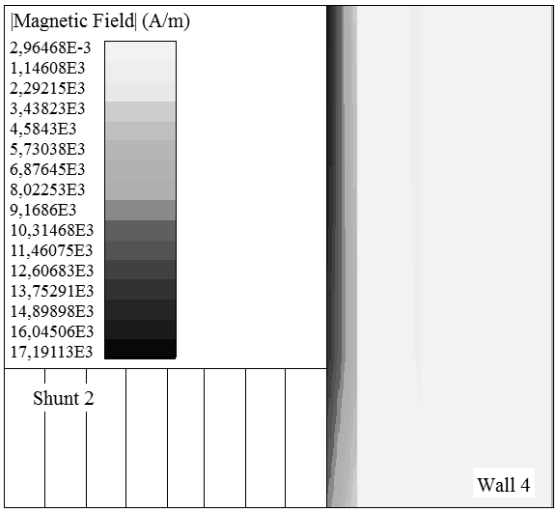

Figure 7.14: Zoom-in of the magnetic field distribution on vertical tank wall computed from FEM.

7.3.6 Tank wall overheating

The maximum value of the magnetic field strength at the surface H_{ms} is responsible for the loss density and therefore sources for the local heating. As already mentioned, prolonged operation of a transformer with significant zero sequence flux can result in potentially harmful heating of metallic structural parts external to the core. To compute the tank wall overheating, the power losses are computed by means of Turowski's equation (3.87) from RNM results and then they are introduced in the thermal FE model. This methodology has been already applied by the authors in transformer covers and tank walls with accuracy, as from the knowledge of the input parameters determined from Chapter 5.

On the other hand, Joule losses (7.10) are computed from FEM and used as heat sources in the thermal FEM model. The ambient temperature is kept at 21 °C. Resultant temperature distribution from the two proposed computational methodologies (RNM and FEM) along tank Wall 4 are compared in Fig. 7.15. It is proven that the computed temperature distribution from both methodologies show good agreement with each other.

It is important to highlight the required effort to implement the electromagnetic FEM model in order to achieve accurate results. Thus, if the skin depth penetration is not taken into account in the model mesh, the computed field, and in consequence, the computed stray loss distribution and temperature values would be far from reality. Such effort is not needed when the temperature is computed from the RNM results. Stray losses computed from the RNM are introduced in the skin depth penetration region in the thermal model, given such accurate results when computing the steady state temperature as those seen in Fig. 7.15.

Hot spots appear when H_{ms} exceeds a certain limit value of $H_{ms,perm}$, permitted

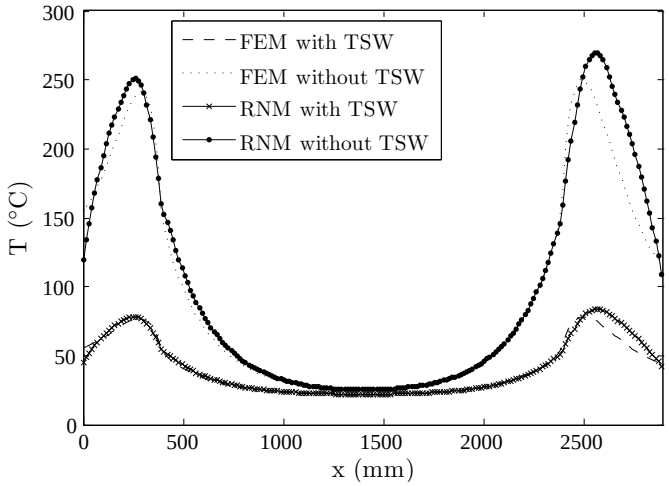

Figure 7.15: Temperature distribution over tank Wall 4 due to the zero-sequence flux with and without TSW actuation.

	Model with TSW	Model without TSW
RNM	83.86 °C	270.03 °C
FEM (1−phase model)	78.43 °C	249.91 °C
FEM (3−phase model)	69.97 °C	255.56 °C

Table 7.3: Hottest spot temperature on tank Wall 4 due to zero-sequence flux for each of the considered computational models.

from the point of view of permitted temperature T_{perm}. From [139] and [15] the permissible value of the temperature in tank walls with convection at both sides is 110 °C corresponding with a $H_{ms,perm}$ value of 6000 A/m, which is clearly exceeded in the model without actuation of the TSW, as seen from Fig. 7.13(a). In the studied transformer, due to the presence of shunts a remarkable non-uniformity of power loss distribution occurs and heat flows out from hot to colder parts. This fact would increase the permissible value of magnetic field, as seen for the model with TSW.

Figure 7.16(a) shows the space temperature distribution from FEM computation with and without actuation of the TSW. It can be seen how the temperature clearly exceeds the maximum value taken as permitted T_{perm} of 110 °C [32] without TSW in Fig 7.16(b). There, the temperature reaches a maximum of 249.91 °C. The temperature computed with the TSW is reduced to 78.43 °C, as seen in Fig. 7.16(a) which is within the maximum permitted values.

Figure 7.17 shows the space temperature distribution for a three-phase model of the same transformer. The input currents in this model are the three-phase unbalanced currents resulting from single-phase load condition shown in Table 7.1. The resulting temperature distribution pattern is compared with the representative one-phase model

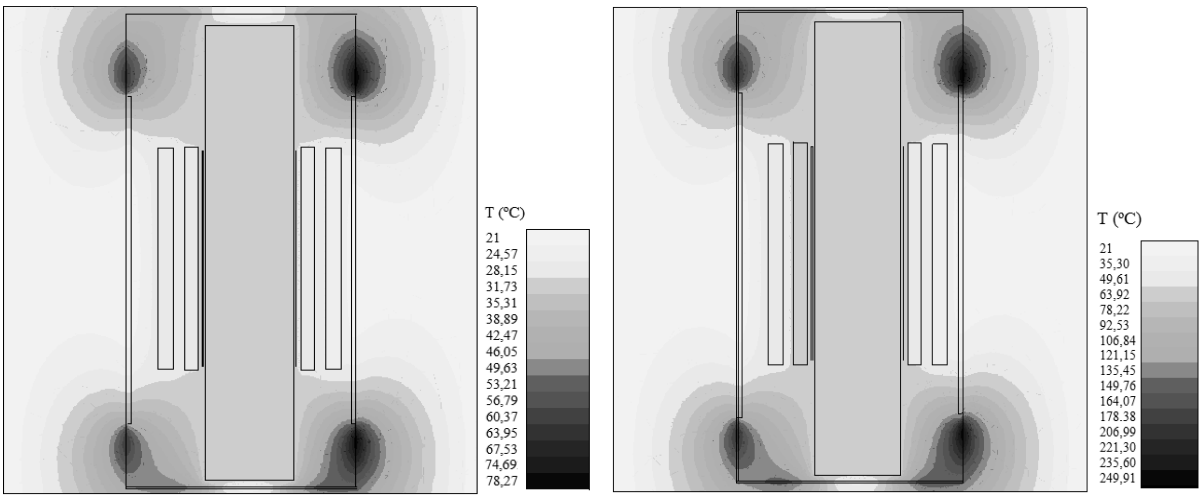

(a) (b)

Figure 7.16: Temperature distribution due to zero-sequence flux from FEM computation a) with connected TSW and b) without TSW.

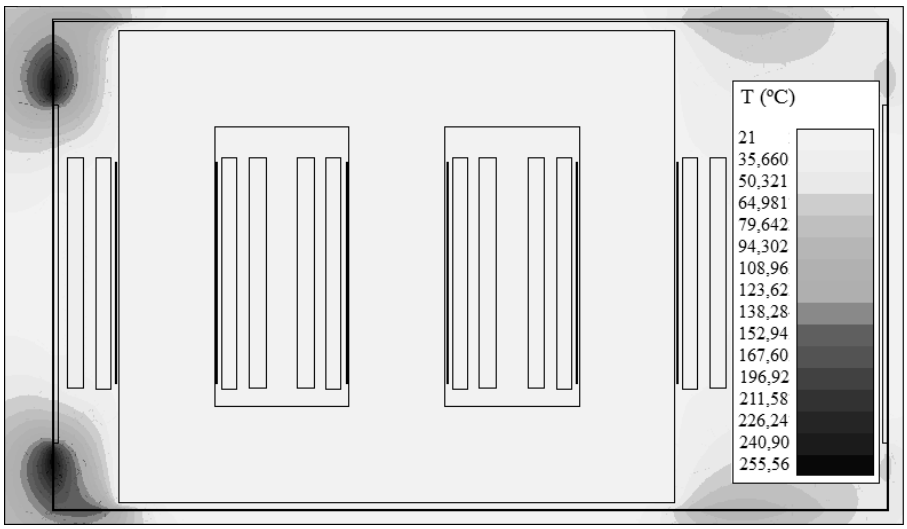

Figure 7.17: Temperature distribution due to zero-sequence flux without connected TSW from FEM computation, three-phase model.

for zero sequence currents analysis. Also, results show good agreement with each other, validating therefore the one-phase model with zero sequence currents as data input. Hottest spot temperature results are compared in Table 7.3 for RNM and the one-phase and three-phase FE models, showing good concordance with each other. Figures 7.16(a) to 7.17 are obtained using the FEM commercial software package Flux2D [114].

7.3.7 Contribution and conclusions

The zero sequence flux and its consequences of overheating hazard in a three-limb core form power transformer have been investigated. Unbalanced faults and load conditions in Yy-connected transformers might result in significant zero sequence flux, closing its path over the tank wall. However, if a delta-connected TSW is considered, it can effectively cancel or diminish the zero sequence flux as it provides an internally closed circuit for zero sequence currents.

In the study presented here zero sequence flux and stray losses are evaluated under single-phase load condition, applying both RNM and FEM methodologies, with and without TSW. The overheating on the transformer structural parts is calculated by means of steady state FEM thermal computations.

Results from the applied methodologies are compared showing good agreement in terms of magnetic field, as well as power losses and temperature distribution. However, the RNM method has been validated as a simpler tool achieving accurate results with less computational effort.

From results of the study case without actuation of the TSW, one can highlight that stray losses values generated on the tank wall and the hottest spot temperatures are of great magnitude, heating to unacceptable values the transformer tank. On the other hand, results considering a delta-connected TSW show that zero sequence flux circulating on the tank under unbalanced conditions is much lowered, and therefore the hottest spot temperature decreases to permitted values.

Chapter 8

Conclusions and Future Work

A 3D methodology has been proposed as a practical tool to evaluate overheating hazard on transformer structural parts taking into account electromagnetic skin depth penetration. Stray losses are computed by means of an electromagnetic analytical approach based on Poynting's Vector. A thermal FE analysis, where calculated losses are introduced as heat sources, computes the space temperature distribution. The presented computational methodology has been applied to several study cases, where the main contributions and conclusions are given in the following sections, including also future lines of research.

8.1 Contribution and Conclusions

Computational Methodology

This research work pays special attention to the particular case of transformer cover plates being more representative. Then the computational methodology is applied to tank walls and other structural parts.

For the computation of the temperature on transformer covers, there arises the need to develop accurate and reliable methods to characterize the induced thermal field taking into account the non-linear magnetic material characteristic.

A non-linear penetration depth magneto-thermal model and its physical aspects are rigorously described and used for the magnetic field computation providing thus more insight of the problem performance when taking into account saturation.

The described model allows to analyze the electromagnetic behavior in detail from weak to strong fields over steel transformer cover plates.

Particularly, the novelty of the model stressed in this dissertation lies in that it clearly defines the non-linear penetration depth of electromagnetic field inside metal, which is crucial in the FE thermal model to set the volume regions where stray losses are introduced as heat sources.

Temperature Measurements

In order to evaluate the overheating hazard due to high current leads an experimental work is described. Several tests are carried out, where steel plates used in transformer structural parts are heated by electromagnetic induction. The temperature is measured over metal surface by means of several sensors, and also by means of thermal imaging.

Tangential and normal field excitation are applied to the steel plates, i.e. the case of transformer cover plate and the tank wall.

Several design parameters are taken into account as e.g. number of conductors and distance between them, distance to the tank wall, amagnetic inserts, or the plate thickness.

Temperature measurements serve on one hand, to validate the temperature results, but on the other hand to calibrate the numerical models.

Calibration Process

A calibration process of computational models is highlighted in the methodology proposed in this dissertation. This process ensures the reliability of results by identifying material properties and boundary condition data which might be inaccurate as they are usually taken from characteristic sheets or from the literature. The calibration process also avoids uncertainties due to that the numerical results also depend on the kind of mathematical solver used for the computation. Thus, a parameter identification technique is described based on multiobjective optimization algorithms, where sensitivity to measurement error is taken into account.

The analytical-numerical approach does provide models with low computational effort and runtime so that the optimization process is successfully implemented.

A set of Pareto-optimal solutions is obtained with Goal Attainment Method (GATT) and Non-dominated Sorting Genetic Algorithm (NSGA-II) for the sake of comparison. Results from GATT and NSGA-II are compared showing good agreement along the tradeoff surface.

The solution from SO optimization is also compared to MO solution stressing the consistency of results, as SO optimization represents a particular solution from the front.

From the MO optimization can be easily obtained the set of parameters chosen for computation according to desired criteria on accuracy and sensitivity to measurement error. The parameter identification taking into account sensitivity to measurement error yields a significant improvement on the accuracy of obtained results.

Experimental Validation

The validation of the computational methodology focus firstly on transformer covers, where induced heating is due to tangential field excitation. Once the identification of the adequate input parameters is done, the presented methodology is applicable to any load condition and any number of conductors.

Temperature results computed from non-linear penetration depth model are compared with measurements for several current values, for one current carrying conductor and

single phase currents according to the performed tests. Good agreement between simulation results and experiments has been achieved, which demonstrate the crucial influence of the non-linear penetration depth on the temperature computation.

The results are validated experimentally by comparing 3D numerical results with measurements from thermal images. It confirms that the novelty of the present dissertation of computing the temperature to localize the hot spots on transformer covers represents one step ahead compared with those proposals existing in the literature, where results are available only in terms of power losses.

Moreover, the accuracy on the temperature distribution for the wide range studied cases indirectly validates the power loss computation.

The results illustrate how overheating clearly appears at commercial rated currents in single-phase and three-phase transformer flat tank cover plates.

Amagnetic Inserts

Means of preventing overheating hazard on transformer tank covers are evaluated, such considering amagnetic inserts in the metal plates, where the influence of metal thickness must be taken into account and screening coefficients must be introduced in the computational methodology.

The calibration process has been successfully implemented to identify unknown material properties. In particular, stainless steel has been found to be slightly magnetic. Model-calculated values are compared with measurements showing that good agreement is achieved for one conductor and single-phase currents through the cover plate.

A practical tool for the design of amagnetic inserts in three-phase flat transformer covers is also presented to be included into the computational methodology, so that cost-effective designs might be achieved.

Tank wall

The proposed 3D methodology is extended to the case of tank wall where the problem might be solved by means of 2D models. FE thermal simulations are compared with measurements validating the obtained results at one current carrying conductor and single-phase currents.

It has been proven that the overheating due to normal field excitation is not as hazardous as the overheating due to tangential field at tested current values.

A practical application is presented, where the tank wall overheating due to the presence of zero-sequence flux is evaluated. The influence of having connected a Tertiary Stabilizing Winding (TSW) is also taken into account in three-phase three-column transformers. Results show that overheating due to zero-sequence flux clearly arises if no TSW is connected.

Complex 3D Structures

The proposed computational methodology is applied to complex 3D structures such are e.g. bushing turrets. Measurements are compared with numerical results, for round and square structure shapes and different materials showing good agreement with each other.

A three-phase system with bushing turrets and flat base is included, considering various combinations of mild steel with stainless steel.

It represents the capability of the models for being implemented in the design stage of large power transformers, with drastic reduction of computation time due to the introduction of the electromagnetic analytical model.

8.2 Future Work

One of the main components of power transformers besides the core and the winding is the tank and therefore its effective and reliable design is crucial. The work presented in this dissertation represents a significant contribution in this area, however it must be continued. Thus, future lines of research would include:

- Further investigation on electromagnetic screening coefficients and screening effectiveness. Thickness of metal plates and screens or double-layer walls combining different materials, e.g. including copper screen, and their experimental testing must be considered.
- Development of models including several configurations of conductors arrangement and phase angles, creating complex problems which should be solved as rapidly as possible.
- Testing different cooling conditions such as oil or forced air convection.
- Testing the implemented models and the proposed computational methodology in real transformers, where the influence of several sources of field might be present.
- Implementation of cost-effective and optimum shape design of structural components. It requires the application of optimization algorithms taking into account design and geometric parameters and possibly a cost function. Including e.g. to automate the design of amagnetic inserts, presented in Chapter 7, considering maximum permitted temperature and total loss values together with material cost.

As first design approach the deep knowledge and understanding of the phenomena occurring in the structure is essential, obtained from parametric investigation and validated with tests. However, this research must be extended in several directions to guarantee the complete development of the presented computational methodology and tools.

Appendix A

Field Calculation

A.1 Biot Savart Law applied to infinite current-carrying conductor

In calculating the magnetic fields due to electric currents, it is sometimes easier to use Biot-Savart's law, which allows to calculate the magnetic field near a long straight current-carrying wire located along the z-axis with current moving in the positive z-direction. Considering a point (x, y) at a distance D from a current element, as seen from Fig. A.1, the magnetic field is can be calculated from A.1

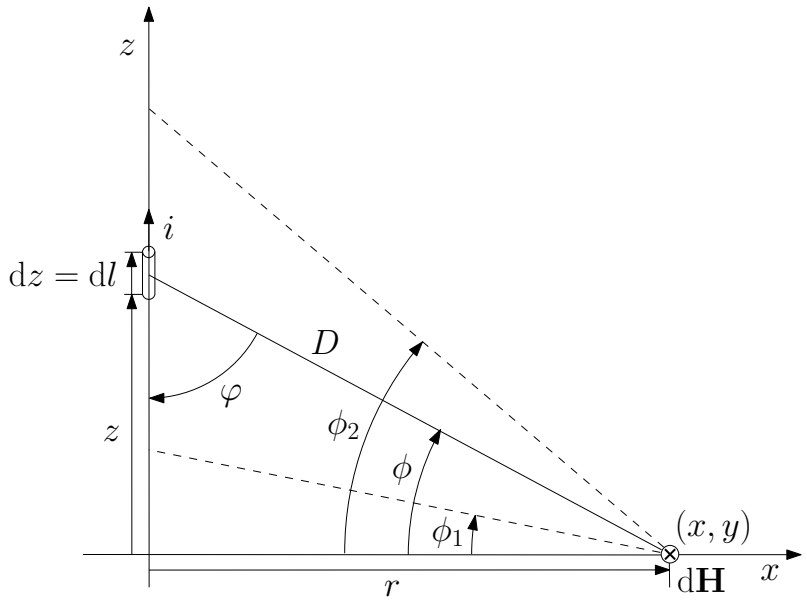

Figure A.1: Biot-Savart law applied to calculate the magnetic field due to an infinite current-carrying conductor.

$$\begin{aligned} \mathrm{d}\mathbf{H} &= \frac{1}{4\pi}\frac{i\,\mathrm{d}\mathbf{l}\times\mathbf{u}_r}{D^2}\sin\varphi \\ &= \frac{1}{4\pi}\frac{i\,\mathrm{d}l}{D^2}\cos\phi\,\mathbf{u}_\theta \end{aligned} \tag{A.1}$$

where $\mathrm{d}l$ is an element of length along the path taken by the current i and r is the position vector of the point at which $\mathbf{H}$ is to be calculated and $\mathbf{u}_r$ and $\mathbf{u}_\theta$ are the unit vectors of the cylindrical coordinates of the considered point (x, y). Thus, equation A.1 can be solved for the magnetic field at any space-point due to a long straight current-carrying wire. Having from A.1 that

$$\begin{aligned} z &= r\tan\phi \\ \frac{\mathrm{d}z}{\mathrm{d}\phi} &= \frac{r}{\cos^2\phi} = \frac{r}{r^2/D^2} = \frac{D^2}{r} \end{aligned} \tag{A.2}$$

yields to

$$\mathrm{d}H = \frac{1}{4\pi}\frac{i}{r}\cos\phi\,\mathrm{d}\phi \tag{A.3}$$

Integrating over an entire current carrying wire, from ϕ_1 to ϕ_2, the magnetic field is calculated as

$$\begin{aligned} H &= \frac{1}{4\pi}\frac{i}{r}\int_{\phi_1}^{\phi_2}\cos\phi\,\mathrm{d}\phi \\ &= \frac{1}{4\pi}\frac{i}{r}\left(\sin\phi_2 - \sin\phi_1\right) \end{aligned} \tag{A.4}$$

In the case of considering a current-carrying conductor of infinite length, the angle ϕ would vary from $\phi_1 = -90°$ to $\phi_2 = 90°$, and the resulting magnetic field is

$$H = \frac{i}{2\pi r} \tag{A.5}$$

Equation A.5 can be therefore applied to calculate the magnetic field distribution on transformer covers, assuming conductors on infinite length, and being thus the magnetic field purely tangential to the metal surface.

Appendix B

Temperature Measurement

B.1 Test equipment technical data

- **Variable Current Source**

Majo System Integrator - QE01	
Variable current	5000 A
Project number	$10MJ047ELE01$
Series number	455
Date	11/2010

- **Three-phase Power Quality Analyzer**

Power Quality and Energy Analyzer Fluke 435	
Voltage inputs	
Number of inputs	4 (3 phases+neutral) dc-coupled
Maximum input voltage	1000 Vrms
Maximum voltage range	50 V to 5000 V
Maximum peak measurement voltage	6 kV
Input Impedance	4 MΩ // 5 pF
Current inputs	
Number of inputs	4 (3 phases+neutral) dc-coupled
Range	0.1 Arms to 3000 Arms
Input Impedance	50 kΩ
Nominal Frequency	40 Hz to 70 Hz

- **Thermal Imaging Camera**

Fluke P3 Series Thermal Imager	
Model	Ti32
Measurable range	−20 °C to 600 °C
IR Resolution	320 × 240
Measurement accuracy	±2 °C or 2%
	(at 25 °C nominal, whichever is greater)

- **Pt100 RTD Sensors 3-wire construction**

RTD sensors using a 3-wire construction as seen in Fig. B.1, provide accurate temperature measurement. These are the most commonly used in industrial applications where the third wire provides a method for removing the average lead wire resistance from the sensor measurement. The 3-wire circuit works by measuring the resistance between terminals A and B (R_{AB}), and subtracting the resistance between B and b (R_{Bb}), which leaves just the resistance of the RTD sensor R_{RTD} B.1. This method assumes that wires 1, 2, and 3 are all the same resistance.

$$R_{AB} - R_{Bb} = (R_A + R_{RTD} + R_B) - (R_B + R_b) = R_{RTD} \tag{B.1}$$

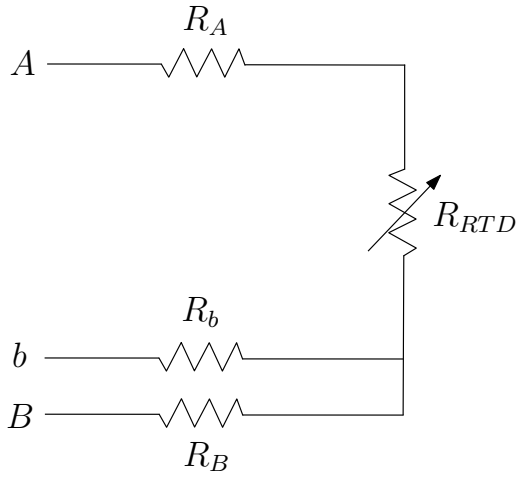

Figure B.1: RTD 3-wire construction.

- **Data Acquisition System**

YOKOGAWA DXAdvanced	
Model	DQStation DX1000
Number of inputs	12
Input type	Resistance Temperature Detector (RTD)
Measurable range	−200 °C to 600 °C
Measuring current	1 mA (Pt100)
Measurement accuracy	±(0.15% of *rdg** + 0.3 °C) (Pt100)

**rdg* is the reading temperature value

DQStation wiring for temperature measurement

The input terminal block from the data acquisition system can be seen in Fig. B.2(a) [93]. Provided that the used Pt100 sensors are 3-wire construction, they are connected for measurement as seen in Fig. B.2(b).

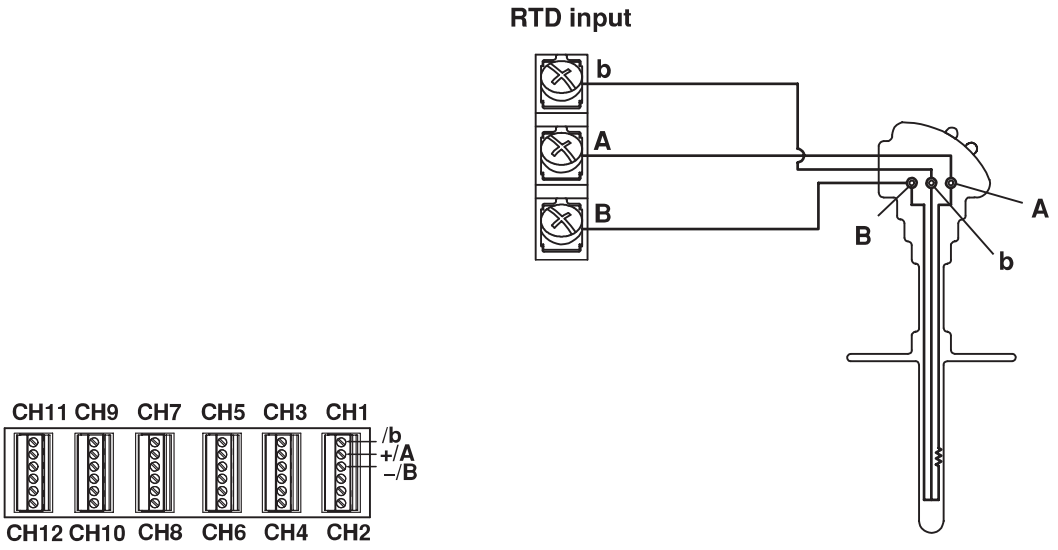

(a) Input terminal block.

(b) Wiring for RTD input.

Figure B.2: DQStation wiring for temperature measurement.

B.2 Measurement error

A sensitivity analysis is introduced in the parameter optimization problem in order to take into account the measurement error, as seen in Section 5.5. Investigation on the accuracy of the temperature measurement is to be investigated in order to perform a more reliable sensitivity analysis. The measurement error introduced from every element present in the measurements is estimated in the next sections.

RTD sensor (Pt100)

Resistance Temperature Detectors (RTDs) are temperature sensors that contain a resistor that changes resistance value as its temperature changes. They have been used for many years to measure temperature in laboratory and industrial processes, and have developed a reputation for accuracy, repeatability, and stability. The IEC standard $60751-2008$ for industrial platinum resistance thermometers and platinum temperature sensors [90] sets two tolerance classes for the accuracy of RTDs.

$$\begin{aligned} &\text{Class A: } \Delta T = \pm(0.30 + 0.005 \cdot |T|) \\ &\text{Class B: } \Delta T = \pm(0.30 + 0.005 \cdot |T|) \end{aligned} \tag{B.2}$$

where $|T|$ is the absolute temperature in °C. Class applies to temperatures from $-200\,°\text{C}$ to $650\,°\text{C}$, and only for RTDs with three- or four-wire configurations (see Appendix B.1). Class B covers the entire range from $-200°\text{C}$ to $850°\text{C}$. Class B is considered for being widely used in industrial applications, thus the highest temperature measured corresponding to a $2500\,\text{A}$ test in sensor T_{s1} is $174.7°\text{C}$, the accuracy is

$$\Delta T = \pm 1.17\,°\text{C} \tag{B.3}$$

and the measurement error due to the RTD sensor, taking T_{s1} as reference is

$$\varepsilon_{\text{Pt100}} = 0.67\,\% \tag{B.4}$$

Data Acquisition Equipment

The error introduced from the acquisition data equipment [93] is given for and integration time greater than $16.7\,\text{ms}$ from

$$\varepsilon_{\text{AcqData}} = \pm 0.15\,\% \text{ of } rdg\ + 0.3\,°\text{C} \tag{B.5}$$

where rdg is the reading temperature, in our case taking temperature of sensor T_{s1} as reference for the error estimation $rdg = 174.7\,°\text{C}$. The integration time used is in auto mode is $16.7\,\text{ms}$ or more, and thus

$$\varepsilon_{\text{AcqData}} = \pm 0.56\,^{\circ}\text{C} = 0.32\,\% \tag{B.6}$$

In addition the is an error of 0.1 °C introduced by the resolution of digital display, resulting

$$\varepsilon_{\text{Display}} = 0.06\,\% \tag{B.7}$$

Measurement Ripple

Due to the influence e.g. of the sensor pressure or other factors, the temperature measurement has some ripple even at steady state. This deviation on the measurement itself is quantified from a 2500 A test measurement and temperature sensor T_{s1}. When steady state is reached, the minimum temperature measured for T_{s1} is 173.3 °C and the maximum value 174.7 °C, yielding thus an error introduced in the measurement of

$$\varepsilon_{\text{Ripple}} = 0.8\,\% \tag{B.8}$$

Sensor Position

To place the temperature sensor on the exact desired position is extremely difficult, introducing thus an error con the comparison measured-computed values. This error is quantified from FE thermal analysis on a 2500 A simulation and temperature sensor T_{s1}. The sensor is positioned at a distance of 30 mm from the steel plate center, and the position error is estimated to be of ±30 mm. The computed temperature of sensor T_{s1} at the exact position is 170.47 °C and at a distance of 33 mm from the steel plate center is 169.19 °C, yielding thus an error introduced in the measurement of

$$\varepsilon_{\text{Position}} = 0.75\,\% \tag{B.9}$$

Source Current

During tests, due to the heating of cables and conductors the resistivity of such conductors varies and so does the current. Although the source current is being controlled during experiments, it is unavoidable that some error is introduced due to the variation of the source current. This error is quantified from simulation, e.g. for a 2500 A test, a ±0.5 % of error in the source current is estimated. Thus, temperature at sensor T_{s1} is calculated for 2500 A and 2512.5 A tests, being 170.47 °C and 171.47 °C respectively, yielding an error in the output temperature of

$$\varepsilon_{\text{Current}} = 0.58\,\% \tag{B.10}$$

Numerical Model

The accuracy of the numerical model is difficult to quantify and though this is not a measurement error, it is involved on the whole methodology of parameter identification, therefore it has to be taken into account. Due to e.g. the FE model mesh, or to the skin depth penetration −volume regions where the power losses are introduced− or other factors, the numerical model does introduce some error on the output temperature. It is difficult to account for this error, but it is estimated as 1 °C, yielding an error of

$$\varepsilon_{\text{Model}} \approx 0.58\,\% \tag{B.11}$$

Appendix C

Nomenclature

$\mathbf{A}$	Magnetic vector potential
A_1, A_2	Coefficients for analytical approximation of BH curve
C_p	Heat capacity
$\mathbf{A_r}$	Reduced magnetic vector potential
$\mathbf{B}$	Magnetic flux density
B_0	Flux density saturation value
$\mathbf{D}$	Electric flux density
$\mathbf{E}$	Electric field
$\mathbf{F}$	Goal objective function
$\mathbf{H}$	Magnetic field
H_k	Magnetic field knee value of BH curve
I	Current
$\mathbf{J}$	Current density
L	Length
N	Winding turns
N_i	Shape function
M	Current image coefficient
P	Power losses, Stray losses
P_v	Hysteresis losses
P_σ	Joule losses
R	Resistance, radius
$\mathbf{S}$	Poynting's Vector
S	Surface
$\mathbf{T}$	Electric vector potential
T	Period, Temperature
T_a	Room temperature
$\mathbf{Z_s}$	Surface Impedance
V	Electric scalar potential, Volume

a	Distance between conductors, distance to tank wall
a_p	Linearization coefficient for non-linear permeability on active power losses
a_q	Linearization coefficient for non-linear permeability on reactive power losses
b	Distance from conductor to x-axis
c_1, c_2	Distance to tank wall, coefficients for analytical approximation of BH curve
d	Plate thickness
d_i	Euclidean distance
f	Frequency, weighting function, objective function
f_1	Accuracy
f_2	Sensitivity
h	Magnetic field instantaneous value, height
h_c	Convective heat exchange coefficient
i	Current instantaneous value
j	Imaginary number, $\sqrt{-1}$
k	Attenuation constant in solid metal, constant coefficient for weighting factor
k_s	Coefficient of wall finite dimensions
k_t	Thermal conductivity
n	Normal direction
n_f	Number of objective functions
n_p	Population size
n_s	Number of sensors
n_Q	Image coefficient
n_v	Number of variables
p	Active power density, loss density
p_σ	Joule loss density
$\mathbf{q_k}$	Heat flux density
q	Reactive power density
t	Time
w_e	Stored electric energy
w_m	Stored magnetic energy
x	Design variable
x, y, z	Components of Cartesian coordinate system
x_p	Stray losses correction factor
$\mathcal{F}$	Magnetomotive force
Γ	Propagation constant
Ω	Domain
Φ	Magnetic scalar potential, Magnetic flux
$\Re$	Magnetic reluctance
$\Re e$	Complex real operator

α	Attenuation constant
β	Phase constant
δ	Field penetration depth
ε	Dielectric permitivity, relative error
ϵ	Radiation heat exchange coefficient or emissivity
λ	Wave length, attain factor
μ	Magnetic permeability
σ	Electric conductivity
σ_r	Stephan-Boltzmann constant
θ	Position angle of cylindrical coordinate system
ω	Angular frequency, search directions
ρ	Electric charge density
$\prec_n$	Crowded comparison operator
ζ	Screening coefficient

Acronyms

3D	Three-dimensional
2D	Two-dimensional
EMF	Electromotive Force
BEM	Boundary Element Method
FDM	Finite Difference Method
FE(M)	Finite Element (Method)
GATT	Goal Attainment Method
HD	Highest Deviation
HV	High Voltage
IBC	Impedance Boundary Condition
IE	Initial Estimation
IEM	Integral Equation Method
IR	Infrared
LV	Low Voltage
MD	Mean Deviation
MO	Multi-Objective
NSGA-II	Non-dominated Sorting Genetic Algorithm-II
PD	Penetration Depth
RNM	Reluctance Network Method
RRN	Reluctance Resistance Network
RTD	Resistance Temperature Detector
SI	Surface Impedance
SO	Single-Objective
TSW	Tertiary Stabilizing Winding

Subscripts

0	Vacuum, initial estimate, zero-sequence
a	amagnetic
abs	Absolute
av	Average
e	Element
h	Hole
i, j, k	Nodal values
im	Imaginary part
L	Linear
l	Lower
m	Maximum
max	Maximum
nl	Non-linear
$perm$	Permitted value
r	Relative, radius, radial component
re	Real part
ref	Reference value
rms	Root mean square
s	Surface, sensor
$subs$	Substitution
sup	Support
Sat	Saturation
U, V, W	Components of a three-phase system
u	Upper
v	Volume
θ	Tangential component
0	Vacuum, initial estimate

Bibliography

[1] J. Sykulski, "Computational electromagnetics for design optimisation: the state of the art and conjectures for the future," *Bulletin of the Polish Academy of Sciences: Technical Sciences*, vol. 57, no. 2, pp. 123–131, 2010.

[2] E. Amoiralis, M. Tsili, and A. Kladas, "Global transformer design optimization using deterministic and non-deterministic algorithms," in *Electrical Machines (ICEM), 2012 XX^{th} International Conference on*, pp. 2323–2331, 2012.

[3] M. Rizzo, A. Savini, and J. Turowski, "Influence of flux collectors on stray losses in transformers," *Magnetics, IEEE Transactions on*, vol. 36, no. 4, pp. 1915–1918, 2000.

[4] A. Pelikant and J. Turowski, "Field and power loss distribution on covers of power transformers," *COMPEL: The International Journal for Computation and Mathematics in Electrical and Electronic Engineering*, vol. 17, no. 3, pp. 302–306, 1998.

[5] J. Turowski, "Rapid evaluation of excessive local heating hazard in bushing turrets of large power transformers," in *Proceedings of International Conference on Electrical Machines, ICEM*, Paper no. 286, Kracow, Poland, Sept. 2004.

[6] J. C. Olivares, J. Canedo, P. Moreno, J. Driesen, R. Escarela, and S. Palanivasagam, "Experimental study to reduce the distribution-transformers stray losses using electromagnetic shields," *Elsvier, Electric Power Systems Research*, vol. 63, pp. 1–7, 2002.

[7] R. Del Vecchio, "Eddy-current losses in a conducting plate due to a collection of bus bars carrying currents of different magnitudes and phases," *Magnetics, IEEE Transactions on*, vol. 39, pp. 549–552, Jan. 2003.

[8] P. Di Barba, M. E. Mognaschi, A. Savini, and J. Turowski, "Cost-effective optimal design of screens in power transformers," in *Computer Engineering in Applied Electromagnetism* (S. Wiak, A. Krawczyk, and M. Trlep, eds.), pp. 41–45, Great Britain: Springer, 2005.

[9] G. Buchgraber, O. Biro, P. Kalcher, and K. Preis, "Computation of temperature rise in transformer bushing adapters," in *Transmission and Distribution Conference and Exposition, 2003 IEEE PES*, vol. 2, pp. 836–840, Sept. 2003.

[10] E. Amoiralis, M. Tsili, and A. Kladas, "Transformer design and optimization: A literature survey," *Power Delivery, IEEE Transactions on*, vol. 24, pp. 1999–2024, Oct. 2009.

[11] S. Kulkarni, J. Olivares, R. Escarela-Perez, V. Lakhiani, and J. Turowski, "Evaluation of eddy current losses in the cover plates of distribution transformers," *Science, Measurement and Technology, IEE Proceedings* -, vol. 151, pp. 313–318, Sept. 2004.

[12] J. Turowski and A. Pelikant, "Eddy current losses and hot-spot evaluation in cover plates of power transformers," *Electric Power Applications, IEE Proceedings* -, vol. 144, pp. 435–440, Nov. 1997.

[13] J. Olivares-Galván, P. Georgilakis, and R. Ocon-Valdez, "A review of transformer losses," *Electric Power Components and Systems*, vol. 37, no. 9, pp. 1046–1062, 2009.

[14] S. Kulkarni and S. Khaparde, "Stray loss evaluation in power transformers-a review," in *Power Engineering Society Winter Meeting, 2000. IEEE*, vol. 3, pp. 2269–2274, Jan. 2000.

[15] J. Turowski, *Technical Electrodynamics*. WNT, Warsaw, 1993.

[16] K. Karsai, D. Kerényi, and L. Kiss, *Large Power Transformers*. Elsvier Science Publication Company, Amsterdam, 1987.

[17] M. Tsili, E. Amoiralis, A. Kladas, and A. Souflaris, "Hybrid numerical-analytical technique for power transformer thermal modeling," *Magnetics, IEEE Transactions on*, vol. 45, no. 3, pp. 1408–1411, 2009.

[18] "Weidmann Electrical Technology - Case studies." `http://www.weidmanntech.com/references/case_studies.htm`. Online; accessed March 2013.

[19] A. Glotic, J. Pihler, N. Sarajlic, M. Kasumovic, and M. Tesanovic, "Differential evolution-based technique for thermal parameters identification of a transformer FEM model," in *Proceedings of* 17^{th} *International Conference on the Computation of Electromagnetic Fields*, pp. 923–924, Florianopolis, Brazil, Nov. 2009.

[20] B. Cranganu-Cretu and M. Schneider, "Coupled electromagnetic-thermal analysis for ABB power transformers," in *International Colloquium Transformer Research and Asset Management*, Cavtat, Croatia, Nov. 2009.

[21] J. Barglik, K. Komeza, B. Ulrych, and S. Wiak, "Numerical modeling of transient heating of solid plate 3D structure," *COMPEL: The International Journal for Computation and Mathematics in Electrical and Electronic Engineering*, vol. 17, no. 1/2/3, pp. 337–341, 1998.

[22] J. Nerg and J. Partanen, "A simplified FEM based calculation model for 3-D induction heating problems using surface impedance formulations," *Magnetics, IEEE Transactions on*, vol. 37, pp. 3719–3722, Sept. 2001.

[23] T. Fawzi, M. Ahmed, and P. Burke, "On the use of the impedance boundary conditions in eddy current problems," *Magnetics, IEEE Transactions on*, vol. 21, pp. 1835–1840, Sept. 1985.

[24] O. Biro, K. Preis, U. Baumgartner, and G. Leber, "Numerical modeling of transformer losses," in *International Colloquium Transformer Research and Asset Management*, Cavtat, Croatia, Nov. 2009.

[25] K. Komeza, H. Welfle, and S. Wiak, "Transient states analysis of 3D transformer structure," *COMPEL: The International Journal for Computation and Mathematics in Electrical and Electronic Engineering*, vol. 17, no. 1/2/3, pp. 252–256, 1998.

[26] S. Wiak, P. Drzymala, and H. Welfle, "3D Computer field model of power transformer - Magnetic field and power losses computation," in *Electrical Machines (ICEM), 2010 XIX International Conference on*, pp. 1–6, 2010.

[27] A. Milagre, M. Ferreira da Luz, G. Cangane, A. Komar, and P. Avelino, "3D calculation and modeling of eddy current losses in a large power transformer," in *Electrical Machines (ICEM), 2012 XXth International Conference on*, pp. 2282–2286, Sept. 2012.

[28] A. Sitzia, A. Baker, A. Davies, and L. Clough, "Specialised software tools for transformer analysis," in *International Colloquium Transformer Research and Asset Management*, Cavtat, Croatia, Nov. 2009.

[29] X. M. Lopez-Fernandez, P. Penabad-Duran, J. Turowski, and P. M. Ribeiro, "Non linear heating hazard assessment on transformer covers and tank walls," *Przeglad Elektrotechniczny (Electrical Review)*, vol. 88, no. 7b, pp. 28–31, 2012.

[30] E. Amoiralis, M. Tsili, and P. Georgilakis, "The state of the art in engineering methods for transformer design and optimization: a survey," *Journal of optoelectronics and advanced materials*, vol. 10, pp. 1149–1158, May 2008.

[31] H. Kerr and S. Palmer, "Developments in the design of large power transformers," *Electrical Engineers, Proceedings of the Institution of*, vol. 111, pp. 823–832, Apr. 1964.

[32] J. Turowski, M. Turowski, and M. Kopec, "Method of three-dimensional network solution of leakage field of three-phase transformers," *Magnetics, IEEE Transactions on*, vol. 26, pp. 2911–2919, Sept. 1990.

[33] A. Krawczyk and J. Turowski, "Recent development in eddy current analysis," *Magnetics, IEEE Transactions on*, vol. 23, pp. 3032–3037, Sept. 1987.

[34] S. V. Kulkarni, "Coupled field computations for analysis of intricate phenomena in transformers," in *Advanced Research Workshop on Transformers, ARWtr*, Baiona, Spain, 29-31, Oct. 2007.

[35] M. Djurovic and C. Carpenter, "3-dimensional computation of transformer leakage fields and associated losses," *Magnetics, IEEE Transactions on*, vol. 11, pp. 1535–1537, Sept. 1975.

[36] X. Dexin, T. Yunqiu, and X. Zihong, "FEM analysis of 3D eddy current field in power transformer," *Magnetics, IEEE Transactions on*, vol. 23, pp. 3786–3788, Sept. 1987.

[37] S. Holland, G. O'Connell, and L. Haydock, "Calculating stray losses in power transformers using surface impedance with finite elements," *Magnetics, IEEE Transactions on*, vol. 28, pp. 1355–1358, Mar. 1992.

[38] O. Biro, K. Preis, W. Renhart, K. Richter, and G. Vrisk, "Performance of different vector potential formulations in solving multiply connected 3-D eddy current problems," *Magnetics, IEEE Transactions on*, vol. 26, pp. 438–441, Mar. 1990.

[39] Z. Valkovic, "Calculation of the losses in three-phase transformer tanks," *Generation, Transmission and Distribution, IEE Proceedings C*, vol. 127, pp. 20–25, Jan. 1980.

[40] M. Jain and L. Ray, "Field pattern and associated losses in aluminum sheet in presence of strip bus bars," *Power Apparatus and Systems, IEEE Transactions on*, vol. PAS-89, pp. 1525–1539, Sept. 1970.

[41] M. Rizzo, A. Savini, and J. Turowski, "Dependence of forces, eddy current and stray losses on screening in power transformers," in *Electrical Machines and Systems, 2001. ICEMS 2001. Proceedings of the Fifth International Conference on*, vol. 1, pp. 182–185 vol.1, 2001.

[42] S. Wiak, A. Pelikant, and J. Turowski, "Solution of TEAM workshop problem 7 by Reluctance Network Method (Asymmetrical conductor with a hole)," *COMPEL: The International Journal for Computation and Mathematics in Electrical and Electronic Engineering*, vol. 13, no. 1, pp. 59–62, 1994.

[43] S. Wiak, A. Pelikant, and J. Turowski, "Magnetostatic field calculation of 3-D non-linear model by reluctance network method (Problem No.13-TEAM

Workshop)," *COMPEL: The International Journal for Computation and Mathematics in Electrical and Electronic Engineering*, vol. 11, no. 1, pp. 217–220, 1992.

[44] R. M. Wojciechowski, A. Demenko, and J. K. Sykulski, "Inducted currents analysis in multiply connected conductors using reluctance-resistance networks," *COMPEL: The International Journal for Computation and Mathematics in Electrical and Electronic Engineering*, vol. 29, no. 4, pp. 908–918, 2010.

[45] L. Turner, "An integral equation approach to eddy-current calculations," *Magnetics, IEEE Transactions on*, vol. 13, pp. 1119–1121, Sept. 1977.

[46] C. Biddlecombe, C. Collie, J. Simkin, and C. Trowbridge, "The integral equation method applied to eddy currents," in *COMPUMAG Conference on the Computation of Magnetic Fields*, pp. 363–371, 1976.

[47] Y. Higuchi, M. Koizumi, and S. Saito, "Three dimensional eddy current calculation with integral equation method for transformers," *Magnetics, IEEE Transactions on*, vol. 33, pp. 1310–1313, Mar. 1997.

[48] K. Ishibashi, "Nonlinear eddy current analysis by volume integral equation method," *Magnetics, IEEE Transactions on*, vol. 23, pp. 3038–3040, Sept. 1987.

[49] T. Renyuan, Y. Junyou, L. Feng, and L. Yongping, "Solutions of three-dimensional multiply connected and open boundary problems by BEM in three-phase combination transformers," *Magnetics, IEEE Transactions on*, vol. 28, pp. 1340–1343, Mar. 1992.

[50] K. Komeza and S. Wiak, "Electromagnetic field calculation of a leakage transformer by means of finite element method with Hermitian elements," *COMPEL: The International Journal for Computation and Mathematics in Electrical and Electronic Engineering*, vol. 13, no. 1, pp. 97–100, 1994.

[51] O. Biro and K. Preis, "Finite element analysis of 3-D eddy currents," *Magnetics, IEEE Transactions on*, vol. 26, pp. 418–423, Mar. 1990.

[52] O. Biro, K. Preis, and K. Richter, "Various FEM formulations for the calculation of transient 3D eddy currents in nonlinear media," *Magnetics, IEEE Transactions on*, vol. 31, pp. 1307–1312, May 1995.

[53] Z. Ren, "T-ϕ formulation for eddy-current problems in multiply connected regions," *Magnetics, IEEE Transactions on*, vol. 38, pp. 557–560, Mar. 2002.

[54] P. R. Kotiuga, "On making cuts for magnetic scalar potentials in multiply connected regions," *Journal of Applied Physics*, vol. 61, pp. 3916–3918, Apr. 1987.

[55] A. T. Phung, O. Chadebec, P. Labie, Y. Le Floch, and G. Meunier, "Automatic cuts for magnetic scalar potential formulations," *Magnetics, IEEE Transactions on*, vol. 41, pp. 1668–1671, May 2005.

[56] *International Compumag Society. Testing electromagnetic analysis methods (T.E.A.M.)*, Dec. 2012. Online.

[57] O. Biro and K. Preis, "An edge finite element eddy current formulation using a reduced magnetic and a current vector potential," *Magnetics, IEEE Transactions on*, vol. 36, pp. 3128–3130, Sept. 2000.

[58] D. Albertz and G. Henneberger, "Calculation of 3D eddy current fields using both electric and magnetic vector potential in conducting regions," *Magnetics, IEEE Transactions on*, vol. 34, pp. 2644–2647, Sept. 1998.

[59] P. Agarwal, "Eddy-current losses in solid and laminated iron," *American Institute of Electrical Engineers, Part I: Communication and Electronics, Transactions of the*, vol. 78, pp. 169–181, May 1959.

[60] Y. Higuchi and M. Koizumi, "Integral equation method with surface impedance model for 3D eddy current analysis in transformers," *Magnetics, IEEE Transactions on*, vol. 36, pp. 774–779, Jul. 2000.

[61] E. Rosenberg, "Eddy currents in iron masses," *Electrician, London, England*, vol. 91, pp. 188–191, Aug. 1923.

[62] F. J. Vogel and E. J. Adolphson, "A stray loss problem in transformer tanks," *Power Apparatus and Systems, Part III. Transactions of the American Institute of Electrical Engineers*, vol. 73, pp. 760–764, Jan. 1954.

[63] H. Poritsky and R. P. Jerrard, "Eddy-current losses in a semi-infinite solid due to a nearby alternating current," *American Institute of Electrical Engineers, Part I: Communication and Electronics, Transactions of the*, vol. 73, pp. 97–106, May 1954.

[64] W. G. Deuring, "Induced losses in steel plates in the presence of an alternating current," *Power Apparatus and Systems, Part III. Transactions of the American Institute of Electrical Engineers*, vol. 76, pp. 166–171, Apr. 1957.

[65] M. Kozlowski and J. Turowski, "Stray losses and local overheating hazard in transformers," in *Conseil International Rèseaux Electriques Conference (CIGRE)*, Paper no. 12-10, Paris-France, Aug. 1972.

[66] M. Krakowski, M. Kazmierski, and I. Kersz, "Effect of current distribution in parallel bars on electromagnetic field at nearby steel wall," *Electric Power Applications, IEE Proceedings B*, vol. 136, pp. 161–167, Jul. 1989.

[67] M. Motalleb, M. Vakilian, and A. Abbaspour, "Calculation of eddy current losses caused by leads and other current sources in high current power transformers," in *Australasian Universities Power Engineering Conference (AUPEC)*, 2008.

[68] D. Koppikar, S. Kulkarni, S. Khaparde, and S. Jha, "Evaluation of eddy losses due to high current leads in transformers," *Science, Measurement and Technology, IEE Proceedings* -, vol. 144, pp. 34–38, Jan. 1997.

[69] G. Sironi and J. Van Hulse, "Eddy current losses in solid iron pieces under three-dimensional magnetic field," *Magnetics, IEEE Transactions on*, vol. 14, pp. 377 – 379, Sept. 1978.

[70] D. Pavlik, D. Johnson, and R. Girgis, "Calculation and reduction of stray and eddy losses in core-form transformers using a highly accurate finite element modelling technique," *Power Delivery, IEEE Transactions on*, vol. 8, pp. 239–245, Jan. 1993.

[71] C. Guerin, G. Tanneau, and G. Meunier, "3D eddy current losses calculation in transformer tanks using the finite element method," *Magnetics, IEEE Transactions on*, vol. 29, pp. 1419–1422, Mar. 1993.

[72] C. Yongbin, Y. Junyou, Y. Hainian, and T. Renyuan, "Study on eddy current losses and shielding measures in large power transformers," *Magnetics, IEEE Transactions on*, vol. 30, pp. 3068–3071, Sept. 1994.

[73] T. Renyuan, L. Yan, L. Feng, and T. Lijian, "Resultant magnetic fields due to both windings and heavy current leads in large power transformers," *Magnetics, IEEE Transactions on*, vol. 32, pp. 1641–1644, May 1996.

[74] S. Saito, K. Inagaki, T. Sato, Y. Inui, K. Okuyama, and H. Otani, "Eddy currents in structure surrounding large current bushings of a large capacity transformer," *Power Apparatus and Systems, IEEE Transactions on*, vol. PAS-100, pp. 4502–4509, Nov. 1981.

[75] T. Renyuan, Y. Junyou, W. Zhouxiong, L. Feng, L. Chunrong, and X. Zihong, "Computation of eddy current losses by heavy current leads and windings in large transformers using IEM coupled with improved R-ψ method," *Magnetics, IEEE Transactions on*, vol. 26, pp. 493–496, Mar. 1990.

[76] Y. Junyou, T. Renyuan, L. Yan, and C. Yongbin, "Eddy current fields and overheating problems due to heavy current carrying conductors," *Magnetics, IEEE Transactions on*, vol. 30, pp. 3064–3067, Sept. 1994.

[77] D. Kim, S. Hahn, and S. Kim, "Improved design of cover plates of power transformers for lower eddy current losses," *Magnetics, IEEE Transactions on*, vol. 35, pp. 3529–3531, Sept. 1999.

[78] J. Olivares, R. Escarela-Perez, S. Kulkarni, F. de Leon, E. Melgoza-Vasquez, and O. Hernandez-Anaya, "Improved insert geometry for reducing tank-wall losses in pad-mounted transformers," *Power Delivery, IEEE Transactions on*, vol. 19, pp. 1120–1126, Jul. 2004.

[79] J. Olivares, R. Escarela-Perez, S. Kulkarni, F. De Leon, and M. Venegas-Vega, "2D finite-element determination of tank wall losses in pad-mounted transformers," *Elsvier, Electric Power Systems Research*, vol. 71, pp. 179–185, 2004.

[80] J. Olivares-Galván, S. Magdaleno-Adame, E. Campero-Littlewood, R. Escarela-Perez, and P. Georgilakis, "Techno-economic evaluation of reduction of low-voltage bushings diameter in single-phase distribution transformers," *Electric Power Components and Systems*, vol. 39, no. 13, pp. 1388–1402, 2011.

[81] X. M. Lopez-Fernandez, P. Penabad-Duran, and J. Turowski, "Three-dimensional methodology for the overheating hazard assessment on transformer covers," *Industry Applications, IEEE Transactions on*, vol. 48, pp. 1549 –1555, Sept.-Oct. 2012.

[82] J. Sykulski, *Computational Magnetics*. Chapman & Hall, 1995.

[83] J. H. Poynting, "On the transfer of energy in the electromagnetic field," *Philosophical Transactions of the Royal Society*, vol. 175, Part II, pp. 343–361, Jan. 1884.

[84] S. Kulkarni and S. Khaparde, *Transformer Engineering Design and Practice*. Marcel Dekker, 2004.

[85] W. Smythe, *Static and dynamic electricity*. McGraw-Hill Book Company, 1950.

[86] W. MacLean, "Theory of strong electromagnetic waves in massive iron," *Journal of Applied Physics*, vol. 25, pp. 1267–1270, Oct 1954.

[87] C. Guerin, G. Meunier, and G. Tanneau, "Surface impedance for 3D nonlinear eddy current problems-application to loss computation in transformers," *Magnetics, IEEE Transactions on*, vol. 32, pp. 808–811, May 1996.

[88] E. Deeley, "Flux penetration in two dimensions into saturating iron and the use of surface equations," *Electrical Engineers, Proceedings of the Institution of*, vol. 126, pp. 204–208, Feb. 1979.

[89] J. A. Dias Pinto, *Thermographic Analysis Aided by Computer of Electromagnetic Devices*. PhD thesis, Univ. Coimbra-Portugal, 1992.

[90] "IEC-60751:2008 - Industrial platinum resistance thermometers and platinum temperature sensors," tech. rep., IEC - International Electrotechnical Commission, 2008.

[91] "Omega engineering - RTD resistance temperature detectors." http://www.omega.com/Temperature/pdf/RTD_Gen_Specs_Ref.pdf. Online; accessed March 2013.

[92] "ARCTIC MX-3 Thermal Compound." http://www.arctic.ac/en/p/detail?sArticle=31.%3F. Online; accessed March 2013.

[93] "Daqstation DX1000 \ DX1000N - Operation Guide & Users manual," tech. rep., DXAdvanced-Yokogawa Electric Corporation, 2005.

[94] "FLIR 600 Series - Users manual," tech. rep., FLIR Systems, 2011.

[95] K. Price, R. Storn, and L. J.A, *Differential Evolution: A Practical Approach to Global Optimization*. Berlin, Germany: Springer-Verlag, 2005.

[96] P. Di Barba, *Multiobjective Shape Design in Electricity and Magnetism*. Springer, 2010.

[97] J. Kennedy and R. Eberhart, "Particle swarm optimization," in *Neural Networks, 1995. Proceedings., IEEE International Conference on*, vol. 4, pp. 1942–1948, Nov./Dec. 1995.

[98] P. Neittaanmäki, M. Rudnicki, and A. Savini, *Inverse problems and Optimal Design in Electricity and Magnetism*. Oxford University Press, USA, 1996.

[99] P. Di Barba, A. Savini, and S. Wiak, *Field Models in Electricity and Magnetism*. Springer, Toronto, ON, Canada, 2008.

[100] P. Di Barba and A. Savini, "Recent advances of automated optimal design in low-frequency electromagnetics - a survey," *COMPEL: The International Journal for Computation and Mathematics in Electrical and Electronic Engineering*, vol. 17, no. 1/2/3, pp. 29–35, 1998.

[101] *Proceedings of Optimization and Inverse Problems in Electromagnetism*. (M. Rudnicki and Wiak, S., eds.), Kluwer Academic Publishers, 2003.

[102] "TDO transformer design optimization." http://tdosolution.com/modules/. Online; accessed March 2013.

[103] K. Bednarek, "Heat and optimization problems in heavy current electric equipment," in *XII International Symposium of Electromagnetic Fields (ISEF)*, Baiona, Spain, Sept. 2005.

[104] P. Di Barba, A. Savini, and S. Wiak, "Application of global optimization strategies to the shape design of a transformer winding," *Elsevier - Advances in Engineering Software*, vol. 19, no. 2, pp. 121–125, 1994.

[105] P. Di Barba, U. Piovan, and A. Savini, "Optimal shape design of the HV winding of a test transformer," *COMPEL: The International Journal for Computation and Mathematics in Electrical and Electronic Engineering*, vol. 17, no. 1/2/3, pp. 128–134, 1998.

[106] E. Amoiralis, P. Georgilakis, M. Tsili, and A. Kladas, "Global transformer optimization method using evolutionary design and numerical field computation," *Magnetics, IEEE Transactions on*, vol. 45, pp. 1720–1723, Mar. 2009.

[107] J. Allegre, C. Marchand, and A. Razek, "Identification of thermal parameters in a coupled magnetic-thermal model with the experimental designs method," *COMPEL: The International Journal for Computation and Mathematics in Electrical and Electronic Engineering*, vol. 17, no. 1/2/3, pp. 331–336, 1998.

[108] P. Kitak, I. Ticar, J. Pihler, O. Biro, and K. Preis, "Improvement in accuracy of thermal FEM model partition wall with the use of optimization algorithm," in *Proceedings of* 17_{th} *International Conference on the Computation of Electromagnetic Fields*, pp. 923–924, Florianopolis, Brazil, Nov. 2009.

[109] P. Kitak, J. Popovic, A. Glotic, and I. Ticar, "Calculation of thermal coefficients of a metal partition wall by FEM analysis," *Przeglad Elektrotechniczny (Electrical Review)*, vol. 87, no. 3, pp. 96–98, 2011.

[110] P. Kitak, A. Glotic, I. Ticar, and J. Pihler, "Multiobjective optimization for determination of the electrothermal parameters in switchgear cell housing," *Magnetics, IEEE Transactions on*, vol. 47, no. 5, pp. 1302–1305, 2011.

[111] M. Battistetti, P. Di Barba, F. Dughiero, M. Farina, S. Lupi, and A. Savini, "Optimal design of an inductor for transverse flux heating using a combined evolutionary-simplex method," *COMPEL: The International Journal for Computation and Mathematics in Electrical and Electronic Engineering*, vol. 20, no. 2, pp. 507–522, 2001.

[112] P. Di Barba and M. E. Mognaschi, "Recent experiences of multiobjective optimisation in electromagnetics - a comparison of methods," *COMPEL: The International Journal for Computation and Mathematics in Electrical and Electronic Engineering*, vol. 24, no. 3, pp. 921–930, 2005.

[113] MATLAB, *version 7.9 (R2009b)*. Natick, Massachusetts: The MathWorks Inc., 2009.

[114] "Flux3D FEM- Software Package (v.11.1.1)." `http://www.cedrat.com/en/software/flux.html`. Online; accessed March 2013.

[115] "Simulink- Simulation and Model Based Design." `http://www.mathworks.com/products/matlab/`. Online; accessed March 2013.

[116] P. Di Barba, "A fast evolutionary method for identifying non-inferior solutions in multicriteria shape optimization of a shielded reactor," *COMPEL: The International Journal for Computation and Mathematics in Electrical and Electronic Engineering*, vol. 20, no. 3, pp. 762–776, 2001.

[117] "Mathworks- Global Optimization Toolbox." `http://www.mathworks.com/products/global-optimization/`. Online; accessed March 2013.

[118] R. Rudramoorthy, *Thermal Engineering*. Tata McGraw-Hill, 2003.

[119] L. Susnjic, Z. Haznadar, and Z. Valkovic, "3D Finite Element determination of stray losses in power transformers," *Elsvier, Electric Power Systems Research*, vol. 78, pp. 1841–1818, 2008.

[120] J. Turowski, "Stray losses, screening, and local excessive heating hazard in large power transformers," in *Transformers. Analysis, design and measurement* (X. M. Lopez-Fernandez, H. B. Ertan, and J. Turowski, eds.), Boca Raton, FL, USA: CRC Press, 2013.

[121] "MatWeb- Material Property Data. AISI 1000 Series Steel." `http://www.matweb.com/search/DataSheet.aspx?MatGUID=81a26031d1b44cbb911f70ab863281f5`. Online; accessed April 2013.

[122] "All about circuits - Temperature coefficient of resistance." `http://www.allaboutcircuits.com/vol_1/chpt_12/6.html`. Online; accessed April 2013.

[123] "Conversion Tables: Electrical Values." `http://www.sapiensman.com/conversion_tables/electric_conversion.htm`. Online; accessed April 2013.

[124] K. Deb, A. Pratap, S. Agarwal, and T. Meyarivan, "A fast and elitist multiobjective genetic algorithm: NSGA-II," *IEEE Transactions on evolutionary computation*, vol. 6, pp. 182–197, Apr. 2002.

[125] F. W. Gembicki, *Vector Optimization for Control with Performance and Parameter Sensitivity Indices*. PhD thesis, Case Western Reserve Univ. - Cleveland, Ohio, 1974.

[126] Y. Collette and P. Siarry, *Multiobjective Optimization: Principles and Case Studies*. Decision Engineering, Springer, 2012.

[127] P. Di Barba, M. Farina, and A. Savini, "An improved technique for enhancing diversity in pareto evolutionary optimization of electromagnetic devices," *COMPEL: The International Journal for Computation and Mathematics in Electrical and Electronic Engineering*, vol. 20, no. 2, pp. 482–496, 2001.

[128] "Euro Inox - Stainless Steel. Tables of Technical Properties." `http://www.euro-inox.org/pdf/map/Tables_TechnicalProperties_EN.pdf`. Online; accessed May 2013.

[129] "United Alloys - Product guide." `http://www.united-alloys.com/catalogues/ua_product_guide_10-11.pdf`. Online; accessed May 2013.

[130] P. Penabad-Duran, X. M. Lopez-Fernandez, J. Turowski, and P. Ribeiro, "3D heating hazard assessment on transformer covers. Arrangement decisions," *COMPEL: The International Journal for Computation and Mathematics in Electrical and Electronic Engineering*, vol. 31, no. 2, pp. 703–715, 2012.

[131] P. Penabad-Duran, C. Alvarez-Mariño, and X. M. Lopez-Fernandez, "Transformer tertiary stabilizing windings. Part II: Overheating hazard on tank walls," in *Electrical Machines (ICEM), 2012 XX^{th} International Conference on*, pp. 2369–2374, 2012.

[132] P. Penabad-Duran, X. M. Lopez-Fernandez, and C. Alvarez-Mariño, "Transformer tertiary stabilizing windings. Part I: Apparent power rating," in *Electrical Machines (ICEM), 2012 XX^{th} International Conference on*, pp. 2362–2368, 2012.

[133] B. Cogbill, "Are stabilizing windings necessary in all y-connected transformers?," *Power Apparatus and Systems, Part III. Transactions of the American Institute of Electrical Engineers*, vol. 78, no. 3, pp. 963–970, 1959.

[134] M. A. Tsili and S. A. Papathanassiou, "Zero sequence flux protection of a three-limb core power transformer," in *Electrical Machines (ICEM), 17^{th} International Conference on*, pp. 1–7, 2006.

[135] O. T. Farry, "Tertiary windings in autotransformers," *Power Apparatus and Systems, Part III. Transactions of the American Institute of Electrical Engineers*, vol. 80, no. 3, pp. 78–82, 1961.

[136] X. M. Lopez-Fernandez, C. Alvarez-Mariño, P. Penabad-Duran, and J. Turowski, "RNM2D_0 Fast Stray Losses Hazard Evaluation on Transformer Tank Wall & Cover due to Zero Sequence," in *Proc. of* 3^{rd} *Advanced Research Workshop on Transformers, ARWtr*, Santiago de Compostela, Spain, 3-6 Oct. 2010.

[137] J. Turowski, "Fast Computation of Coupled Fields in Complex, 3-D, Industrial Electromagnetic Structures," *COMPEL: The International Journal for Computation and Mathematics in Electrical and Electronic Engineering*, vol. 17, no. 4, pp. 489–505, 1998.

[138] X. M. Lopez-Fernandez, J. Turowski, D. Souto-Revenga, and A. Soto-Rodriguez, "Upgrading of Large Transformers 3D-Design: Energy-Saving and Reliability of Electric Power System," in *Proc. of* 2^{nd} *International Conference on Electrical Engineering (CEE)*, pp. 580–585, 2007.

[139] J. Turowski, "Reluctance networks," in *Computational Magnetics* (J. Sykulski, ed.), London: Chapman & Hall, 1990.

[140] P. Penabad-Duran and X. M. Lopez-Fernandez, "Part A: Introduction to FEM Analysis," in *ARWtr FEM Turotial. Finite Element Method applied to design and analysis in power transformers* (X. M. Lopez-Fernandez, ed.), 2010, ISBN:978-84-614-3527-2.

[141] R. Allcock, S. Holland, and L. Haydock, "Calculation of zero phase sequence impedance for power transformers using numerical methods," *Magnetics, IEEE Transactions on*, vol. 31, no. 3, pp. 2048–2051, 1995.

[142] *Electrical Transmission and Distribution Reference Book*. East Pittsburgh, Pennsylvania: Westinghouse Electric Corporation, 1964.